Electrochemical reduction of NOx

Traulsen, Marie Lund

Publication date:
2012

Document Version
Publisher's PDF, also known as Version of record

Department of Energy Conversion and Storage

Technical University of Denmark

Electrochemical reduction of NO_x

PhD Thesis

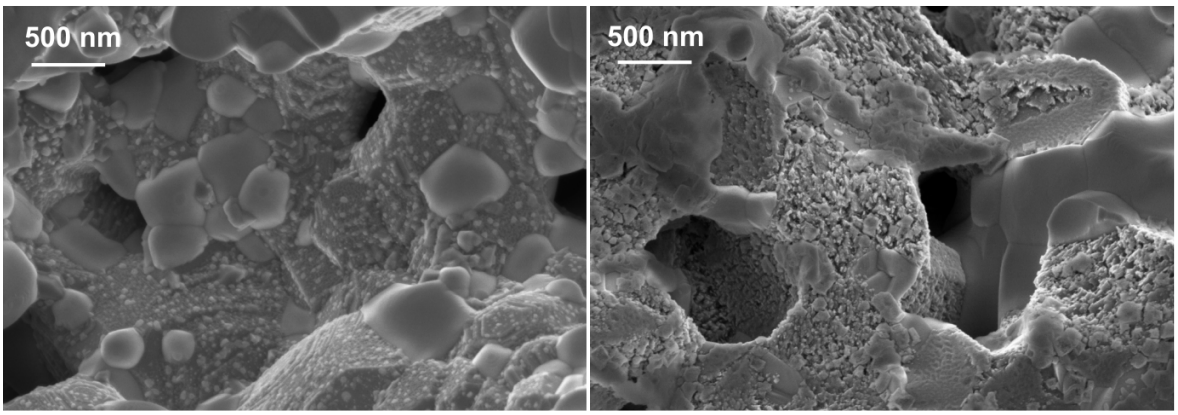

Marie Lund Traulsen

April 2012

Cover: $La_{0.85}Sr_{0.15}MnO_{3-\delta}$-$Ce_{0.9}Gd_{0.1}O_{1.95}$ electrode of a porous 11-layer cell stack impregnated with BaO. On this kind of electrode 60% NO_x conversion was achieved in a gas composition of 1000 ppm NO + 10% O_2 at 400 °C. The image to the left shows the electrode microstructure before test and the image to the right the microstructure after test.

Preface

This thesis is submitted to the Technical University of Denmark to finalise the PhD study *Electrochemical Reduction of NO_x* which was carried out from 1st May 2009 to 30th April 2012. The PhD study was financed by the Danish Strategic Research Council under contract no. 09-065186. The project was hosted by the Fuel Cell and Solid State Chemistry Division at Risø DTU, which due to organisational changes became part of the newly established Department of Energy Conversion and Storage at Technical University of Denmark from the 1st January 2012. These organisational changes had no influence on the accomplishment of the PhD project.

The PhD project was supervised by senior scientist Kent Kammer Hansen and the daily work was carried out in the Gas Purification Work Group.

After three years of PhD studies I owe thanks to many colleagues, who have been a great help during the project. This help has been greatly appreciated and invaluable for the completion of the project.

Especially I would like to thank:

- my supervisor Kent Kammer Hansen for patient encouragement during the project and for giving me time and space to grow as a researcher.
- the entire Gas Purification Work Group for being excellent colleagues both during work and during relaxed lunch conversations.
- the technical staff, who many times have helped me solving both predicted and unpredicted practical issues.

Marie Lund Traulsen, Roskilde, Denmark, April 2012

Abstract

NO and NO_2 (collectively referred to as NO_x) are air pollutants, and the largest single contributor to NO_x pollution is automotive exhaust. This study investigates electrochemical deNO_x, a technology which aims to remove NO_x from automotive diesel exhaust by electrochemical reduction of NO_x to N_2 and O_2. The focus in this study is on improving the activity and selectivity of solid oxide electrodes for electrochemical deNO_x by addition of NO_x storage compounds to the electrodes.

Two different composite electrodes, $La_{0.85}Sr_{0.15}MnO_{3-\delta}$-$Ce_{0.9}Gd_{0.1}O_{1.95}$ (LSM15-CGO10) and $La_{0.85}Sr_{0.15}FeO_{3-\delta}$-$Ce_{0.9}Gd_{0.1}O_{1.95}$ (LSF15-CGO10), have been investigated in combination with three different NO_x storage compounds: BaO, K_2O and MnO_x. The main focus in the investigation has been on conversion measurements and electrochemical characterization, the latter by means of electrochemical impedance spectroscopy and cyclic voltammetry. In addition, infrared spectroscopy has been performed to study how NO_x adsorption on the electrodes is affected by the presence of the aforementioned NO_x storage compounds. Furthermore, non-tested and tested electrode microstructures have been thoroughly evaluated by scanning electron microscopy.

The studies reveal addition of MnO_x or K_2O to the electrodes cause severe degradation problems, and addition of these compounds is thus unsuitable for electrode improvement. In contrast, addition of BaO to LSM15-CGO10 electrodes is shown to have a very positive impact on the NO_x conversion. The increased NO_x conversion, following the BaO addition, is attributed to a combination of 1) a decreased electrode polarisation resistance and 2) an altered NO_x adsorption. The NO_x conversion is observed to increase strongly with polarisation, and during 9 V polarisation of an 11-layer porous cell stack, 60% NO_x conversion in a mixture of 1000 ppm NO and 10% O_2 is achieved at 400 °C on entirely ceramic electrodes.

This project thus demonstrates electrochemical deNO_x is possible without the presence of noble metals at realistic operating conditions. However, several questions remain, among these how the the BaO interacts with the solid oxide electrodes and how the electrochemical cell is optimally operated during electrochemical deNO_x.

Dansk resumé

NO_x er en fællesbetegnelse for gasserne NO og NO_2. NO_x udledning bidrager til luftforureningen, og det største enkeltbidrag til NO_x forureningen stammer fra biludstødning. I dette projekt studeres teknologien elektrokemisk deNO_x, som er rettet mod rensning af dieseludstødning ved hjælp af elektrokemisk reduktion af NO_x til N_2 og O_2. Fokus i projektet er på forbedring af fastoxid elektroders aktivitet og selektivitet i forhold til elektrokemisk deNO_x, forbedringen forsøges opnået ved tilføjelse af NO_x lagrings forbindelser til elektroderne.

To forskellige typer komposit elektroder, $La_{0.85}Sr_{0.15}MnO_{3-\delta}$-$Ce_{0.9}Gd_{0.1}O_{1.95}$ (LSM15-CGO10) og $La_{0.85}Sr_{0.15}FeO_{3-\delta}$-$Ce_{0.9}Gd_{0.1}O_{1.95}$ (LSF15-CGO10), er blevet undersøgt i kombination med tre forskellige NO_x lagrings forbindelser: BaO, K_2O og MnO_x. Hovedfokus i undersøgelsen har været på omsætningsmålinger og elektrokemisk karakterisering, sidstnævnte ved hjælp elektrokemisk impedans spektroskopi og cyklisk voltammetri. Derudover er der udført infrarød spektroskopi for at undersøge, hvordan NO_x adsorptionen på elektroderne påvirkes af tilstedeværelsen af de førnævnte NO_x lagrings forbindelser. Endelig er mikrostrukturen af testede og ikke-testede elektroder blevet grundigt undersøgt med scanning elektron mikroskopi.

Undersøgelsen viser, at tilføjelse af MnO_x og K_2O er uegnet til forbedring af elektroderne, da tilstedeværelse af MnO_x og K_2O medfører en fatal degradering. Derimod har tilføjelse af BaO til elektroderne en klart positiv effekt på NO_x omsætningen. Den øgede NO_x omsætning som følge af BaO tilsætning kan tilskrives en kombination af 1) en sænkning af elektrodens polariserings-modstand og 2) en ændring i NO_x adsorptionen. NO_x omsætningen stiger kraftigt med stigende polarisering og ved 9 V polarisering ved 400 °C af en 11-lags, porøs cellestak opnås 60 % NO_x omsætning i en blanding bestående af 1000 ppm NO og 10 % O_2, denne omsætning opnås på udelukkende keramiske elektroder.

Dette projekt demonstrerer dermed, at elektrokemisk deNO_x er mulig under realistiske forhold uden brug af ædelmetaller. Flere spørgsmål savner dog stadig et svar, heriblandt hvordan BaO interagerer med fastoxid elektroderne samt hvordan en elektrokemisk celle skal drives optimalt under elektrokemisk deNO_x.

Table of Contents

Table of Contents

Table of Contents

1 Introduction

NO_x is the collective name for the compounds NO (nitric oxide) and NO_2 (nitrogen dioxide), which both are atmospheric pollutants[1]. The largest single contributor to NO_x emission in Europe is road transport, which in 2008 was responsible for 39.6% of the total European NO_x emissions[2]. In order to decrease the NO_x emissions from road transport increasingly stricter emission limits has been imposed on the NO_x emission during the last 20 years[3] which has established a need for technologies, which can remove NO_x from automotive exhaust, just as excess hydrocarbons and CO needs to be removed. This project is related to the development of a new technology for NO_x removal from automotive diesel exhaust, the name of the technology is electrochemical deNO_x. The project deals with studies and improvement of the catalyst/electrodes used during electrochemical deNO_x, as the activity and selectivity of the electrodes must be improved before the technology can be developed into a commercial state[4]. In a future perspective the goal is to expand the electrochemical deNO_x technology to also include electrochemical oxidation of hydrocarbon and soot, and thus develop a technology, which in one single component can clean automotive diesel exhaust from both NO_x, hydrocarbons and soot. This is however the future goal, and as stated the focus in this project is only on electrochemical deNO_x.

In this introduction chapter the formation of the NO_x in diesel engines will be briefly explained and an overview will be given of alternative technologies for NO_x removal from diesel exhaust. Thereafter a literature survey of the development within electrochemical deNO_x will be given.

1.1 NO_x pollution

NO is formed in high-compression internal combustion engines in three ways[5]: 1) by oxidation of nitrogen-containing hydrocarbons in the fuel; 2) by reaction between fuel hydrocarbons and N_2 and subsequent oxidation, or 3) by reaction between N_2 and O_2 in the air through the Zeldovich mechanism. The majority of the NO in engine exhaust is formed by the Zeldovich mechanism, in which activated N* and O*creates a chain reaction as described by equation 1.1 and 1.2[6]:

$$N_2 + O^* \rightarrow NO + N^* \quad (1.1)$$

$$N^* + O_2 \rightarrow NO + O^* \quad (1.2)$$

After the NO has been formed part of the NO will react with O_2 and form NO_2 according to the equilibrium:

$$2\,NO + O_2 \leftrightarrows 2\,NO_2. \quad (1.3)$$

The NO_x concentration in the exhaust and the ratio between NO and NO_2 depend on the engine and the driving mode of the engine, but typically a total NO_x concentration in the range 300-1200 ppm[7, 8] is expected of which 5-10% is NO_2[5, 9, 10]. With respect to the impact of NO_x on health and environment, NO_2 is the most harmful substance, as NO_2 may contribute to the formation of acid rain and cause respiratory problems when the concentration is >0.3 ppm[11]. Furthermore both NO and NO_2 participate in the formation of photochemical smog, which is damaging to plants and detrimental to human health[11]. Due to these negative impacts of NO_x on health and environment, increasingly stricter emission limits have been imposed on the NO_x emission from automotive exhaust. In the U.S this has been done by the introduction of the TIER 1-2 emission standards and in Europe by the introduction of the Euro 1-6 emission standards[12]. For illustration, the NO_x emission standards according to Euro 1-6 are stated in table Table 1. The dramatic decrease in the allowable NO_x emission means NO_x-removal technologies become a necessity as engine control of diesel engines previously used to reduce the NO_x emission no longer is enough to comply with the NO_x emission standards[13].

Table 1. Emission standards for diesel personal cars and long distance vehicles in Europe[3, 12]

Standard	Implementation Year	NO_x [g/km]
Euro 1	1992	0.90*
Euro 2	1996	0.67*
Euro 3	2000	0.50
Euro 4	2005	0.25
Euro 5	2008	0.18
Euro 6	2013	0.08

*Regulations set a standard for the sum of HC and NO_x emissions. The value quoted in the table is an inferred value based on typical HC/NO_x split.

1.2 NO_x removal from automotive exhaust

The exhaust gas from gasoline cars is efficiently cleaned for NO_x, hydrocarbons and CO by means of the three-way-catalyst (TWC)[14]. The TWC does not work for cleaning of diesel engine exhaust due the higher air/fuel ratio in diesel engines, which means exhaust from diesel engines contain 10-15% O_2[7]. For this reason other technologies have been developed or are under development for NO_x-removal from diesel exhaust, the three dominant technologies being selective catalytic reduction with ammonia (NH_3-SCR), selective catalytic reduction with hydro-carbons (HC-SCR) and the NO_x-storage and reduction (NSR) catalyst[7, 14].

1.2.1 NH_3-SCR

NH_3-SCR is based on the reduction of NO and NO_2 with NH_3 according to the reaction schemes[7]:

$$4\ NO + 4\ NH_3 + O_2 \rightarrow 4\ N_2 + 6\ H_2O \quad (1.4)$$

$$6\ NO_2 + 8\ NH_3 + O_2 \rightarrow 7\ N_2 + 12\ H_2O \quad (1.5)$$

The NH_3-SCR process was originally developed for stationary sources and then later developed further for mobile sources[14]. Typically the catalyst consist of a TiO_2 monolith on which the active catalyst V_2O_5 is deposited together with different promoters (WO_3 or MoO_3)[7, 14]. The ammonia is usually supplied in the form of an aqueous urea-solution (AdBlue®). However recently a technology has been developed in which the ammonia is stored in solid form (AdAmmine) and

then evaporated to gasous NH_3 before reaction in the SCR catalyst[15]. Even though NO_x conversion higher than 95% can be achieved with NH_3-SCR[16], the technology has a significant drawback as it is necessary to have a separate supply system for the ammonia. Furthermore the ammonia supply must be carefully controlled to prevent ammonia slip in the exhaust. Despite of these drawbacks NH_3-SCR is expected to be dominant technology for diesel exhaust cleaning in the future in combination with particle filters and oxidation catalysts units[3, 13].

1.2.2 HC-SCR

As explained in the previous section one of the disadvantages by NH_3-SCR is the necessity of adding a separate ammonia supply system. In order to avoid a separate supply system for the addition of a NO_x reductant, it has been suggested to use excess hydrocarbons from the fuel as the NO_x reductant in the technology named HC-SCR.

The overall reaction scheme for the reduction of NO_x to N_2 with hydrocarbons is illustrated with propene as an example:

$$2\ NO + 3.5\ O_2 + C_3H_6 \rightarrow N_2 + 3\ CO_2 + 3\ H_2O \qquad (1.6)$$

In the investigation of suitable catalysts for HC-SCR the main focus has been on zeolite-catalysts[17], especially the ZSM-5 zeolite, and on noble metals, especially Ag, on alumina support[18]. Despite the extensive research in HC-SCR, the technology has not reached commercialization yet, mainly due to unsolved problems with activity and catalyst stability[17, 18].

1.2.3 NSR catalysis

The NSR catalyst for NO_x removal from diesel exhaust was developed by Toyota in 1990's[19]. The catalyst consist of a precious metal and a NO_x storage compound (typically BaO) on an alumina support, and for the catalyst to work the engine must be cycled between 2 operating modes: 1) normal lean operation of the engine, during which the NO_x in the exhaust is stored as nitrate on the NO_x-storage compound, 2) operation with excess fuel-to-air ratio during which the excess fuel is used for reduction of the nitrate into N_2. The storage and reduction of NO_x is described by the following two equations[20]:

NO_x storage: $$NO \xrightarrow[Pt]{O_2} NO_2 \xrightarrow[Ba]{O_2} Ba(NO_3)_2 \quad (1.7)$$

Reduction: $$Ba(NO_3)_2 \xrightarrow{HC, H_2, CO} BaO + NO_2 \xrightarrow[Pt]{HC, H_2, CO} N_2 + CO_2 + H_2O \quad (1.8)$$

Even though the NSR catalyst has been introduced on the Japanese market[20], the technology has some drawbacks/challenges to be solved with respect to fuel penalty, sensitivity to fuel sulfur levels and control under transient engine operation[21].

1.2.4 Electrochemical deNO_x

Electrochemical deNO_x is the NO_x removal technology studied in this project. The principle in electrochemical deNO_x is, the NO_x is reduced to N_2 in an electrochemical cell by means of the electrons supplied to the cell. Thereby addition of reductants becomes unnecessary. Typically electrochemical cells similar to solid oxide fuel cells are used, which means the electrolyte is an oxygen ion conductor and the desired reactions on the cathode and anode become:

Cathode: $$NO + 2\ e^- \rightarrow 0.5\ N_2 + O^{2-} \quad (1.9)$$

Anode: $$O^{2-} \rightarrow 0.5\ O_2 + 2\ e^- \quad (1.10)$$

A competitive reaction on cathode in oxygen containing atmosphere is the reduction of O_2 (equation 1.11), which will lead to a waste of energy during electrochemical deNO_x.

$$0.5\ O_2 + 2\ e^- \rightarrow O^{2-} \quad (1.11)$$

The idea electrochemical reduction could be used for NO_x removal was initiated when Pancharatnam et al. in 1975 discovered NO could be reduced on polarised zirconia surfaces[22]. The active site for the NO_x reduction was suggested to be F-centers[i,22], which was later confirmed in a

[i] An F-center is an oxygen ion vacancy with one electron trapped.

study by Gür et al.[23], but since these studies were made in the absence of oxygen, they were of little relevance for NO_x removal in oxygen containing atmospheres, i.e. at conditions realistic for exhaust gasses. In a review of the application of ceramic membranes Cicero et al. reported in 1990 the Helipump Corporation had developed an electrochemical membrane which could remove NO_x in the presence of up to 8% O_2[24]. The electrochemical membrane/cell had an yttria stabilized zirconia electrolyte and transition metal based electrodes, and was reported to remove up to 91% NO_x[24], but unfortunately no further details were given on the experiments conducted and the electrode materials used. In 1995 Reinhardt et al. performed studies of the reaction between O_2, NO and NO_2 on LSM electrodes with yttria stabilized zirconia (YSZ) electrolyte and found the O_2 exchange reaction on the LSM was very slow below 600 °C, while addition of 1000-3000 ppm NO increased the current densities significantly in oxygen containing atmosphere due to reactions with NO_2 on the electrode surface[25]. Hibino et al. reported in 1994-1995 experiments on NO_x conversions in oxidizing atmosphere on YSZ based cells with Pd electrodes[26, 27], and later the studies were expanded to include Rh, Au, and Pt[28]. The results by Hibino et al. showed Pd was the best electrode material at 800 °C, and in the presence of 1500 ppm NO and 3% O_2 15% NO conversion could be obtained with current efficiency ≈1%[28]. Furthermore it was shown by Hibino et al. both NO_x conversion and current efficiency decreased dramatically with increasing O_2 content, and the use of AC voltage rather than DC voltage would decrease the degradation of the electrochemical cell[28]. Walsh et al. studied the NO reduction at a slighter lower temperature range compared to Hibino et al., namely at 500-600 °C rather than 700-800 °C, and studied Ir and Pt electrodes on YSZ electrolytes[29, 30]. On the Ir electrodes Walsh et al. demonstrated the selectivity towards NO_x reduction compared to O_2 reduction increased with decreasing temperature[29], while on the Pt electrodes it was demonstrated the NO conversion increased with NO concentration, polarisation and temperature[30]. Bredikhin et al. also studied NO_x conversion in an electrochemical cell with YSZ electrolyte and Pt electrodes, but in the work by Bredikhin et al. the Pt cathode was covered by a Ni-YSZ or LSCF($La_{1-x}Sr_xFe_{1-y}Co_yO_3$)-YSZ electrode layer and a strong dependency of the NO_x conversion on the microstructure of this layer was found[31, 32]. While the studies described so far all used a precious metal electrode, apart from the work briefly reported by Cicero et al.[24], the cylic voltammetry studies made by Hansen et al. in 2000 indicated that transition metal oxides without addition of noble metals could be used for electrochemical NO_x reduction, and especially LSM15 appeared promising[33-35]. It was also demonstrated by Hansen et al. the redox properties of

the electrode material was crucial for the NO reduction[35]. The work by Hansen et al. was further elaborated by Werchmeister al., who demonstrated by careful impedance analysis NO_2 is an important reaction intermediate for electrochemical deNO_x on LSM, LSF and LSCF electrodes[36-38]. Furthermore Werchmeister et al. made conversion studies on LSM-CGO cells, and found that impregnation with CeO_2, CGO10 and CPO20 ($Ce_{0.8}Pr_{0.2}O_{1.9}$) increased the NO_x conversion, however at 400 °C in 1000 ppm NO + 5% O_2 the NO_x conversion was only 1% with a current efficiency of 2%[37, 39].

1.2.5 Electrochemical deNO_x combined with a NO_x storage compound

A subgroup of the studies on electrochemical deNO_x deals with electrochemical deNO_x in combination with a compound for NO_x storage, as known from the NSR catalyst. One of the first reports on combined electrochemical deNO_x and NO_x storage was made in 2002, where Kobayashi et al. reported increased NO_x conversion when a Pt/BaO/Al_2O_3 layer was added on top of a Pt cathode on a YSZ electrolyte[40]. Li et al. reported in 2005 on a NO_x storage-reduction electrochemical catalyst consisting of dense YSZ tube on which a thin Pt film was deposited and impregnated with BaO[41]. But rather than using the potential to affect the NO_x conversion, Li et al. used the electrode potential to monitor the progress of the NO_x-storage on BaO, the storage was observed in the temperature range 350-400 °C[41]. MacLeod et al. used thin porous Pt, Pd or Rh electrodes on electrolytes of Na-β''alumina and K-β''alumina, and during polarisation a decrease in the NO_x concentration was observed, which was suggested to be due NO_x storage/nitrate formation, a suggestion which was confirmed by IR spectroscopy showing KNO_3 and KNO_2 formation[42]. In a set-up with a cone-shaped point electrode Simonsen et al. made cyclic voltammetry studies on NO_x reduction on LSM15 electrodes combined with BaO, and the results indicated BaO addition would increase the NO_x conversion on LSM electrodes[43]. In the work by Hamamoto et al. YSZ and CGO based cells with NiO+Pt or LSM+Pt electrodes were investigated for electrochemical deNO_x[44, 45]. Hamamoto et al. studied the effect of a NO_x-storage compound added in a separate adsorbent layer on top of the electrode and found an adsorbent layer with K increased the NO conversion and current efficiency significantly more than adsorbent layers with Na or Cs[44]. Furthermore increasing the oxygen concentration from 0.5 to 10% decreased the NO conversion, even though 50% NO still was converted in the presence of 10% O_2[44]. The adsorbent layer used by Hamamoto et al. contained 3 wt% Pt and an increase in NO conversion was observed

when a square-wave voltage was applied rather than DC voltage[44]. In a series of papers Lucas-Consuegra et al. reported on an electrochemically assisted NSR catalyst consisting of a Pt/K-βAl_2O_3 cell[46-48]. The Pt/K-βAl_2O_3 cell investigated by Lucas-Consuegra et al. showed the best performance at 300 °C, and two different forms of nitrate were identified to be formed during the storage process: a weakly bonded surface nitrate and a bulk nitrate[46]. Furthermore the influence of water in the gas was investigated, and even though the performance of the catalyst decreased during wet conditions, the decrease was not detrimental[46, 47]. Yoshinobu et al. reported recently studies on electrochemical deNO_x in combination with electrochemical oxidation of particulate matter (PM); the studies were made both in a disk-electrode set-up and in a honeycomb module tested in real diesel engine exhaust[49]. The electrodes investigated were composite electrodes of Pt or Ag in combination with YSZ or CGO[49]. The addition of BaO to the electrodes was proven to be crucial for the NO_x conversion, however in the presence of CO_2 a performance decrease was observed due to the formation of $BaCO_3$[49]. During the tests in real engine exhaust 97 wt% of the PM was removed and 74% of the NO_x was reduced at a fuel penalty of 9%, which are promising results, however a higher NO_x conversion and lower fuel penalty must be achieved for the technology to become commercially attractive[49].

1.3 Objective and lay-out of the thesis

This projects deals with electrochemical deNO_x, a method under development for NO_x removal from automotive diesel engines. The objective of the PhD project is to investigate how the NO_x conversion during electrochemical deNO_x is affected, when NO_x-storage compounds are added to noble metal-free ceramic electrodes. The investigation is centered around three main questions:

1) How much is the activity and selectivity of the ceramic electrodes towards NO_x conversion affected by the addition of a NO_x storage compound?

2) What are the optimal conditions for NO_x conversion on ceramic electrodes combined with NO_x storage compounds?

3) Which mechanisms/reaction steps are included in the oxidation/storage of NO_x on the electrodes and the subsequent reduction?

1 Introduction

The main focus of the project is on conversion measurements and electrochemical characterization, primarily by means of electrochemical impedance spectroscopy (EIS). Furthermore scanning electron microscopy (SEM) is used to study the microstructure of the electrodes before and after testing. In addition to this an infrared spectroscopy study is performed to investigate the NO_x adsorption on electrode materials without and with the addition of a NO_x-storage compound. Finally a small sub-project was made on the development of a set-up for performing *in situ* X-ray absorption studies on ceramic electrodes.

The thesis contains 12 chapters and one appendix, four of the chapters and the appendix are manuscripts accepted for publication in scientific journals. The content of chapters and appendix is the following:

Chapter 1: The introduction chapter contains a description of the NO_x formation in diesel engines, a brief overview of technologies for NO_x removal from automotive exhaust, and a literature survey of electrochemical deNO_x studies.

Chapter 2: The choice of electrode materials and NO_x storage compounds investigated in this project is explained, and literature findings regarding the properties and compatibility of the investigated materials are summarized.

Chapter 3: An overview is given of the experimental test set-ups and techniques used in the project, with the X-ray absorption experiments as the one exception, as these experiments only are described in chapter 11.

Chapter 4: The manuscript "Diffuse Reflectance Infrared Fourier Transform Study of NO_x Adsorption on CGO10 Impregnated with K_2O or BaO" accepted for publication in The Journal of Physical Chemistry A. The authors of the manuscript are Marie Lund Traulsen, Hanna Härelind Ingelsten and Kent Kammer Hansen.

Chapter 5: The manuscript "Improvement of LSM15-CGO10 Electrodes for Electrochemical Removal of NO_x by KNO_3 and MnO_x Impregnation" accepted for publication in Journal of the Electrochemical Society. The authors of the manuscript are Marie Lund Traulsen and Kent Kammer Hansen.

Chapter 6: The manuscript "NO_x conversion on porous LSF15-CGO10 cell stacks with KNO_3 or K_2O impregnation" accepted for publication in Journal of Solid State Electrochemistry. The authors of the manuscript are Marie Lund Traulsen, Frantz Bræstrup and Kent Kammer Hansen.

Chapter 7: Describes results from measurements on porous LSF15-CGO10 cell stacks with BaO impregnation and thus supplements the results described in Chapter 6.

Chapter 8: The manuscript "NO_x conversion on LSM15-CGO10 cell stacks with BaO impregnation" accepted for publication in Journal of Materials Chemistry. The authors of the manuscript are Marie Lund Traulsen, Kjeld Bøhm Andersen and Kent Kammer Hansen.

Chapter 9: Describes the results from measurements on LSM15-CGO10 cell stacks with K_2O impregnation and thus supplements the results described in Chapter 8.

Chapter 10: Describes experiments performed in 3-electrode set-up on LSM15 electrodes without and with BaO.

Chapter 11: Describes a small project made in cooperation with Anke Hagen, Bjørn Sejr Johansen and Ragnar Kiebach on construction of an *in situ* XANES testhouse for measurements on solid oxide electrodes.

Chapter 12: Overall discussion, conclusion and outlook.

Appendix A: Manuscript "Spectroelectrochemical Cell for *In Situ* Studies of solid Oxide Fuel Cells". The article was based on the project described in Chapter 11 and the authors of article are Anke Hagen, Marie Lund Traulsen, Ragnar Kiebach and Bjørn Sejr Johansen.

2 Materials

In this project two different electrode compositions were investigated for electrochemical deNO_x, namely LSM15-CGO10 and LSF15-CGO10. The selectivity and activity of these electrodes towards electrochemical deNOx was attempted improved by addition of NO_x-storage compound, as known from NSR-catalysis, to the electrodes. Three different NO_x-storage materials were investigated, the main focus was on BaO and K_2O with a few additional experiments performed on MnO_x, all storage compounds were added to the electrodes by impregnation. In this chapter the reason for choosing each of the mentioned materials will be explained, and a short comment will be made on the impregnation method. Furthermore the literature on the compatibility and properties of the investigated materials will be briefly reviewed.

2.1 Material Choice

2.1.1 LSM15

LSM has for many years been the favourite material for solid oxide fuel cell cathodes, mainly due to the activity of LSM towards oxygen reduction, the good thermal and chemical compatibility with the commonly used YSZ electrolyte and the high stability of the material[50]. Numerous studies have for this reason been made on LSM, with focus on conductivity[51-53], the oxygen reduction reaction mechanism[54, 55], defect structure[56, 57], effect of polarisation[58-60] and the compatibility of the LSM with electrolyte materials[61]. In addition to activity towards oxygen reduction LSM has also been shown to have activity towards NO_x reduction[34, 35, 39] and when the strontium dopant levels x=0.05, 0.15, 0.25, 0.35 and 0.50 were compared, LSM15 was observed to have the highest performance with respect to NO_x reduction[34]. As LSM15 is a well-investigated cathode material which has shown activity towards NO_x reduction, and since LSM15 had the largest NO_x-reduction activity compared to LSM with other Sr-dopant levels, LSM15 was chosen as one of the electrode materials investigated in this work.

2.1.2 LSF15

Even though LSM has shown activity towards NO_x-reduction, one of the concerns related to using LSM for electrochemical deNO_x is that LSM cathodes in general show low performances below 800 °C[62]. As an alternative SOFC cathode material for operation at lower temperatures LSF has been

investigated and shown promising results[63-65]. The better performance of the LSF electrodes compared to the LSM electrodes at lower temperatures may to a large extent be explained by the fact that the LSF is a mixed ionic-electronic conductor[66], while LSM is considered an electronic conductor[52, 53]. With respect to electrochemical deNO_x some initial investigations have shown nitrous oxide (N_2O) is reduced on LSF electrodes, with the largest activity observed for the LSF15 when the strontium dopant levels x=0.05, 0.15, 0.25 and 0.35 were compared[67], and furthermore reactivity between NO and LSF has been demonstrated[38]. Due to the indications that LSF electrodes may be able to convert NO_x, and the expected higher performance of LSF electrodes compared to LSM electrodes in the temperature range investigated, LSF15 was chosen as one of the electrode materials investigated in this work.

2.1.3 CGO10

In solid oxide fuel cells, which usually are operated in the temperature range 600-900 °C, the most commonly used electrolyte is YSZ. In electrochemical deNO_x the desired operating temperature is lower compared to solid oxide fuel cells, namely around 300 °C. For this reason CGO10 was chosen as electrolyte material, since CGO10 has been identified to be superior to YSZ as electrolyte below 600 °C[68].

2.1.4 BaO

BaO was chosen as NO_x-storage compound, as BaO is the most commonly used NO_x-storage compound in conventional NSR catalysis[21] and NO_x-storage on BaO for this reason is thoroughly described in literature[69-71]. The work by Simonsen et al.[43] indicated LSM15 combined with BaO could be an efficient catalyst for electrochemical deNO_x, and furthermore studies by Li et al.[41] and Yoshinobu et al.[49] showed increased NO_x conversion when electrochemical deNO_x was combined with BaO. However, both Li et al.[41] and Yoshinobu et al. [49] used Pt in combination with BaO in their electrodes for electrochemical deNO_x, whereas this project investigates electrochemical deNO_x in purely ceramic electrodes without addition of any precious metals.

2.1.5 K_2O

K_2O was investigated as a NO_x storage compound in this work for several reasons: Firstly, because K_2O has been shown to act as a NO_x storage compound during NSR catalysis[72, 73] and shown promising results during electrochemical deNO_x[42, 46, 47]; and secondly because K is a commonly

used promoter in conventional heterogenous catalysis[74] and has been shown to increase simultaneous NO_x and soot removal[75, 76]. Impregnation with K_2O is for this reason of interest for electrochemical deNO_x combined with a NO_x storage compound, both with respect to the NO_x conversion itself, but also in the perspective of developing the technology into a stage, which also involves soot/excess hydrocarbon removal from the exhaust.

2.1.6 MnO_x

MnO_x was added as a NO_x-storage compound as MnO_x has shown capability to store NO_x[77]. Furthermore impregnation with MnO_x is expected to cause a general increase in electrode performance, since Mn can exist in a number of oxidation states, and for this reason is the redox active center in perovskites used for redox catalysis[78] and has been proven to affect the oxygen reduction reaction on electrodes[79]. As for K_2O, addition of MnO_x may also be of interest for a future combination of electrochemical deNO_x with electrochemical hydrocarbon oxidation, as MnO_x is an active hydrocarbon oxidation catalyst[80-82].

2.2 Impregnation

Impregnation[ii] was the method used for addition of the NO_x storage compounds to the electrodes in this work. In conventional heterogeneous catalysis impregnation is a standard method for addition of a more active catalyst component to a less active support material[83] and in NSR catalysts the BaO is usually introduced into the catalyst by impregnation[84, 85]. In the 1990'es the first papers were published on preparation/modification of solid oxide electrodes by means of impregnation[86, 87]. As impregnation in the first studies appeared to improve the electrode performance significantly, many research groups have since then been working with impregnation on solid oxide electrodes and the number of publications in the field has increased dramatically, for extensive reviews on solid oxide electrode impregnation see for instance Jiang [88] or Vohs et al.[89].

[ii] The terms "impregnation" and "infiltration" are both used in literature for the same process, in this thesis "impregnation" will consistently be used.

2.3 Materials compatibility

One of the major concerns when impregnating the NO_x-storage compounds into the electrodes is whether the storage compounds may react with the electrode materials. This concern is not significant with respect MnO_x impregnation on LSM electrodes, as the LSM used for the LSM electrodes from the beginning was synthesized as being slightly overstochiometric with respect to MnO_x, and thus already contained some MnO_x. However with respect to both K_2O and BaO impregnation on LSM15-CGO10 and LSF15-CGO10 electrodes the risk of alternative phase formation should be taken more seriously. In the work by Simonsen et al.[43] no reaction between BaO and LSM15 was observed, when a mixture of these two materials had been sintered for 12 h at 1250 °C, and neither was any reaction between Ba-containing materials and LSM observed in the work by Ai et al.[90] or Jin et al.[91] which altogether indicates no reaction between the BaO and the LSM should be expected. This is however contradicted by the study made by Yang et al.[92], which showed diffusion of Ba from BSCF ($Ba_{1-x}Sr_xFe_{1-y}Co_yO_3$) into LSM. In conclusion, even though most studies indicate there will be no reaction between LSM and BaO, this cannot be entirely excluded. With respect to reactivity between BaO and CGO, several studies report on the use of Ba-containing electrodes together with CGO electrolytes, but none of the studies show reaction between Ba and CGO as long as the temperature stays below 900 °C[93-95]. To the best of the author's knowledge no studies are reported on the compatibility between LSM and KNO_3/K_2O. The best study for comparison is for this reason likely the study by Kim et al.[96], in which Mn_3O_4 impregnated with 0.5 wt% K was investigated as an hydrocarbon oxidation catalyst. The study showed no new phase formation after impregnation and calcination of the sample; however XPS indicated the K impregnated had increased the defect concentration in the Mn_3O_4[96]. Furthermore a number of potassium containing manganese compounds are known to exist, namely potassium permanganate ($KMnO_4$) and potassium manganate (K_2MnO_4)[1], which possibly could form during reaction between K and excess manganese in the electrode. With respect to the combination of LSF15 with BaO and K_2O no information was found in literature, however due to the similarity in oxidation state and ionic radii of Mn and Fe ions in LSM15 and LSF15 respectively, similar behaviour with respect to BaO and K_2O may be expected.

2.4 Material properties

In addition to a possible reaction between electrode materials and impregnated NO_x-storage compounds as described in the previous section, there is also the possibility the presence of the NO_x-storage compounds may significantly alter the current passage through the electrodes and the cell stacks, especially if the impregnated compounds have a much higher conductivity than the electrodes and form an interconnected network through the cell stacks. Furthermore if the NO_x-storage compounds are molten at the operating temperatures during electrochemical deNO_x, an increased risk of degradation/coalescence must be expected. For these reasons it is important to know both the conductivities of electrode materials and the NO_x-storage compounds, and the melting points of the NO_x-storage compounds. The relevant conductivities and melting points found from literature are stated in Table 2. No conductivities could be found for K_2O and BaO; likely since these two oxides can be considered insulators. When the conductivities in Table 2 are compared, the conductivities for LSF15 and LSM15 are consistently highest. By comparison of the conductivities for CGO10 and KNO_3 it is evident, that in sections of an electrochemical cell with only CGO10, for instance through a porous CGO electrolyte, an easier current path may be established through molten KNO_3 at 350-500 °C. In the temperature range 300-500 °C investigated for electrochemical deNO_x it is also clear from Table 2, that only KNO_3 will be present as a melt, while the other NO_x storage compounds will remain in solid form.

Table 2. Conductivities and melting points electrode materials and NO_x-storage compounds.

Compound	Conductivity [S/cm]	Ref.	Melting point [97] [°C]
LSM15	90-110 (300-600 °C)	52, 53	
LSF15	110 (500 °C)	98	
CGO10	0.005 (500 °C)	68, 99	
K_2O	-		740
KNO_3	0.660-1.094 (350-500 °C)	100	334
BaO	-		1973
$Ba(NO_3)_2$	1x10-6 (300 °C)	101	590
MnO_x	$5x10^{-7}$ - $3x10^{-3}$ S/cm^2 at RT(MnO_2)	102	1842 (MnO), 1567 (Mn_3O_4), 1080 (Mn_2O_3)
$Mn(NO_3)_2$	-		*

*Melting point cannot be determined, as $Mn(NO_3)_2$ decomposes to MnO_x before melting [103]

3 Experimental

In this chapter an overview is given of the experiments conducted to investigate the effect of NO_x storage compounds on electrochemical deNO_x. The overview includes the different test set-ups used for the electrochemical characterisation of the electrodes, the fabrication of the electrodes including addition of the NO_x storage materials to the electrodes and the experimental techniques used to characterise the electrodes.

3.1 Test set-ups for electrochemical characterisation

Three different test-set-ups were used for electrochemical testing of the electrodes. The test-set-ups were:

1) Symmetric cell test set-up
2) Porous cell stack test set-up
3) 3-electrode pellet (3EP) test set-up

In general it applies for all the set-ups they can be used for electrochemical testing of solid oxide electrodes at temperatures up to 500 °C in atmospheres containing NO_x gases, oxygen and argon in various proportions.

3.1.1 Symmetric cell test set-up

In Figure 1a a sketch of a symmetric cell mounted for electrochemical testing is shown, and Figure 1b shows the set-up used for simultaneous testing of 4 symmetric cells. The set-up is placed inside a raku furnace and sealed; whereafter testing can be performed at elevated temperatures in controlled atmospheres. The advantage of the symmetric cell test set-up is it allows for simultaneous test of 4 cells, and since the symmetric cells are fairly easy to fabricate, the symmetric cell test set-up allows for fast screening of many electrode materials. The disadvantage of the symmetric cell test set-up is it is not suitable for gas analysis, which means any conversion of NO_x during the measurements is not detected, and the set-up can only be used for electrochemical characterisation of electrodes without use of a reference electrode.

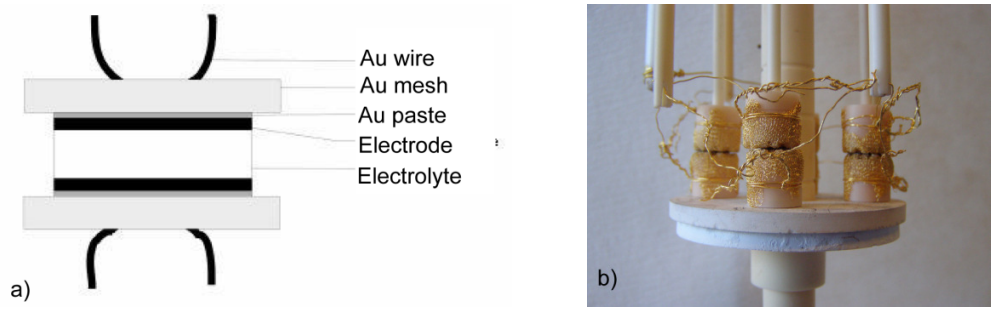

Figure 1. Symmetric cell test set-up a) sketch of set-up for single symmetric cell, b) Image of test set-up for simultaneous testing of 4 symmetric cells**.**

3.1.2 Porous cell stack test set-up.

The principle of the porous cell stack test set-up is shown in Figure 2. The porous cell stacks consist of 11 alternating layers of porous electrode and electrolyte, corresponding to a stack of 5 single cells. The outer electrodes of the porous cell stack are covered by a gold current collector and the stack is mounted in between two vertical alumina tubes. The alumina tubes contain channels for the gas flow and measurement probes, which are used for the electrochemical characterisation and polarisation of the cell stacks. The principle is, the gas flow passes through the porous cell stack, and the large contact area between gas flow and electrode layers assures a high conversion of the NO_x gasses, if the electrode is active enough. The outlet gas from the porous cell stack is analysed by a mass spectrometer and a chemiluminiscence detector, which each will be described in further detail in section 3.5. The advantage of the porous stack test set-up is, it allows for gas analysis of the outlet gas in combination with electrochemical characterisation, the disadvantage is the lack of a reference electrode in the set-up limits the electrochemical characterisation.

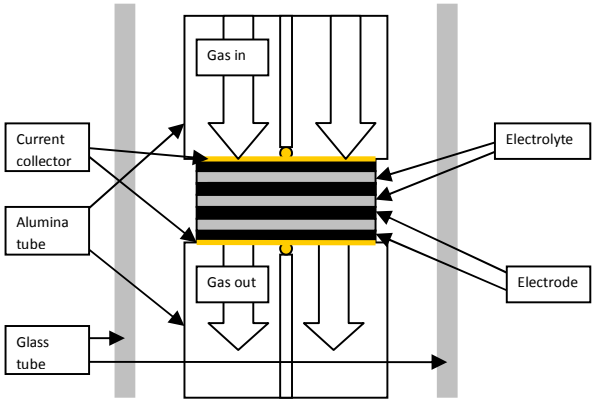

Figure 2. Schematic of porous cell stack setup

3.1.3 3-electrode pellet set-up

In Figure 3 a principle sketch of the 3 electrode pellet (3EP) set-up is shown. The geometric design of the 3EP was determined in the work by Winkler et al.[104] as a very well suited design for characterisation of solid oxide electrodes due to the assurance of a uniform current distribution at the working electrode. The 3EP set-up makes it possible to perform electrochemical characterisation by use of reference electrode with a well-defined potential, which means the exact potential of the working electrode during the measurements may be determined. Furthermore the outlet gas from the working electrode in this set-up can be analysed to detect NO_x-conversion. During this project the outlet gas was analysed by chemiluminiscence detector, which will be described further in section 3.5. The advantage of the 3EP set-up is it allows for a detailed electrochemical characterisation of the solid oxide electrode in combination with gas conversion measurements. The disadvantage is the 3EPs are fairly time-consuming to produce and only one 3EP can be tested at a time.

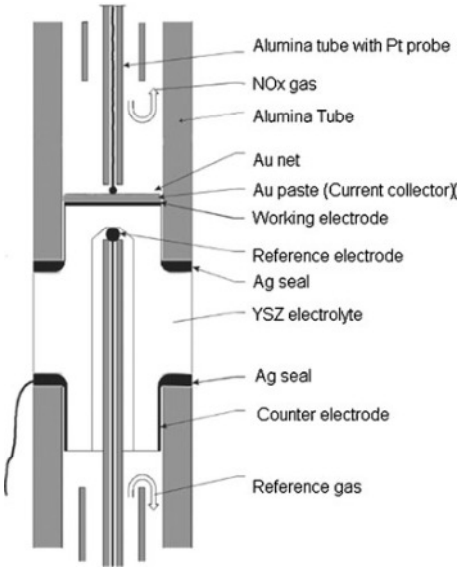

Figure 3. Set-up of 3-electrode pellet, note in this work CGO electrolyte was used instead of YSZ electrolyte as stated in the image.

3.2 Fabrication of electrodes

The tested solid oxide electrodes were fabricated in two different ways. For testing in symmetric cell test-set-up and 3EP experiments the electrodes were screen-printed onto a dense electrolyte tape or pellet respectively. For testing in the porous cell stack test-set-up the electrodes were tape casted and laminated together with likewise tape casted electrolyte layers. The most significant differences between the screen-printed and the tape casted electrodes is the porosity of the electrodes, due to the addition of poreformers during fabrication of the tape casted electrodes. The difference in porosity is illustrated by comparison between the screen-printed electrode in Figure 4 and the tape casted electrode in Figure 5. More details on fabrication of the screen-printed electrodes and tape casted electrodes are given in the experimental sections in chapter 5 and chapter 6 respectively.

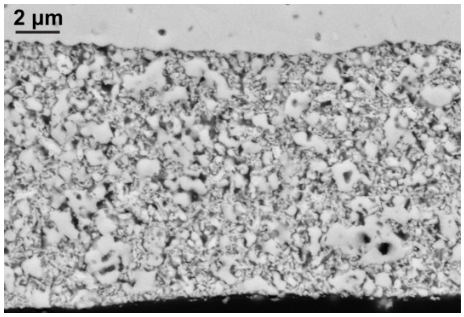

Figure 4. Microstructure of screen-printed LSM15-CGO10 electrode on symmetric cell

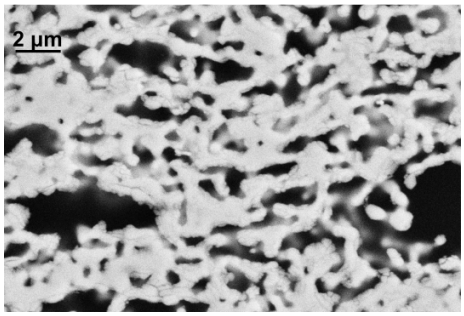

Figure 5. Microstructure of tape-casted LSM15-CGO10 electrode on porous cell stack

3.3 Impregnation

The impregnation procedures used for impregnation of the screen-printed electrodes and the tape-casted electrodes tested in this work are stated in the following two subsections. The two different impregnation procedures are based on in-house procedures in the department and were chosen, as they turned out to give functional results. The first method used for the screen printed electrodes was a method developed in-house based on the method described by Sholklapper et al.[105] but without using a gel-step. The second method used for tape casted electrodes was based on the method described by Lundberg et al. for synthesis of high-surface-area CeO_2[106]. It should be emphasized that the procedures have not been carefully optimized, and some of the steps in the procedures, like the use of a surfactant and vacuum during the impregnation, may turn out to be unnecessary, if the impregnation methods are optimized.

3.3.1 Screen-printed electrodes

Impregnation of screen-printed electrodes involved the following steps:

1) Preparation of an aqueous precursor solution of the metal-nitrate
2) For the MnO_x and the BaO impregnations purely aqueous nitrate solutions were used, while for the KNO_3 impregnation ≈1wt% Triton-X45 surfactant (Fluka) was added to the impregnation solution, this addition of Triton-X45 may however have been unnecessary.
3) Immersion of the cells into precursor solution
4) Vacuum treatment of the cells immersed in the precursor solution for ≈10 s at pressure <0.1 bar
5) Heat treatment depending on the pre-cursor/desired impregnation
6) Repetition of step 3)-4) until the desired impregnation weight load was obtained, usually 2-4 times.

3.3.2 Tape-casted electrodes

Impregnation of tape-casted electrodes involved the following steps:

1) Preparation of an aqueous precursor solution of the metal nitrate
2) Addition of P123 surfactant (BASF) to the precursor solution in a concentration corresponding to 10 wt% P123 relative to the water.

3) Covering the cell stacks with the precursor solution by dripping the solution on with a pipette.
4) Placing the cell stacks covered with impregnation solution in the vacuum chamber and evacuate for ≈10 s.
5) Removing the cell stacks from the vacuum chamber and wiping off excess precursor solution.
6) Heat treatment depending on the pre-cursor/desired impregnation.
7) Repeating step 3)-6) until the desired impregnation load was achieved, usually 2-3 times.

3.4 Electrochemical characterisation

A Gamry Reference 600 potentiostat was used for the electrochemical characterisation. The main focus during the electrochemical characterisation was on electrochemical impedance spectroscopy, as impedance spectra when deconvoluted may yield detailed information on the processes contributing to the polarisation resistance of the electrodes. The impedance spectra were during the data analysis deconvoluted by use of the ZView 2 software[107]. In addition to the impedance measurements cyclic voltammetry was also used for electrode characterisation. Details on how the impedance measurements and the cyclic voltammetry were performed are given together with the results in the chapters 5 to 10.

3.5 Gas Analysis

The composition of the outlet gas from the porous cell stack set-up was analysed by means of both a mass spectrometer and a chemiluminiscence detector, while the outlet gas from the 3EP set-up was only analysed by a chemiluminiscence detector. In this section the operating principle of the two gas analysis instruments will briefly be explained.

3.5.1 Mass spectrometer

The mass spectrometer used for determination of the O_2, N_2 and N_2O concentrations in this work was a type Omnistar^{TM} GSD 301 from Pfeiffer Vacuum. The basic principle of a mass spectrometer is the gas components are first ionized, then sorted according to mass and finally detected. A very simplified sketch of the components in a mass spectrometer is shown in Figure 6. In the Omnistar^{TM} GSD 301 mass spectrometer used in this work the sample gas was continuously sucked into the mass spectrometer through a 1 m long capillary, while the vacuum in the system was established by the combination of a turbo pump and a diaphragm pump. The ion source used was a tungsten filament and the mass analyser a quadropole mass analyser. The detector used was a channeltron detector, where channeltron is an abbreviation of channel electron multiplier. For control of the mass spectrometer and data acquisition the Quadstar 32-bit software from Pfeiffer Vacuum was used. This software can be used for logging of the ionic current signal detected during the measurements, when the MID (Multiple Ion Detection) operating mode is chosen. Furthermore the software can be used converting the ionic current signal into concentrations after a suitable calibration when the MCD (Multiple Concentration Detection) operating mode is chosen. The MCD operating mode was used for the conversion measurements in this work.

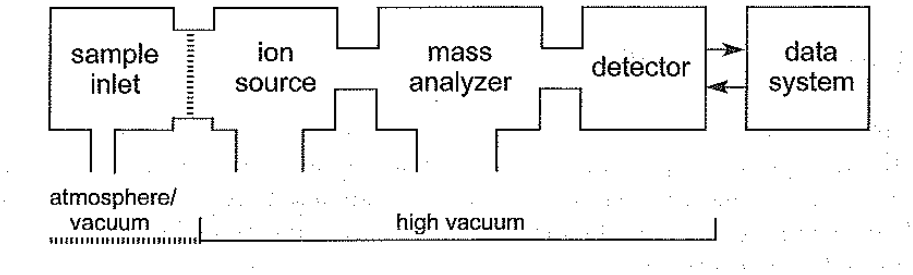

Figure 6. General schematic of mass spectrometer.

3.5.2 Chemiluminiscence detector

The concentration of NO, NO_2 and NO_x was detected by a chemiluminiscence detector Model 42*i* High Level from Thermo Scientific. The operating principle of the chemiluminiscence detector is based on the detection of light emission from excited chemical species, also known as chemiluminiscence. In the chemiluminiscent detector the NO reacts with ozone and forms excited

NO_2* which decays to an un-excited state during emission of light/luminescence, the two reactions are stated in equation 3.1 and 3.2.

$$NO + O_3 \rightarrow NO_2^* + O_2 \quad 3.1$$

$$NO_2^* \rightarrow NO_2 + hv \quad 3.2$$

The intensity of the luminiscence is proportional to the NO concentration, which therefore is determined as described by equation 3.1 and 3.2. For detection of NO_2, the sample gas is led through a converter, in which the NO_2 is converted to NO. By subtracting the NO concentration measured when the converter is bypassed, from the concentration measured when the gas passes through the converter, the NO_2 concentration in the sample gas is determined.

3.6 FTIR spectroscopy

FTIR spectroscopy was employed to investigate the effect of the NO_x storage compounds on the NO_x adsorption on CGO. The specific FTIR technique used was Diffuse Reflectance Infrared Fourier Transform (DRIFT) Spectroscopy, which makes it possible to measure directly on powder samples at elevated temperatures in controlled atmospheres. The spectrometer used for the DRIFT measurements was a Biorad FTS 6000 FTIR spectrometer equipped with high-temperature reaction cell (Harrick Scientific, Praying Mantis). More details on the FTIR measurements can be found in chapter 4 dealing with the DRIFT spectroscopy.

3.7 Microscopy

The electrode microstructure before and after testing was investigated by scanning electron microscopy (SEM) on a Zeiss Supra 35 microscope equipped with a thermal field emission gun. For elucidation of the microstructure of the impregnated compounds the cells were broken and the broken cross section investigated without any coating at low accelerating voltage (3 kV) using the in-lens detector. For more overall images of the electrode structure the cells were mounted in epoxy, polished and carbon coated prior to investigation with the SE2 or the QBSD detector.

4 Diffuse Reflectance Infrared Fourier Transform Study of NO_x Adsorption on CGO10 Impregnated with K_2O or BaO

This chapter is the manuscript "Diffuse Reflectance Infrared Fourier Transform Study of NO_x Adsorption on CGO10 Impregnated with K_2O or BaO" accepted for publication in the Journal of Physical Chemistry A. The experiments described in this chapter were conducted at Chalmers University of Technology in Sweden.

4.1 Abstract

In the present work Diffuse Reflectance Infrared Fourier Transform (DRIFT) spectroscopy is applied to study the adsorption of NO_x at 300-500 °C in different atmospheres on gadolinium doped ceria (CGO), an important material in electrodes investigated for electrochemical NO_x removal. Furthermore, the effect on the NO_x adsorption when adding K_2O or BaO to the CGO is investigated. The DRIFT study shows mainly the presence of nitrate species at 500 °C, while at lower temperature a diversity of adsorbed NO_x species exists on the CGO. Presence of O_2 is shown to have a strong effect on the adsorption of NO, but no effect on the adsorption of NO_2. Addition of K_2O and BaO dramatically affects the NO_x adsorption and the results also show that the adsorbed NO_x species are mobile and capable of changing adsorption state in the investigated temperature range.

4.2 Introduction

Nitrogen oxides (NO_x) affect the respiratory system negatively, increases the formation of ozone at ground level, cause formation of acid rain, contribute to smog formation and also act as green house gas[11]. Even though the NO_x emission from road transport in Europe has been significantly reduced during the last 10 years, road transport is still the largest single contributor to the NO_x pollution[2]. The reduction of NO_x emission from road transport has mainly followed from the introduction of the three-way-catalyst for cleaning of the exhaust from gasoline engines[2]. Unfortunately, the three-way catalyst cannot remove NO_x from diesel engine exhaust due to the higher oxygen content in diesel exhaust. Much research is currently focused on improving the technologies for removing NO_x from diesel exhaust, with main focus on the three technologies: 1) selective catalytic reduction with urea (urea-SCR), 2) selective catalytic reduction with

hydrocarbons (HC-SCR) and 3) the NO_x-storage and reduction (NSR) catalyst, for a review on the different techniques see Kaspar et al.[7] or Skalska et al.[108].

An alternative method under development for NO_x-removal is the electrochemical reduction of NO_x [109-111], where NO_x reduction to N_2 and O_2 occurs in an electrochemical cell. The NO_x is reduced by the electrons supplied to the cell during operation, which makes it unnecessary to add other reducing agents like urea or extra hydrocarbons, as necessary in urea-SCR, HC-SCR and NSR catalysis. In the electrochemical cell the NO_x is reduced on the cathode and afterwards the O^{2-} migrates through an oxygen ion conducting electrolyte and is subsequently oxidized to O_2 on the anode, a sketch of the principle in electrochemical deNO_x is shown in Figure 7.

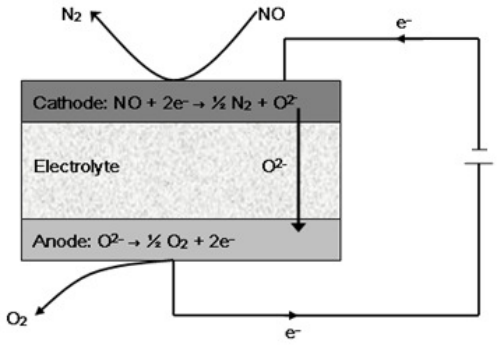

Figure 7. Principle of electrochemical deNO_x (reprinted with permission from [37])

In the investigation of suitable electrode materials for electrochemical deNO_x a major challenge is to find electrode materials which have a sufficiently high activity and selectivity, i.e. which are capable of reducing NO_x but not O_2, as reduction of O_2 is a competing reaction on the cathode[111]. Several electrode materials have been investigated for electrochemical deNO_x, for example noble metals[22, 27, 30], spinels[112] and perovskites[35, 39, 45]. Frequently a composite electrode is applied, i.e. an electrode with both an electron conducting phase (for instance a perovskite) and an O^{2-} conducting phase (for instance yttria stabilized zirconia (YSZ) or CGO)[39, 45, 113]. An obstacle in the investigation and understanding of electrochemical deNO_x is a limited knowledge of the adsorption of NO_x on the electrode materials, and how this adsorption changes in the temperature ranges investigated for electrochemical deNO_x (usually 300-600 °C) and depending on the presence of NO or NO_2. The aim in this work is to apply DRIFT (Diffuse Reflectance Infrared Fourier Transform) spectroscopy to study the NO_x adsorption at conditions relevant for electrochemical

deNO_x. The study will be made on CGO10 ($Ce_{0.9}Gd_{0.1}O_{1.95}$), a material frequently used in electrodes for electrochemical deNO_x. Moreover the effect on the NO_x adsorption of impregnating the CGO10 with K_2O or BaO is investigated as several studies show that addition of these compounds, known from the NSR catalyst, may increase the NO_x conversion during electrochemical deNO_x[43, 44, 46]. The findings in this work are in the results and discussion section related to literature on NO_x adsorption on compounds similar to the electron conducting perovskites frequently used in deNO_x-electrodes. Altogether this will offer a possibility of relating observations on activity and selectivity during electrochemical deNO_x to the adsorption capabilities of the electrode materials.

Even though the DRIFT measurements in this work are performed at relevant temperatures and gas compositions, they cannot be considered "true" in-situ measurements with respect to electrochemical deNO_x since they are performed on powders and not electrodes under polarization. Martinez-Arias et al. pointed out that NO adsorption depends on the vacancy concentration at the surface of CeO_2[114]. Since the vacancy concentration of CGO based electrodes likely is significantly altered during cathodic polarization, due to the pumping of O^{2-} away from the electrode surface, there may be some differences between the NO adsorption observed on CGO10 powders and on CGO10 in electrodes under polarization. However, since an important aim in this work is to study the influence of K_2O and BaO impregnation on the NO_x adsorption on CGO10, it is believed that altered properties of the powder sample, owing to impregnation with K_2O or BaO, reflects similar effects on electrodes under polarization.

4.2.1 NO_x adsorption on CeO_2

To the best of the author's knowledge there is no reporting on IR-studies of NO_x adsorption on CGO10 in the temperature range 300-500 °C. However, several studies have been made of NO_x-adsorption on CeO_2 in the temperature range from RT to 400 °C [114-117]. Even though the assignment of the adsorption peaks observed is not unambiguous, the references in general agree on the presence of several different adsorbed NO_x-species on CeO_2, and usually assign the peaks to the presence of NO_2^- (nitrite), $N_2O_2^{2-}$ (hyponitrite) and NO_3^- (nitrate) species. In the work by Philip et al. it was pointed out, how NO adsorption without oxygen mainly led to the formation of NO_2^-, whereas in the presence of oxygen NO_3^- was formed through the steps: NO adsorption/NO_2^- formation → oxidation to NO_3^-[116]. Philip et al. also showed, how the NO_x, adsorption decreased, when the temperature was increased from 50 °C to 300 °C[116].

4.2.2 NO_x adsorption on K_2O and BaO

Numerous studies have been made on the NO_x adsorption on K- and Ba- containing catalysts, as both elements are of interest for the NSR-catalyst[69-71, 85, 118-122]. On Ba, NO_x mainly adsorbs in the form of NO_2^- or NO_3^- [69, 70, 119]. Similar for K-containing catalysts, the NO_x adsorption mainly leads to formation of NO_2^- and NO_3^- [72, 120], but as pointed out by Lesage et al.[72] NO_2^- formation is only detected at lower temperatures (200 °C). At higher temperatures (400 °C) only NO_3^- formation is observed, implying that either NO_3^- is formed directly at higher temperatures or that NO_2^- conversion into NO_3^- is so fast the NO_2^- cannot be detected.

4.3 Experimental Methods

4.3.1 Sample preparation

Three different samples were prepared for the measurements on CGO: 1) A non-impregnated CGO sample, 2) a K_2O impregnated sample, and 3) a BaO impregnated sample.

The CGO10 was a commercially available powder from Rhodia. For the preparation of the impregnated samples an aqueous solution of either KNO_3 or $Ba(NO_3)_2$ was made. The nitrate solutions were mixed with CGO powder for several hours, and subsequently the mixtures were dried at 80 °C. After drying the samples were heated to 700 °C to decompose the nitrate into oxide. Amounts were chosen to give a weight percentage in the dry mixture of 3 wt% K_2O and 1 wt% BaO, respectively.

4.3.2 IR measurements

The DRIFT measurements were performed on a Biorad FTS 6000 FTIR spectrometer equipped with a high-temperature reaction cell (Harrick Scientific, Praying Mantis) with KBr windows. The gasses (NO, NO_2, O_2 and Ar) were supplied by mass flow controllers (Bronkhorst Hi-Tech) and the total flow to the cell during pre-treatment and measurements was 100 ml/min. The sample crucible was heated during the experiment and the temperature was controlled by a K-type thermocouple connected to a Eurotherm 2416 temperature controller.

Each sample was first pre-treated at 500 °C in 10% O_2 for 1 h, whereafter background spectra were recorded from 500 to 300 °C in steps of 50 °C, while the sample was supplied with 10% O_2. The sample was re-heated to 500 °C and the inlet gas was changed to one of the following compositions:

a. 1000 ppm NO, balance Ar
b. 1000 ppm NO, 10% O_2, balance Ar
c. 1000 ppm NO_2, balance Ar
d. 1000 ppm NO_2, 10% O_2, balance Ar

IR spectra were recorded with resolution 1 cm^{-1} in the range 4000-1000 cm^{-1} from 500 °C to 300 °C in steps of 50 °C, with the temperature hold for 30 min at each temperature step to let the adsorbed species stabilize. For each of the gas compositions the sample was changed to a fresh sample.

4.3.3 Temperature programmed desorption

Temperature programmed desorption (TPD) was made on all samples according to the following sequence:

1. Pre-treatment at 500 °C in 10% O_2 for 1 h
2. Cooling to 30 °C followed by adsorption for ½ h in 1000 ppm NO + 10% O_2
3. Flush at 30 °C for ½ h in 10% O_2
4. TPD at ramp rate 15 °/min from 30 °C to 500 °C in 10% O_2
5. Cool down

The spectra recorded at 30 °C in 10% O_2 just prior to the TPD were used as background for the recorded IR-spectra. Unfortunately the maximum temperature in the experimental set-up was 500 °C, otherwise it would have been of interest to increase the temperature to even higher values, since many of the adsorbed NO_x species appeared to be stable at 500 °C in 10% O_2. In none of the experiments it was possible to detect any desorption peaks on the mass spectrometer due to the stability of the NO_x species and/or small amount of sample used. However, interesting observations were made on the IR spectra recorded during the experiment; these observations will be described in the results and discussion section.

4.4 Results and discussion

For evaluation of the infrared spectra the absorbance is plotted as a function of wavenumber. The absorbance is defined as in equation 4.1:

$$A = \log \frac{I_0}{I} \qquad 4.1$$

- where I_0 is the intensity of the background spectra, and I is the intensity during the actual measurement. It follows from equation (1) that a positive peak on the absorbance plot corresponds to formation of an adsorbed specie, and a negative peak correspond to removal and/or blocking of an adsorbed specie. The background spectra were as previously stated recorded in 10% O_2 in Ar at 500-300 °C. In Figure 8 the background spectra recorded on the non-impregnated CGO10 sample are shown. Clearly there is very little effect of the temperature on the background and in order to simplify the data treatment the background spectrum recorded at 500 °C was used for calculation of the absorbance at all temperatures.

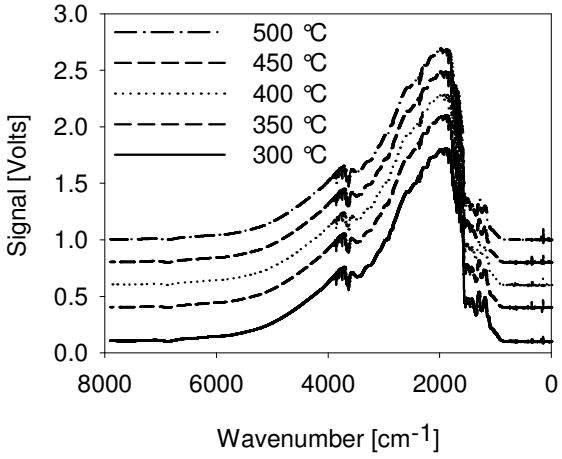

Figure 8. Background spectra recorded in 10% O_2 in Ar on non-impregnated CGO10 sample. The spectra originally overlaid each other but has been elevated to ease comparison.

4.4.1 Evolution of surface species over CGO10

When the CGO10 powder sample is exposed to NO (1000 ppm) and O_2 (10%), the most pronounced features of the IR spectra over the entire temperature range from 500 °C to 300 °C, are two groups of peaks located around 1600 cm^{-1} and 1200 cm^{-1}, see Figure 9 and Figure 10. In between these two features a broad negative peak is observed. This negative peak becomes more and more negative when the temperature decreases, indicating that adsorbed species are removed during the experiment. In addition to these peaks several smaller peaks, both negative and positive, are observed in the range 1900-4000 cm^{-1}. In general, the peak intensities increases with decreasing temperature, which indicates that the adsorbed species are more readily adsorbed at lower temperatures. Some peaks, which are not observed at 500 °C, become visible at lower temperatures, see Figure 10, which indicates there is a change in the type of adsorbed species with temperature. With respect to the time dependence of the peaks, no new peaks appear after the first minute of exposure at each temperature; however the peak intensity tends to increase with time, most pronounced for the measurement at 500 °C.

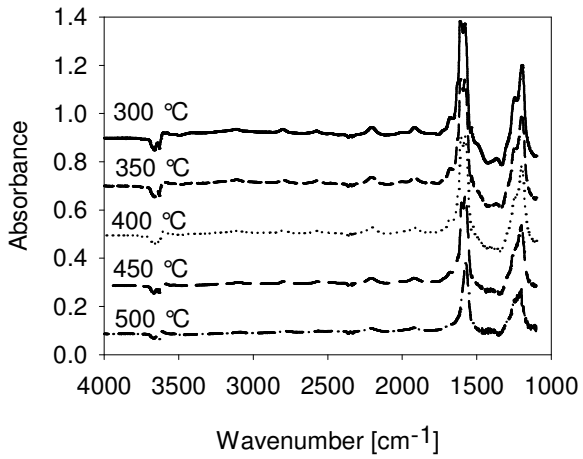

Figure 9. DRIFT spectra recorded on non-impregnated CGO sample in 1000 ppm NO + 10% O_2 at 300-500 °C.

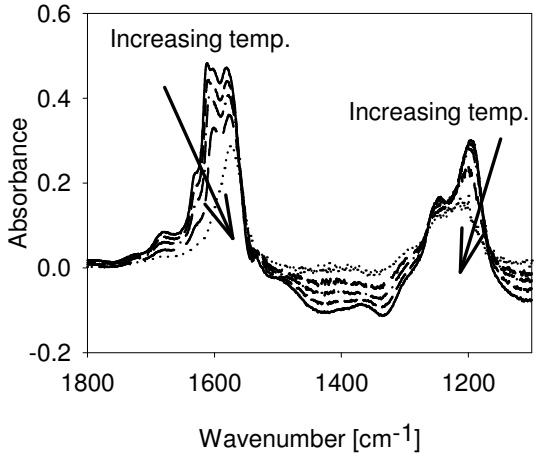

Figure 10. Close-up of DRIFT spectra shown in Figure 9. The spectra were recorded in 1000 ppm NO + 10% O_2 at 300-500 °C.

The presence of many peaks, which in several cases are overlapping, combined with previous reports on NO-adsorption, which are not always in agreement, makes an unambiguous assignment of each peak to a specific adsorbed specie a difficult, if not impossible task. However, with this in mind it is still possible to make some reasonable suggestions and to point out tendencies, especially when comparing spectra recorded with different gasses, at different temperatures and on different samples.

First of all the negative peaks observed on the spectra at 3600-3700 cm^{-1}, 2300 cm^{-1} and 1300-1500 cm^{-1} are assigned to OH-groups[123], adsorbed CO_2[124] and carbonate/carboxylate[125] groups respectively. These three types of species are removed or blocked during the experiment, which causes the negative peaks. The small, positive peaks observed at wavenumbers higher than 2500 cm^{-1} could not be identified by comparison to literature, but are believed to be overtones from peaks observed at lower wavenumbers. These peaks will not be discussed any further.

As previously mentioned the largest absorption peaks are observed in the spectra as two features located at 1600 cm^{-1} and 1200 cm^{-1}. In the literature pairwise absorption peaks due to NO_3^- was reported on α-Fe_2O_3 at ≈1550cm^{-1} and ≈1270 cm^{-1} [126] and similar peaks were later found on CeO_2 and $Ce_{0.62}Zr_{0.38}O_2$ [116, 117, 127]. For this reason it seems likely that the peaks observed in this work at

1520-1580 cm^{-1} and 1200-1250 cm^{-1} can be ascribed to NO_3^-. However, it should be mentioned, Cerrutti et al. ascribed peaks at 1208-1222 cm^{-1} to chelating NO_2^- instead of NO_3^- [128], but the broad shape of the peak around 1200 cm^{-1} observed in this work also indicates the peak may be due to several adsorbed species, for instance due to both NO_3^- and chelating NO_2^- adsorbed on the CGO surface.

With respect to the region around 1600 cm^{-1} only one, clearly distinctive peak is observed at 500 °C at 1573 cm^{-1}, ascribed to NO_3^- (see above). The peak at 1573 cm^{-1} has two low asymmetric shoulders on the left/high wavenumber side. When the temperature is decreased to 300 °C, these two shoulders increase in size, and in addition two peaks appear at 1603 and 1610 cm^{-1}, respectively. By comparison to literature these two peaks are suggested to be due to adsorbed NO^- and adsorbed NO_2, as these two species were ascribed by Busca et al. to 1595 cm^{-1} and 1605 cm^{-1} [126], respectively. It also seems reasonable that more weakly adsorbed species like NO^- and NO_2 only adsorbs at lower temperatures as observed in this work, while at 500 °C only strongly adsorbed species like NO_3^- can stay adsorbed on the CGO surface.

Finally minor peaks are observed at 1673-1680 cm^{-1}, 1720 cm^{-1} and 2207-2212 cm^{-1}, and suggested to be due to N_2O_4 [126], cis-$N_2O_2^{2-}$ [129] and N_2O [114, 126, 130] respectively.

4.4.2 Influence of gas phase conditions on the formation of surface species

The adsorption peaks described in the previous section were observed on DRIFT spectra recorded on a non-impregnated CGO10 sample subjected to 1000 ppm NO + 10% O_2. Spectra were also recorded on non-impregnated CGO10 while subjected to three other atmospheres: 1000 ppm NO, 1000 ppm NO_2 and 1000 ppm NO_2 + 10% O_2. In general the spectra recorded in 1000 ppm NO + 10% O_2, 1000 ppm NO_2 and 1000 ppm NO_2 + 10% O_2 look very much alike (se Figure 11 and Figure 12), with dominating peak groups located at ≈1600 cm^{-1} and ≈1200 cm^{-1}, ascribed as previously mentioned to adsorbed NO_2 (≈1610 cm^{-1}), NO_3^- (≈1580 cm^{-1}), and at 1197-1245 cm^{-1} overlapping NO_3^- and NO_2^- peaks. In addition to these peaks smaller peaks ascribed to N_2O (2207 cm^{-1})[130], cis-$N_2O_2^{2-}$ (≈1720 cm^{-1})[129], N_2O_4 (1671-1680 cm^{-1})[126] and NO_2 (1610-1614 cm^{-1})[126] are also observed. On the spectra recorded in 1000 ppm NO + 10% O_2 an extra peak is visible at 1603 cm^{-1} in between the 1610 cm^{-1} and 1580 cm^{-1} peak (see Figure 10), which likely can be ascribed to NO^- [126]. From the results it is not possible to conclude, whether this peak is not present in the NO_2 containing

atmospheres, or if the peak simply is overshadowed by the NO_2(ads) peak at 1610 cm^{-1}, which as expected is very strong in the NO_2 containing atmospheres. At 500 °C the NO^- peak is no longer discernible, and the NO_2(ads) peak is only visible as a weak shoulder, as the region around 1600 cm^{-1} has become entirely dominated by the nitrate peak at 1573 cm^{-1}.

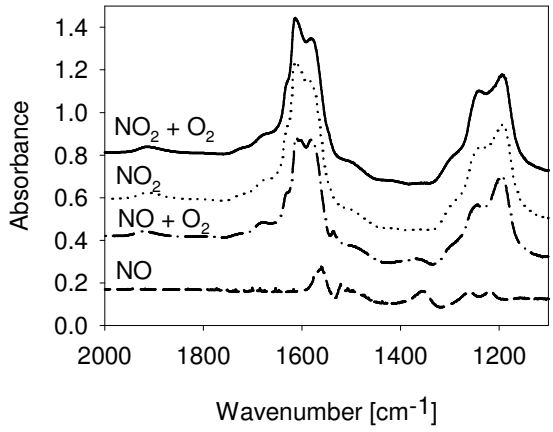

Figure 11. DRIFT spectra recoded on non-impregnated CGO sample at 300 °C.

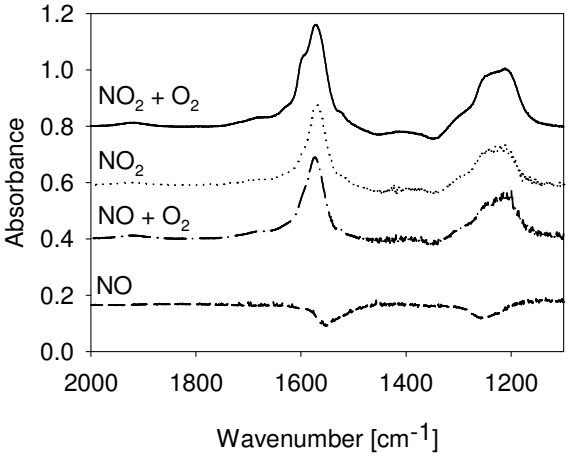

Figure 12. DRIFT spectra recorded in different atmospheres on non-impregnated CGO sample at 500 °C.

When the spectra recorded in 1000 ppm NO are compared to the spectra recorded in the three other atmospheres significant differences are observed, mainly as much fewer peaks are present in the IR spectra when the sample is supplied with only 1000 ppm NO in Ar. At 300 °C three adsorption peaks are clearly visible, at 1560 cm^{-1}, 1269 cm^{-1} and 1211 cm^{-1}, as in the previous section these peaks are ascribed to NO_3^- (1560 cm^{-1}, 1269 cm^{-1}, 1211 cm^{-1}) and/or NO_2^- (1269 cm^{-1}, 1211 cm^{-1}). At first hand it is surprising to find dominating peaks due to a NO_3^-, i.e. a highly oxidized NO specie, when there is no oxygen in the atmosphere and also since the IR spectra recorded by Philip et al. under similar conditions mainly seemed to be dominated by NO_2^- species[116]. Still the results in this work indicate, when CGO10 is supplied with 1000 ppm NO at 300 °C, NO is adsorbed and NO_3^- are formed by reaction of the NO with adsorbed oxygen or lattice oxygen at the CGO10 surface. It should be kept in mind; the CGO surface due to the pre-treatment in 10% O_2 likely is fairly rich in O_2 from the beginning of the experiment.

At 500 °C it is not possible to observe adsorption peaks at all, but curiously enough two clear desorption peaks are observed at 1552 cm^{-1} and 1255 cm^{-1}, i.e. almost exactly at the wavenumbers where the NO_3^-/NO_2^- adsorption peaks were observed at lower temperatures, see Figure 12. This could indicate that when the background spectrum was recorded, i.e. prior to the treatment in NO-containing atmosphere, a small amount of NO was already adsorbed on the CGO and this NO then subsequently is removed at 500 °C when the sample is treated in 1000 ppm NO without O_2. It is unknown where this small amount of pre-adsorbed NO should have come from, as the sample prior to experiment had not been near any NO source, and the experimental set-up was flushed in 10% O_2 between all the experiments to avoid any residual NO in the gas supply system during the start-up of a new experiment.

A summary of the NO-related peaks observed in the four different atmospheres is given in Table 3 together with the assignment of the peaks to different NO_x-species. The wavenumbers are stated for peaks observed at 300 °C, and if the wavenumber is written in bold the peak was also observed at 500 °C.

Table 3. Wavenumbers (cm^{-1}) at which peaks ascribed to adsorbed NO_x-species were observed on CGO in the following atmospheres: 1000 ppm NO, 1000 ppm NO + 10% O_2, 1000 ppm NO_2, 1000 ppm NO_2 + 10% O_2. The peaks were observed at 300 °C, and if the wavenumber is written in bold letters, also at 500 °C.

NO	**NO+O_2**	**NO_2**	**NO_2+O_2**	**Assignment**	**Reference**
	2207			N_2O	114, 126, 130
	2004	2199	2196	?	
	1922	**1912**	**1914**	NO(ads)	131
	1720	1720	1718	cis-$N_2O_2^{2-}$	129
	1680	**1671**	**1674**	N_2O_4	126
	1630	1630	**1630**	NO_2	132, 133
	1610	1614	**1612**	NO_2(ads)	126
	1603			NO^-	126
1560*	**1581**	**1581**	**1578**	NO_3^- (bidentate)	116, 126, 127
	1536			NO_3^- (bidentate)	117, 126, 127
	1286'			NO_2^- (chelating)	114-117, 129, 134
1263'	**1245**	1242	1239	NO_3^- (monodentate)/chelating NO_2^-	126, 128, 135/128
1219	**1197**	**1196**	**1190**	NO_3^- (bidentate)/ NO_2^-	126, 128, 135/127

*positive peaks at 300 °C, negative peaks at 500 °C; 'Only observed at 500 °C

4.4.3 Influence of catalyst composition on the formation of surface species

Already on the background spectra recorded in 10% O_2 a clear difference is seen between the non-impregnated and the K_2O impregnated sample, see Figure 13. On the K_2O impregnated sample four negative peaks are observed a 2757, 2400, 2069 and 1767 cm^{-1}. Negative peaks observed on background spectra are caused by IR-absorbing species and the 4 aforementioned peaks correspond exactly to the 4 peaks measured for KNO_3 by Bates et al.[136]. The presence of KNO_3 is somewhat surprising, since the sample during the preparation was heated to 700 °C, and the KNO_3 by this was expected to decompose to K_2O. However, from the background spectra it must be concluded that either was all the KNO_3 not completely thermally decomposed, or the K_2O has after the heat-treatment at 700 °C taken up some NO_x and formed KNO_3 again.

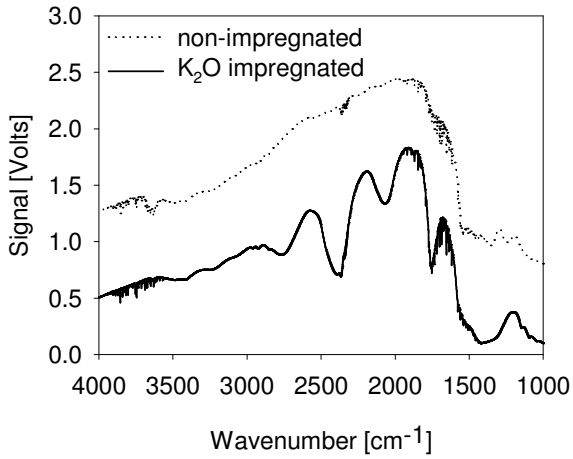

Figure 13. Comparison between background spectra recorded at 500 °C in 10% O_2 on non-impregnated and K_2O impregnated sample.

The absorbance spectra recorded on the K_2O impregnated sample looks much different compared to the spectra recorded on the non-impregnated sample, see Figure 14 for comparison of the spectra recorded at 300 °C and 500 °C in 1000 ppm NO +10% O_2 and Table 4 for an overview of the peaks observed at 300 °C and 500 °C . For the K_2O impregnated sample the IR spectra show four significant adsorption peaks at 2757, 2400, 2069 and 1767 cm^{-1}, which as just described are due to KNO_3 [136]. A few other adsorption peaks are also observed at 300 °C at the following wavenumbers: 1883 cm^{-1} (NO on potassium)[137], 1514 cm^{-1} (NO_3^-)[126] and 1343 cm^{-1} (NO_3^- in KNO_3)[136]. As for the

blank sample, the K_2O impregnated sample also shows negative peaks in the region 2333-2364 cm^{-1}, corresponding to removal of adsorbed CO_2. More surprising is however the K_2O impregnated sample shows a large negative peak, both at 300 and 500 °C, at 1560-1573 cm^{-1}, i.e. at the same wavenumbers as the dominating peak ascribed to NO_3^- on the non-impregnated sample. This could indicate that NO_3^- adsorbed on CGO-sites of the K_2O-impregnated sample during testing at 300-500 °C desorbs more easily or eventually migrates/spills over from the CGO sites to K_2O/KNO_3-sites.

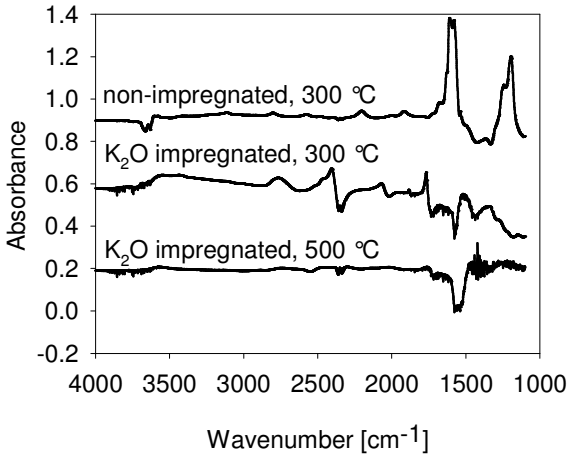

Figure 14. DRIFT spectra recorded at 300 °C on non-impregnated sample and at 300 °C and 500 °C on K_2O imp. CGO samples supplied with 1000 ppm NO + 10% O_2.

Table 4. Wavenumbers (cm^{-1}) at which peaks ascribed to adsorbed NO_x-species were observed on K_2O impregnated CGO at 300 °C and at 500 °C, while the sample was supplied with 1000 ppm NO + 10% O_2. The assignment of the peaks with references is also stated.

300 °C	**500 °C**	**Assignment**	**Ref**
2757		$(K)NO_3^-$	[136]
	2553(neg)	?	
2522		?	
2467		?	
2400		$(K)NO_3^-$	[136]
2356		?	
2069		$(K)NO_3^-$	[136]
	2018	?	
1883		NO	[137]
1767		$(K)NO_3^-$	[136]
1731(neg)	1723(neg)	cis-$N_2O_2^{2-\cdot}$	[129]
1573(neg)	1560(neg)	NO_3^- (bidentate)	[116, 126, 127]
1514		NO_3^- (bidentate)	[117, 126, 127]
1343		solid KNO_3/molten KNO_3	[136]

For the BaO impregnated sample the background spectra looked similar to the background spectra of the non-impregnated sample. In the absorbance spectra recorded on the BaO impregnated sample clear peaks were observed, see Figure 15 and Table 5. Several peaks observed at the highest wavenumbers could not be identified by comparison to literature, but the peak observed at ≈2390 cm^{-1} is likely ascribed to $Ba(NO_3)_2$[138] and the small peak observed at 2221 cm^{-1} to N_2O[114, 126, 130]. All the peaks observed at lower wavenumbers (below 1800 cm^{-1}) could by comparison to literature be assigned to either $Ba(NO_3)_2$[70, 120, 138] or $Ba(NO_2)$ (monodentate nitrite)[70]. When the temperature is increased from 300 to 500 °C the intensity of the peaks decreases, i.e. there becomes less of the adsorbed species, but only the N_2O and the $Ba(NO_3)_2$ at 1358 cm^{-1} disappears entirely due to the temperature increase.

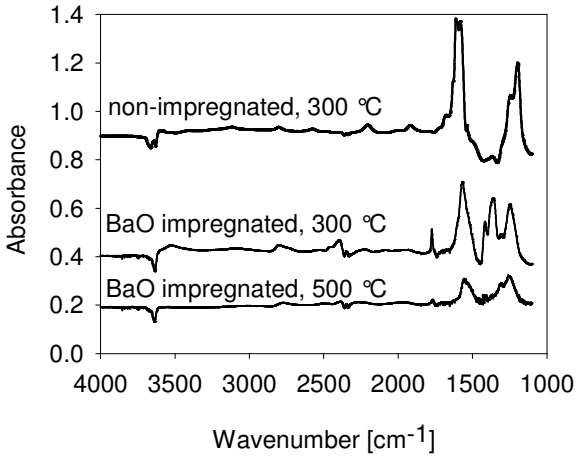

Figure 15. DRIFT spectra recorded at 300 °C on a non-impregnated sample and at 300 °C and 500 °C on a BaO impregnated sample supplied with 1000 ppm NO + 10% O_2.

Table 5. Wavenumbers (cm^{-1}) at which peaks ascribed to adsorbed NO_x-species were observed on BaO impregnated CGO at 300 °C and at 500 °C, while the sample was supplied with 1000 ppm NO + 10% O_2. The assignment of the peaks with references is also stated.

300 °C	**500 °C**	**Assignment**	**Ref**
2457		?	
2392	2390	$Ba(NO_3)_2$	138
	2276	?	
2221		N_2O	114, 126, 130
	1974	?	
1772	1767	$Ba(NO_3)_2$	138
1565	1550	$Ba(NO_3)_2$	70
1415	1414	$Ba(NO_3)_2$)/ $Ba(NO_2)$	120, 138/ 70
1358		$Ba(NO_3)_2$	120, 138
1307	1304	$Ba(NO_2)$	70
1247	1252	$Ba(NO_3)_2$	138

4.4.4 Influence of temperature on the formation of surface species

The TPD itself on the non-impregnated sample did not yield any new information on the NO_x adsorption and desorption, which had not already been gained during the previously performed adsorption experiments in different atmospheres. However during the cool-down after the TPD a somewhat surprising observation was made. After the feature around 1600 cm^{-1} at 500 °C had been reduced to only one peak at 1573 cm^{-1}, a clear peak at 1612 cm^{-1} re-appeared during cool down, see Figure 16. Further, a redistribution is appearing in the feature around 1200 cm^{-1} during cool down (Figure 16). It should be emphasized the redistribution of the NO peaks occurred, even though the sample was kept in 10% O_2 and had been so for more than one hour, when the sample was cooled down. Overall the results from cooling down indicate that changing the temperature does not only affect the gaseous NO_x capability to adsorb in different ways, but also may re-configure already adsorbed NO_x.

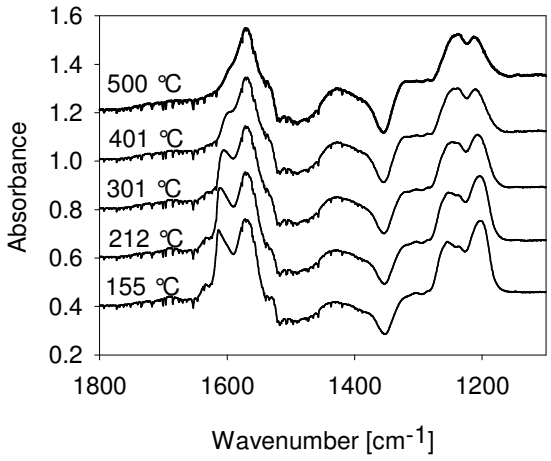

Figure 16. DRIFT spectra recorded during cool down of non-impregnated sample after TPD. Both TPD and cool down was performed in 10% O_2 in Ar.

During the TPD from 30 °C to 500 °C a significant change in the adsorbed species was observed on the K_2O impregnated sample. This is illustrated in Figure 17 where the entire spectra recorded in the beginning (30 °C) and in the end (500 °C) of the TPD are shown.

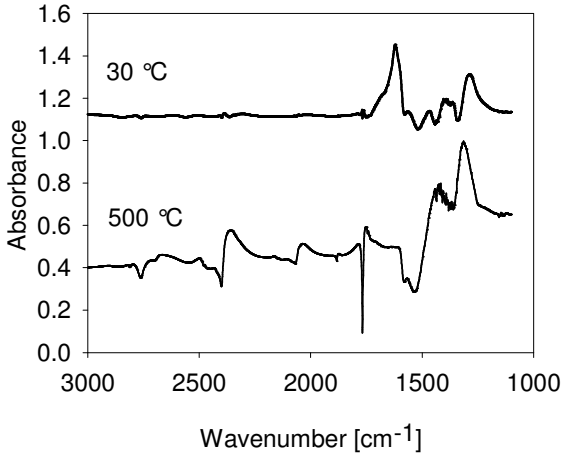

Figure 17. DRIFT spectra recorded on the K_2O impregnated sample at the beginning of the TPD (30 °C) and at the end (500 °C).

In order to identify any tendencies during the TPD the peak areas were fitted with the Bio-Rad Win-IR Pro software. The result from fitting the dominant peaks at different temperatures is shown in Figure 18. Three peaks are increasing in size with increasing temperature, namely the peaks located around 2384 cm^{-1}, 2054 cm^{-1} and 1288. The two first peaks likely correspond to peaks observed for KNO_3 by Williamson et al. at 2390 cm^{-1} and 2050 cm^{-1} [139]. The peak at 1288 cm^{-1} could be related to chelating NO_2^-, as a peak ascribed to this specie had been observed in several studies at 1270-1290 cm^{-1} [114-117, 129, 134]. This peak was also observed at 500 °C on the non-impregnated CGO sample treated in 1000 ppm NO + 10% O_2. The peak located at 1382 cm^{-1} is either decreasing in size or remaining constant until 180 °C, whereafter it no longer is discernible. Just as the two growing peaks observed at 2384 $cm^{-1}$and 2054 cm^{-1}, the peak at 1382 cm^{-1} is likely ascribed to KNO_3, even though it seems to be a contradiction that the two first peaks are growing with temperature whereas the last one is decreasing in size. The explanation is likely the peak at 1382 cm^{-1} is located in a region where different oxygenated carbon species also are absorbing in the spectra[125], and the change in these specie's corresponding IR-signal may interfere with the KNO_3 peak at 1382 cm^{-1}. At 1619 cm^{-1} a peak which shows a consistent decrease with temperature is observed, until the peak disappears near 400 °C. The peak is located slightly above 1605 cm^{-1} where Busca et al.[126] identified a peak ascribed to adsorbed NO_2, and slightly below 1630 cm^{-1},

where Adelman et al.[132] and Delahay et al.[133] identified a peak which was ascribed to N-bound NO_2. In conclusion the 1619 cm^{-1} peak is likely ascribed to an adsorbed NO_2 specie, which is removed with increasing temperature, likely because the NO_2 is moving to K-sites and adsorbed as KNO_3, since the peaks related to this compound are increasing with temperature. Finally, three negative peaks are also appearing during the TPD, namely at 1882 cm^{-1}, 1766 cm^{-1} and 1517 cm^{-1}. The negative peak at 1517 cm^{-1} is likely ascribed to removal of a NO_3^- -species[126, 127]. For the two negative peaks at 1882 cm^{-1} and 1766 cm^{-1} they are suggested to belong to the same species, the $(NO)_2$ dimer, as the frequencies of this dimer are 1862 cm^{-1} and 1768 cm^{-1} [140].

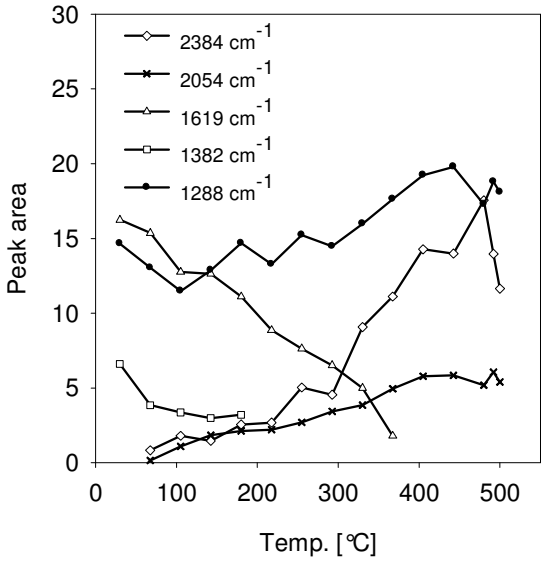

Figure 18. Development of the peak area during TPD on the K_2O impregnated sample. The graph shows the development in the major peaks located at wavenumbers 2384 cm^{-1}, 2054 cm^{-1}, 1619 cm^{-1}, 1382 cm^{-1} and 1288 cm^{-1}. Lines are for visual guidance only.

Overall with increasing temperature there seem to be a change from adsorbed NO_2 and NO_3^- on the CGO surface to NO_3^- adsorbed on KNO_3 and also chelating NO_2^-. Since the sample was not supplied with NO during the temperature increase this shows that the adsorbed NO_x species on the catalyst surface are mobile, and also a change in the preferred/most favorable adsorption mode with temperature.

As previously described redistribution of the adsorbed NO was observed on the non-impregnated sample during cooling down. Similarly redistribution of the adsorbed NO_x-species is observed on the BaO impregnated sample, not during the cool down step, but during the TPD while the sample was kept in 10% O_2. This is illustrated in Figure 19 which shows the spectrum recorded at 30 °C at the very beginning of the TPD and the spectrum recorded when the sample had reached 300 °C. In the range between 1700 cm^{-1} and 1200 cm^{-1} the peaks disappearing or decreasing in size are ascribed to adsorbed NO_2 (1607 cm^{-1})[126] NO_2^- (1329 cm^{-1})[128] and chelating NO_2^- (1276 cm^{-1})[114-117, 129, 134], and the peaks remaining and eventually increasing in size (1420 cm^{-1}, 1358 cm^{-1}, 1250 cm^{-1}) are ascribed to $Ba(NO_3)_2$ [70, 120, 138] or just NO_3^- adsorbed directly on the CGO (1573 cm^{-1})[116, 126, 127]. The peak at 1573 cm^{-1} is assigned to NO_3^- adsorbed directly on the CGO since a peak at exactly the same position was observed during the experiments on the non-impregnated CGO sample. It should also be noted that the peak at 1250 cm^{-1} could be ascribed to $Ba(NO_3)_2$ but possibly also to NO_3^- [135] or chelating NO_2^- [128] bound directly to the CGO; as a peak at 1250 cm^{-1} also was observed on the non-impregnated CGO sample.

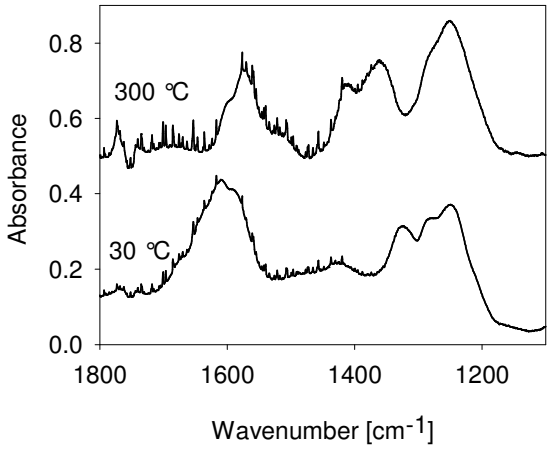

Figure 19. Spectra recorded at the beginning of the TPD (30 °C) and during the TPD (300 °C). Before the heating ramp was started (15 °C/min in 10% O_2) the sample was first treated at 30 °C for ½ h in 1000 ppm NO + 10% O_2 and subsequent flushed ½ h in 10% O_2.

4.4.5 NO_x adsorption properties and electrochemical deNO_x

One of the intentions in this work is to relate the adsorption studies on CGO to findings on electrochemical removal of NO_x. Three of the main findings from the conversion studies on electrochemical cells are[39, 44, 113, 141]:

- The highest NO_x conversion is found in NO atmospheres without presence of O_2 on both non-impregnated and impregnated electrodes.
- On non-impregnated electrodes the conversion increases with temperature, but the selectivity/current efficiency decreases.
- Addition of a NO_x storage compound significantly increases the NO_x conversion and current efficiency at lower temperatures.

The DRIFT spectra recorded on the non-impregnated CGO sample showed the largest NO_x adsorption in O_2 containing atmospheres at the lowest temperatures (300 °C), and vice versa the smallest NO_x adsorption at the highest temperature (500 °C) without O_2 present. This is at first sight in contradiction to finding 1) and 2) listed above, where the largest conversion is found at 500 °C without O_2 present. Part of the explanation of this apparent contradiction could be the presence of the perovskite (LSM/LSF) in the electrodes during the conversion/polarisation experiments. Liu et al.[142] measured increased NO_x adsorption on a La-perovskite with increasing temperature, which is more consistent with the highest NO_x conversion found at the highest temperature. This illustrates the importance of taking both the adsorption properties of the perovskite and the CGO into consideration, when comparing to measurements on composite electrodes. With respect to the importance of O_2 for the NO_x adsorption the results from DRIFT spectroscopy in different atmospheres (1000 ppm NO, 1000 ppm NO + 10% O_2, 1000 ppm NO_2 and 1000 NO_2 + 10% O_2) show the presence of either O_2 together with NO or just the presence NO_2 dramatically increases NO_x adsorption on CGO. For the perovskites the results by Klingenberg et al.[143] show that NO is adsorbed on La_2O_3 at 500 °C without the presence of O_2. Werchmeister et al. previously identified NO_2 as an important reaction intermediate during electrochemical reduction of NO_x[36, 38]. With the results from the DRIFT spectroscopy in mind, it is suggested that the NO_2 is an important intermediate, as NO_2 adsorbs much more readily on the electrode surface, even though it may not be crucial for the NO_x adsorption on the perovskite.

With respect to finding 2): the highest selectivity for NO_x conversion being found at the lowest temperatures, this finding may be explained by the adsorption properties found for CGO. There are at least two potential ways of explaining the higher selectivity. One explanation could be that the higher NO_x adsorption-ability of the CGO at lower temperatures simply hinders the O_2 accessibility to the CGO surface, and thereby increases the selectivity of the electrodes. Another explanation could be the larger amount of adsorbed NO_x at low temperatures on CGO in the vicinity of the perovskite, which makes it easier for the NO_x to react at the perovskite or at the CGO-perovskite interface, at the temperatures where the adsorption capabilities of the perovskite is low.

As mentioned in finding 3) a significant improvement of the NO_x conversion and the current efficiency was found for the impregnated samples. The DRIFT spectroscopy clearly shows that impregnation with K_2O and BaO strongly affects the NO_x adsorption on CGO; this is observed even though the impregnated mass is only 3 wt% (K_2O) or 1 wt% (BaO) of the total sample mass. For this reason it seems likely that increased NO_x adsorption indeed is one of the reasons why impregnation with NO_x-storage compounds increases the conversion on composite electrodes during electrochemical deNO_x.

Moreover an interesting finding from the TPD measurements was that the adsorbed NO_x was able to change adsorption state with changing temperature, and also capable of moving between CGO-adsorption sites and K- or Ba-adsorption sites. Mobility of the adsorbed NO_x on the electrode surface is crucial, as the reactive zone of the electrodes is at the triple-phase boundary, and movement of the NO_x to the triple-phase boundary likely is a necessity for the NO_x-reduction to occur.

4.5 Conclusions

From the results presented the following conclusions can be drawn:

- on CGO treated in 1000 ppm NO + 10% O_2 the variety of adsorbed NO_x species decreases from 300 °C to 500 °C, at 500 °C the dominant species are adsorbed NO_3^- and NO_2^-.
- NO_x adsorbtion on CGO is significantly larger in the presence of either NO + O_2 or NO_2 compared to when only NO is present.
- when NO_x conversion measurements on the composite electrodes are related to NO_x adsorption, both the NO_x adsorption properties of the oxygen-ion conducting CGO and the electron conducting perovskite must be considered,
- higher NO_x selectivity observed during conversion measurements at low temperature may be explained by the increased NO_x adsorption on CGO at low temperatures.
- impregnation with K_2O or BaO significantly alters the NO_x adsorption on CGO
- the adsorbed NO_x species are mobile on the surface of impregnated CGO

4.6 Acknowledgement

This work was supported by the Danish Strategic Research Council under contract no. 09-065183. The DRIFT work presented was conducted at Competence Centre for Catalysis (KCK), which is financially supported by Chalmers University of Technology, the Swedish Energy Agency and the member companies: AB Volvo, Volvo Car Corporation AB, Scania CV AB, Saab Automobile Powertrain AB, Haldor Topsø A/S and ECAPS AB. The stay at KCK was facilitated by Professor Anders Palmqvist, who is acknowledged for his great help in making this possible.

5 Improvement of LSM15-CGO10 electrodes for electrochemical removal of NO_x by KNO_3 and MnO_x impregnation

This chapter is the manuscript "Improvement of LSM15-CGO10 Electrodes for Electrochemical Removal of NO_x by KNO_3 and MnO_x Impregnation" accepted for publication in Journal of The Electrochemical Society.

5.1 Abstract

LSM15-CGO10 ($La_{0.85}Sr_{0.15}MnO_3$-$Ce_{0.90}Gd_{0.1}O_{1.95}$) electrodes were impregnated with either KNO_3 or MnO_x, and the effect of the impregnations on the activity in NO containing atmospheres was investigated by electrochemical impedance spectroscopy and cyclic voltammetry. The electrodes were tested in 1000 ppm NO, 10% O_2 and 1000 ppm NO + 10% O_2 in the temperature range 300-500 °C and the electrodes were investigated by scanning electron microscopy before and after testing. At 400-450 °C a NO_x-storage process was observed on the KNO_3-impregnated electrodes, this process appeared to be dependent on preceding catalytically formation of NO_2. Despite a marked difference in the microstructure of the impregnated KNO_3 and MnO_x, both impregnations caused a significant reduction in the polarisation resistance of the electrodes, due to a general decrease in resistance of all the identified electrode processes. The effect of the impregnation was strongest at low temperatures, likely because the microstructure of the impregnated compounds changed at higher temperatures. Scanning electron microscopy images revealed a significant change in the microstructure of the impregnated samples after the test.

5.2 Introduction

Air pollution from road traffic has due to the harmful effects on human health and environment got more and more attention during the last decades. In order to reduce air pollution, restrictions has been imposed on the emissions from vehicles, which on European level has been done by the introduction of the Euro I-VI standards. These standards impose increasing restrictions on the emission of CO, NO_x, hydrocarbons and particulate matter[12].

The increased restrictions on NO_x emissions are adopted, as NO_x has a negative impact on the respiratory system, increase the formation of ozone at ground level, cause formation of acid rain and also act as green house gas[11]. To reduce the NO_x emission from vehicles several technologies

have been developed, for NO_x-removal under lean conditions (i.e. in excess of oxygen) the three most known technologies are selective catalytic reduction with urea (urea-SCR), selective catalytic reduction with hydrocarbons (HC-SCR) and the NO_x-storage and reduction (NSR) catalyst[108].

An alternative way to remove NO_x under lean conditions is the electrochemical removal of NO_x, which was first suggested by Pancharatnam et al.[22]. Since then several investigations has been made of electrochemical removal of NO_x[29, 30, 34, 36, 44, 144]. A general challenge in electrochemical removal of NO_x is to find electrodes, which both have a sufficient activity and show a high selectivity for NO_x reduction compared to reduction of O_2[4]. For this reason the aim in this work is to investigate if the activity and selectivity of LSM15-CGO10 electrodes towards NO_x can be improved by impregnating the electrodes with either KNO_3 or MnO_x.

KNO_3 is chosen for the impregnation, since K_2O/KNO_3 has shown potential as a NO_x-storage compound in nitrogen storage and reduction catalysts[72, 73, 145, 146], and for this reason is expected to improve selectivity and activity for NO_x reduction on the LSM15-CGO10 electrodes.

Just as KNO_3, MnO_x is also reported to have capability to store NO_x[77] and may for the same reasons improve the NO_x reduction selectivity and activity. Moreover, impregnated MnO_x may increase the general activity of the LSM/CGO electrode, as nano-sized MnO_x-particles may extend the triple-phase-boundary, and an extension of the triple-phase boundary in the literature is considered to be one of the important effects of electrode impregnation[147-149]. An increased activity with impregnation with MnO_x is expected, since Mn can exist in a number of oxidation states, and for this reason is the redox active center in perovskites used for redox catalysis[78] and also has been proven to affect the oxygen reduction reaction on electrodes[79].

In the present work symmetric cells with LSM15-CGO10 ($(La_{0.85}Sr_{0.15})_{0.99}MnO_{3+\delta}$-$Ce_{0.9}Gd_{0.1}O_{1.95}$) composite electrodes were prepared. LSM was chosen for this work due to the good stability of this perovskite compared to other perovskites like $La_{1-x}Sr_xFe_{1-y}Co_yO_3$ and $Ba_{1-x}Sr_xFe_{1-y}Co_yO_3$, eventhough these have a higher activity in the investigated temperature range[62]. The cells were after the preparation divided into three groups and treated in three different ways: one group was impregnated with KNO_3, one group was impregnated with MnO and one group was left without any impregnation. The cells were following tested with electrochemical impedance spectroscopy

and cyclic voltammetry. In addition to this cells from each of the three groups were investigated by scanning electron microscopy before and after testing.

5.2.1 Conductivity of KNO_3 and MnO_x compared to electrode materials

A point which must be considered is the conductivity of the impregnated materials, as an impregnated phase with conductivity much higher than the electrode materials could significantly alter the current distribution in the electrode. In the temperature range 350 °C – 500 °C the conductivity of KNO_3 increases from 0.669 S/cm to 1.094 S/cm[100]. No information has so far been found concerning the conductivity of MnO_x at 300 °C – 500 °C, but MnO_2 is reported to have electronic conductivities in the range $5x10^{-7}$-$3x10^{-3}$ S/cm^2 at room temperature, the large range of the conductivities being due to a strong dependence on the crystallographic form of MnO_2[102]. Since MnO_2 is a semiconductor the conductivity will increase with increasing temperature. The electronic conductivity of LSM16/LSM20 is reported to be in the range 90-110 S/cm at 300-600 °C[52,53] and for CGO10 the total conductivity at 500 °C is 0.005 S/cm[99]. By comparing the conductivities of the impregnated compounds to the conductivities of the electrode materials it is clear the highest electronic conductivity will be found in the LSM15. For this reason the current distribution in the electrode is not expected to change due to the introduction of an "easier" current pathway in the electrode by the impregnation.

5.3 Experimental

5.3.1 Cell preparation

The LSM15 used for the electrodes was prepared by the glycine-nitrate combustion synthesis[150] with a molar ratio of 0.548 glycin/nitrate. The nitrates used for the synthesis were all from Alfa Aesar. The LSM was synthesized as $(La_{0.85}Sr_{0.15})_{0.99}MnO_3$, i.e. as being slightly deficient on the A-site. After the synthesis the LSM powder was calcined at 1000 °C for 6 hours, and subsequent the phase-purity of the powder was confirmed by XRD on a theta/theta Stoe diffractometer. The CGO10 powder used for the electrodes was supplied by Rhodia and had a BET area of 7.29 m^2/g.

The symmetric cells were manufactured by screen-printing a terpineol based LSM15-CGO10 paste on 200 µm thick CGO10 tapes from Kerafol. The ratio between LSM15 and the CGO10 in the screen-printing paste was 50 wt% LSM15/50 wt% CGO10, and before mixing d50 was ≈1 µm for LSM15 and ≈0.5 µm for CGO10. After screen-printing the 50 x 50 mm^2 cells were sintered at 1050

°C for 2 h. The cells were after the sintering cut into small 6 x 6 mm^2 cells with a diamond toll. Finally a gold current collector was applied on the cells by painting the cells with a gold paste containing 20 wt% graphite. The cells were then heated to 800 °C in order to burn away the graphite, leaving behind a porous, electronic conductive gold current collector on top of the electrodes.

For the impregnation with KNO_3 an aqueous solution containing 1.7 M KNO_3 and Triton-X45 surfactant was prepared. The concentration of Triton-X45 was 1 wt% with respect to the water. For the impregnation with $Mn(NO_3)_x$ a purely aqueous solution with 1.7 M $Mn(NO_3)_x$ was used. The impregnation was made by soaking the cells in the impregnation solution in a small beaker, which was placed in a vacuum chamber. The vacuum chamber was for less than a minute evacuated to a pressure below 0.1 mbar. After the impregnation the cells were heated in a furnace to 350 °C for one hour in order to:

1) Decompose the Triton-X45
2) Decompose the $Mn(NO_3)_x$ into MnO_x[103].

In addition to this the KNO_3 would melt during the heat treatment (mp(KNO_3)=334 °C[97]), and for this reason probably redistribute in the electrode. The impregnation procedure just described was repeated twice for both the KNO_3 and the $Mn(NO_3)_x$ impregnation.

5.3.2 Electrochemical characterization

For the electrochemical cell testing a four sample set-up was used in which each of the four cells was fixed between two gold meshes, which also acted as current collectors. The set-up was placed in a furnace, sealed and attached to the gas supply system. Before the set-up was heated a leak test was made.

During the cell test electrochemical impedance spectra (EIS) and cyclic voltammograms (CVs) were recorded in each of the three atmospheres: (1) 1000 ppm NO in Ar, (2) 10% O_2 in Ar and (3) 1000 ppm NO + 10% O_2 with balance Ar. These concentrations of NO and O_2 were chosen as they resemble the concentrations which may be found in the exhaust from a diesel car[7]. The EIS and CVs were recorded in the temperature range 300-500 °C, as this is the temperature range expected for diesel car exhaust[151]. The measurements were made with 50 °C intervals, starting

from 300 °C and going to higher temperatures. At 500 °C flow variations were made by changing the flow from 100 ml/min to 50 ml/min in all three atmospheres. In addition to this variations in the NO concentration and O_2 concentration were made, but only for the cells without impregnation. After the measurements at 500 °C the temperature was decreased to 300 °C, and EIS were recorded once again in 1000 ppm NO + 10% O_2 to estimate the change during the cell test, before the furnace finally was cooled down. In general the EIS were recorded in the frequency range 1 MHz-0.0008 Hz with 6 points pr. decade and 36 mV rms amplitude, a few spectra were however recorded with a slightly different low frequency limit. The cyclic voltammograms were recorded between the voltage limits ±1V with scan rate 10 mV/s, step size 5 mV and 4 scans recorded for each measurement. Both the EIS and CV were recorded with a Gamry Reference 600 potentiostat.

It should be noted only in the test on LSM15-CGO10 cells without impregnation 4 cells were subjected to electrochemical cell testing (EIS and CVs), whereas in the two tests on impregnated cells only 3 cells were tested in each test. The fourth cell in the set-up in these two tests was not subjected to the electrochemical cell testing but experienced the exactly same temperature profile as the three electrochemically tested cells, and was later investigated in the scanning electron microscopy to observe the effect of the temperature on the microstructure.

5.3.3 Scanning Electron Microscopy

Tested and non-tested cells were investigated in a Zeiss Supra 35 scanning electron microscope. In order to be able to observe structures smaller than 200 nm, the cells were broken manually and the cross-section was investigated directly in the microscope without application of any coating. In order to ensure a high resolution most of the images were recorded with the in-lens detector and low accelerating voltage (3kV).

5.4 Results

5.4.1 Impregnation

The cells were weighed before and after impregnation to determine the impregnation load on the tested cells. For the cells impregnated with KNO_3 the final load was 0.3 ±0.1 wt% for three of the cells, whereas the last cell apparently lost weight during the impregnation. For the cells impregnated with MnO_x the final load was 0.5 ±0.2 wt%.

5.4.2 Cyclic voltammetry

For the 3-4 cells tested in each test good reproducibility is observed for cyclic voltammograms recorded at the same conditions within each test, both with respect to shape of the cyclic voltammogram and current densities. A general feature of the cyclic voltammograms recorded on both blank and impregnated cells is their shape depend on the atmosphere as illustrated in Figure 20 for the blank cells. Clear peaks were only observed on the CVs recorded in 1000 ppm NO at 400 and 450 °C on the KNO_3 impregnated sample, see Figure 21 where a comparison is made to a CV recorded on one of the blank cells.

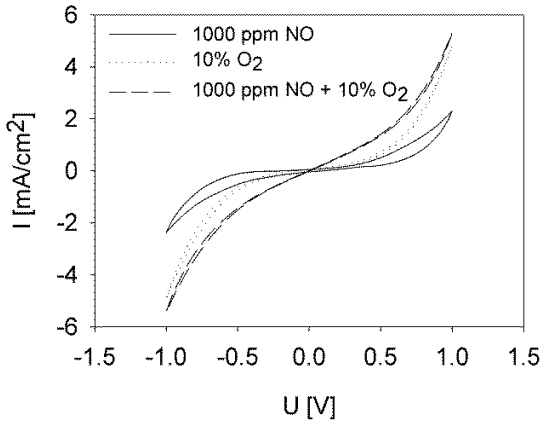

Figure 20. Cyclic voltammograms recorded on a blank LSM15-CGO10 symmetric cell in different atmospheres at 400 °C.

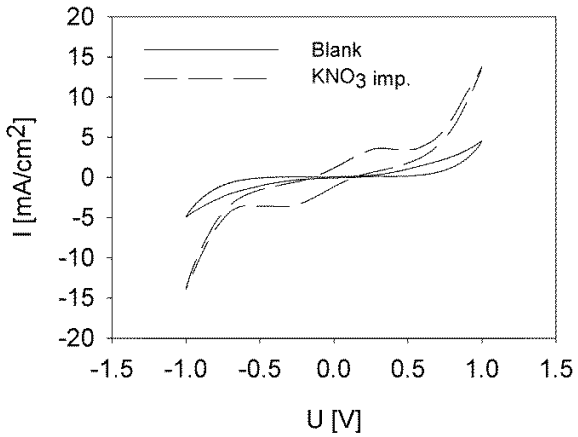

Figure 21. Cyclic voltammograms recorded at 450 °C in 1000 ppm NO on a LSM15-CGO10 cell without impregnation and impregnated with KNO_3.

From the cyclic voltammograms recorded in 1000 ppm NO + 10% O_2 the current densities at 0.9 V was found for the three tests, the result is shown in Table 6; where the stated values are the averages from the 3-4 tested cells at both negative and positive polarisation. As the result for one of the cells impregnated with MnO_x deviates from the two other cells the values are stated separately in Table 6. In general the largest current densities are observed for impregnated samples, with the difference between the impregnated and the blank samples being most pronounced at low temperatures.

Table 6. Current densities in mA/cm^2 observed at the cyclic voltammograms (2. scan) at 0.9 V polarisation in 1000 ppm NO + 10% O_2 on blank, KNO_3 and MnO_x impregnated LSM15-CGO10 symmetric cells. The numbers stated in the parenthesis are the uncertainties.

Temp. [°C]	Blank	KNO3	MnO_x	
			Cell A and C	Cell D
300	0.46(0.04)	0.6 (0.03)	3.03(0.06)	2.8(0.1)
350	1.2(0.1)	3(0.1)	7(1)	7.6(0.4)
400	4.2(0.3)	9(0.4)	12(3)	15.2(0.8)
450	10.3(0.5)	18(3)	12(3)	25(1)
500	27(1)	30(1)	13(3)	63(5)

5.4.3 Fitting procedure

For fitting of the impedance spectra the program ZView 2, version 3.1c was used[107]. An equivalent circuit was used which contained a serial resistance R_s and a number of RQ subcircuits, where a resistance (R) is in parallel with a constant phase element (Q). The admittance of the constant phase element may be written as[152]

$$Y = Y_0 (j\omega)^n \qquad 5.1$$

- where Y is the admittance, Y_0 is the amplitude of the constant phase element admittance, j is the imaginary number, ω is the angular frequency and n is the frequency exponent of the constant phase element. For the physical interpretation of the constant phase element, the near-equivalent capacitance (C_ω) was calculated according to the formula[153]

$$C_\omega = R^{(1-n)n} Y_0^{\,1/n} \qquad 5.2$$

All impedance spectra were fitted with one serial resistance and between 2 and 4 RQ-subcircuits. The fitting process consisted of two sessions: During the first session all the resistances and parameters for the constant phase elements were allowed to adjust during the fitting of a total number of at least 40 impedance spectra for each test. After this first session identical processes were identified by comparing the characteristic frequencies, C_ω and the n-values, and the average n-value was calculated for each of the identified processes. During the second session the impedance spectra were fitted once again, with the n-values fixed at the average values.

5.4.4 Conductivity

The average serial resistance of the cells was found for each test and converted to conductivities. The conductivities are stated in Figure 22 together with literature data for the conductivity of CGO calculated from the results found by Omar et al.[154].

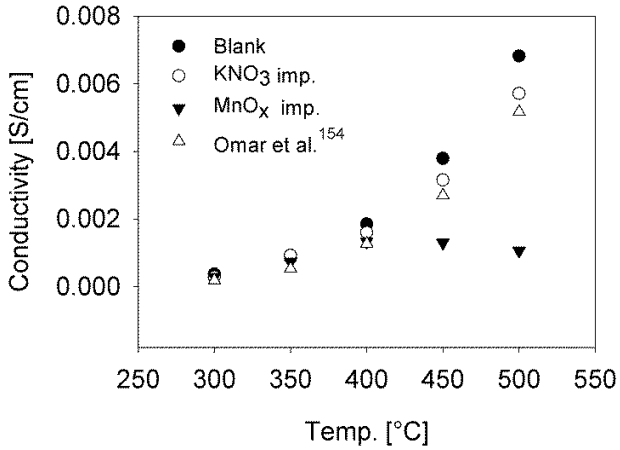

Figure 22. Conductivity of the three tests with LSM15-CGO10 electrodes on CGO electrolyte compared to literature values for the conductivity of CGO.

In general fairly good agreement is achieved between conductivities of the blank cells and the KNO_3-impregnated cells compared to the conductivity of CGO reported in the literature, but especially at higher temperatures the conductivity of the blank sample is higher. The conductivity of the MnO_x-impregnated samples follow the conductivity of the other samples until 400 °C, whereafter the conductivity start to decrease even though the temperature increases.

5.4.5 Polarisation resistance

When comparing the size of the polarisation resistances between the three tests, see Table 7, the polarisation resistance of both the impregnated samples is below the polarisation resistance of the blank samples in the temperature range 300-450 °C. At 500 °C the impregnated samples still have a lower polarisation resistance compared to the blank samples in 1000 ppm NO, but in 10% O_2 and 1000 ppm NO + 10% O_2 the polarisation resistance is either equal to or slightly larger for the impregnated samples. In all the three tests the polarisation resistance depends strongly on the atmosphere. Independent of whether the cells are impregnated or not the lowest polarisation resistance is at all temperatures found in 1000 ppm NO + 10% O_2. The highest polarisation resistance is below 400 °C found in 10% O_2, and above 400 °C in 1000 ppm NO. For the blank cell stack the polarisation resistance consistently decreased with increasing temperature, whereas for the KNO_3-impregnated samples an increase in the polarisation resistance was observed from 450 °C to 500 °C in 1000 ppm NO and 10% O_2, and for the MnO_x-impregnated cell an increase was observed from 400 to 450 °C in all atmospheres.

Table 7. Average polarisation resistances in 1000 ppm NO, 10% O_2 and 1000 ppm NO + 10% O_2 obtained for symmetric LSM15-CGO10 cells without impregnation (labelled "blank") with KNO_3 impregnation and with MnO_x-impregnation. The values are stated in Ωcm^2.

	1000 pppm NO			10% O2			1000 ppm NO + 10% O2		
Temp. [°C]	Blank	KNO_3	MnO_x	Blank	KNO_3	MnO_x	Blank	KNO_3	MnO_x
300	$1.0\cdot10^4$	$4.1\cdot10^3$	$1.1\cdot10^3$	$1.8\cdot10^5$	$7.8\cdot10^4$	$4.2\cdot10^3$	$7.6\cdot10^3$	$3.2\cdot10^3$	$7.6\cdot10^2$
350	$4.2\cdot10^3$	$1.4\cdot10^3$	$4.5\cdot10^2$	$3.1\cdot10^4$	$5.1\cdot10^3$	$1.2\cdot10^3$	$2.2\cdot10^3$	$9.9\cdot10^2$	$3.5\cdot10^2$
400	$2.9\cdot10^3$	$9.7\cdot10^2$	$2.4\cdot10^2$	$5.8\cdot10^3$	$1.1\cdot10^3$	$4.3\cdot10^2$	$7.8\cdot10^2$	$5.1\cdot10^2$	$2.2\cdot10^2$
450	$2.0\cdot10^3$	$6.0\cdot10^2$	$1.1\cdot10^3$	$1.2\cdot10^3$	$2.1\cdot10^2$	$4.6\cdot10^2$	$3.1\cdot10^2$	$2.7\cdot10^2$	$2.3\cdot10^2$
500	$1.3\cdot10^3$	$9.4\cdot10^2$	$9.0\cdot10^2$	$2.6\cdot10^2$	$2.6\cdot10^2$	$3.2\cdot10^2$	$1.2\cdot10^2$	$1.4\cdot10^2$	$1.8\cdot10^2$

5.4.6 Characteristics of processes/arcs

All the impedance spectra were fitted with 2-4 RQ subcircuits. In Figure 23 to Figure 25 representative examples from the fitting of the impedance spectra are shown, with the arcs used for the deconvolution of the spectra numbered according to the description in the results section. The shown spectra were recorded at 400 °C in 1000 ppm NO + 10% O_2 on cells from each of the three tests: 1) without impregnation; 2) with KNO_3 impregnation and 3) with MnO_x impregnation.

In the following sections the results from fitting of the impedance spectra recorded during the three different tests will be described in more detail.

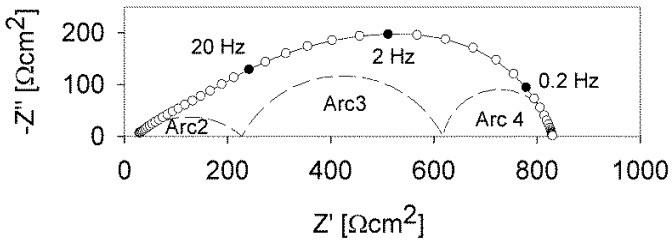

Figure 23. Impedance spectrum recorded on cell without impregnation at 400 °C in 1000 ppm NO + 10% O_2. The circles represents the experimental values, the full line the total fit and the dashed lines the arcs used for deconvolution of the spectrum. Filled circles mark the stated frequencies.

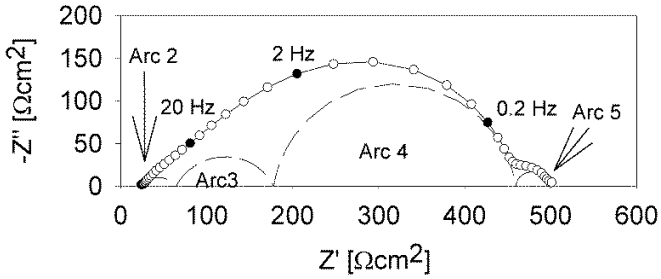

Figure 24. Impedance spectrum recorded on cell with KNO_3 impregnation at 400 °C in 1000 ppm NO + 10% O_2. The circles represents the experimental values, the full line the total fit and the dashed lines the arcs used for deconvolution of the spectrum. Filled circles mark the stated frequencies.

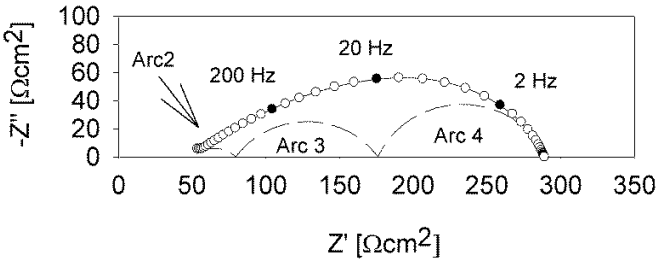

Figure 25. Impedance spectrum recorded on cell with MnO_x impregnation at 400 °C in 1000 ppm NO + 10% O_2. The circles represents the experimental values, the full line the total fit and the dashed lines the arcs used for deconvolution of the spectrum. Filled circles mark the stated frequencies.

5.4.6.1 Blank cells

The impedance spectra recorded on the LSM15-CGO10 symmetric cells without impregnation were all fitted with 4 RQ-subcircuits at 300 °C, and 3 RQ-subcircuits at higher temperatures. Each RQ-subcircuit corresponds to an arc in the Nyquist plot, and in the following the arcs are numbered from 1 to 4, with number 1 being the arc observed at the highest frequencies (only observed at 300 °C), and number 4 being the arc observed at the lowest frequencies. A discussion of how the arcs may relate to different electrode processes will be found in the discussion section.

An overview of some characteristics of the arcs found during the fitting are stated in Table 8.

Table 8. Characteristics of the four arcs/RQ-subcircuits used during fitting of the impedance spectra recorded on symmetric LSM15-CGO10 cells. In the table n-value is the n-value of the CPE, Ea the activation energy, Stdev states the standard deviation of Ea and R^2 is the estimate of the linearity between the points used for the calculation of Ea.

					Results at 300-500 °C		
Atm.*	Arc	Freq. at 300 °C Hz	Freq. at 500 °C Hz	n-value	Ea eV	Stdev	R^2
NO	1	19952		0.90			
	2	9	137	0.45	0.78	0.02	0.997
	3	3	4	0.68	0.69	0.07	0.962
	4	0.3	0.08	0.89	?	?	?
O_2	1	18458		0.90			
	2	7	1049	0.45	0.96	0.05	0.991
	3	0.09	20	0.54	0.98	0.05	0.999
	4	0.0007	0.8	0.89	1.29	0.05	0.992
NO + O_2	1	21745		0.90			
	2	22	492	0.45	0.74	0.02	0.993
	3	5	27	0.69	0.69	0.01	0.972
	4	0.8	2	0.89	0.88	0.02	0.984

*The concentrations were 1000 ppm NO, 10% O_2 and 1000 ppm NO +10% O_2, in all cases with balance Ar.

In the first section of Table 8 the characteristic frequency of the individual arcs are stated at 300 °C and 500 °C together with the n-value of the constant phase element. With respect to the n-values it is noted the values were the same for arc 1, 2, and 4 independent of the atmosphere, whereas for arc 3 variation in the n-value was observed between the atmospheres. In the second section

the activation energy for the process corresponding to each arc is stated together with the standard deviation and R^2-value of the linear regression, which was used for calculation of the activation energy. In this second section the stated activation energies are calculated from the results obtained in the entire temperature range from 300-500 °C, which means 5 points are used for the linear regression. Even though the R^2-values were close to 1 a small bend at 400 °C was observed on the Arrhenius plot for arc 3 in 1000 ppm NO and 1000 ppm NO + 10% O_2, se Figure 26 for an example. Since this small bend was consistently observed for all 4 cells, it could reflect a change in the process around 400 °C.

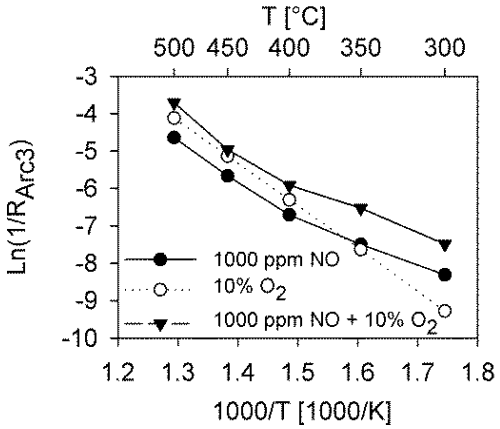

Figure 26. Arrhenius plot of the arc 3 resistance in 1000 ppm NO, 10% O2 and 1000 ppm NO + 10% O_2. Note the apparent change in slope in the atmospheres containing NO.

A comparison between the activation energies for arc 2 shows an activation energy of 0.78 eV in 1000 ppm NO, which is close to the activation energy observed in 1000 ppm NO + 10% O_2, but deviates from the 0.96 eV activation energy which is observed for process 2 in 10% O_2.

Finally, with respect to arc 4, no activation energy could be calculated in 1000 ppm NO, as no linear Arrhenius plot could be made from the fitting results. This was likely because this low frequency arc in 1000 ppm NO was distorted by a continued degradation. The activation energy for arc 4 was in 10% O_2 significantly higher when compared to 1000 ppm NO + 10% O_2, independent of whether the entire temperature range or only the higher part of the temperature range was considered.

5.4.6.2 KNO_3 impregnated cells

The impedance spectra recorded on the 3 symmetric LSM15-CGO10 cells impregnated with KNO_3 could all be fitted with between 2 and 4 RQ-subcircuits. Independent of the atmosphere, a small arc at very high frequencies was observed at 300 and 350 °C on all spectra. In 1000 ppm NO and in 10% O_2 two arcs/processes were consistently observed at all temperatures. These two arcs are named arc 3 and arc 4 in Table 9, but so far in the text it is not considered, whether these arcs represents the same processes or not in the different atmospheres. In addition to these two arcs in 1000 ppm NO, one additional smaller arc is observed at 350 °C (arc 2) and in the temperature range 400-500 °C a quite large arc (arc 5) appear at the lowest frequencies. Due to the limited temperature range at which arc 2 and arc 5 were observed it was not possible to calculate any activation energy for these two arcs.

Table 9. Characteristics of the arcs/RQ-subcircuits used during fitting of the impedance spectra recorded on symmetric LSM15-CGO10 cells impregnated with KNO_3. In the table n-value is the n-value of the CPE, Ea the activation energy and R^2 is the estimate of the linearity between the points used for the calculation of Ea.

					Results at 300-450 °C		
Atm.*	Arc	Freq. at 300 °C Hz	Freq. at 500 °C Hz	n-value	Ea eV	Stdev	R
NO	1	19878		0.82			
	2			0.83			
	3	0.5	599	0.59	1.16	0.12	0.977
	4	0.05	8	0.76	0.42	0.14	0.984
	5		0.10	0.88	?	?	?
O_2	1	21333		0.79			
	2			0.51			
	3	0.1	33	0.59	1.16	0.04	0.997
	4	0.002	1	0.85	1.40	0.18	0.983
O_2	1	17370		0.81			
	2	47	7670	0.60	1.05	0.07	0.988
	3	2	48	0.70	0.76	0.08	0.974
	4	0.3	3	0.90	0.52	0.04	0.980
	5		0.3	0.97	?	?	?

*The concentrations were 1000 ppm NO, 10% O_2 and 1000 ppm NO +10% O_2, in all cases with balance Ar.

In addition to the dominating arc 3 and 4 observed in 10% O_2, a smaller high frequency arc is observed at 500 °C, but also for this arc no activation energy can be calculated as the arc was only observed at one temperature.

In 1000 ppm NO + 10% O_2 3 arcs are consistently observed at all temperatures (arc 2, arc 3 and arc 4) and in addition to these arcs a small arc (arc 5) is observed in the temperature range 400-500 °C.

An overview of the arcs found in the different atmospheres, their characteristic frequencies, n-values and activation energies are found in Table 9. It should be noted only for arc 4 in 1000 ppm NO data recorded at 500 °C were used in the calculation of the activation energies, for all the other arcs the data at 500 °C was excluded from the calculation, as these data did not show linearity on the Arrhenius plot used for the calculation of the activation energy.

5.4.6.3 MnO_x-impregnated cells

Due to an insufficient number of datapoints and an apparent change in some of the processes at 400 °C, no activation energies could be calculated for the processes in 1000 ppm NO on the cells impregnated with MnO_x. In both 10% O_2 and 1000 ppm NO + 10% O_2 up to 4 arcs were identified in the impedance spectra, the characteristics of these arcs are stated in Table 10. In both atmospheres a small arc, denoted arc 1, was observed at the high frequencies at 300 and 350 °C. Two arcs, denoted arc 3 and arc 4 were consistently observed at all temperatures and in addition to this an extra arc denoted arc 2 was on some of the spectra observed in the frequency region between arc 1 and arc 3. In 10% O_2 arc 2 was consistently observed in the temperature range 300-400 °C, which made it possible to calculate the activation energy for this arc. In 10% O_2 the Arrhenius plot for arc 3 showed an abrupt change between 400 and 450 °C, for this reason the activation energy could only be calculated based on the resistances in the region 300-400 °C.

Table 10. Characteristics of the arcs/RQ-subcircuits used during fitting of the impedance spectra recorded on symmetric LSM15-CGO10 cells impregnated with MnO_x. In the table n-value is the n-value of the CPE, Ea the activation energy and R^2 is the estimate of the linearity between the points used for the calculation of Ea. Due to an insufficient number of datapoints and an apparent change in the process no activation energies could be calculated for the 1000 ppm NO atmosphere, for which reason no results from this atmosphere is included in the table.

Atm.*	Arc	Freq. 300 °C Hz	Freq. 500 °C Hz	n-value	Ea eV	Stdev	R	T. range [°C]
O_2	1	36919		0.90				
	2	64		0.65	0.87	0.05	1.000	300-400
	3	3.1	80	0.59	1.18	0.36	0.995	300-400
	4	0.137	3	0.73	0.64	0.01	0.977	300-500
NO + O_2	1	41585		0.87				
	2			0.50				
	3	42	129	0.61	0.78	0.02	1.000	300-500
	4	3.8	6	0.74	0.38	0.05	0.967	300-500

*The concentrations were 10% O_2 and 1000 ppm NO +10% O_2, in all cases with balance Ar.

5.4.7 Near-equivalent capacitance (C_ω)

From the fitting results the near-equivalent capacitances C_ω were calculated for the individual arcs. In Table 11 to Table 13 the results for the different atmospheres are stated. It is observed there is no significant difference between the C_ω of the blank and the impregnated samples.

Only for the blank cells a consistent trend was observed with respect to the temperature dependency of the C_ω in the three atmospheres. In 1000 ppm NO the C_ω for both arc 2, arc 3 and arc 4 increased with temperature. In 10% O_2 the C_ω of arc 2 and arc 3 remained constant with temperature, whereas for arc 4 a slight decrease in C_ω was observed. In 1000 ppm NO + 10% O_2 the C_ω of arc 2 stayed more or less constant, whereas for both arc 3 and arc 4 an increase in the C_ω was observed with temperature.

Table 11. C_ω in 1000 ppm NO in the temperature range 300 °C – 500 °C (for Arc 1 only for 300 °C). The values are stated in F/cm^2.

	Blank	KNO_3 imp.	MnO_x imp.
Arc 1	$2\cdot10^{-7}$-$3\cdot10^{-7}$	$6.0\cdot10^{-8}$-$6.5\cdot10^{-8}$	$3\cdot10^{-8}$-$5\cdot10^{-8}$
Arc 2	$5\cdot10^{-6}$-$1\cdot10^{-4}$		$4\cdot10^{-6}$-$4\cdot10^{-5}$
Arc 3	$5\cdot10^{-6}$-$5\cdot10^{-4}$	$1\cdot10^{-5}$-$2\cdot10^{-4}$	$3\cdot10^{-6}$-$3\cdot10^{-4}$
Arc 4	$5\cdot10^{-5}$-$2\cdot10^{-3}$	$2\cdot10^{-4}$-$2\cdot10^{-2}$	$2\cdot10^{-3}$-$4\cdot10^{-1}$
Arc 5		$2\cdot10^{-3}$-$5\cdot10^{-1}$	

Table 12. C_ω in 10% O_2 in the temperature range 300 °C – 500 °C (for Arc 1 only for 300 °C). The values are stated in F/cm^2.

	Blank	KNO_3 imp.	MnO_x imp.
Arc 1	$2\cdot10^{-7}$-$3\cdot10^{-7}$	$5.5\cdot10^{-8}$-$5.6\cdot10^{-8}$	$3\cdot10^{-8}$-$5\cdot10^{-8}$
Arc 2	$4\cdot10^{-6}$-$1\cdot10^{-5}$		$4\cdot10^{-6}$-$4\cdot10^{-5}$
Arc 3	$1\cdot10^{-4}$-$3\cdot10^{-4}$	$3\cdot10^{-5}$-$3\cdot10^{-4}$	$1\cdot10^{-5}$-$5\cdot10^{-4}$
Arc 4	$1\cdot10^{-3}$-$2\cdot10^{-3}$	$5\cdot10^{-4}$-$3\cdot10^{-3}$	$2\cdot10^{-4}$-$1\cdot10^{-2}$

Table 13. C_ω in 1000 ppm NO + 10% O_2 in the temperature range 300 °C – 500 °C (for Arc 1 only for 300 °C). The values are stated in F/cm^2.

	Blank	KNO_3 imp.	MnO_x imp.
Arc 1	$2\cdot10^{-7}$-$3\cdot10^{-7}$	$6.0\cdot10^{-8}$-$6.5\cdot10^{-8}$	$3\cdot10^{-8}$-$5\cdot10^{-8}$
Arc 2	$2\cdot10^{-6}$-$1\cdot10^{-5}$	$5\cdot10^{-7}$-$1\cdot10^{-4}$	$2\cdot10^{-6}$-$5\cdot10^{-5}$
Arc 3	$2\cdot10^{-5}$-$2\cdot10^{-4}$	$5\cdot10^{-6}$-$4\cdot10^{-4}$	$5\cdot10^{-6}$-$3\cdot10^{-4}$
Arc 4	$5\cdot10^{-5}$-$3\cdot10^{-3}$	$5\cdot10^{-4}$-$1\cdot10^{-3}$	$5\cdot10^{-5}$-$3\cdot10^{-4}$
Arc 5		$2\cdot10^{-3}$-$5\cdot10^{-1}$	

5.4.8 Flow variations

At 500 °C flow variations were made in the three different atmospheres: 1000 ppm NO, 10% O_2 and 1000 ppm NO + 10% O_2 in all three tests. The flow variation was made by first recording an impedance spectrum in 100 ml/min gasflow, and immediately thereafter record an impedance spectra in 50 ml/min gasflow. In Table 14 the percentage change in resistance between the different flow rates is stated for the different arcs. A negative value corresponds to a smaller resistance in 50 ml/min and a positive value corresponds to a larger resistance in 50 ml/min compared to in 100 ml/min. In the NO-containing atmospheres the largest change in arc resistance is found for the arc observed at the lowest frequencies, and consistently the arc resistance decreases with decreasing flow rate. For the MnO_x-impregnated sample no measurements were made in 10% O_2, for this reason those results are missing in the Table 14.

Table 14. The percentage difference in resistance between cells flushed in a 100 ml/min flow and 50 ml/min flow. A negative value states the resistance become lower in 50 ml/min flow compared to 100 ml/min flow.

	1000 ppm NO	10% O_2	1000 ppm NO + 10% O_2
Blank test			
Arc 2	3	0	-1
Arc 3	1	0	-2
Arc 4	-37	0	-8
KNO_3			
Arc 2		-5	0
Arc 3	-1	-2	0
Arc 4	-2	1	-5
Arc 5	-18		-7
MnO_x			
Arc 2	-9	-	
Arc 3	-15	-	2
Arc 4	-18	-	-5

5.4.9 Concentration change

During the test of the LSM15-CGO10 cells without impregnation, variations were made in the both the NO concentration and the O_2 concentration at 500 °C. At first the NO content was kept constant at 1000 ppm NO while the oxygen concentration was varied in the order 10, 5 and 15%

O_2. Secondly the oxygen concentration was kept constant at 10% and the NO content was varied in the order 1000, 500 and 1500 ppm NO. The resistances and C_ω corresponding to the concentration variations are stated in Table 15 for the variation in oxygen concentration and in Table 16 for the variation in NO concentration. With increasing oxygen content no influence is observed on the resistance of arc 2, a small decrease is observed in the resistance of arc 3, and a significant decrease in the resistance of arc 4 is observed. Only the C_ω of arc 4 appear to depend on the oxygen content, the C_ω of this arc appear to increase with increasing oxygen content. The resistances change with increasing NO concentration in a manner similar to when the oxygen content increases: the resistance of arc 2 remain unchanged, the resistance of arc 3 decreases slightly and the resistance of arc 4 decreases significantly. With respect to the C_ω and the influence of increasing NO concentration the C_ω of arc 2 remains constant but increases for arc 4, a behaviour similar to what was observed with increasing O_2 content. However for arc 3 the C_ω appears to decrease with increasing NO content, a behaviour which was not observed with an increase in the O_2 content.

Table 15. Resistance and C_ω during variations in the oxygen concentration. The data were recorded on one cell at 500 °C and the NO concentration was constant at 1000 ppm NO.

	Resistance [Ω cm^2]			C_ω [Ω/cm^2]		
	5% O_2	10% O_2	15% O_2	5% O_2	10% O_2	15% O_2
Arc2	35	34	34	$8.7\cdot10^{-6}$	$8.4\cdot10^{-6}$	$8.1\cdot10^{-6}$
Arc3	50	48	46	$1.4\cdot10^{-4}$	$1.4\cdot10^{-4}$	$1.4\cdot10^{-4}$
Arc4	65	48	40	$2.0\cdot10^{-3}$	$2.2\cdot10^{-3}$	$2.4\cdot10^{-3}$

Table 16. Resistance and C_ω during variations in the NO concentration. The data were recorded on one cell at 500 °C and the oxygen concentration was constant at 10% O_2.

	Resistance [Ω cm^2]			C_ω [Ω/cm^2]		
	500 ppm NO	1000 ppm NO	1500 ppm NO	500 ppm NO	1000 ppm NO	1500 ppm NO
Arc2	36	35	34	$4.0\cdot10^{-6}$	$8\cdot10^{-6}$	$7.6\cdot10^{-6}$
Arc3	47	46	44	$1.5\cdot10^{-4}$	$1.3\cdot10^{-4}$	$1.2\cdot10^{-4}$
Arc4	72	47	35	$1.7\cdot10^{-3}$	$2.3\cdot10^{-3}$	$2.9\cdot10^{-3}$

5.4.10 Degradation

Degradation during the entire cell test was estimated from impedance spectra recorded in the beginning and the end of the cell test. The spectra were recorded at 300 °C in 1000 ppm NO + 10% O_2. In Table 17 the average serial and polarisation resistances obtained from the spectra are stated. In the blank test a minor increase is observed in both the serial resistance and the polarisation resistance during the cell test. For the cells impregnated with KNO_3 a minor decrease is observed in the serial resistance, and 51% increase is observed in the polarisation resistance. The cells impregnated with MnO_x show a significant degradation in the serial resistance, and a huge degradation (>3000%) in the polarisation resistance.

Table 17. Serial resistance and polarisation resistance in 1000 ppm NO + 10% O_2 in the beginning and the end of the tests. The values stated are the average values of the 3 or 4 cells tested in each test, and the number in the parenthesis state the uncertainties.

	Rs			Rp		
	Begin [Ωcm^2]	End [Ωcm^2]	Diff. [%]	Begin [Ωcm^2]	End [Ωcm^2]	Diff. [%]
Blank	54(3)	57(3)	5	7635(911)	8460(689)	11
KNO_3 imp.	72(1)	64(3)	-11	4484(596)	6774(241)	51
MnO_x imp.	69(21)	212(101)	207	761(165)	11960(6193)	3650

Since an increase was observed in the polarisation resistance for all the three tests, it was of interest to estimate which of the arcs/processes mainly contributed to this degradation. For this reason the change in the resistance of each arc was calculated and divided by the total change in the polarisation resistance. The result from this calculation is shown in Figure 27, where positive values means the arc resistance increases and negative values the arc resistance decreases.

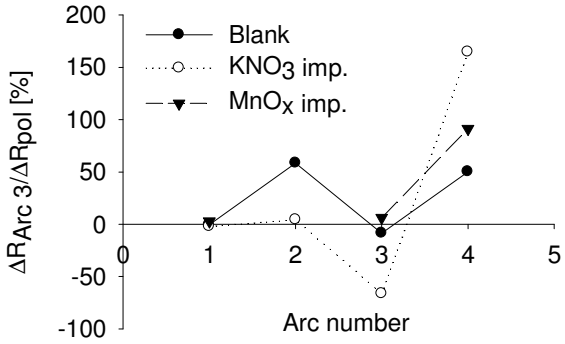

Figure 27. Change in arc resistance relative to the entire change in polarisation resistance when spectra recorded at 300 °C in 1000 ppm + 10% O_2 at beginning and the end of the cell test are compared. Positive values state the arc increases in resistance, negative values the arc decreases in resistance.

For the blank test the relatively small increase in polarisation resistance was equally caused by an increase in the resistance of arc 2 and 4. For the samples impregnated with KNO_3 the change in polarisation resistance was caused by an increase in the resistance of arc 4, and a decrease in the resistance of arc 3. In the test with MnO_x-impregnated samples only 3 arcs were observed at 300 °C, and the increase in polarisation resistance in this test was entirely caused by an increase in the resistance of the arc labelled 4. When comparing all three tests it is a consistent trend the increase in polarisation resistance either is solely or to a large extent explained by an increase in the resistance of arc 4.

5.4.11 Demounting

When the samples were demounted no visible change was seen before and after testing on the cells without impregnation and the cells impregnated with KNO_3. In contrast to this a very obvious change was observed between before and after cell testing on the cells impregnated with MnO_x. After the test these cells had become extremely brittle, and were all cracked into tiny pieces when they were demounted. It should be noted this only was seen for the three cells subjected to electrochemical cell testing, whereas the fourth cell, which only had experienced the temperature profile, at the demounting looked exactly as before testing.

5.4.12 SEM characterisation

SEM images were recorded on the cells before and after the electrochemical cell testing. In addition to this images were recorded on impregnated cells which had experienced the same temperature profile as the electrochemically tested cells, in order to investigate if changes observed in the microstructure mainly should be ascribed to electrochemical cell testing or to the temperature profile experienced by the cells during the testing. Representative SEM images of the samples are shown in Figure 28.

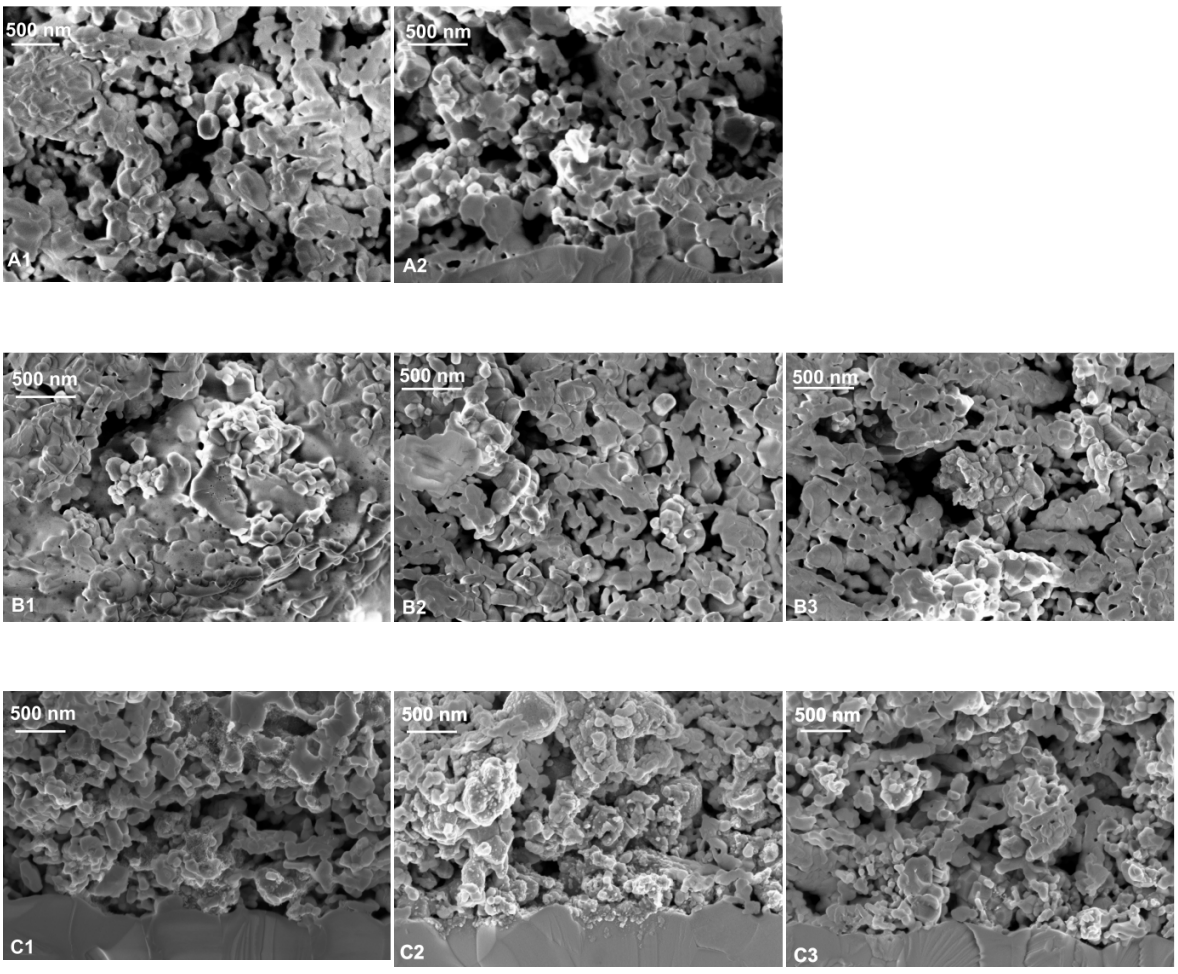

Figure 28. SEM images of blank and impregnated LSM15-CGO10 electrodes before testing, after testing and after heat-treatment as the tested cells. The images show A1: Blank electrode before testing, A2: Blank electrode after testing, B1: KNO_3 impregnated electrode before testing, B2: KNO_3 impregnated electrode after testing, B3: KNO_3 impregnated electrode after heat treatment, C1: MnO_x impregnated electrode before testing, C2: MnO_x impregnated electrode after testing, C3: MnO_x impregnated electrode after heat treatment.

The blank sample before cell testing shows a fairly smooth surface on the electrode grains and the porosity evenly distributed in the electrode (Image A1). In the electrode impregnated with KNO_3 the KNO_3 is present in the electrode in big lumps with a slightly porous surface (Image B1). In the areas where the KNO_3 lumps are present, they more or less seem to block the electrode porosity, but most of the electrode is left without any sign of the KNO_3. After the electrochemical testing and also when the cell only had experienced the temperature profile as the tested cells, the areas with KNO_3 filling the porosity had disappeared, and the electrodes looks like the un-impregnated electrodes (Image B2 and Image B3). In the electrode impregnated with MnO_x the MnO_x appear to be present as fine nanoparticles distributed through the entire electrode before testing (Image C1). After the electrochemical cell testing a significant change is observed in the electrode microstructure, where bigger, round nanoparticles with a diameter around 50 nm are observed on the grain surfaces, which at the same time appear to have a rougher surface (Image C2). Yet another microstructure is found on the sample which only was subjected to the heat treatment. On this sample the nanoparticles seem to have vanished and the electrode appear similar to a blank, non-impregnated electrode (Image C3).

5.5 Discussion

5.5.1 Cylic voltammetry

One of the reasons why the cyclic voltammetry was made, was in order to see if oxidation and/or reduction of the KNO_3/K_2O NO_x storage compound could be observed on the CVs, as this has previously been observed on a similar system[46]. In the cyclic voltammograms recorded in this work, a peak appeared only in NO containing atmosphere at 400 and 450 °C on the KNO_3-impregnated samples. It seems likely this peak may be ascribed to the NO_x-storage compound. The fact this peak is only observed in 1000 ppm NO and not in 1000 ppm NO + 10% O_2, could be explained by presence of O_2 making it more favourable to reduce O_2 compared to reduce KNO_3.

When the current densities for the three tests obtained during cyclic voltammetry are compared to the polarisation resistances, the highest current densities are observed for the impregnated tests with also had the lowest polarisation resistances determined from the EIS. This indicates the information gained from the EIS recorded at OCV may also to some extent be applicable to the situation when the cells are under current load.

5.5.2 EIS results - Identification of processes

5.5.2.1 Blank cells

On the LSM15-CGO10 cells without impregnation 4 processes were identified to contribute to the polarisation resistance at 300 °C, and 3 processes to contribute at higher temperatures. In order to identify these processes comparison will be made to literature, and the effect of varying the atmosphere and the flow rates will be taken into consideration.

Starting from the high frequency end of the impedance spectra, arc 1 with a summit frequency around 20000 Hz is observed in all atmospheres, but only at 300 °C. The n-value of the arc is 0.9, and the near-equivalent capacitance is in the range $3*10^{-7}$-$6*10^{-7}$ F/cm^2. As the summit frequency and the C_ω of this arc is independent on the atmosphere, the arc is likely ascribed to transport of oxygen intermediates/oxygen ions between the electrolyte and the LSM and through the electrolyte part of the composite electrode, as identified by Jørgensen et al.[54] for LSM/YSZ electrodes and later also found for LSM/CGO electrodes[36].

In all atmospheres and temperatures an arc labelled arc 2 is identified. The n-value of the arc is in all atmospheres 0.45, but the C_ω of the arc shows much dependency on whether oxygen is present in the atmosphere or not. While the C_ω in the oxygen containing atmospheres (10% O_2 and 1000 ppm NO + 10% O_2) remains more or less constant with increasing temperature, the C_ω in 1000 ppm NO continues to increase. The arc shows no dependency on the flowrate, or on variations in the pO_2 within the range 5-15% and variations in the NO concentration in the range 500-1500 ppm. In the temperature range 300-500 °C the calculated activation energy is close to 1 eV in 10% O_2, but only around 0.76 eV in the NO containing atmospheres. The difference in activation energy for arc 2 between the NO containing atmospheres and 10% O_2 could indicate the arc represents one process in NO containing atmospheres and another process in 10% O_2. In 10% O_2 the activation energy around 1 eV corresponds well with the activation observed by Jørgensen et al. for the transport/transfer of oxygen intermediates between the LSM and the electrolyte material and through the electrolyte material. As explained by Jørgensen et al.[54] these processes may give rise to two arcs in the impedance spectrum, named arc A and arc B, and could for this reason account for both arc 1 and arc 2 observed in 10% O_2 in this work. However, on the impregnated samples arc 2 decreases significantly or disappears entirely (described later in the

article), which would not be the case if arc 2 was related to oxygen ion transport in the CGO. For this reason arc 2 is so far ascribed to one of the processes dissociative adsorption, diffusion or charge transfer at the TPB.

Arc 3 was fitted with the n-values 0.68 (1000 ppm NO), 0.54 (10% O_2) and 0.69 (1000 ppm NO + 10% O_2). The C_ω in 1000 ppm NO for arc 3 behaved similar to for arc 2, with a continued increase with temperature. In 10% O_2 and 1000 ppm NO + 10% O_2 some divergence is found in the C_ω below 400 °C, with the lowest C_ω found in 1000 ppm NO + 10% O_2, but at 400 °C and above the C_ω in these two atmospheres become almost equal. If only the temperature range 400-500 °C is considered the activation energy of this arc is close to 1 eV in all 3 atmospheres, but if the lower temperatures are included in the calculation of the C_ω, the activation energies in the NO containing atmospheres decreases to 0.69. The decrease in the calculated activation energy is likely due a shift in the process around 400 °C, visible as a bend on the Arrhenius plot for the NO-containing atmospheres. Arc 3 shows no dependency on flow variations, but the resistance decreases slightly when the oxygen content is increased from 5-15% or the NO content is increased from 500 to 1500 ppm NO. The change between 5 to 15% oxygen does not affect the C_ω, whereas the increase in NO content from 500 to 1500 ppm decreases the C_ω of arc 3 slightly. Arc 3 appears to be dependent on the atmosphere and show no dependency on the flow rate. In the literature a process being dependent on the atmospheres is dissociative adsorption, transfer of species at the triple-phase- boundary (TPB) and surface diffusion[54]. The activation energy for this process in air was by Jørgensen et al. reported to be in the range 1.5-2 eV[54], which is above the reported activation energy of 1 eV in 10% O_2 reported in this work. But Werchmeister et al. reported the activation energy for the TPB process to be 0.64 eV in 1% NO[36], which shows the activation energy of this process is lower in NO compared to in air. As mentioned, a bend was observed on the Arrhenius curve in NO containing atmospheres around 400 °C. Combined with the attribution of arc 3 to TPB-related proceeses, a possible explanation of the bend could be a change in the adsorbed NO_x-species with increasing temperature. In-situ DRIFT measurements of NO adsorption on a model NO_x-storage catalyst and on La_2O_3 showed a change in the adsorbed NO_x-species during temperature increase from 300 °C to 500 °C[71, 143]. This makes it likely a similar change will be observed when NO_x is adsorbed on LSM15-CGO10 electrodes, and a change in the adsorbed NO_x species would likely affect processes related to the TPB process like surface

diffusion and dissociative adsorption, thereby causing the observed bend on the Arrhenius curved for arc 3.

The arc observed at the lowest frequencies, arc 4, behaves quite differently depending on the atmosphere, but is in all cases fitted with the n-value 0.89. In the NO containing atmospheres the arc resistance decreases with decreasing flowrate, most significantly when only 1000 ppm NO is present. No activation energy could be calculated for this arc in 1000 ppm NO, but the fact the arc decreases with decreasing flow rate makes it likely the arc is a NO_2 conversion arc as previously reported by Werchmeister et al.[36]. The NO_2 conversion arc was reported to have an activation energy of 0.34 eV in 1% NO in Ar[36]. This is below the activation energy 0.88 eV reported for arc 4 in 1000 ppm NO + 10% O_2 in this work.

5.5.2.2 KNO_3-impregnated cells

The impedance spectra recorded on the KNO_3-impregnated cell were fitted with between 2 and 4 RQ-subcircuits. Compared to the spectra recorded on the blank cells, the impedance spectra recorded on the KNO_3-impregnated cells have an additional smaller arc present in the low frequency region in 1000 ppm NO + 10% O_2.

In the following the processes will be described one by one, starting from high frequency and with the arcs numbered from 1 to 5 as in the results section.

Independent of the atmosphere, a high frequency arc is observed at 300 and 350 °C, with a summit frequency around 20000 Hz at 300 °C. The n-value of the arc is 0.8, the C_ω around 1.2×10^{-7} F/cm^2 at 300 °C, and since the summit frequency and C_ω does not depend on the atmosphere, the arc is likely ascribed to transport of oxygen intermediates/oxygen ions between the electrolyte and the LSM and through the electrolyte part of the composite electrode[54].

In 1000 ppm NO + 10% O_2 an arc labelled arc 2 is consistently observed at all temperatures. The arc is fitted with the n-value 0.6. The arc does not change when the flow is changed at 500 °C, and the activation energy of the process corresponding to the arc is close to 1 eV. This activation energy is lower than the activation energy for the TPB-process of 1.5-2 eV reported by Jørgensen et al.[54] for LSM/YSZ composite electrodes in air, and higher than the activation energy of 0.64 eV reported by Werchmeister et al.[36] for the TPB-process in 1% NO on LSM15/CGO10 composite

electrodes. It should be noted in the two other atmospheres, 1000 ppm NO and 10% O_2, an arc labelled arc 2 is also found in some of the impedance spectra, but since this arc is so rarely observed no activation energy could be calculated, and it will not be discussed further.

Arc 3 is consistently observed at all temperatures in all atmospheres. In 1000 ppm NO and 10% O_2 the arc is fitted with n-value 0.59, whereas in 1000 ppm NO + 10% O_2 the n-value 0.7 is used. The C_ω is in all atmospheres in the range $1x10^{-5}$-$8x10^{-4}$ F/cm^2. In 1000 ppm NO and 10% O_2 the activation energy of the arc is 1.16 eV, whereas in 1000 ppm NO + 10% O_2 the activation energy is only 0.76 eV. As described for arc 2, these activation energies lies between the activation energies reported for the TPB process by Jørgensen et al.[54] and Werchmeister et al.[36] .

In addition to arc 3 arc 4 is the only other arc consistently observed in all atmospheres at all temperatures. In the three different atmospheres the arc is fitted with the n-values 0.76 (1000 ppm NO), 0.85 (10% O_2) and 0.90 (1000 ppm NO + 10% O_2). The C_ω of the arc is in the range $4x10^{-4}$-$4x10^{-2}$ F/cm^2. The activation energies found for the arc were 0.42 eV (1000 ppm NO), 1.4 eV (10% O_2) and 0.52 eV (1000 ppm NO + 10% O_2). When the flow rate is decreased, the arc resistance decreases in the NO containing atmospheres, but stays more or less constant in 10% O_2. The significant difference in activation energy observed between the NO-containing atmospheres and in 10% O_2 combined with the different behaviour during the flow rate variations, indicates this arc represents a different process depending on whether NO is present is not. Exactly which process the arc represents is hard to decide, as the activation energies for the arc lies in between the activation energies determined by Werchmeister et al. for the arc related to the TPB-processes (0.64 eV) and the NO_2 conversion arc (0.34 eV) in 1% NO[36]. It can also be discussed whether the decrease in arc resistance with decreasing flowrate is big enough to be considered a true change, or may just be a false effect caused by a change in resistance of the low frequency arc 5 located next to arc 4.

Arc 5 appear in the low frequency region in the temperature range 400-500 °C in 1000 ppm NO and 1000 ppm NO + 10% O_2. Whereas arc 5 in 1000 ppm NO + 10% O_2 is a small arc adjacent to the much bigger arc 4, the result is quite different in 1000 ppm NO, where arc 5 is the major contributor to the cell resistance. The arc was fitted with the n-value 0.88 in 1000 ppm NO and 0.97 in 1000 ppm NO + 10% O_2. The C_ω of the arc decreased strongly with temperature in both

atmospheres, in 1000 ppm NO from around 1 to $4x10^{-3}$ F/cm^2, and in 1000 ppm NO + 10% O_2 from 1 to around $7x10^{-2}$ F/cm^2. Of all the arcs identified on the KNO_3 impregnated sample arc 5 shows the most significant dependency on flow rate, with a decrease in flow rate causing a decrease in arc resistance. The dependency on flow rate combined with a high n-value could indicate the arc is an NO_2 conversion arc as previously reported by Werchmeister et al.[36], on the other hand the arc could also be due to a process related only to the presence of impregnated KNO_3 and NO in the atmosphere, this will be discussed further in the section "Effect of impregnation – overall comparison of tests"

5.5.2.3 MnO_x-impregnated cells

The spectra recorded on the MnO_x-impregnated cells are all fitted with 2-4 RQ-subcircuits. As previously written, no activation energies could be calculated for the processes in 1000 ppm NO, for this reason only the results found in 10% O_2 and 1000 ppm NO + 10% O_2 will be discussed.

Consistent with the results from the blank and the KNO_3-impregnated cells, a high frequency arc, labelled arc 1, is observed at 300 °C and 350 °C on the MnO_x-impregnated cells. The summit frequency of this arc is in the range 30000-50000 Hz, which is higher than the summit frequency around 20000 Hz observed for this arc in the other tests. Again the arc will be ascribed to transport of oxygen intermediates/oxygen ions between the electrolyte and the LSM and through the electrolyte part of the composite electrode[54], as the presence only at lower temperatures and the distinct separation to the rest of the impedance spectra seems to be quite characteristic features of this arc.

On the impedance spectra recorded in 10% O_2 an arc labelled arc 2 is observed in the temperature range 300-400 °C. The arc is fitted with the n-value 0.65 and the activation energy is calculated to be 0.87 eV. In 1000 ppm NO + 10% O_2 an arc labelled arc 2 is only observed a few times, and the arc will for this reason not be discussed any further for this atmosphere.

The arc labelled arc 3 is consistently observed at all temperatures in both 10% O_2 and 1000 ppm NO + 10% O_2. In 10% O_2 the arc is fitted with n-value 0.59, and the activation energy is calculated to 1.18 eV, while in 1000 ppm NO + 10% O_2 the arc is fitted with n-value 0.61 and the activation energy is calculated to 0.78 eV. In both atmospheres the C_ω of the arc is found in the range $1x10^{-5}$-$1x10^{-3}$ F/cm^2. The difference in activation energy between arc 3 in the two atmospheres indicates

the arc represents two different processes, but when compared to Jørgensen et al.[54] and Werchmeister et al.[36] it seems likely the process in both atmospheres is related to dissociative adsorption, transfer of species at TPB and surface diffusion. The difference between the two atmospheres is then likely the species which participate in the reactions at the TPB, and it seems plausible NO_x-species participate in these reactions when NO is present in the atmospheres.

Finally arc 4 is observed at all temperatures in both atmospheres as well. In 10% O_2 the arc is characterised by n-value 0.73, activation energy 0.64 eV and C_ω in the range $8x10^{-5}$-$1x10^{-3}$ F/cm^2. In 1000 ppm NO + 10% O_2 the arc is characterized by n-value 0.74, activation energy 0.38 eV and C_ω in the range $1x10^{-5}$-$8x10^{-4}$ F/cm^2. During the flow variation the arc resistance decrease with decreasing flow rate in 1000 ppm NO +10% O_2, which together with the low activation energy is in agreement with characteristics Werchmeister et al. found for the NO_2 conversion arc[36]. Contrary to the observations made by Werchmeister al.[36], who as expected for a conversion arc observed an n-value close to 1, the NO_2-conversion arc observed on the MnO_x-impregnated samples is lower, around 0.74.

5.5.3 Effect of impregnation – overall comparison of tests

As stated in the beginning of the results section, impregnation with KNO_3 and MnO_x significantly decreased the polarisation resistance of LSM15/CGO10 electrodes in the temperature range 300-450 °C, both in 1000 ppm NO, in 10% O_2 and in 1000 ppm NO + 10% O_2. It would be of great interest to understand, which of the electrode processes are affected by the impregnation and especially how they are affected. For the NO-containing atmospheres it also of interest to see, if any NO-storage effect can be found for the KNO_3 and/or MnO_x-impregnation. For this reason the preceding description of fitting of impedance spectra was given, as these results may yield information on the effect of the impregnation on the electrode processes. In the following the impedance results from the three tests will be compared, and the effect of the impregnations on the individual processes will be discussed. An underlying assumption in the discussion is the majority of the processes identified in the three tests will be the same, as the impregnations are expected to affect the electrode processes but not totally alter all of them.

To summarize the results, all the impedance spectra were fitted with 2-4 RQ-subcircuits, independent of whether the samples were impregnated or not. Independent of the atmosphere, a

high frequency arc (Arc 1) was observed on all spectra at low temperatures, and ascribed to transport/transfer of oxygen intermediates/oxide ions between the LSM and CGO and through the CGO electrolyte. In both the NO containing atmospheres a NO_2 conversion arc (arc 4) was found in the low frequency end of the impedance spectra in all tests. In between the just-described high frequency arc and low frequency arc, two other arcs (arc 2 and arc 3) were present in 1000 ppm NO and in 1000 ppm NO + 10% O_2. Both arcs are ascribed to processes at or nearby the TPB (adsorption/diffusion/charge transfer). In addition to these arcs one more arc is observed in NO-containing atmospheres on the KNO_3 impregnated sample. As this arc is only observed on the KNO_3-impregnated sample, and only when NO is present in the atmosphere, it seems reasonable to ascribe the arc to a NO_x-storage process, or at least a process related to interaction between the NO and the impregnated KNO_3. It should be pointed out, the resistance of both arc 4 and arc 5 decreased with decreasing flow rate in NO containing atmospheres. For arc 4 this was explained in accordance with the results from Werchmeister et al who ascribed the arc to conversion of the intermediate NO_2 formed catalytically from the NO on the LSM[36]. For arc 5, which in this work is ascribed to a NO_x-storage process, a similar dependence on the flow rate, i.e. the concentration of NO_2, could be expected for the following reason: In conventional NSR-catalysis the reaction sequence is reported to consist first of catalytic conversion of NO to NO_2 on the platinum sites, and subsequent storage of the NO_2 on the NO_x-storage compound[19, 21]. On LSM-electrodes combined with a NO_x-storage compound a similar mechanism would be catalytic conversion of NO to NO_2 on LSM instead of platinum, and subsequent storage/adsorption of the NO_2 on the NO_x-storage compound. A decrease in flow rate would in this case decrease the resistance of the NO_x-storage process due to the higher concentration of NO_2, as observed in this work.

In the atmosphere with 10% O_2 two to three arcs are observed in addition to the high frequency arc. From the results obtained in this work it is not possible with certainty to assign these arcs to specific electrode processes, but they are so far ascribed to processes at or around the TPB. It should be noted in literature it is reported gas phase diffusion resistance may be significant below 10% O_2[155], i.e. at a pO_2 range close to the pO_2 during testing in this work. But as gas phase diffusion resistance is expected to be temperature independent[54], and all the processes identified in 10% O_2 show a strong temperature dependency, gas phase diffusion cannot explain any of the arcs observed in 10% O_2 in this work.

In order to evaluate if all the processes have been affected equally by the impregnation, it is useful to compare how the impregnation affects the resistance of the different arcs. In Figure 29 to Figure 31 the resistances found in 1000 ppm NO + 10% O_2 are shown for the three different tests, and it is observed how the impregnation causes a general decrease in resistance, with arc 4/the NO_2 conversion at 400 to 500 °C as the one exception.

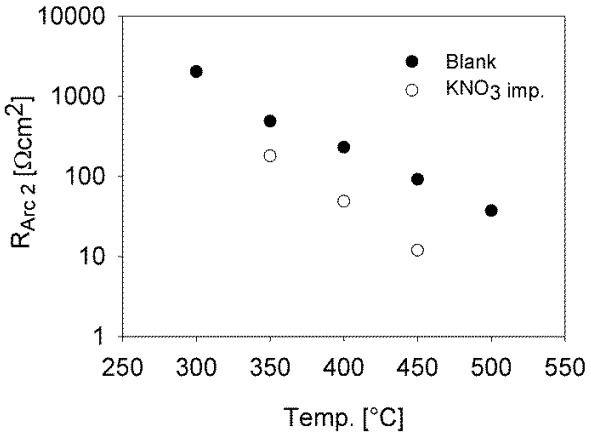

Figure 29. Resistance of arc 2 in 1000 ppm NO + 10% O_2.

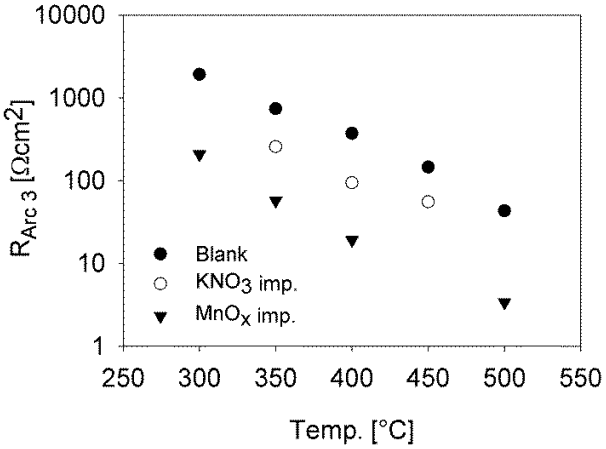

Figure 30. Resistance of arc 3 in 1000 ppm NO + 10% O_2.

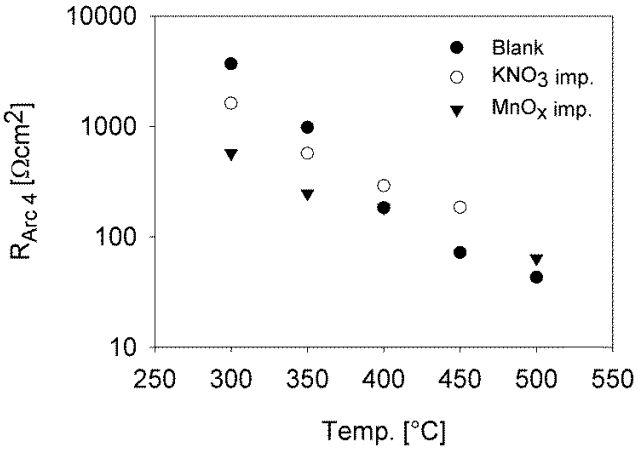

Figure 31. Resistance of arc 4 in 1000 ppm NO + 10% O_2.

5.5.4 Activation energies in 1000 ppm NO + 10% O_2

In addition to the change in resistances due to the impregnation the change in activation energies should also be considered. A change in the activation energy would usually be interpreted as a change in the reaction mechanism, which for instance could be due to a different reaction intermediates, other available reactions sites etc. However a change in activation energy could also be the result from a change in the microstructure during the test. If the microstructure is dominated by impregnated nano-particles at low temperatures, and the microstructure becomes coarser at high temperatures, an apparent change in activation energy will be observed for processes dependent on the electrode microstructure. This change will be due to the micro structural changes and the correlated change in resistances, and not due to a change in the actual reaction mechanism.

In 1000 ppm NO + 10% O_2 the activation energy of arc 2 has increased from 0.74 eV to 1.05 eV when the electrodes were impregnated with KNO_3. When the impregnation was made with MnO_x, no activation energy could be calculated for arc 2, as the arc was only found on very few EIS spectra. This could indicate the MnO_x-impregnation decreased the resistance of arc 2 so much; the arc no longer can be separated on the impedance plot and no activation energy could be calculated.

In the same atmosphere, none of the impregnations seemed to alter the activation energy of arc 3, as it only varies between 0.69 (blank), 0.76 (KNO_3 imp.) and 0.78 (MnO_x imp.) which will be considered within the uncertainty of the experiment and the fitting. Arc 3, which was ascribed to a TPB related process, has for this reason not changed reaction mechanism (E_a is constant) due to the impregnation, but the resistances of the arc has in general decreased, which would agree with the impregnations causing an increase in the triple-phase boundary length.

For arc 4/the NO_2 conversion arc no activation energy could be calculated for the KNO_3 impregnated sample, whereas for the MnO_x-impregnated sample the activation energy had decreased significantly, from 0.88 eV (blank sample) to 0.38 (MnO_x-impregnated sample). The decrease in activation energy for the MnO_x- impregnated sample could be explained by the MnO_x increasing the catalytic conversion of NO to NO_2 thereby increasing the NO_2 concentration in the electrode.

5.5.5 Activation energies in 10% O_2

Looking at the effect of the impregnation on the processes in 10% O_2 both impregnations seemed to decrease the activation energy of arc 3, whereas for arc 4 the KNO_3 impregnation left the activation energy unchanged while the MnO_x impregnation decreased the activation energy of the arc. So far both arc 3 and arc 4 are ascribed to processes related to the TPB. For the arc 3 process both impregnations seem to introduce or enhance a reaction path way with lower activation energy, whereas for arc 4 this only seem to be the case for the MnO_x impregnation.

Finally, with respect to the effect of impregnating with MnO_x and KNO_3, it was unexpected the impregnation with KNO_3 had such a significant impact on the resistances not only in the NO containing atmospheres, but also in 10% O_2. This was unexpected as KNO_3 was expected to interact with NO during the NO_x-storage, but not to have any effect on electrode reactions involving only oxygen species. Also the fact the MnO_x and KNO_3 impregnation was distributed so differently in the electrodes before testing made it quite surprising both impregnations in general decreased the resistances contributing to the polarisation resistances. This shows, a clear understanding of how impregnation in general and especially the KNO_3 impregnation affects the electrode processes is still missing. To clarify this more experiments are needed, as a first suggestion the impregnation of KNO_3 should be improved to get the KNO_3 more evenly distributed

in the electrode, and more impedance spectra should be recorded with variations in the NO and O_2 concentration to gain more insight into the processes occurring in the KNO_3 impregnated electrodes.

5.5.6 Degradation

As shown in the results section the degradation of the impregnated samples is in general larger compared to the blank samples. The majority of the degradation in the polarisation resistance was caused by an increase in the resistance of arc 4, which is ascribed to the NO_2 conversion process. This resistance increase could be explained in two different ways:

1. The LSM had lost ability to convert NO to NO_2 during degradation, thereby decreasing the NO_2 concentration.
2. The ability of the electrodes to convert NO_2 had decreased during testing.

Of course a combination of the two cases above could be a possibility as well.

For the KNO_3-impregnated sample a 51% increase in the polarisation resistance was observed. This increase was due to a combination of a resistance decrease for process 3 (related to TPB-processes) and a resistance increase for arc 4 (the NO_2 conversion arc). From the SEM images it is clear a significant redistribution of the impregnated KNO_3 has taken place, which may correlate with the decrease of the TPB resistance. The increase in the arc 4 resistance may be explained by point 1 or point 2 stated above.

The SEM images reveal a clear change in the microstructure, when the images recorded on the MnO_x-impregnated sample before and after testing are compared. The microstructural change, deterioration of the electrode grain surfaces and formation of round shaped particles, is obviously related to the polarisation of the electrode, as the same change in microstructure is not observed for cells which had only been heat treated as the tested samples. Lee et al. showed manganese ions in LSM lattice and interstitial sites were reduced to Mn^{2+} under cathodic polarisation, which led to the formation of oxygen ion vacancies on the LSM electrode surface[156]. This, combined with high surface mobility of Mn^{2+} ions, was by Jiang et al. used to explain the formation of sphere-like structures on LSM cathodes which had been polarised at 500 mA at 1000 °C in 3 hours[58]. A similar phenomenon could explain the changes in microstructure observed in this work: During the

polarisation, the manganese ions in the impregnated MnO_x may be reduced to Mn^{2+}. If a large excess of manganese ions are present at the LSM surface, and they all are reduce to Mn^{2+}, a large number of oxygen vacancies will be created in the LSM lattice. The diffusion of manganese ions and oxygen vacancies may lead to formation of sphere shaped particles and weakening of the bonding between the particles in the electrode similar to the observations made by Jiang et al.[58]. This could then explain both the change in microstructure observed on the SEM images and the reduced mechanical strength of the MnO_x-impregnated cell after the electrochemical characterisation. On the MnO_x-impregnated cells only subjected to the heat-treatment and not to the electrochemical testing, no trace of the impregnated MnO_x was observed in the electrode, which looked like the electrode of the un-impregnated cell. This may be due to incorporation of the impregnated MnO_x-into the LSM of the electrode during the heat treatment.

5.6 Conclusion

Both EIS and cyclic voltammograms show impregnation with KNO_3 introduce a NO_x-storage process in the electrode; this storage process apparently takes places after NO_2 has been formed catalytically on the electrode. Impregnation with MnO_x does not introduce a NO_x- storage process, but both the MnO_x- and the KNO_3-impregnation cause a significant decrease in the polarisation resistance of the electrodes in both 1000 ppm NO, 10% O_2 and 1000 ppm NO + 10% O_2. The decrease in polarisation resistance is caused both by a decrease in resistance of the processes related to the TPB, and a decrease in the resistance of the NO_2 conversion process in the NO containing atmospheres. It is remarkable a general decrease in these resistances is observed with both impregnations, even though the microstructure of the two impregnations appears fairly different. The impregnated samples degrade significantly more than the non-impregnated samples during testing. Based on SEM images and literature it is concluded the increased degradation follows from redistribution of the impregnated compound during testing, and with respect to the MnO_x-impregnated sample formation and diffusion of Mn^{2+} and oxygen vacancies may explain the severe degradation observed.

5.7 Acknowledgements

This work was supported by the Danish Strategic Research Council under contract no. 09-065186. Technicians at the Fuel Cell and Solid State Chemistry Division, Technical University of Denmark, are thanked for invaluable help and advice.

6 NO_x-conversion on Porous LSF15-CGO10 Cell Stacks with KNO_3 or K_2O Impregnation

This chapter is the manuscript "NO_x-conversion on Porous LSF15-CGO10 Cell Stacks with KNO_3 or K_2O impregnation" accepted for publication in Journal of Solid State Electrochemistry.

6.1 Abstract

In the present work it was investigated how addition of KNO_3 or K_2O affected the NO_x conversion on LSF15-CGO10 ($La_{0.85}Sr_{15}FeO_3$-$Ce_{0.9}Gd_{0.1}O_{1.95}$) composite electrodes during polarisation. The LSF15-CGO10 electrodes were part of a porous 11-layer cell stack with alternating layers of LSF15-CGO10 electrodes and CGO10 electrolyte. The KNO_3 was added to the electrodes by impregnation, and kept either as KNO_3 in the electrode or thermally decomposed into K_2O before testing. The cell stacks were tested in the temperature range 300-500 °C in 1000 ppm NO, 10% O_2 and 1000 ppm NO + 10% O_2. During testing the cells were characterized by electrochemical impedance spectroscopy (EIS) and the NO conversion was measured during polarization at -3 V for 2 h. The concentration of NO and NO_2 was monitored by a chemiluminiscence detector, while the concentration of O_2, N_2 and N_2O was detected on a mass spectrometer. A significant effect of impregnation with KNO_3 or K_2O on the NO_x conversion was observed. In 1000 ppm NO both impregnations caused an increased conversion of NO into N_2 in the temperature range 300-400 °C with a current efficiency up to 73%. In 1000 ppm NO + 10% O_2 no formation of N_2 was observed during polarisation, but the impregnations altered the conversion between NO and NO_2 on the electrodes. Both impregnations caused increased degradation of the cell stack, but the exact cause of the degradation has not been identified yet.

6.2 Introduction

NO_x is an air pollutant which has a number of negative effects on human health and the environment, as NO_x affects the respiratory system negatively, increase the formation of ozone at ground level, cause formation of acid rain, contribute to smog formation and also act as green house gas[11]. In gasoline vehicles NO_x can be removed sufficiently from the exhaust by the Three-Way-Catalyst (TWC), but this catalyst does not work for diesel vehicles due to a higher oxygen content in diesel engine exhaust[108]. For this reason other technologies are used for NO_x-removal

from diesel engine exhaust; the three most well-known technologies being selective catalytic reduction with urea (urea-SCR), selective catalytic reduction with hydrocarbons (HC-SCR) and the NO_x-storage and reduction (NSR) catalyst[108].

An alternative technology under development for NO_x-removal is electrochemical deNO_x[109-111], which compared to the three aforementioned technologies has the advantage no extra reducing agents needs to be supplied, as the NO is reduced by electrons during polarisation. Pancharatnam et al. discovered in 1975 NO can be reduced to N_2 during polarisation in absence of oxygen[22] and later it was discovered NO can also be reduced during polarisation in the presence of oxygen[24,26], which made electrochemical deNO_x of interest for cleaning of oxygen containing exhaust gasses.

Since then several studies have been carried out within electrochemical deNO_x[27, 29, 34, 39, 44, 141, 144], however the main challenges in the development of electrochemical deNO_x continues to be to achieve a sufficiently high activity and selectivity[111]. In this work it is attempted to improve the selectivity and activity of the LSF15-CGO10 composite electrodes for electrochemical deNO_x by adding a NO_x-storage compound, as known from NSR catalysis, to the electrodes.

The addition of the NO_x-storage compound to the electrodes is expected to improve the NO_x, conversion by concentrating the NO_x in the form of nitrates on the electrode surface. Promising results has so far been achieved with combining electrochemical deNO_x and a NO_x storage compound by Nagao et al.[141] and Hamamoto et al.[44] however in both cases the electrode contained platinum. Two important questions arises when adding a NO_x storage compound to the electrodes used in this work: 1) As no platinum is present in the electrodes, will the electrode material itself be able to oxidize NO to NO_2, as this step needs to precede the formation of nitrate on the storage compound? 2) How will the presence of a NO_x-storage compound alter the electrode processes?

With respect to question 1), Werchmeister et al. has shown electrochemical reduction of NO on LSM ($La_{1-x}Sr_xMnO_3$)-CGO, LSF-CGO and LSCF ($La_{1-x}Sr_xCo_{1-y}Fe_yO_{3-\delta}$)-CGO electrodes was preceded by catalytically formation of NO_2[38, 39]. For this reason formation of nitrates for NO_x-storage is likely possible, even when platinum is not present on the electrodes used for electrochemical deNO_x.

Question 2) is not easy to answer but a suggestion can be made for the overall electrode processes, which may be useful to keep in mind during the later interpretation of the results. On a cell without a NO_x-storage compound the expected electrode processes for electrochemical reduction of NO is:

Cathode: $NO + 2\ e^- \rightarrow 0.5\ N_2 + O^{2-}$ 6.1

Anode: $O^{2-} \rightarrow 0.5\ O_2 + 2\ e^-$ 6.2

Note the equations above state the overall processes and do not take into account any catalytic formation of NO_2. On the cathode a dominating, competing reaction to the reduction of NO is the reduction of O_2: $O_2 + 4\ e^- \rightarrow 2\ O^{2-}$.

When a NO_x-storage compound like K_2O/KNO_3 is added to the electrodes, one could imagine the electrode processes to become:

Cathode: $2\ KNO_3 + 10\ e^- \rightarrow K_2O + N_2 + 5\ O^{2-}$ 6.3

Anode: $4\ NO_2 + 2\ K_2O + 2\ O^{2-} \rightarrow 4\ KNO_3 + 4\ e^-$ 6.4

However, the formation of KNO_3 is not necessarily an electrochemical process as described in the anode equation above, but could just be a chemical reaction: $4\ NO_2 + 2\ K_2O + O_2 \rightarrow 4\ KNO_3$ as in conventional NSR catalysis, in that case O_2 could be supplied from oxidation of the O^{2-} at the anode or from the surrounding atmosphere. An improved performance for electrochemical deNO_x could eventually be gained by repeatedly changing the current direction through the cell, and thereby making the electrodes act alternately as cathodes and anodes, as shown by Hibino et al.[28] and Hamamoto et al.[44]. However, such experiments were not made in this work, since the available test set-up did not allow for precise measurements of the effect of alternating polarisation on the gas composition.

In this work three different LSF15-CGO10 cell stacks were tested with respect to conversion of NO_x in the temperature range 300-500 °C. The stacks were subjected to electrochemical impedance

spectroscopy and conversion/polarisation experiments while the gas composition was monitored by a mass spectrometer (MS) and a chemiluminiscense detector (CLD). The cell stacks differed from each other in the way they were impregnated: one stack had no impregnation, one stack was impregnated with KNO_3 and one stack was impregnated with K_2O. LSF was chosen as electrode material, since LSF as a mixed conductor[157,66] has been evaluated to be a promising material for intermediate temperate solid oxide electrodes[64] while CGO was chosen as an electrolyte, as CGO has superior oxygen ion-conductivity below 600 °C when compared to yttria stabilized zirconia[68]. KNO_3/K_2O was chosen for impregnation, as potassium is known to act both as a NO_x-storage compound[72] and also to improve simultaneous NO_x and soot removal[75, 76], the latter being of interest for future development of the electrochemical deNO_x technique. With respect to the development of the electrochemical deNO_x technique it must emphasized, the work presented in this paper is at the very early stage of the development process, and only deals with investigated materials ability to electrochemically convert NO_x in model atmospheres containing only NO_x, O_2 and Ar, even though real diesel exhaust also contain significant amounts of CO_2 and H_2O[7]. The presence of CO_2 and H_2O may influence the performance and degradation of the electrochemical deNO_x electrodes. In that context it is important formation of stable carbonate species does not appear to be a problem on potassium containing catalysts in the presence of NO_x[72, 158], while the influence of H_2O on the potassium impregnated LSF15-CGO10 electrodes is not clear and will have to be investigated in the future.

6.3 Experimental

6.3.1 Fabrication of porous cell stacks

The cell stacks tested in this work were ceramic, porous cell stacks consisting of 11 alternating layers of electrode and electrolyte. The porous stack design was chosen for this work, as the large contact area between gas and cell in this design makes it easy to measure the NO-conversion.

The electrode layers in the porous cell stacks were a LSF15-CGO10 composite with 65 wt% LSF15 and 35 wt% CGO10. The LSF had been synthesized in house by the glycine-nitrate combustion synthesis[150] from nitrate solutions supplied by Alfa Aesar. The LSF15 was synthesized with the exact composition $La_{0.84}Sr_{0.149}FeO_{3-\delta}$. The CGO10 was supplied by Rhodia. For the fabrication of the composite electrode the LSF15 and CGO10 were mixed with solvent, binder, dispersant and

poreformer (graphite), ball milled and subsequent tapecasted. For more detailed information on the tapecasting procedure see He et al.[159]. The porous CGO electrolyte was tapecasted like the electrode tape and afterwards the green electrode and electrolyte tapes were laminated together with 6 electrode layers alternating with 5 electrolyte layers. Round cell stacks with a diameter of 18 mm were stamped out of the green laminated tapes and thereafter sintered at 1250 °C. During the sintering the graphite poreformer was burned off leaving behind the pores in the stack. Before testing a porous Au current collector was applied to the cell stack by painting the outer electrodes with a gold paste containing 20 wt% carbon, and subsequent heat the cell stack to 800 °C to decompose the graphite. An image of the 11-layer cell stack with the porous current collector is shown in Figure 32.

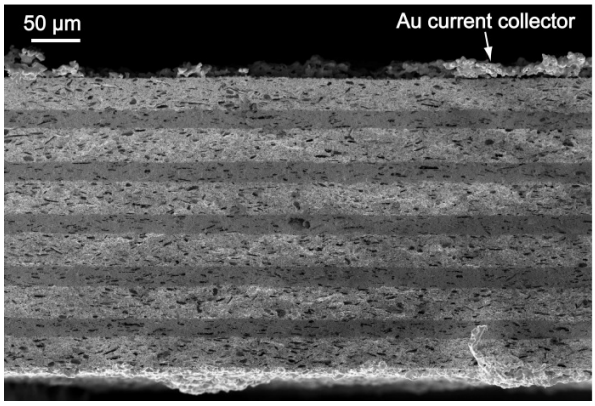

Figure 32. Cross-section of a non-impregnated LSF15-CGO10 cell stack. The six light grey layers are porous LSF15-CGO10 electrode layers, the 5 dark grey layers are porous CGO10 electrolyte layers and on each side of the cell stack the porous Au current collector is observed (only marked on the top side).

6.3.2 Impregnation

For impregnation of the cell stacks an aqueous solution of 3.1 M KNO_3 (Alfa Aesar) was prepared. The solution also contained 10 wt% P123 (BASF) with respect to the water. The impregnation was made by covering the cell stack with impregnation solution and then placing the cell stack in a vacuum chamber and evacuate to a pressure below 0.1 mbar for approximately 15 s. Excess impregnation solution was wiped of the surface of the cell stack, and thereafter the cells were

heated to 350 °C to decompose the P123. The cell impregnated with K_2O was prepared in exactly the same way, apart from the cell was heated to 700 °C to decompose the KNO_3 into K_2O.

6.3.3 Test set-up

For electrochemical cell testing the stack was mounted in between two alumina tubes, which contained channels for the gas flow and measurement probes for the electrochemical characterization. The cell and the alumina tubes were inclosed in a quartz tube and mounted vertically in a furnace. A sketch of the set-up is shown in Figure 33.

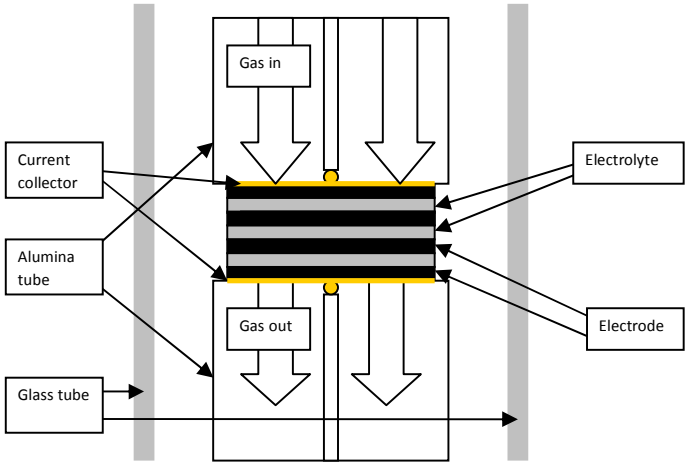

Figure 33. Sketch of set-up for testing of porous cell stacks (reprinted with permission from Werchmeister et al.[13].

6.3.4 Electrochemical characterization

A Gamry reference 600 potentiostat was used for the electrochemical characterization of the cell stack. Electrochemical impedance spectra were recorded in the frequency range 1 MHz to 0.001 Hz with 36 mV rms amplitude and 6 points pr. decade. For the conversion experiments the cell stack was first kept at Open Circuit Voltage (OCV) for 2 h, then polarized at -3 V for 2 h, and afterwards left at OCV for 2 h again. The electrochemical characterization was made first at 300 °C, and then repeated for each 50 °C until 500 °C was reached. After this the cell was cooled down to 300 °C, one EIS spectrum was recorded to evaluate the degradation during the cell test, and thereafter the test was finished.

6.3.5 Conversion measurements

The cell stack was supplied with NO, O_2 and Ar from Brooks mass flow controllers. The conversion measurements were made in 1000 ppm NO and 1000 ppm NO + 10% O_2 in both cases with balance Ar. These concentrations of NO and O_2 were chosen as they resemble the concentrations which may be found in the exhaust from a diesel car[7]. The NO and NO_2 content in the gas stream from the cell was monitored by a chemiluminiscense detector Model 42*i* High Level from Thermo Scientific; while the N_2, N_2O and O_2 concentration was monitored by a mass spectrometer from Pfeiffer Vacuum, type Omnistar GSD 301.

6.3.6 Scanning Electron Microscopy

The cell stacks were examined in a Zeiss Supra 35 scanning electron microscope equipped with a field emission gun. SEM images were recorded in two ways: In order to obtain high magnification images of the electrode microstructure images were recorded with the in-lens detector and 3 keV acceleration voltage on cells just broken and put directly into the microscope. To get more overall images of the cell stacks and the different layers in the stacks a part of each stack was mounted in epoxy, polished and carbon coated prior to the microscopy investigation.

6.4 Results and Discussion

6.4.1 Microstructure of electrodes before and after testing

Figure 34 shows the microstructure of the electrodes in the three different tested cell stacks. In the non-impregnated cell stack (Figure 34a) all the electrode grains appear to have a well-defined shape and very smooth surfaces. In the KNO_3 impregnated cell stack (Figure 34b) the infiltrated KNO_3 is present around in the electrode structure as lumps with a porous looking surface. The porous looking KNO_3-surface is likely due to interaction between the electron-beam and the KNO_3, as focusing the electron beam on the KNO_3 altered the look of the KNO_3 lumps. Figure 34b also shows even though the KNO_3 is present as big lumps in the electrode, there is still open porosity left for the gas to pass through. The electrode of the cell stack which had been impregnated with KNO_3 and subsequent heated to 700 °C to decompose the KNO_3 into K_2O is shown in Figure 34c. In the electrode KNO_3 lumps are observed together with other irregular shaped K_2O grains.

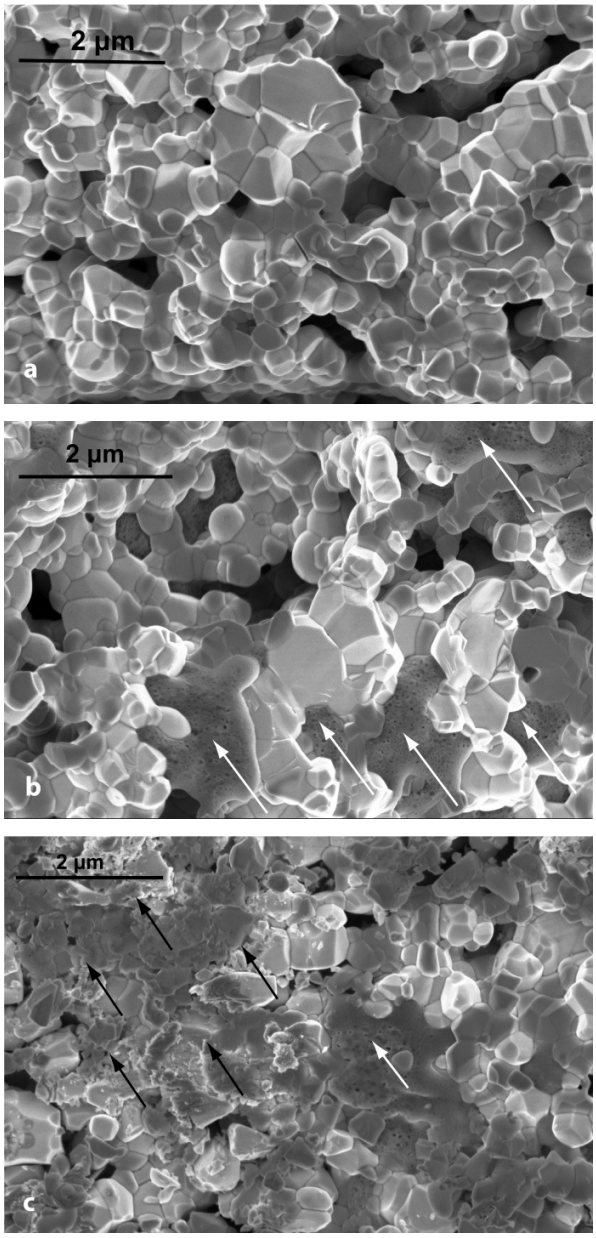

Figure 34. Microstructure of the electrode of a) a non-impregnated LSF15-CGO10 cell stack, b) cell stack impregnated with KNO_3 and c) cell stack impregnated with KNO_3 and subsequently heated to 700 °C to decompose the KNO_3 into K_2O. White arrows point at impregnated KNO_3 and black arrows on K_2O.

Samples from before and after electrochemical cell testing were mounted in epoxy and examined in the microscope to obtain information about changes in the electrode microstructure during testing. No change due to the testing was observed on the non-impregnated sample. However, both the KNO_3 impregnated sample and the K_2O impregnated sample showed a significant change in microstructure after the testing. The change in microstructure is best described as the grain size had been reduced and/or the attachments between the electrode grains decreased. The change in microstructure was most pronounced in the outer electrodes of the cell stack and is illustrated in Figure 35 for the KNO_3 impregnated sample.

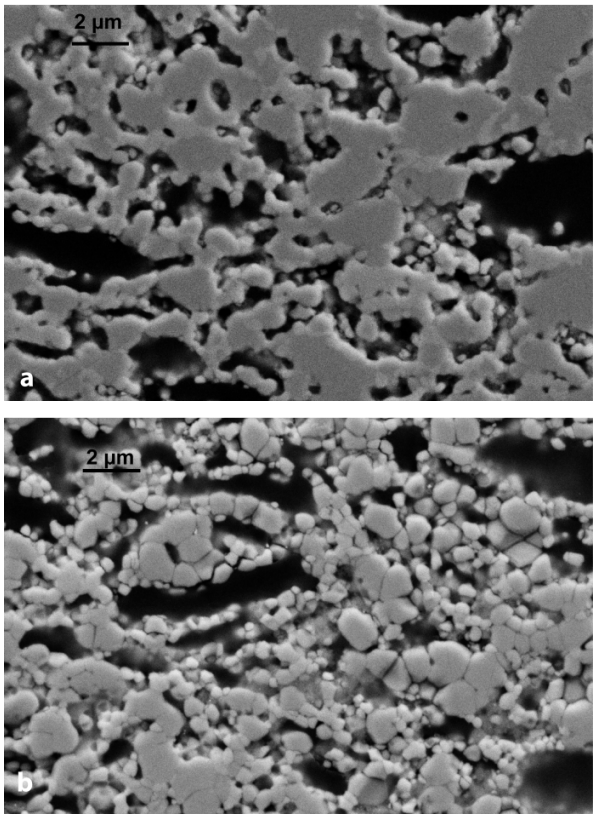

Figure 35. Outer electrode of KNO_3 impregnated cell stack a) before electrochemical cell testing and b) after electrochemical cell testing.

6.4.2 Conversion and Current efficiency

No purely catalytic effect of the KNO_3 or K_2O impregnation was detected, as no difference between the impregnated and non-impregnated cell stacks was observed in the outlet NO concentration, when the stacks before polarisation were flushed in either 1000 ppm NO or 1000 ppm NO + 10% O_2.

In 1000 ppm NO zero conversion of NO_x into N_2 during 3 V polarisation for 2 h was observed at 300 and 350 °C on the non-impregnated cell stack. However, from 400 °C to 500 °C the conversion into N_2 increased from 4% to 43%, see Table 18. On the impregnated cell stacks NO_x conversion in the range 2-17% was observed at 300-350 °C, which means higher NO_x conversion was observed at low temperatures on the impregnated cell stacks compared to the non-impregnated cell stack. In contradiction to this the NO_x conversion was lower on the impregnated cell stacks compared to the non-impregnated sample at higher temperatures. A significant decrease in NO_x conversion on the KNO_3 impregnated sample was observed from 350 °C to 400 °C.

Table 18. NO_x conversion [%] for a non-impregnated cell stack, a KNO_3 impregnated cell stack and a K_2O impregnated cell stack.[a]

Temperature [°C]	Non-impregnated	KNO_3 imp.	K_2O imp.
300	0	2	3
350	0	17	15
400	4	-1*	13
450	15	3	
500	43		15

[a] The cell stack was supplied with 1000 ppm NO and polarised at -3V for 2h. The stated values are the percentage of NO_x converted into N_2.

*-1% conversion of NO_x into N_2 corresponds in principle to conversion of N_2 into NO_x. But since this -1% corresponds to only 4 ppm N_2, it is considered to be within the general uncertainty of the experiment.

The current efficiency during the 2 h polarisation was calculated according to Eq. 6.5:

$$\text{Current efficiency} = \frac{I_{N_2}}{I_{\text{applied}}} \cdot 100\% \qquad 6.5$$

- where I_{N2} is the current corresponding to the reduction of NO into the N_2, which was detected by the MS, and I_{applied} is the current applied on the cell during the polarisation. In Table 19 the current efficiencies in the different tests are stated for the atmosphere with 1000 ppm NO in Ar. It is observed impregnation with KNO_3 and K_2O increases the current efficiencies in the temperature range 300-400 °C. Improved current efficiency at 500 °C is also observed for the K_2O impregnated sample. The current not used for reduction of NO is used for the competing reduction of O_2. The O_2 likely had been adsorbed on the cell stack during treatment in 10% O_2 in between the polarisation experiments or originate from a small leak in the system, as 70-100 ppm $O_{2,leak}$ was measured by the MS while the sample was supplied with 1000 ppm NO in Ar.

Table 19. Current efficiency [%] for a non-impregnated cell stack, a KNO_3 impregnated cell stack and a K_2O impregnated cell stack.*

Temperature [°C]	Non-impregnated	KNO_3 imp.	K_2O imp.
300	0	8	38
350	0	59	73
400	5	-8	37
450	10	4	
500	11		15

* The current efficiency is calculated according to Eq.(5). The cell stack was supplied with 1000 ppm NO in Ar and polarised at -3V for 2 h.

In addition to conversion into N_2 oxidation of NO into NO_2 takes place during polarisation of the cell stacks in 1000 ppm NO. In Figure 36 it is illustrated how the conversion into NO_2 is highest at 300-400 °C for the impregnated cell stacks, whereas for the non-impregnated cell stack conversion into NO_2 is only observed in the temperature range 400-500 °C. With respect to the non-impregnated cell stack a decrease in $O_{2,leak}$ was observed during polarisation/formation of NO_2. The oxygen balance over the blank cell stack at all temperatures showed a deviation below 15 ppm O_2,

when comparing the concentrations of NO, NO_2 and $O_{2,leak}$ before and during polarisation. For the impregnated cell stacks the oxygen balance showed in general an excess O_2 concentration during polarisation (up to 100 ppm), indicating previously adsorbed O_2 was released from the cell stack during polarisation.

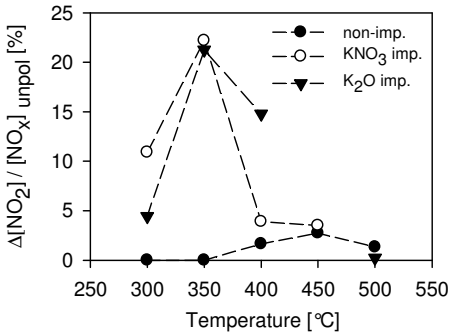

Figure 36. Conversion of NO into NO_2 relative to the NO_x concentration before polarisation in 1000 ppm NO. The cell stacks were polarized at 3 V for 2 h and the stacks were supplied with 1000 ppm NO in Ar. The dashed lines are for visual guidance only**.**

When oxygen was present in the atmosphere, conversion of NO_x into N_2 was not observed for any of the samples. It should be noted even though the gas composition when oxygen was present in this article is stated as 1000 ppm NO + 10% O_2 the actual concentration of NO was in the range 700-900 ppm due to the equilibrium 2 NO + O_2 ⇆ 2 NO_2.

Instead of reduction of NO_x into N_2 an increased conversion between NO and NO_2 was observed on the samples during polarisation in oxygen containing atmospheres. A significant difference between the cell stack without impregnation and the impregnated stacks was observed: without impregnation NO was formed during polarisation due to conversion of NO_2, whereas for the samples impregnated with KNO_3 or K_2O NO_2 was formed during polarisation due to conversion of NO. This is clear when Figure 37 and Figure 38 are compared, where Figure 37 shows the change in NO concentration during polarisation and Figure 38 shows the change in NO_2 during polarisation, in both cases relative to the NO concentration before the samples were polarized. The current through the cell stacks was in the range 1-20 mA during the polarisation at -3V for both the non-impregnated and the impregnated cell stacks.

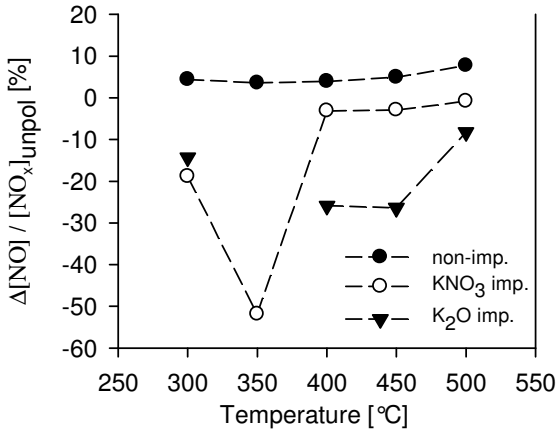

Figure 37. Relative conversion of NO during 2 h polarisation at 3 V on non-impregnated and impregnated LSF cell stacks. Positive values correspond to formation of NO and negative values to removal of NO. The dashed lines are for visual guidance only**.**

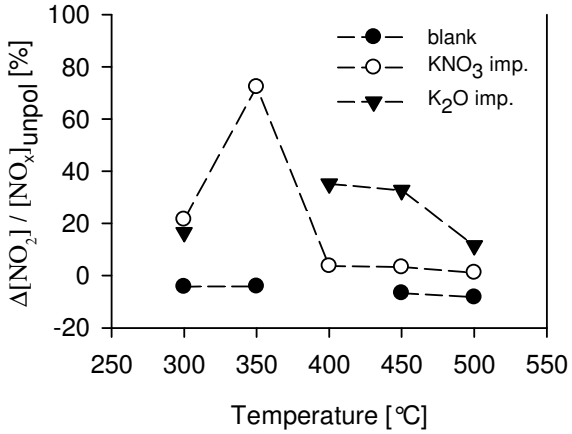

Figure 38. Relative conversion of NO_2 during 2 h polarisation at 3 V on non-impregnated and impregnated LSF cell stacks. Positive values correspond to formation of NO_2 and negative values to removal of NO_2. The dashed lines are for visual guidance only**.**

The increased NO conversion due to the presence of potassium observed in this work is in agreement with results reported by Hamamoto et al.[44]. Hamamoto et al. [44] observed increased NO conversion and a decrease in the onset temperature when a potassium-containing adsorbent layer was added to a NiO-YSZ (nickel oxide-yttria stabilized zirconium oxide) or NiO-CGO based cell for electrochemical deNO_x. Hamamoto et al. ascribed the increased performance to potassium's ability to adsorb NO and also saw NO decomposition when oxygen was present, which was not observed in this work. The difference could be due to the LSF15-CGO10 electrode used in this work has a larger affinity for O_2 reduction than the NiO-YSZ and NiO-CGO cell used by Hamamoto et al. Another explanation of the increased performance after addition of KNO_3 and K_2O may be the K act as promoter, a phenomenon well-known from heterogeneous catalysis[74]. However based on the results in this work it is not possible to distinguish whether the KNO_3 and K_2O mainly improves the performance by increasing the adsorption or by acting as promoters.

With respect to the results obtained in 1000 ppm NO + 10% O_2, it should be noted since the current densities are similar for both the non-impregnated cell stacks and the impregnated cell stacks, but the conversion from NO to NO_2 is higher for the impregnated stacks, the effect of the K-species is not to generally increase the performance of the cell stacks, i.e. to increase both the O_2 and the NO conversion, but specifically to increase the NO conversion.

A clear observation in this work was increased NO_2 concentrations during polarisation at the temperature range where the largest NO conversion was observed, i.e. in the high temperature range for the non-impregnated samples and in the low temperature range for the impregnated samples. For the non-impregnated electrodes this likely show just as reduction of NO into N_2 on the cathodes increases with temperature, so does the oxidation of NO into NO_2 on the anodes of the cell stack. One may speculate if the effect of the KNO_3 and K_2O on the impregnated electrodes only is to act as an NO_x adsorbent, or if KNO_3 and K_2O may also facilitate the catalytic formation of NO_2, thereby increasing the total NO_x removal by increasing the concentration of the intermediate NO_2. This is of interest since NO_2 has been identified as an important intermediate for electrochemical reduction of NO_x by Werchmeister et al.[36, 38]. However, according to literature K-compounds are very poor in catalyzing the oxidation of NO to NO_2[160]. The most likely explanation of the increased NO_2 level in the low temperature range for the impregnated samples is due to

release of NO_2 during the reduction of the KNO_3-storage compound, as NO_x release is also observed for conventional NSR catalysts during the reduction cycle[161].

The results from the conversion measurements show at 350 °C a marked jump in the activity and the current efficiency for the impregnated cells stacks. 350 °C is above the melting point of KNO_3 (m.p. 334 °C[97]) and the better performance at 350 °C may for this reason be due to the presence of molten KNO_3, which may increase the performance by being more mobile compared to solid KNO_3. The performance decrease from 350 °C to higher temperatures may be due to the degradation phenomena which also caused the degradation of the electrode microstructure as observed on the SEM images.

6.4.3 Effect of impregnation on serial and polarisation resistance

The impedance spectra of the non-impregnated cell stack were fitted with the equivalent circuit $R_s(R_1Q_1)(R_2Q_2)(R_3Q_3)$, where R is a resistance and Q a constant phase element. For the impregnated cell stacks the same equivalent circuit was used, apart from for some spectra a fourth (RQ) element had to be included in order to obtain a satisfactory fit. Representative examples of impedance spectra and their deconvolution are shown in Figure 39 to Figure 41 for the three different samples.

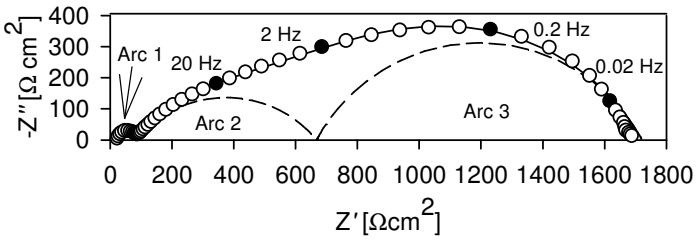

Figure 39. Impedance spectrum recorded in 1000 ppm NO + 10% O_2 at 400 °C on non-impregnated cell stack. The solid line represents the deconvolution of the entire spectrum and the dashed lines the deconvolution of the individual processes. For solid points the frequency of the data point is stated.

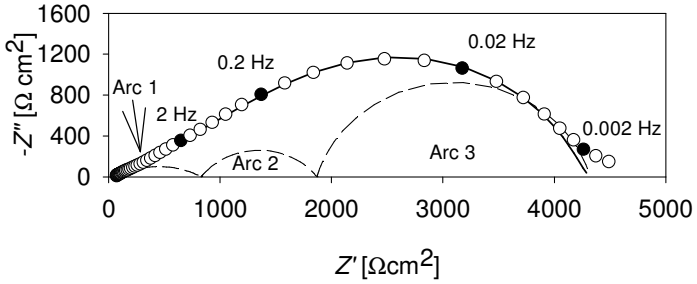

Figure 40. Impedance spectrum recorded in 1000 ppm NO + 10% O_2 at 400 °C on KNO_3 impregnated cell stack. The solid line represents the deconvolution of the entire spectrum and the dashed lines the deconvolution of the individual processes. For solid points the frequency of the data point is stated.

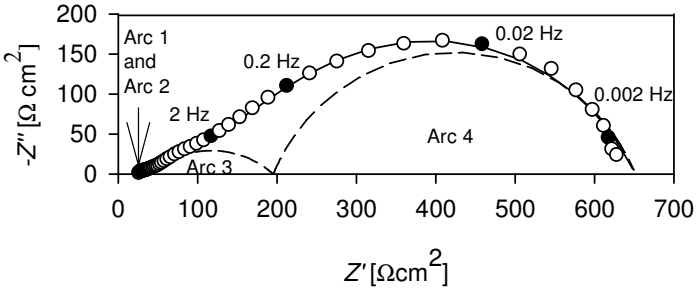

Figure 41. Impedance spectrum recorded in 1000 ppm NO + 10% O_2 at 400 °C on K_2O impregnated cell stack. The solid line represents the deconvolution of the entire spectrum and the dashed lines the deconvolution of the individual processes. For solid points the frequency of the data point is stated.

The serial resistance (R_s) and polarisation resistance (R_p) obtained from the fitting are stated in Table 20. In general the serial resistances of the impregnated stacks are lower than for the non-impregnated stacks at low temperatures, but higher than for the non-impregnated stacks at higher temperatures.

Table 20 Serial resistance (R_s) and polarisation resistance (R_p) for three LSF15-CGO10 porous cell stacks without impregnation ("non-impregnated"), with KNO_3 impregnation and with K_2O impregnation.*

	R_s [Ωcm^2]			R_p [Ωcm^2]		
Temp. [°C]	Non-imp.	KNO_3 imp.	K_2O imp.	Non-imp.	KNO_3 imp.	K_2O imp.
300	140	110	100	5700		
350	47	110	31	3200		1700
400	19	64	20	1700	4300	630
450	11	110	16	920	780	190
500	8	40	15	420	210	250
300(post)'	140	810	1000	9700	24000	23000

* The cell stacks were supplied with 1000 ppm NO + 10% O_2 while the EIS spectra were recorded.

' 300(post) refers to the impedance spectra recorded at the end of the experiment, i.e. after temperature variations and polarisation experiments had been performed.

A possible explanation of the lower serial resistance for the impregnated cell stacks at low temperatures could be improved sintering of the stack due to the presence of potassium[162, 163], or establishment of an easier current pathway through some part of the cell stack. The latter point follows from the conductivities of CGO being ≈0.001 S/cm at 350 °C[68] while the conductivity of the molten KNO_3 at 350 °C is 0.699 S/cm[164], which means at 350 °C the reduced serial resistance observed for the KNO_3 impregnated sample may be explained by the current passing through the KNO_3 instead of the CGO electrolyte. Unfortunately it has despite of extensive search not been possible to find information on the conductivity of K_2O and solid KNO_3 at 300 °C, for this reason it cannot be estimated here, if an alternative current path is a realistic explanation of the reduced serial resistance observed on the impregnated cell stacks at 300 °C. It is also noticed, while the serial resistance of the non-impregnated cell stacks is almost unchanged from the beginning to the end of the cell test, the serial resistance of the impregnated samples increases by a factor 8-10.

With respect to the polarisation resistance missing values in Table 20 for the impregnated samples are due to poor quality of the impedance spectra recorded at low temperatures. With one exception the polarisation resistance during the cell test is always lower on the impregnated cell

stacks compared to the non-impregnated cell stack. The polarisation resistance of the K_2O impregnated sample is between 40 and 80% smaller than the polarisation resistance of the non-impregnated cell, even though from 450 °C to 500 °C the polarisation resistance of the K_2O impregnated sample starts to increase. With respect to the polarisation resistance at 300 °C after the test, the resistance of both the impregnated cell stacks is more than twice the polarisation resistance of the non-impregnated cell stack.

The impedance results are consistent with the results from the conversion measurements and the SEM images, as they show the impregnations increases the electrochemical performance of the cell stacks, but also causes severe degradation. The degradation causes the pronounced increased in R_s and R_p from the beginning to the end of the test, and is related to the breakdown of the electrode microstructure observed on the SEM images. Due to the degradation problems it was not possible to identify the processes contributing to the polarisation resistance of the impregnated cell stacks. However for the non-impregnated cell stack some of the processes could be identified, as described in the following.

6.4.4 Electrochemical processes in the non-impregnated cell stack

As previously mentioned, the impedance spectra recorded in 1000 ppm NO+ 10% O_2 could be fitted with the equivalent circuit $R_s(R_1Q_1)(R_2Q_2)(R_3Q_3)$. The process located at the highest frequency and fitted by the subcircuit (R_1Q_1) had the activation energy 1 eV and a near-equivalent capacitance of 2×10^{-8} F/cm^2, the near-equivalent capacitance remains constant with temperature. This process was recognized in spectra recorded in all the tree different atmospheres: 1000 ppm NO + 10% O_2, 1000 ppm NO and in 10% O_2. The independency on the atmosphere combined with the size of the activation energy identifies the arc as belonging to intrinsic processes in the cell stack, like oxygen ion transport in the electrolyte and across the electrolyte electrode interface[54].

The process located in the middle frequency region in 1000 ppm NO + 10% O_2 has the activation energy 0.57 eV. The near-equivalent capacitance associated with the process increases with temperature, from 1.7×10^{-5} F/cm^2 at 300 °C to 5.2×10^{-5} F/cm^2 at 500 °C. In 10% O_2 the characteristics of the middle frequency arc were similar, but not totally identical to in 1000 ppm NO +10% O_2. In 10% O_2 the arc had the activation energy 0.67 eV and the capacitance increased with temperature, but a little less steeply compared to in 1000 ppm NO + 10% O_2. The fact that the

middle frequency arc depends on the atmosphere indicates the arc may be related to processes like adsorption, diffusion and charge transfer at or near the triple-phase boundary (TPB)[54]. This also correlates well with the temperature dependency observed for the capacitance, as increasing temperature will increase the TPB zone and thereby increase the associated capacitance. It should be noted the activation energy in 1000 ppm NO + 10% O_2 is in good agreement with the activation energies reported by Werchmeister et al. for the TPB process in 1% NO on LSF/CGO electrodes[38]. In contradiction to this the activation energy 0.67 eV found in 10% O_2 is considerably below the activation energy observed by Werchemister et al. in air, where the activation energies was in the range 1.2-1.5 eV[38].

The process located at the lowest frequency has the activation energy 0.52 eV in 1000 ppm NO + 10% O_2, and 0.20 eV in 10% O_2. The large discrepancy between the two activation energies indicate this arc represent two different processes depending on whether NO is present in the atmosphere or not. The lack of temperature dependency for the process in 10% O_2 combined with the appearance at the lowest frequencies in the spectrum indicates this process could be related to gas phase diffusion[54]. The low frequency process when NO is present is likely not a gas phase diffusion process due to the relatively high activation energy observed. In the work by Werchmeister et al.[38] the arc observed at the lowest frequencies in NO containing atmospheres was ascribed to conversion of intermediately formed NO_2. However, for this NO_2 conversion arc a low activation energy in the range 0.2-0.3 eV was reported, which makes it unlikely the arc observed in this work is an NO_2 conversion arc. The best explanation of the low frequency arc is so far it is related to one of the processes dissociative adsorption, surface diffusion and charge transfer at or near the TPB. One or more of these processes were also expected to account for the middle frequency process observed in this work. It is interesting to note the activation energies 0.57 eV and 0.52 eV found in this work for the middle and low frequency process respectively, are in good agreement with the activation energies observed by Werchmeister et al. for the TPB related processes on LSF and LSCF electrodes.

6.5 Conclusion

In the present work the effect of KNO_3 and K_2O impregnation on the NO_x-conversion on LSF15-CGO10 electrodes was investigated. In an atmosphere only containing 1000 ppm NO in Ar impregnation with KNO_3 and K_2O increased the conversion of NO significantly in the temperature range 300-350 °C. Increased NO_2 concentration was observed in the temperature range where the cell stacks were most active, i.e. for the impregnated cell stacks the highest NO_2 concentrations were observed in the low temperature range, and for the non-impregnated cell stack the highest NO_2 concentrations were observed in the high temperature range.

When oxygen was present in the atmosphere together with the NO neither the non-impregnated nor the impregnated cell stacks were able to convert NO_x into N_2. However a marked difference was observed between the non-impregnated and the impregnated cell stacks in 1000 ppm NO + 10% O_2: Whereas the non-impregnated cell stack converted NO into NO_2 under polarisation the impregnated cell stacks converted NO_2 into NO under polarisation.

The impregnation with KNO_3 and K_2O overall decreased the polarisation resistance of the cell stacks, but also introduced severe degradation problems into the stack, as breakdown of the electrode microstructure was observed. Due to the degradation it was not possible to identify the processes contributing to the polarisation resistance of the impregnated stacks. However for the non-impregnated stack oxygen-ion transport and TPB related processes were found to dominate the polarisation resistance in 1000 ppm NO + 10% O_2.

Further experiments are needed to clarify, how KNO_3 and K_2O impregnation affects the NO_x conversion under polarisation, among this the role of NO_2 in the reaction mechanism. Also the exact cause of the increased degradation observed on impregnated samples is currently not well-understood.

6.6 Acknowledgements

This work was supported by the Danish Strategic Research Council under contract no. 09-065183. Colleagues at the Fuel Cell and Solid State Chemistry Division, Technical University of Denmark, are thanked for help and fruitful discussions.

7 NO_x-conversion on LSF15-CGO10 cell stacks with BaO impregnation

This chapter deals as the previous chapter with results obtained during measurements on porous LSF15-CGO10 cell stacks. Whereas the previous chapter dealt with the effect of K_2O-impregnation on the NO_x conversion, the present chapter deals with the effect of BaO impregnation on the NO_x-conversion. Results from tests on two BaO-impregnated stacks (B1 and B2) are reported. For comparison results from a non-impregnated stack (N1) are also reported. The results for the non-impregnated cell stack were also described in the previous chapter, but are in this chapter repeated to clarify the effect of the BaO-impregnation.

7.1 Experimental

7.1.1 Cell stack fabrication and impregnation

As the cell stacks described in this chapter essentially are the same as the cell stacks described in the previous chapter the reader is referred to chapter 6 for information on the fabrication of the stacks. For impregnation of the porous cell stacks with BaO a 0.3 M aqueous $Ba(NO_3)_2$ (Merck) solution with 10 wt% P123 (BASF) was prepared. The cell stacks were covered with the $Ba(NO_3)_2$ solution and put under vacuum for ≈10 s, whereafter excess impregnation solution was wiped of the surface. The impregnated cell stacks were then heated to 700 °C for 1 h to decompose the $Ba(NO_3)_2$ into BaO, and the final BaO load on the tested cell stacks was 1.7±0.1 wt%.

7.1.2 Electrochemical testing and conversion measurements

The electrochemical testing and conversions measurements performed on the BaO impregnated LSF15-CGO10 cell stacks were essentially the same as the measurements performed on the K_2O impregnated cell stacks described in the previous chapter. In short, conversion measurements were made with 3V polarisation in the temperature range 300-500 °C in 1000 ppm NO and 1000 ppm NO + 10% O_2. The conversion measurements were supplemented by an extensive impedance analysis with variation in gas compositions and flow rates to allow for identification of the processes contributing to the polarisation resistance of the BaO impregnated stacks. For a detailed description of how the electrochemical testing and conversion measurements were performed the reader is referred to chapter 6.

7.1.3 SEM

Before and after testing the cell stacks were examined in a Zeiss Supra 35 scanning electron microscope. In order to obtain high magnification images of the electrode microstructure images were recorded with the in-lens detector and 3 keV acceleration voltage on cells just broken and put directly into the microscope.

7.2 Results

7.2.1 Conversion and current efficiencies

In Table 21 and Table 22 the NO_x conversion to N_2 and the current efficiency are stated for the conversion measurements performed in 1000 ppm NO. The NO_x conversion in the temperature range 350-450 °C is higher on the BaO impregnated stacks compared to the non-impregnated stack, whereas at 500 °C one BaO impregnated stack (B1) shows a much lower and the other (B2) a much higher NO_x-conversion compared to the non-impregnated stack. With respect to the current efficiency an increased efficiency is observed on the BaO impregnated stacks at 350-400 °C, while at higher temperatures the BaO impregnated stacks show in three measurements out of four measurements a lower current efficiency compared to the non-impregnated stack. It is noted, that B1 which had the lowest NO_x conversion at 500 °C, at the same temperature had the highest current efficiency when compared to the other stacks.

Table 21. NO_x conversion to N_2 [%] during 2 h polarisation in 1000 ppm NO on non-impregnated (N1) and BaO impregnated (B1, B2) LSF15-CGO10 cell stacks.

Temperature [°C]	N1	B1	B2
300	0	0	0
350	0	6	2
400	4	19	6
450	15	75	41
500	43	9	67

Table 22. Current efficiency [%] during 2 h polarisation in 1000 ppm NO on non-impregnated (N1) and BaO impregnated (B1, B2) LSF15-CGO10 cell stacks.

Temperature [°C]	N1	B1	B2
300	0	0	0
350	0	18	9
400	5	22	19
450	10	7	5
500	11	15	5

When 10% oxygen was present in the gas with 1000 ppm NO, formation of N_2 was in no cases observed during 3 V polarisation. Apparently the polarisation caused a slight conversion between NO and NO_2, which on both the non-impregnated stack and the BaO-impregnated stacks resulted in NO_2 being converted into NO, as seen when Figure 42 and Figure 43 are compared.

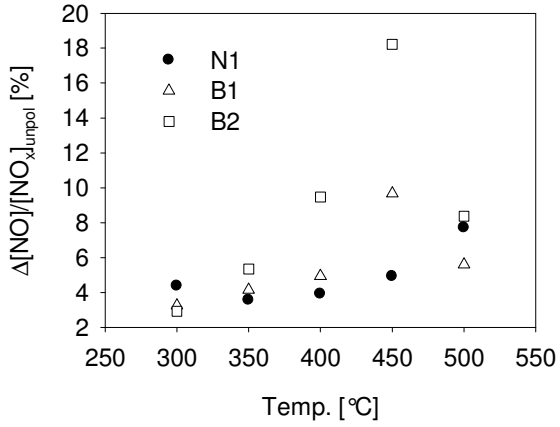

Figure 42. NO conversion during polarisation relative to the total NO_x concentration before polarisation in 1000 ppm NO + 10% O_2. The positive values mean NO is formed.

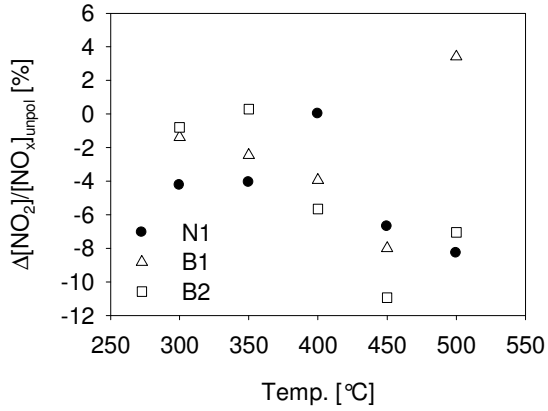

Figure 43. NO_2 conversion during polarisation relative to the total NO_x concentration before polarisation in 1000 ppm NO + 10% O_2. Negative values means NO_2 is removed.

7.2.2 SEM

Figure 44 shows the electrodes of a non-impregnated LSF15-CGO10 stack before and after test. Before test all the electrodes in the stack appeared as in Figure 44a, with very well-defined grains and smooth grain surfaces. After test the microstructure of the middle electrodes was unchanged (Figure 44b), while on the outer-electrodes nano-particles (<20 nm) had appeared on the electrode grains (Figure 44c). Figure 45 shows the electrodes of a BaO impregnated cell stack before and after test. On the BaO impregnated stacks before test the BaO was visible as nanoparticles (>20nm) on the electrode grains (Figure 45a). There seemed to be some tendency for the BaO particles to have a preferred orientation on the electrode grains. After test the microstructure of the electrodes was significantly altered (Figure 45b and Figure 45c). The microstructure of the electrodes was not the same for all the electrodes in the stack. In Figure 45b one of the outer electrodes is shown, and a very profound change in microstructure is observed, as all the electrode grains appears more or less “covered” in a rugged layer. On the other outer electrode of the same cell stack, see Figure 45c, the change in microstructure appears less dramatic, as only some of the electrode grains appear to be covered by nanometer sized particles. In contrast to the microstructure of the two outer electrodes in the tested cell stack, the middle electrode of the cell stacks appeared similar to the electrodes on the non-impregnated and untested cell stack.

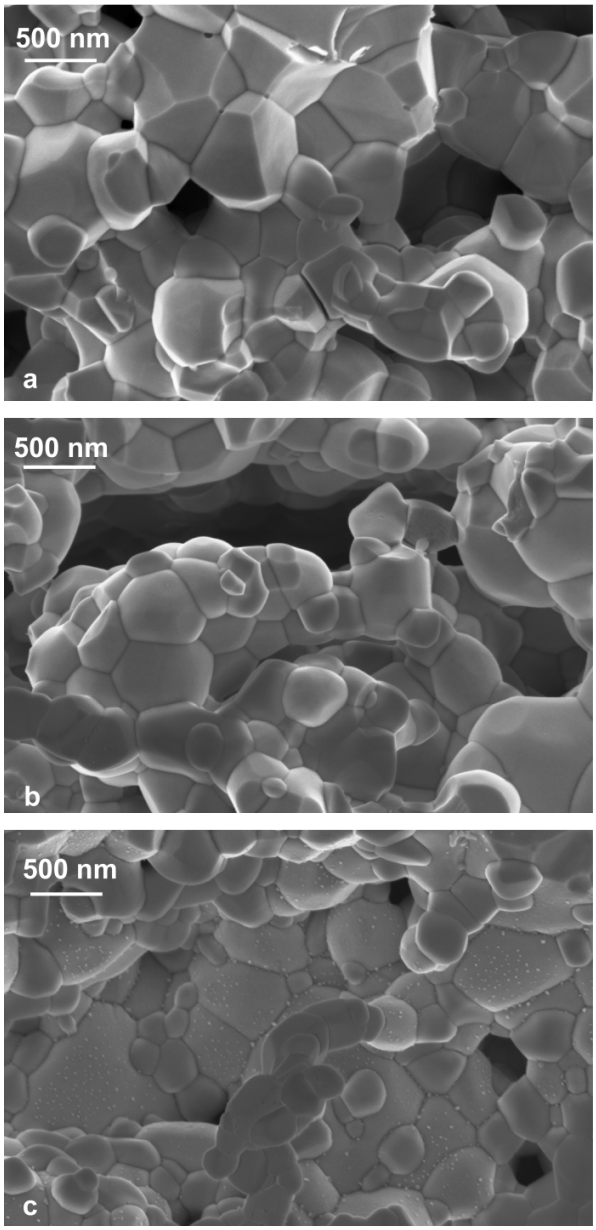

Figure 44. SEM images of non-impregnated LSF15-CGO10 electrodes a) outer electrode before test b) middle electrode after test and c) outer electrode after test.

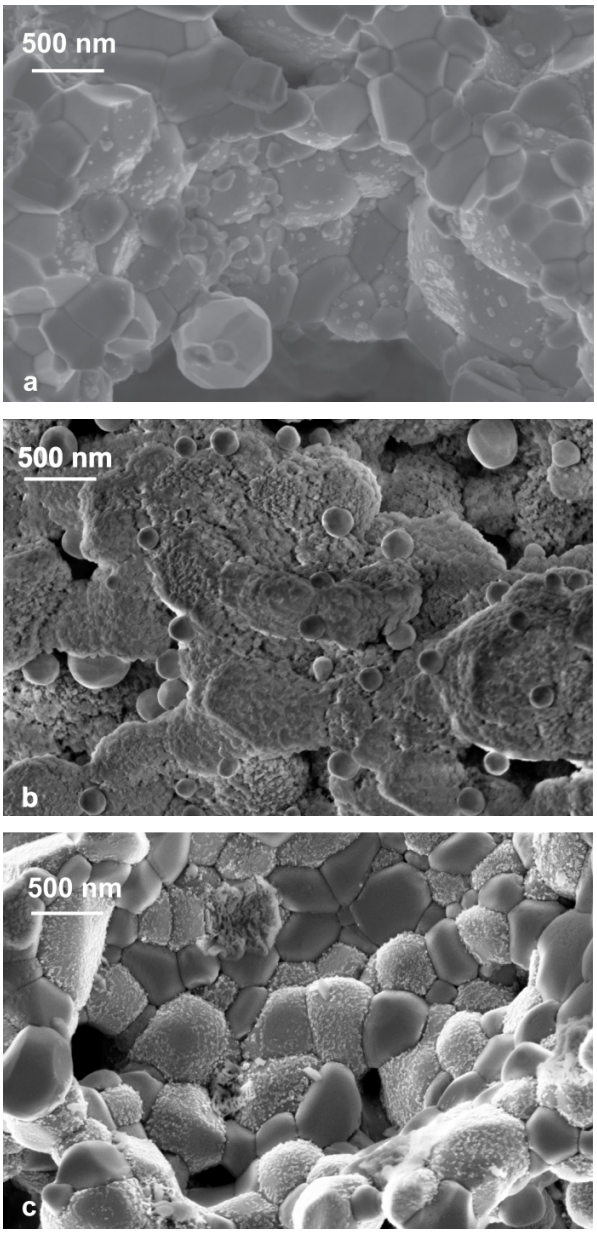

Figure 45. Electrodes of BaO impregnated LSF15-CGO10 electrodes a) before test b) outer electrode after test c) outer electrode on the other side after test.

7.2.3 Impedance

Impedance spectra of both non-impregnated and BaO impregnated cell stacks were fitted with the equivalent circuit $R_s(R_1Q_1)(R_2Q_2)(R_3Q_3)$ using the fitting software ZView Vers. 3.2[107]. In the equivalent circuit R represents a resistance and Q a constant phase element. In Table 23 the serial resistance and total polarisation resistance obtained from the fitting are stated. The serial resistances are fairly alike for all the cell stacks, with the one exception that the BaO impregnated cell stacks at 300 °C in the beginning of the test had a serial resistance higher when compared to the non-impregnated cell stack, while at 300 °C in the end of the test the situation is the opposite: the serial resistance of the BaO impregnated cell stacks is in the end significantly lower compared to the non-impregnated stack. With respect to the polarisation resistance the two BaO impregnated cell stacks shows a quite different behaviour at the beginning of the test, one of the stacks (B1) has a polarisation resistance much larger than the polarisation resistance of the non-impregnated cell stack, while the other one (B2) has a polarisation resistance only slightly larger compared to the non-impregnated stack. When the temperature is increased to 400 °C and higher, the polarisation resistance of the BaO impregnated cell stacks become significantly smaller than the polarisation resistance of the non-impregnated cell stack. At 300 °C in the end of the test both the BaO impregnated stacks had a polarisation resistance lower that the non-impregnated cell stacks, contrary to in the beginning.

Table 23. Serial resistance (R_s) and polarisation resistance (R_p) in Ωcm^2 for a non-impregnated stack (N1) and for two BaO-impregnated (B1, B2) LSF15-CGO10 cell stacks subjected to 1000 ppm NO + 10% O_2. Values are stated determined at 300 °C in the beginning of the test and at the end of the test, the latter labelled 300(post).

	R_s			R_p		
Temp.	N1	B1	B2	N1	B1	B2
300	140	190	180	5700	19000	6400
350	47	60	37	3200	7000	2100
400	19	14	14	1700	1000	960
450	11	6	7	920	400	280
500	8	9	4	420	160	48
300(post)	140	34	84	9700	7500	8200

In order to investigate, if the difference in polarisation resistance between the non-impregnated and BaO impregnated cell stacks was due to a difference in one specific process, Arrhenius plots were made for each of the three processes contributing to the polarisation resistance, see Figure 46, Figure 47 and Figure 48. From the Figure 46 it is observed, that the resistance of process 1 located at the highest frequencies is lower for the BaO-impregnated cell stacks over almost the entire temperature range, with 500 °C as the one exception. When Figure 47 and Figure 48 are compared to Table 23 it is observed, the higher polarisation resistance of the BaO impregnated stacks at low temperatures can be attributed to a higher resistance in the process located at the lowest frequencies (process 3), while the smaller polarisation resistance observed at higher temperatures is due to a lower resistance of both the middle frequency process (process 2) and the low frequency process (process 3) .

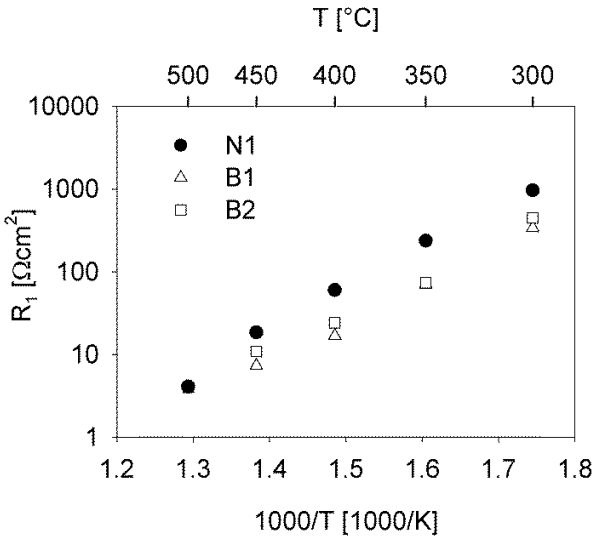

Figure 46. Arrhenius plot of high frequency arc (Arc 1) resistance in 1000 ppm NO +10% O_2.

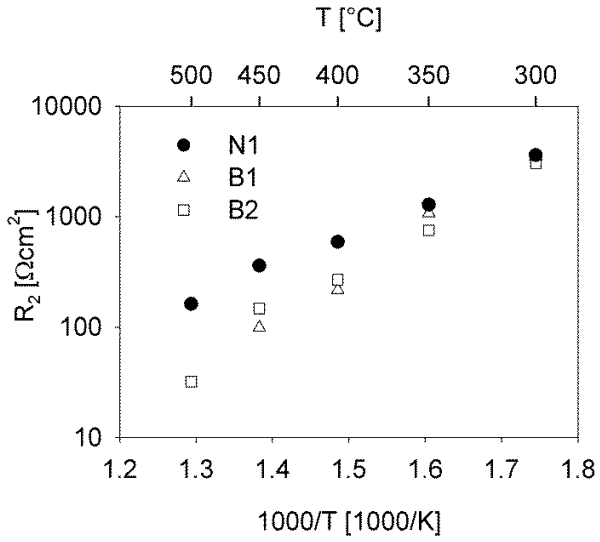

Figure 47. Arrhenius plot of middle frequency arc (Arc 2) resistance in 1000 ppm NO + 10% O_2.

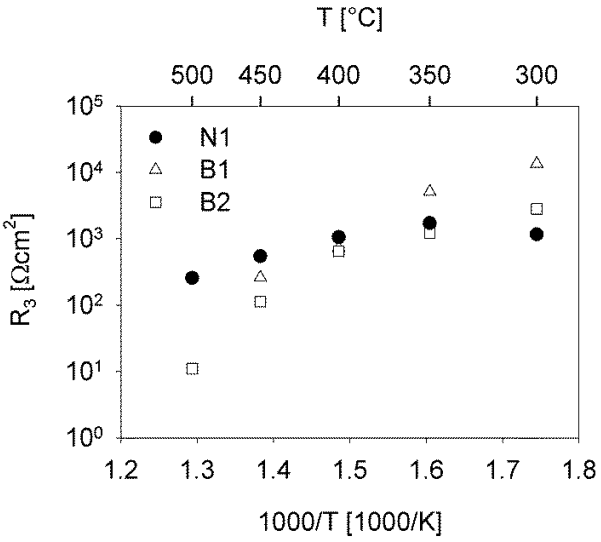

Figure 48. Arrhenius plot of low frequency arc (Arc 3) resistance in 1000 ppm NO + 10% O_2.

In order to characterize the processes contributing to the polarisation resistance further, impedance spectra were recorded while the "standard" atmosphere 1000 ppm NO + 10% O_2 was varied, first by varying the NO content between 1500 ppm NO and 500 ppm NO, and then by varying the O_2 content between 5% and 15%. Furthermore the flowrate was varied from the "standard" 2 L/h to 2.5 and 3 L/h and impedance spectra were also recorded during current load.

These experiments were performed at 300 °C and the characteristics found for the individual processes are stated in Table 24. Furthermore impedance spectra recorded at OCV and under current load are shown in Figure 49. The characteristics of the individual processes and a possible identification of the processes will be discussed in the Discussion section.

Table 24. Characteristics of the three processes contributing to the polarisation resistance of BaO-impregnated cell stacks in 1000 ppm NO + 10% O_2. The stated frequency range covers the temperature range 300-500 °C. The dependency of R and C_ω on pO_2, pNO and polarisation was only investigated at 300 °C.

Proces	Freq. range	Charactistic
1	15000->1MHz	- C_ω temperature independent - R dependent on pO_2 (decrease with decreasing pO_2) - R dependent on pNO (decrease with decreasing pNO) - C_ω dependent on pO_2 and pNO (increase with decreasing pO_2/pNO)
2	0.1-30 Hz	- C_ω increases with temperature - C_ω dependent on pO_2 and pNO (increase with decreasing pO_2/pNO) - R dependent on pO_2 (increase with decreasing pO_2) - R dependent on pNO (increase with decreasing pNO)
3	0.01-0.1 Hz	- C_ω increases with temp. (B1) or show no clear temp. dependency (B2) - R dependent on pNO (increase with decreasing pNO) - R decreases with polarisation

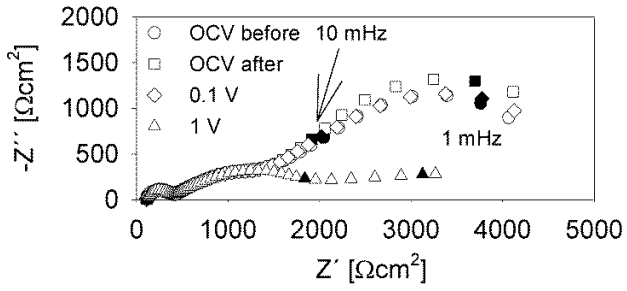

Figure 49. Impedance spectra recorded at OCV before and after polarisation, and during polarisation in 1000 ppm NO + 10% O_2 on BaO impregnated LSF15-CGO10 cell stack. The frequencies are stated for the filled symbols.

7.3 Discussion

7.3.1 Stability of the serial resistance

A discrepancy between the serial resistance of the non-impregnated cell stack and the BaO-impregnated cell stacks was observed at the beginning of the tests. Since both the non-impregnated and the BaO impregnated stacks were from the same batch of LSF15-CGO10 cell stacks, the difference in serial resistance at the beginning of the tests may likely be ascribed to the impregnation. A higher serial resistance is typically related to a poorer electric contact, and a possible explanation is for this reason that three times impregnation including heat treatment at 700 °C has lead to a slightly poorer contact between the Au current collector and the cell stack on the BaO impregnated stacks, leading to a higher serial resistance at the beginning of the test.

Furthermore, a decrease in the serial resistance of the BaO impregnated stacks was observed during testing. Part of the decrease might be explained by the Au current collector on the BaO impregnated stacks regaining good contact with the cell stack. However, this is likely not the only explanation, as the serial resistance on the BaO impregnated cell stacks at the end is much lower than the serial resistance of the non-impregnated sample. A possible explanation of this could be that the BaO during testing has reacted with the electrode materials and formed new phases with a higher conductivity. This thesis is supported by the SEM images of the BaO impregnated electrodes after test, which show profound microstructural changes in the electrodes.

It should be noted, that a change in the serial resistance/the electric contact during the test also will affect the polarisation resistance[165]. However, as the R_s/R_p ratio is not same for the BaO impregnated cell stacks at the beginning and the end of the test, changes in the serial resistance/electric contact cannot solely explain the decrease in the polarisation resistance during the test, and another activation process must for this reason also take place.

7.3.2 Identification of processes

In the previous chapter it was suggested, that the processes contributing to the polarisation resistance on the non-impregnated cell stack in 1000 ppm NO + 10% O_2 was the following: Firstly a process was located at the high frequencies and related to oxygen ion transport in the electrolyte and across the electrolyte-electrode interface. Secondly, two processes were located at lower

frequencies and ascribed to TPB related processes like adsorption, diffusion and charge transfer, however exactly which processes and species were involved could not be identified.

On the BaO impregnated stacks described in this chapter, three processes were also identified to contribute to the polarisation resistance; some of the characteristics of these processes were listed in Table 24 in the results section. At the high frequency part of the impedance spectra a process was located, which had a C_ω of approximately $1 \cdot 10^{-8}$ F/cm^2 independent of temperature, an activation energy of 0.9 eV and with the resistance and the C_ω being dependent on both the oxygen content and the NO content in the gas. The two first characteristics, activation energy and C_ω, indicate the high frequency process is the process related to oxygen ion transport in the electrolyte and across the electrolyte-electrode interface[36, 54, 166]. This process was previously identified on the non-impregnated cell stacks, but on the BaO impregnated cell stacks the assignment of the high frequency process to oxygen ion transport is contradicted by the apparent dependency of the process on the atmosphere. The suggestion is here, that the high frequency process on the BaO impregnated cell stack is indeed the process related the oxygen ion transport. The apparent dependency on the atmosphere is suggested to be an artefact due to poor separation between the high frequency process and the middle frequency process. As observed in Table 24 the resistance of the middle frequency process also depends on the O_2 and NO content, and if the high frequency and middle frequency processes are overlapping, the dependency of the middle frequency process on the atmosphere may interfere with the resistance of the high frequency process.

With respect to the middle frequency process, the process shows as mentioned dependency on the atmosphere, with the resistance increasing with decreasing O_2 and NO concentration, and furthermore C_ω shows dependency on both the atmosphere and the temperature. The dependency of the process on both atmosphere and temperature, together with a C_ω around $1 \cdot 10^{-4}$ F/cm^2 is consistent with the behaviour expected for a TPB related process. For this reason the middle frequency process is ascribed to a TPB related process.

Finally, process 3 located at the lowest frequencies show a very strong dependency on the polarisation, as shown in Figure 49. Furthermore the resistance of the process increases with decreasing NO content, and in one of the tests the C_ω of the process shows a clear dependency on

the temperature. The dependency on polarisation and temperature is consistent with the expectations for TPB related process, as both the polarisation and temperature increase should lead to a broadening of the TPB zone end thereby a decrease in resistance and increase in capacitance. Furthermore the dependency on the NO content but not the O_2 content indicates that this TPB process located at the lowest frequencies is closely connected to a NO_x specie either in the gas phase or adsorbed at the electrode surface.

7.3.3 Effect of BaO impregnation NO_x conversion and electrodeprocesses

As shown in the results section, the BaO impregnation increased the NO_x conversion at 350-450 °C and the current efficiency at 350-400 °C when no O_2 was present. However, when 10% oxygen was present in the atmosphere, the conversion on the BaO impregnated sample was similar to the conversion on the non-impregnated sample, i.e. a bit of NO_2 was converted to NO, but no conversion to N_2 was observed. This could at first indicate, the BaO had no effect on the electrode processes in oxygen-containing atmosphere, but as shown by the impedance analysis, all three electrode processes were to a smaller or larger extent affected by the BaO impregnation, which mainly led to a decrease in polarisation resistance. This shows, that even though the BaO decreases the resistance of the electrode processes, the selectivity towards N_2 formation is not increased on the LSF15-CGO10 cell stacks at the investigated conditions.

7.4 Conclusion

The effect of BaO impregnation on the NO_x conversion on LSF15-CGO10 cell stacks was investigated. In an atmosphere with 1000 ppm NO and no O_2 the BaO impregnation increased both the NO_x conversion to N_2 and the current efficiency. However, in the presence of 10% O_2, no conversion of NO_x to N_2 was observed. The impedance analysis showed the BaO impregnated in most cases decreased the polarisation resistance in 1000 ppm NO + 10% O_2, but as apparent from the conversion measurements an increased selectivity towards N_2 formation during polarisation was not observed.

8 NO_x-conversion on LSM15-CGO10 cell stacks with BaO impregnation

This chapter is the manuscript "NO_x-conversion on LSM15-CGO10 cell stacks with BaO impregnation" accepted for publication in Journal of Materials Chemistry.

8.1 Abstract

The electrochemical conversion of NO_x on non-impregnated and BaO-impregnated LSM15-CGO10 ($La_{0.85}Sr_{0.15}MnO_3$-$Ce_{0.9}Gd_{0.1}O_{1.95}$) porous cell stacks has been investigated, and extensive impedance analysis have been performed to identify the effect of the BaO on the electrode processes. The investigation was conducted in the temperature range 300-500 °C, a polarisation range from 3 V to 9 V and in atmospheres containing 1000 ppm NO, 1000 ppm NO + 10% O_2 and 10% O_2. On the non-impregnated cell stacks no NO_x conversion was observed at any of the investigated conditions. However, BaO impregnation greatly enhanced the NO_x conversion and at 400 °C and 9 V polarisation a BaO-impregnated cell stack showed 60% NO_x conversion into N_2 with 8% current efficiency in 1000 ppm NO + 10% O_2. This demonstrates high NO_x conversion can be achieved on an entirely ceramic cell without expensive noble metals. Furthermore the NO_x conversion and current efficiency was shown to be strongly dependent on temperature and polarisation. The impedance analysis revealed that the BaO-impregnation increased the overall activity of the cell stacks, but also changed the adsorption state of NO_x on the electrodes; whether the increased activity or the changed adsorption state is mainly responsible for the improved NO_x conversion remains unknown.

8.2 Introduction

In Europe the NO_x-emission from the road transport has been significantly reduced during the last 10 years, mainly due to the introduction of the three-way-catalyst on gasoline vehicles[2]. Due to the negative impact of NO_x-emissions on both human health and the environment[11], a further reduction in the NO_x emissions from the car fleet is desirable. However a major challenge in that connection is the increased number of diesel vehicles, as the conventional three-way-catalyst is incapable of removing NO_x from diesel exhaust. For this reason much research is currently focused on NO_x-removal technologies for diesel exhaust, the most heavily investigated technologies being selective catalytic reduction with ammonia (NH_3-SCR), selective catalytic reduction with

hydrocarbons (HC-SCR) and the NO_x-storage and reduction (NSR) catalyst[108]. In all these three technologies there is the need for a reducing agent, either coming from operating the engine occasionally in an excess fuel to air-ratio (HC-SCR and NSR) or supplied by a separate system (NH_3-SCR). A NO_x removal technology without the need for the addition of a reducing agent would be simpler and therefore advantageous compared to the aforementioned technologies.

A suggestion for such a technology is electrochemical NO_x removal, where the NO_x is reduced to N_2 and O_2 by electrons supplied to a polarised electrode[4]. The technology is inspired by the finding in 1975 by Pancharatnam et al.[22] that NO can be reduced to N_2 during polarisation of a zirconia based cell in the absence of oxygen, and later it was shown by Cicero et al.[24] and Hibino et al.[26] that NO_x also could be electrochemically reduced in the presence of oxygen. Since then several studies has been made in the field of electrochemical deNO_x by different research groups[24, 26, 28, 30, 39, 44, 45, 167]. For electrochemical NO_x removal to become a technology of practical interest, a first and major obstacle to be overcome is to find electrode materials with a sufficiently high activity and selectivity for NO_x reduction[4].

With respect to selectivity the major problem is the competing reduction of O_2; in equation 8.1 the desired NO reduction on the cathode is stated and the competing O_2 reduction is stated in equation 8.2.

$$NO + 2\ e^- \rightarrow 0.5\ N_2 + O^{2-} \qquad 8.1$$

$$0.5\ O_2 + 2\ e^- \rightarrow O^{2-} \qquad 8.2$$

In this work it is investigated if the conversion of NO_x at 300-500 °C on LSM15-CGO10 composite electrodes can be increased by impregnating the electrodes with BaO. BaO is the most commonly used NO_x storage compound in the NSR catalyst[21], and the idea in this work is to increase the NO_x conversion by up-concentrating the NO_x on the electrode surface in the form of $Ba(NO_3)_2$. Previous work by Li et al.[41] and Yoshinobu et al.[49] have shown good results from combining BaO and electrochemical deNO_x, but in both cases the investigated electrode systems contained Pt or other noble metals, which increases the cost of the system. The work by Simonsen et al.[43] showed LSM15 in combination with Ba could be an efficient catalyst for electrochemical NO_x removal;

however the work did not include any conversion measurements. Conversion measurements are included in this work, where electrochemical NO_x removal is investigated on an entirely ceramic system, i.e. a system without expensive noble metals. LSM15 is chosen as electrode material for this investigation, as LSM15 has good stability compared to other perovskites like $La_{1-x}Sr_xFe_{1-y}Co_yO_3$ and $Ba_{1-x}Sr_xFe_{1-y}Co_yO_3$, eventhough these have a higher activity in the investigated temperature range[62]. CGO10 was chosen as electrolyte and component in the electrode, as the ionic conductivity of CGO10 is superior to the ionic conductivity of YSZ (Yttria Stabilized Zirconia) below 600 °C[68]. The non-impregnated and BaO-impregnated electrodes were investigated in a set-up with a porous 11-layer cell stack, as the large contact area between gas flow and cell stack in this set-up increases the conversion and makes it easy to detect any changes in the gas composition. Two complementary approaches were used to investigate the effect of the BaO-impregnation on the electrode performance. The one approach involved measurements of the NO_x conversion as function of temperature, polarisation and gas composition. This approach was supplemented by an extensive impedance analysis aimed at clarifying which processes contributed to the polarisation resistance of the cell stacks, and how these processes were affected by the BaO impregnation.

8.3 Experimental

8.3.1 Cell stack fabrication:

The 11-layer porous cell stacks consisted of 11 alternating layers of composite electrode (65 wt% LSM15 (Haldor Topsøe) and 35 wt% CGO10 (Rhodia)) and electrolyte (CGO10). The porous composite electrode layers were manufactured by mixing LSM15, CGO10, solvent (mixture of ethanol and butanone), binder (polyvinylbuyral), dispersant (polyvinylpyrrolidone) and pore former (graphite) into a slurry, ball mill the slurry and thereafter tape caste the slurry into green tapes of approximately 40 µm thickness, for more details see Hee et al.[159]. The porous CGO10 layers were prepared in a similar manner, and subsequent the green electrode and electrolyte layers were laminated together and round cell stacks were stamped out. The cell stacks were sintered with the maximum temperature 1250 °C held for 4 hours and thereby achieved a diameter of ≈14 mm. Prior to mounting in the test-set-up the cell stacks were painted with gold paste (ESL Electro-Science) mixed with 20% carbon (Graphit Kropfmühl AG), which was burned off at 800 °C in order to create porous gold current collectors on each side of the cell stack.

8.3.2 Impregnation

For impregnation of the porous cell stacks with BaO a 0.3 M aqueous $Ba(NO_3)_2$ (Merck) solution with 10 wt% P123 (BASF) was prepared. The cell stacks were covered with the $Ba(NO_3)_2$ solution and put under vacuum for ≈10 s, whereafter excess impregnation solution was wiped of the surface. The impregnated cell stacks were then heated to 700 °C for 1 h to decompose the $Ba(NO_3)_2$ into BaO. 700 °C was chosen to assure total decomposition, since a DTA experiment showed $Ba(NO_3)_2$ decomposed at 600-640 °C, even though the decomposition temperature reported by literature in general were lower, in the range 500-600 °C[168-170].

8.3.3 Test-set-up

For electrochemical cell testing the stack was mounted in between two alumina tubes, which contained channels for the gas flow and measurement probes for the electrochemical characterization. The cell and the alumina tubes were inclosed in a quartz tube and mounted vertically in a furnace. A sketch of the set-up is shown in Figure 50.

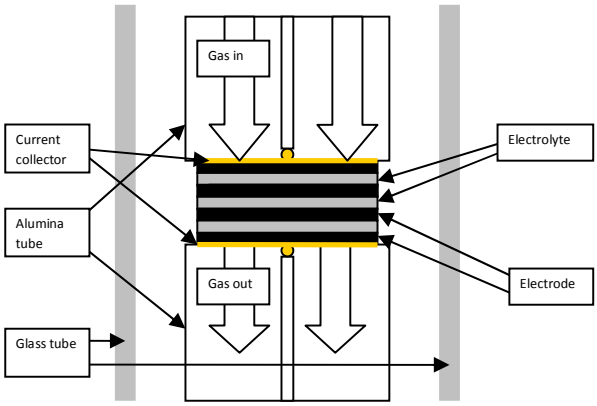

Figure 50. Sketch of test-set-up for porous 11-layer cell stack. Reprinted with permission from Werchmeister et al.[13]

8.3.4 Electrochemical Testing and Conversion measurements:

During the tests the cell stacks were characterized by electrochemical impedance spectroscopy (EIS). The impedance spectra were recorded with a Gamry Reference 600 potentiostat in the frequency range 1 MHz to 0.001 Hz with 6 points pr. decade and 36 mV rms amplitude. The Gamry Reference 600 potentiostat was also used for polarisation of the cells during the conversion

measurements. During the experiments the outlet gas from the cell stack was constantly monitored. The NO and NO_2 concentrations were monitored by a chemiluminiscense detector Model 42*i* High Level from Thermo Scientific, while the N_2, N_2O and O_2 concentrations were monitored with a mass spectrometer from Pfeiffer Vacuum, type Omnistar GSD 301. In total five cell stacks were tested, two non-impregnated stacks named N1 and N2, and three BaO-impregnated stacks named B1, B2 and B3.

8.3.5 Test conditions

The conversion measurements were made at the flow rate 2 L/h in 1000 ppm NO and 1000 ppm NO + 10% O_2 in both cases with balance Ar. These concentrations of NO and O_2 were chosen as they resemble the concentrations which may be found in the exhaust from a diesel car[7]. It should be noted, that 1000 ppm NO + 10% O_2 are the concentrations set during the experiments, while in reality the gas composition will contains some NO_2 due to the equilibrium NO + ½ O_2 ⇆ NO_2. Moreover impedance measurements were recorded in 10% O_2 with balance Ar for comparison to impedance spectra recorded in NO containing atmospheres. The experiments were carried out in the temperature range 300-500 °C which is close to the expected temperature of diesel engine exhaust of 100-400 °C[171]. Polarisation experiments were made in the range 3-9 V. As each 11 layer cell stacks contain 5 “cells”, the polarisation range pr. cell was 0.6-1.8 V.

8.3.6 SEM

Before and after testing the cell stacks were examined in a Zeiss Supra 35 scanning electron microscope equipped with a field emission gun. In order to obtain high magnification images of the electrode microstructure images were recorded with the in-lens detector and 3 keV acceleration voltage on cells just broken and put directly into the microscope.

8.4 Results

8.4.1 Conversion and current efficiency

On the non-impregnated cell stacks no conversion of NO into N_2 was observed during 3 V polarisation in the temperature range 300-500 °C, neither when the cell stacks were supplied with 1000 ppm NO + 10% O_2 nor when the stacks were supplied with only 1000 ppm NO. However, on the BaO impregnated cell stacks conversion of NO_x into N_2 was observed both without presence of O_2 and in the presence of 10% O_2. In Figure 51 the results from the conversion measurement

without O_2 in 1000 ppm NO on the BaO impregnated stacks are stated, the results are based on measurements on three different stacks. Figure 51 shows the NO_x conversion increases with temperature, and especially from 400 °C to 450 °C a significant increase in the conversion is observed from below 20% to above 60%. A significant increase in the current efficiency is also observed from 400 to 450 °C, as the current efficiency increases from 4% to 16%.

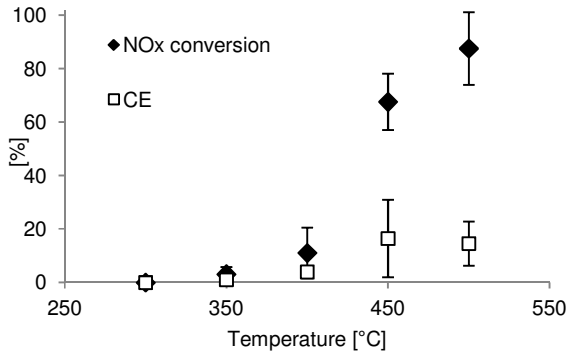

Figure 51. Percentage of NO_x converted into N_2 and the current efficiency (CE) during 3 V polarisation for 2 h in 1000 ppm NO on a BaO impregnated cell stack.

When the BaO impregnated cell stacks were supplied with 1000 ppm NO + 10% O_2 and polarised at 3 V the NO_x conversion also increased with temperature, however the average NO_x conversion achieved at 500 °C was only 4% and the corresponding current efficiency only 0.3%.

On one of the BaO impregnated cell stacks the influence of varying the polarisation between 3 V, 5 V, 7 V and 9 V was investigated at 300 °C, 400 °C and 500 °C. At each temperature the first measurements was made at 3 V whereafter the voltage was increased stepwise till 9 V was reached, each time with the voltage kept at the specified value for one hour, with a one hour break at OCV in between. After 9 V had been reached the measurements at 7 V, 5 V and 3 V were repeated while going down in voltage. The results for the NO_x conversion are shown in Figure 52 and for the current efficiency in Figure 53.

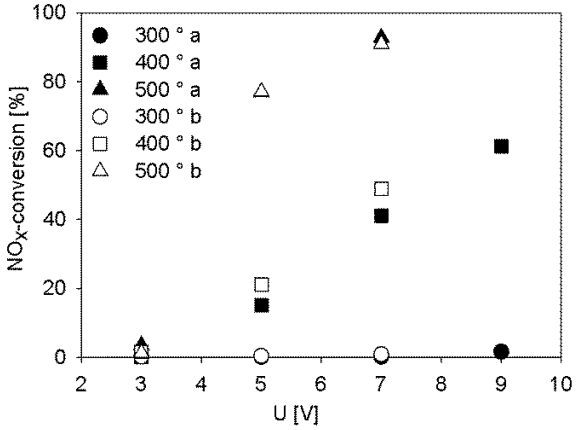

Figure 52. Percentage of NO_x converted into N_2 during polarisation for 2 h in 1000 ppm NO + 10% O_2 on a BaO impregnated cell stack. Closed symbols labelled a were recorded during the stepwise voltage increase from 3 to 9 V, while open symbols labelled b were recorded during the subsequent voltage decrease from 9 V to 3 V.

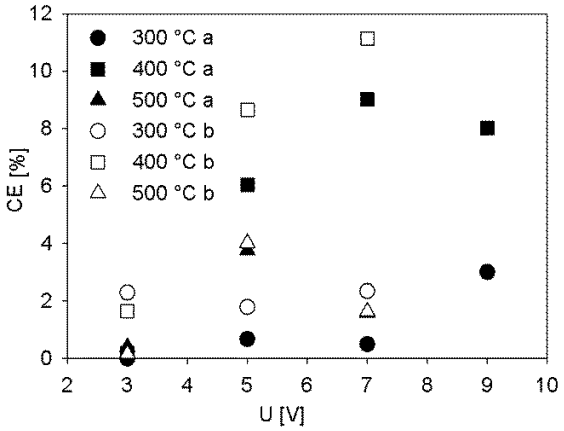

Figure 53. Current efficiency for conversion of NO_x into N_2 during polarisation for 2 h in 1000 ppm NO + 10% O_2 on a BaO impregnated cell stack. Closed symbols labelled a were recorded during the stepwise voltage increase from 3 to 9 V, while open symbols labelled b were recorded during the subsequent voltage decrease from 9 V to 3 V.

With respect to the NO_x-conversion, only a negligible effect of increasing the voltage is observed at 300 °C, where the NO_x conversion only increased from 0% at 3 V to 2% at -9 V. Contrary to this a distinct effect is observed from increasing the voltage at 400 °C, where the NO_x conversion increased from 0% at 3 V to 61% at 9 V. Moreover an activation effect is observed at 400 °C on both NO_x-conversion and current efficiency, as both had increased when the measurements at 7 V, 5 V and 3 V were repeated during the second half of experiment. For comparison a similar polarisation experiment was made at 400 °C on a non-impregnated cell stack, but no formation of N_2 was observed not even at 9 V polarisation. At 500 °C a distinct effect is again observed from increasing the voltage on the BaO-impregnated stack, the relative largest increase in NO_x conversion per voltage increase is observed when the voltage is increased from 3 V to 5 V, which makes the NO_x conversion increase from 4% to 77%. The measurement at 9 V is missing at 500 °C, as the corresponding current exceeded the maximum current of the Gamry Ref 600 Potentiostat and the experiment for this reason was interrupted. In general with respect to the current efficiencies they appear to be more or less independent on the voltage at 300 °C and 500 °C and do in no cases exceed 5%, whereas at 400 °C the current efficiencies clearly increase with voltage until 7 V, where it reaches a maximum value of ≈10%.

8.4.2 Deconvolution of impedance spectra

The impedance spectra recorded on the non-impregnated and the BaO-impregnated cell stack were all fitted with a serial resistance and a series connection of 3-4 sub-circuits, each sub circuit containing a resistance and a constant phase-element in parallel. In general the process located at the highest frequencies was clearly separable from the lower frequency processes, which on the other hand were strongly overlapping in the impedance spectra. Due to the strong overlap in the low frequency region it was not possible to obtain a linear Arrhenius plot for the individual resistances in this frequency region. To enlighten the processes in the low frequency region the sum of the low frequency resistances (R_2, R_3 and in some cases R_4) were instead plottet together. The Arrhenius plot of the serial resistance, R_1 and R_2+R_3+R_4 are shown in Figure 54, Figure 55 and Figure 56 respectively.

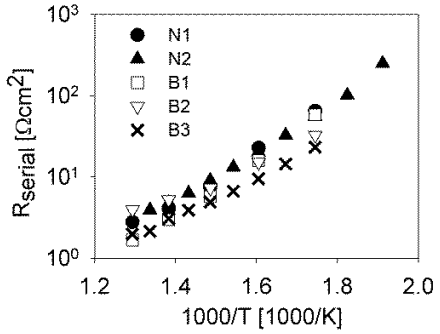

Figure 54. Arrhenius plot of the serial resistance obtained from fitting of impedance spectra recorded in 1000 ppm NO + 10% O_2 on non-impregnated (N1 and N2) and BaO-impregnated (B1, B2 and B3) cell stacks.

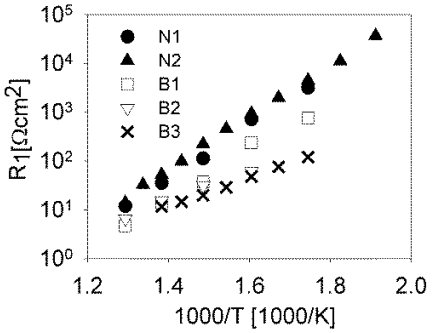

Figure 55. Arrhenius plot of the high frequency process resistance obtained from fitting of impedance spectra recorded in 1000 ppm NO + 10% O_2 on non-impregnated (N1 and N2) and BaO-impregnated (B1, B2 and B3) cell stacks.

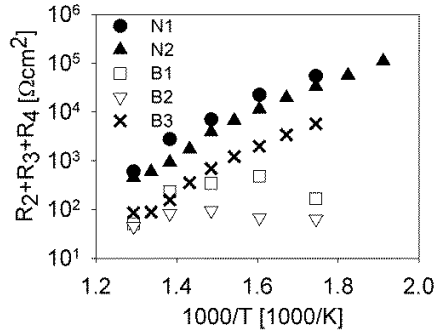

Figure 56. Arrhenius plot of the sum of the low frequency processes resistance. The resistances were obtained from fitting of impedance spectra recorded in 1000 ppm NO + 10% O_2 on non-impregnated (N1 and N2) and BaO-impregnated (B1, B2 and B3) cell stacks.

The serial resistance of the two non-impregnated cell stacks is in almost exact agreement, which is also the case for the resistance of the high frequency process (R_1) and the low frequency processes (R_2+R_3+R_4). This means good reproducibility is obtained for the non-impregnated cell stacks. The serial resistances of the BaO-impregnated cell stacks are very close to those of the non-impregnated, however with a tendency to be slightly lower. For the high frequency process the serial resistance is consequently lower for the impregnated cell stacks, the difference between non-impregnated and impregnated stacks being largest at low temperatures. For the low frequency processes some discrepancy is observed between the impregnated stacks, but in all cases the low frequency resistances are lower on the BaO-impregnated stacks compared to non-impregnated. One of the impregnated stacks (B3) shows an activation energy in the low frequency region similar to the activation energy of the non-impregnated stacks. The two other impregnated stacks show in the low frequency region a quite different behaviour, as the resistance show very little temperature dependency. At the highest measured temperature (500 °C), the resistance of all the impregnated cell stacks is quite equal.

For comparison to the just described resistances in the cell stack in 1000 ppm NO + 10% O_2, the total polarisation resistance in non- and BaO-impregnated cell stacks subjected to only 10% O_2 is shown in Figure 57. A decrease in the polarisation resistance on the impregnated stacks similar to the one observed in 1000 ppm NO + 10 % O_2 is also observed in 10% O_2. This indicates the BaO impregnation cause a general increase in the activity of the electrodes.

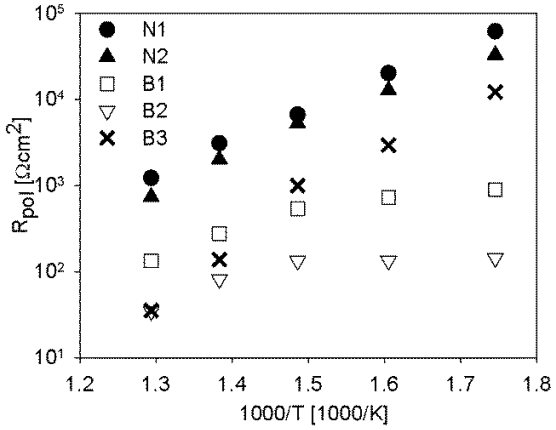

Figure 57. Polarisation resistance of non-impregnated and impregnated cell stacks in 10% O_2.

8.4.3 Characteristics of processes

In addition to the impedance spectra recorded during temperature variations impedance spectra were also recorded during variation in gas composition, flow rate and polarisation. For the concentration variations the "standard" gas composition 1000 ppm NO + 10% O_2 was varied first by changing the NO content to 1500 ppm and to 500 ppm while keeping pO_2 constant, whereafter the NO concentration was fixed at 1000 ppm NO while pO_2 was changed to 5% and 15%. These experiments were repeated at several temperatures on the cell stacks. During flow variations the standard flow 2 L/h was increased to 2.5 L/h and 3 L/h. The majority of the reported impedance spectra were recorded at OCV, but at 400 °C a series of impedance spectra were recorded under 0.1V, 1 V and 3 V polarisation on both the non- and the BaO-impregnated stacks. From the impedance spectra recorded at different conditions different characteristics could be found for the processes contributing to the polarisation resistance. These characteristics are listed for the non-impregnated stacks in Figure 50 and for the BaO-impregnated stacks in Table 26. It should be noted the characteristics are stated for the 3 dominating processes observed at all temperatures, while a fourth process occasionally appearing at 500 °C is not included. In addition to the process characteristics listed in the tables the impedance spectra recorded during polarisation on the non-impregnated stack and BaO-impregnated stack are shown in Figure 58 and Figure 59 respectively, and show a profound change in the low frequency region during polarisation.

Table 25. Characteristics of processes contributing to the impedance spectra recorded on non-impregnated cell stacks in an atmosphere containing 500-1500 ppm NO and 5-15% O_2 within the temperature range 300-500 °C.

Process	Freq. range	Characteristic
1	300-80000 Hz	- C_ω* temperature independent
2	0.5-25 Hz	- C_ω increases from 300 to 400 °C, then decreases to 500 °C
		-C_ω dependent on pO_2 (increase with decreasing pO_2)
		- R dependent on pO_2 (increase with decreasing pO_2)
3	0.02-0.5 Hz	- C_ω increases with temperature
		- C_ω dependent on pO_2 (increase with decreasing pO_2)
		- R decreases with polarisation
		- R dependent on pNO (increase with decreasing pNO)

* C_ω is the near-equivalent capacitance of the process

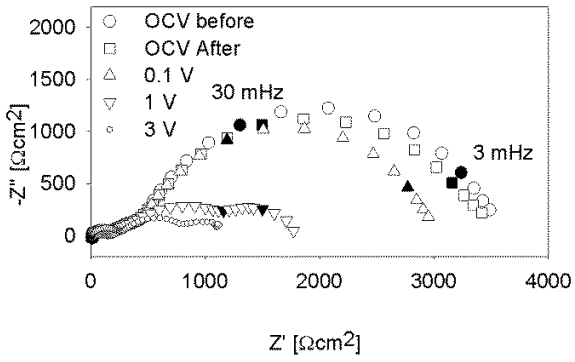

Figure 58. Impedance spectra recorded on non-impregnated cell stack at OCV and during polarisation. The stack was at 400 °C and supplied with 1000 ppm NO + 10% O_2. The stated frequencies are marked with closed symbols. The spectra labelled “OCV before” and “OCV after” refers are impedance spectra recorded at OCV immediately before and after impedance spectra were recorded under current load.

Table 26. Characteristics of processes contributing to the impedance spectra recorded on BaO-impregnated cell stacks in an atmosphere containing 500-1500 ppm NO and 5-15% O_2 within the temperature range 300-500 °C.

Process	Freq. range	Characteristic
1	5000-70000Hz	- C_ω decreases with temp (B3) or increases with temp. (B1) and (B2)
		- R increases with polarisation
2	8-40 Hz	- C_ω increases with temperature
		- C_ω dependent on pO_2 (decrease with decreasing pO_2)
		- R decreases with polarisation
3	4mHz-0.2 Hz	- C_ω increases with temperature
		- C_ω dependent on pO_2 (increase with decreasing pO_2)
		- C_ω dependent on pNO (increase with decreasing pNO)
		- R decreases with polarisation
		- R dependent on pNO (increase with decreasing pNO)

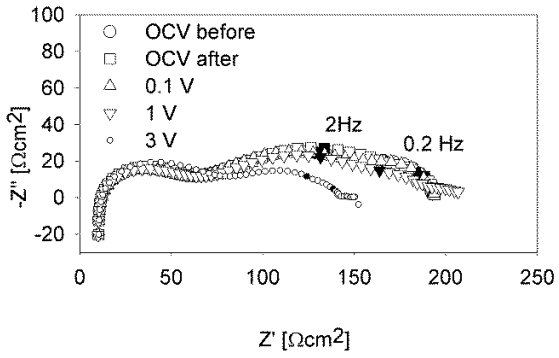

Figure 59. Impedance spectra recorded on BaO-impregnated cell stack at OCV during polarisation. The stack was at 400 °C and supplied with 1000 ppm NO + 10% O_2. The stated frequencies are marked with closed symbols. The spectra labelled “OCV before” and “OCV after” refers are impedance spectra recorded at OCV immediately before and after impedance spectra were recorded under current load.

8.4.4 Degradation

On all the cell stacks an impedance spectrum was recorded at 300 °C in 1000 ppm NO + 10% O_2 at the very beginning of the test and at the end of the test, i.e. after the temperature variations, polarisation experiments etc., had been performed. From these spectra the serial and polarisation resistances were determined (Table 27) and the percentage change in R_s, R_1 and $R_2+R_3+R_4$ during the cell tests was calculated (Table 28). The non-impregnated cell stacks and one of the BaO impregnated cell stacks (B3) activated during the cell test, as both R_s, R_1 and $R_2+R_3+R_4$ decreased. A decrease in R_s indicates an improved electric contact through the cell stack, but as the percentage change in the polarisation resistance differs from the percentage change in the serial resistances, improved contact cannot solely explain the changes observed in the polarisation resistances. The two BaO impregnated cell stacks, which had the lowest polarisation resistance in the beginning of the test (B1 and B2), degraded during the test which caused a large increase in the resistance of the low frequency processes, while R_s and R_1 during the tests decreased as for the other cell stacks. It is worth noticing, that even though the BaO impregnated cell stacks have a very different initial performance and degradation behaviour, they all at the end of the cell test have a polarisation resistance significantly below the polarisation resistance of the non-impregnated stacks.

Table 27. Serial resistance (R_s) and polarisation resistance (R_p) in 1000 ppm NO + 10% O_2 at 300 °C at the start of the test and the end of the test. The values stated for non-impregnated samples are average values for two different tests, the deviation between resistances in the two tests were below 6%.

	Test start		Test end	
	R_s [Ωcm^2]	R_p [Ωcm^2]	R_s [Ωcm^2]	R_p [Ωcm^2]
Non-impregnated	67	46070	48	25320
B1	60	923	30	1090
B2	48	110	38	300
B3	68	66253	44	7643

Table 28. Percentage change in serial resistance (R_s), resistance of the high frequency process (R_1) and the sum of the low frequency processes (R_2+R_3+R_4) between the start and the end of the test. The resistances are obtained from impedance spectra recorded in 1000 ppm NO + 10% O_2 at 300 °C.

	R_s	R_1	R_2+R_3+R_4
Non-impregnated	-29	-91	-39
B1	-50	-83	477
B2	-20	-30	5277
B3	-36	-96	-88

8.4.5 SEM microscopy

Representative SEM images from the microscopy investigation of the electrodes are shown in Figure 60. The SEM images of the non-impregnated electrodes before test (Figure 60a) show slightly rugged LSM15 grains in between smooth CGO10 grains. No evident differences are observed between the non-impregnated electrode before test (Figure 60a) and after test (Figure 60b). On the BaO impregnated electrodes before test (Figure 60c), the impregnated BaO is clearly visible as distinct particles located on the LSM15 grains. After testing the microstructure of the BaO impregnated electrodes had clearly changed, and three different kinds of microstructure were observed even within the same cell stack: electrode grains being almost entirely covered by nanometer sized, round and well-defined particles (Figure 60d), electrode grains covered in a more “fluffy” structure (Figure 60e) and electrode grains covered entirely in flake-like particles (Figure 60f). The weight load of BaO on the cell stacks used for the microscopy was 2±0.1wt%, which means differences in microstructure likely cannot be ascribed to differences in BaO weight load. Furthermore the SEM images showed a similar microstructure of the B1 and the B3 cell stacks, even though these stacks degraded/activated quite differently during the testing.

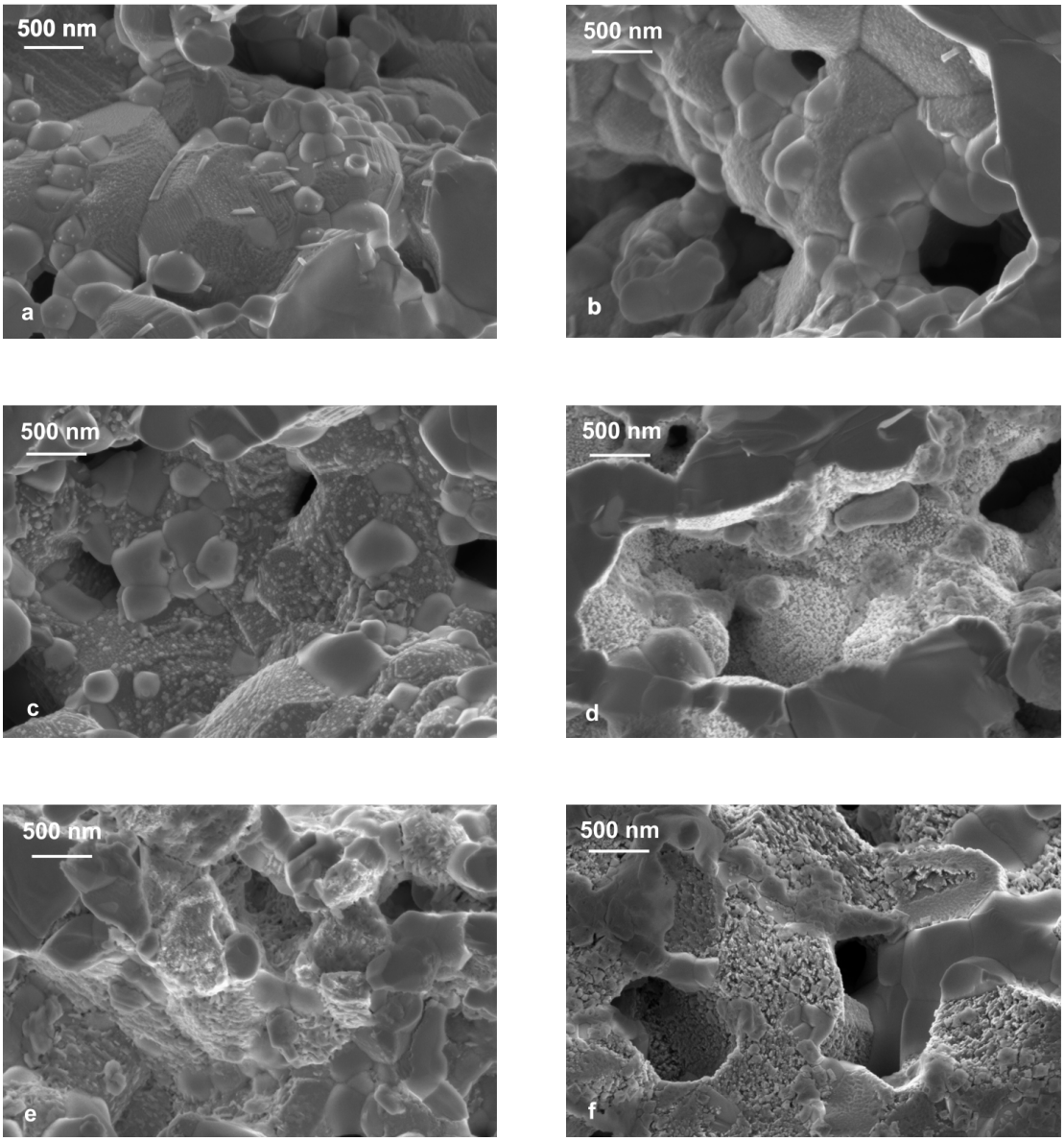

Figure 60. SEM images of the following LSM15-CGO10 cell stacks: a) non-impregnated before test b) non-impregnated after test c) BaO-impregnated before test and d)-f) BaO-impregnated after test.

8.5 Discussion

8.5.1 Processes on non-impregnated electrodes

Three processes were dominating the polarisation resistance of the non-impregnated electrodes. The high-frequency process was characterized by a temperature independent C_ω with a value around $1 \cdot 10^{-7}$ F/cm^2, a resistance independent on atmosphere and an activation energy of 1.08±0.01eV in 1000 ppm NO + 10% O_2. These characteristics are consistent with characteristics reported in literature for processes related to transfer of oxygen ions between the perovskite and the electrolyte[36, 54, 166]. For the middle frequency process R increased with decreasing pO_2 which indicate O_2 or an O-specie is participating in the middle frequency process. The C_ω of the middle frequency arc varied in the range $1 \cdot 10^{-5}$-$1 \cdot 10^{-4}$ F/cm^2, a range in fairly good agreement with the capacitance associated with adsorption and dissociation of oxygen on composite cathodes[152]. The C_ω of the middle frequency arc showed a strange behaviour with respect to the temperature dependency as the C_ω increases from 300 °C to 400 °C and decreases from 400 °C to 500 °C, the observation was made on two different stacks. The best explanation of this observation is the middle frequency process contains contributions from two different processes, which change relative importance with temperature. The low frequency process is characterized by C_ω increasing with temperature and decreasing pO_2, and R decreasing with polarisation. This is consistent with the low frequency process being dependent on the vacancy concentration of the oxide electrode materials and/or the extension/broadening of the triple phase boundary zone. As the resistance of the low frequency process also increases with decreasing NO concentration, the process is ascribed to a NO_x specie (NO or NO_2) which is adsorbing, diffusing on the surface or participating in charge-transfer related processes at or near the triple phase boundary. The presence of such a process on perovskite/CGO10 electrodes is in good agreement with previous findings in our group[36, 113].

8.5.2 Processes on impregnated electrodes

The impedance spectra recorded on the BaO-impregnated cell stacks are dominated by three processes. The high frequency process shares several characteristics with the high frequency process observed on the non-impregnated cell stack, namely summit frequency range, a C_ω around $1 \cdot 10^{-7}$ F/cm^2 and lack of dependency on gas composition. Therefore the high frequency arc is ascribed to the same process, as it also seems reasonable the process related to transfer of oxygen

ions/intermediates between the perovskite and the electrolyte, should be visible for both non-impregnated and impregnated cell stacks. However, Figure 55 showed the resistance of the high frequency process is consequently lower for the impregnated stacks. The decrease in the resistance could be related to the profound microstructural changes observed in the BaO impregnated electrodes observed in Figure 60. The characteristics of the middle frequency arc are C_ω increasing with temperature and decreasing with decreasing pO_2, while R decreases with polarisation. The difference in characteristics between the non-impregnated and BaO-impregnated samples makes it less probable the middle frequency process is the same on the two different kinds of cell stacks. Due to the dependency on temperature and polarisation the middle frequency process on the BaO-impregnated stacks is likely due to a triple phase boundary related process, but exactly which process and which species are involved cannot be determined from the available data. Finally the low frequency process on the BaO-impregnated sample show almost identical characteristics with the low frequency process on the non-impregnated cell stack, the one exception being on the BaO-impregnated sample the C_ω also depend on the pNO. Due to the similar characteristics the process is for the BaO-impregnated cell stack also ascribed to triple-phase boundary related adsorption, diffusion and/or charge transfer involving NO or NO_2. However, an important difference between the non- and BaO-impregnated samples is the resistance of the process is much smaller on the BaO-impregnated samples, for instance at 500 °C approximately an order of magnitude smaller compared to the non-impregnated sample. The difference in the low frequency arc resistance to a large extent explains the decreased resistance in the low frequency region of the impregnated samples observed in Figure 56. It is suggested the decreased resistance of the low frequency process is due to NO/NO_2 getting adsorbed on the BaO in the form of $Ba(NO_3)_2$ rather than getting adsorbed on the LSM15 and/or CGO10 as in the non-impregnated cell stack. The implication of the difference in adsorption for the entire electrode process and NO_x-reduction will be discussed in the next section.

8.5.3 Effect of BaO-impregnation on electrode processes and NO_x conversion

In the previous two sections the electrode processes on the non-impregnated and the BaO-impregnated cell stacks were identified and compared and it was suggested the difference in electrode processes in 1000 ppm NO + 10% O_2 could be explained by NO_x adsorbing either directly on the LSM15-CGO10 or on the BaO. From FTIR studies of NO_x adsorption it is known that NO_x at

higher temperatures is adsorbed in the form of NO_3^-, and that the NO_3^- formation is preceded by either NO/O_2 co-adsorption or NO_2 formation and subsequent adsorption, these observations has been made both on CGO10/ceria[116] and perovskites[142]. Moreover it was shown in the work by Werchmeister et al. that NO_2 is an important reaction intermediate in electrochemical deNO_x[36, 38], considering the findings from FTIR studies this is likely because NO_2 must be formed before adsorption/formation of nitrate on the electrode surface can occur, a step which necessarily must preceed the electrochemical reduction. Formation of NO_3^- from NO_2 requires an O^- specie according to the reaction scheme $NO_2+O^- \rightarrow NO_3^-$ (or presence of an adsorbed O-atom and an electron). For the non-impregnated electrode two of the identified processes were one related to O_2 adsorption and dissociation (Process 2) and one related to NO_x adsorption/diffuse/charge transfer at the triple phase boundary (Process 3). This is in very good agreement with the expected mechanism, were O^-/O(ads) needs to be formed (corresponding to Process 2), before NO_3^- can be formed and react in the triple phase boundary region (corresponding to Process 3). With respect to adsorption of NO_x on BaO and formation of $Ba(NO_3)_2$, this process has been shown by FTIR to proceed fastest with NO_2[117] even though the exact mechanism of $Ba(NO_3)_2$ formation is still under discussion[69-71]. The reaction scheme for $Ba(NO_3)_2$ formation with NO_2 is BaO + 2 NO_2 + ½ $O_2 \rightarrow$ $Ba(NO_3)_2$ and in NSR catalysis this storage process takes place without involving any electrochemical steps. It is suggested that during electrochemical deNO_x the NO_x storage process also takes place without involving any electrochemical steps. This is supported by the fact that the polarisation resistance on the impregnated cell stack show no dependency on O_2 adsorption and dissociation related processes. By combining the results from the impedance analysis with the observation from the conversion measurements, which showed increased NO_x conversion on BaO impregnated cell stacks, it becomes likely that the increased NO_x conversion at least to some extent is due to the adsorption on BaO rather than on LSM15-CGO10, which establishes an easier reaction path for the electrochemical reduction of NO_x in the cell stacks. The suggestion, that the NO_x adsorption on the BaO impregnated cell stack proceeds via a route only dependent on O_2(g) and not electrochemically enhanced O_2 adsorption/dissociation, does however not explain the increased NO_x conversion in 1000 ppm NO without oxygen. A detailed impedance analysis was not carried out in 1000 ppm NO, as the very low oxygen partial pressure in 1000 ppm NO alters the stochiometry of the oxide electrode materials during time and this instability hinders a reasonable interpretation of the impedance spectra. However, the increased NO_x conversion in 1000 ppm NO

could be explained by the general increase in electrode activity caused by the BaO-impregnation. In the results section it was also shown the BaO-impregnation in general caused an increased electrode activity, as the BaO-impregnation also decreased the polarisation resistance in 10% O_2, which is in agreement with the reportings on BaO-containing cathodes being superior in activity to conventional LSM15 cathodes. Therefore it can from this work be concluded, that impregnation with BaO definitely increases the NO_x-conversion on LSM15-CGO10 cathodes, but whether the increased conversion in 1000 ppm NO + 10% O_2 mainly is caused by a change in adsorption state or by a general increase in electrode activity remains an unanswered question.

8.5.4 Degradation/activation behaviour of cell stacks related to microstructural changes

The SEM images showed profound changes in the microstructure of the BaO-impregnated cell stacks after testing. The microstructure appeared similar between cell stacks even though they degraded/activated differently during testing. Moreover the images clearly showed areas with different microstructure, which were characterized by 1) Round and well-defined particles, 2) "Fluffy" structure and 3) Flake-like particles. Eventually the differences in microstructure could be different stages of the same process going on in the electrodes. A possible explanation of the microstructural changes could be the BaO may react with the electrode materials, LSM15 and/or CGO10, and form new compounds. A possible compound could be $BaCeO_3$ or $BaCe_{1-x}Gd_xO_y$, however it is hard from literature to estimate the risk for $BaCeO_3$ formation. In many studies CGO is used as electrolyte in connection with Ba-containing cathodes and none of the studies report $BaCeO_3$ formation below 900 °C[93-95], however the aforementioned studies only consider the temperature effect on material stability and do not consider the effect of polarisation. With respect to the LSM studies some studies indicate there will be no reaction between Ba-containing compounds and LSM[90, 91] while the work by Yang et al. show Ba diffusing from $Ba_{0.5}Sr_{0.5}Co_{0.8}Fe_{0.2}O_{3-\delta}$ into LSM[92]. In conclusion further microstructural and elemental analysis must be conducted to investigate, if cations have migrated and/or new phases have formed in the BaO-impregnated samples in this work.

8.6 Conclusion

The electrochemical conversion of NO_x on non-impregnated and BaO-impregnated LSM15-CGO10 porous cell stacks has been investigated, and extensive impedance analysis have been performed to identify the effect of the BaO on the electrode processes. Non-impregnated LSM15-CGO10 cell stacks were not capable of converting NO_x into N_2 at any of the investigated conditions (300-500 °C, 3 V-9 V polarisation, 1000 ppm NO or 1000 ppm NO + 10% O_2). In contrast BaO impregnated cell stacks could convert NO_x to N_2, even in the presence of 10% O_2, which shows NO_x conversion can be achieved in an entirely ceramic, noble metal-free electrochemical cell. The NO_x conversion to N_2 on the impregnated stacks was significantly enhanced when the temperature was increased from 300 °C to 400 °C or higher, and when the polarisation was increased from 3 V to 5 V or higher. The impedance analysis revealed that the BaO-impregnation both increased the overall activity of the cell stacks and also changed the adsorption state of NO_x on the electrodes, which of the effects are mainly responsible for the increased NO_x conversion remains unknown. The BaO-impregnated cell stacks showed a profound change in microstructure after testing, the cause of this change needs to be investigated further.

8.7 Acknowledgement

This work was supported by the Danish Strategic Research Council under contract no. 09-065183. Colleagues at the Fuel Cell and Solid State Chemistry Division, Technical University of Denmark, are thanked for help and fruitful discussions.

9 NO_x-conversion on LSM15-CGO10 cell stacks with K_2O impregnation

This chapter deals as the preceding chapter with NO_x conversion on porous LSM15-CGO10 cell stacks. In the preceding chapter the effect of BaO impregnation on the NO_x conversion was investigated, whereas in this chapter the effect of K_2O impregnation is investigated. The effect of the K_2O impregnation is studied in conversion measurements and by means of impedance spectroscopy. Two K_2O impregnated cell stacks were investigated (K1 and K2). Of these two samples, one was used for conversion measurements (K1), while both of them were studied by impedance spectroscopy. For comparison results from two tests on non-impregnated LSM15-CGO10 cell stacks (N1 and N2) are also reported. The results from the non-impregnated cell stacks were also reported in the preceding chapter, but are in this chapter repeated to make it easier to identify the effect of the K_2O impregnation.

9.1 Experimental

9.1.1 Cell stack fabrication and impregnation

The LSM15-CGO10 cell stacks described in this chapter were from the same batch as the cell stacks previously described in chapter 8. For this reason the reader is referred to chapter 8 for information regarding the fabrication of the cell stacks. The impregnation of the cell stacks with K_2O was made in the following way: An aqueous solution of 3.1 M KNO_3 (Alfa Aesar) was prepared. The solution also contained 10 wt% P123 (BASF) with respect to the water. The cell stacks were covered with the impregnation solution and placed in a vacuum chamber, which was evacuated to a pressure below 0.1 mbar for approximately 15 s. Excess impregnation solution was wiped of the surface of the cell stack, and thereafter the cells were first heated to 350 °C to decompose the P123. After cool down the cell stacks were reheated to 700 °C to decompose the KNO_3 into K_2O. In principle the decomposition of P123 and KNO_3 could just as well have been performed in one step, simply by heating the cell stacks to 700 °C from the beginning. However at the time of the experiments it was considered to do some experiments in which the KNO_3 was kept as KNO_3 in the cell stacks, which was the reason the heating was split into two steps. The final load of K_2O on the tested cell stacks was 1.6±0.02 wt%.

9.1.2 Electrochemical testing and conversion measurements

The electrochemical testing and conversion measurements performed on the K_2O impregnated cell stacks were essentially the same as described in chapter 8. This means conversion measurements and impedance spectroscopy were made in the temperature range 300-500 °C in atmospheres containing 1000 ppm NO or 1000 pppm NO + 10% O_2. The conversion measurements were made at 3V polarisation and as previously stated only one of the K_2O impregnated cell stacks (K1) was subjected to conversion measurements. The other stack (K2) was subjected to an extensive impedance analysis, including temperature variations, concentration variations and flow variations. For more details on the how the conversion and impedance measurements were performed the reader is referred to chapter 8.

9.1.3 SEM

The K_2O impregnated stacks were investigated in two different ways. In order to enlighten the microstructure of the impregnated K_2O in the electrodes, the cell stacks were simply broken and placed directly in the microscope, whereafter the fractured surface was investigated using the in-lens detector at a low accelerating voltage (3 kV). To investigate the electrode structure on a slightly larger scale the cell stacks were mounted in epoxy, polished and carbon coated prior to a microscopy investigation with the back-scattered detector. The advantage of the latter method is this method makes it possible to study the connection between the electrode grains and the distribution of CGO10 and LSM15 in the electrodes.

9.2 Results

9.2.1 Conversion and current efficiency

On the non-impregnated LSM15-CGO10 cell stack no conversion of NO into N_2 was detected, neither when the cell stacks were supplied with 1000 ppm NO + 10% O_2, nor when the cell stack was supplied with only 1000 ppm NO. On the K_2O impregnated cell stack some conversion of NO to N_2 was observed in 1000 ppm NO when the cell stack was polarised at 3V, see Figure 61, which shows the NO_x conversion and the current efficiency for N_2 formation. Figure 61 shows that both the NO_x conversion and the current efficiency was highest at 350 °C, where the NO_x conversion was 12% and the current efficiency 1.4%.

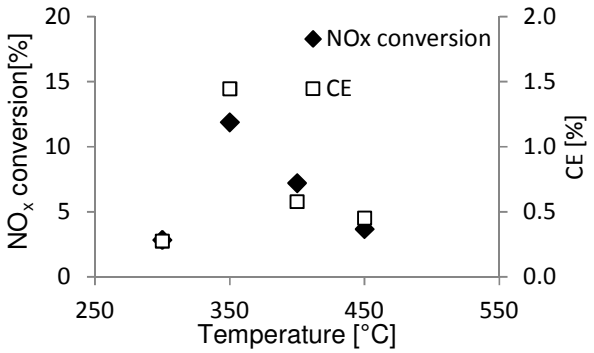

Figure 61. NO_x conversion to N_2 and current efficiency during 3V polarisation in 1000 ppm NO of LSM15-CGO10 cell stack impregnated with K_2O.

When 10% O_2 was present in the atmosphere, no conversion of NO into N_2 was detected. Instead a change was observed in the conversion between NO and NO_2. This can be seen when comparing Figure 62 and Figure 63, which shows the change in NO and NO_2 concentration during polarisation relative to the NO_x concentration before polarisation. On the non-impregnated cell stacks a small amount of NO_2 (arising from the NO + ½ O_2⇆ NO_2 equilibrium) is converted to NO during polarisation, whereas on the K_2O impregnated cell stack, a small amount of NO is converted to NO_2 during polarisation.

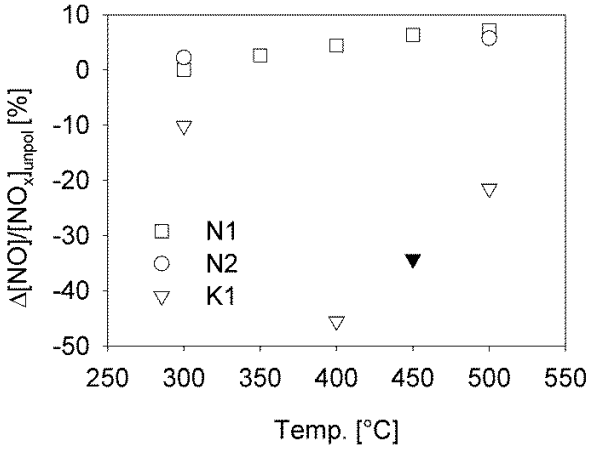

Figure 62. Change in NO concentration during 3V polarisation in 1000 ppm NO + 10% O_2 relative to the NO_x concentration before polarisation. N1 and N2 are non-impregnated LSF15-CGO10 cell stacks while K1 is impregnated with K_2O. Negative values mean NO is removed while positive values mean NO is formed. The data point marked by a filled triangle was by mistake recorded at only 1.5V polarisation.

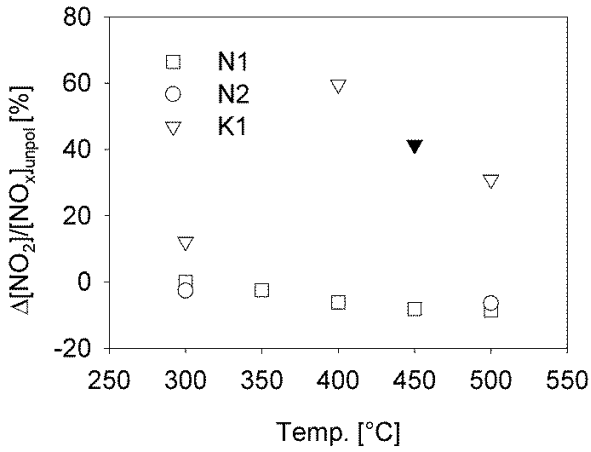

Figure 63. Change in NO_2 concentration during 3V polarisation in 1000 ppm NO + 10% O_2 relative to the NO_x concentration before polarisation. N1 and N2 are non-impregnated LSF15-CGO10 cell stacks while K1 is impregnated with K_2O. Negative values mean NO_2 is removed while positive values mean NO_2 is formed. The data point marked by a filled triangle was by mistake recorded at only 1.5V polarisation.

9.2.2 Impedance results

9.2.2.1 Serial and polarisation resistances

Impedance spectra were recorded in 1000 ppm NO + 10% O_2 in the temperature range 300-500 °C. The serial resistance (R_s) and polarisation resistance (R_p) determined from the impedance spectra are stated in Table 29. As observed in Table 29, good reproducibility was obtained for the two non-impregnated cell stacks, both with respect to R_s and R_p, even though one of the non-impregnated stacks (N2) consistently had a slightly lower R_p compared to the other one. Moreover both the non-impregnated cell stacks showed activation and/or improved electric contact during the cell test, which resulted in a decrease of both R_s and R_p, which is observed when the values at 300 °C in the beginning and the end of the cell tests are compared. The two K_2O impregnated stacks behaved much different from the non-impregnated cell stacks, as the K_2O impregnated stacks had a lower R_s and especially a much lower R_p. In addition to this the two K_2O impregnated stacks differed significantly from each other. First of all the K1 stack in general had a much lower R_p compared to the K_2 cell stack. Secondly the impregnated cell stacks behaved differently during the test when the temperature was increased. Whereas the K_2 stack, which was not subjected to longer conversion/polarisation experiments, showed a decrease in both R_s and R_p with increasing temperature as expected, the K1 cell stack showed an increase in R_s in the temperature range 400-500 °C and a more or less constant R_p in the temperature range 350-500 °C. It is believed the difference in the initial performance between the impregnated cell stacks is due to an inadequate reproducibility of the impregnation step. The difference in behaviour during the cell test was likely caused by the one stacks being subjected to polarisation while the other was not. The difference in degradation behaviour will be discussed further in the discussion section, where also the difference between the non-impregnated and the impregnated cell stacks will be discussed.

Table 29. Serial resistance (R_s) and polarisation resistance (R_p) of non-impregnated (N1, N2) and K_2O impregnated LSF15-CGO10 cell stacks in 1000 ppm NO + 10% O_2. The bottom line labelled 300(post) states the resistance at 300 °C at the end of the test.

	$R_s[\Omega cm^2]$				$R_p[\Omega cm^2]$			
Temp.	N1	N2	K1	K2	N1	N2	K1	K2
300	66	68	31	48	47000	45000	86	1800
350	25	20	6	10*	19000	12000	54	880*
400	9	9	7	6*	6100	4100	65	450*
450	6	5	16	4*	2400	980	53	220*
500	5	4	20	3	920	480	63	180
300(post)	48	48	35	42	26000	25000	117	880

* For all the measurements the temperature was the stated temperature with a deviation less then 2 °C. The one exception is the values labelled with an asterisk, where the exact temperature due to a poor temperature control was 355, 408 and 461 °C at 350, 400 and 450 °C respectively.

9.2.2.2 Characterization of processes

One of the aims by recording impedance spectra during the cell stack test was to use the impedance spectra to identify the processes contributing to the polarisation resistance in 1000 ppm NO + 10% O_2. However, as explained in the previous section on serial resistance and polarisation resistance, the K_2O impregnated cell stack subjected to polarisation during testing degraded heavily, and furthermore the two K_2O impregnated stacks showed a quite different initial performance. The heavy degradation on the one stack makes it difficult to use the impedance spectra recorded on this stack in a meaningful study of the electrode processes, and the difference in initial performance raises the question whether electrode processes identified on the less degrading cell stack (K_2) also are descriptive for the electrode processes occurring on the other cell stack. The latter question cannot be answered before more experiments have been performed on LSM15-CGO10 cell stacks with K_2O impregnation.

As a starting point an attempt to identify the processes occurring on the one K_2O impregnated cell stack (K2) will be made, and the reader should bear in mind, that this identification is based on one test only. The identification is based on impedance spectra recorded during temperature

variations, during variations in the NO and O_2 concentrations and during flow variations. First of all temperature variations were made in the interval 250-500 °C, and impedance spectra were recorded for each 25 °C in 1000 ppm NO + 10% O_2. The recorded impedance spectra were deconvoluted by using the ZView software[107] and an equivalent circuit consisting of a serial resistance and 3-4 RQ elements in series, where R is a resistance and Q is a constant phase element. As illustrated in Figure 64 a change of slope was observed in the Arrhenius plot for both the serial resistance and the resistance of the low frequency arc/arc4 between 325 °C and 350 °C. This temperature interval covers the melting point of KNO_3 (mp= 334 °C[97]) and the results thus indicate, that presence of molten KNO_3 alters the current path through the cell stack and the electrode processes. The concentration and flow variations were made at 400 and 500 °C, and the results obtained during these variations are thus descriptive for processes occurring above 350 °C. However, as indicated in Figure 64 different processes may have dominated the impedance spectra below 350 °C.

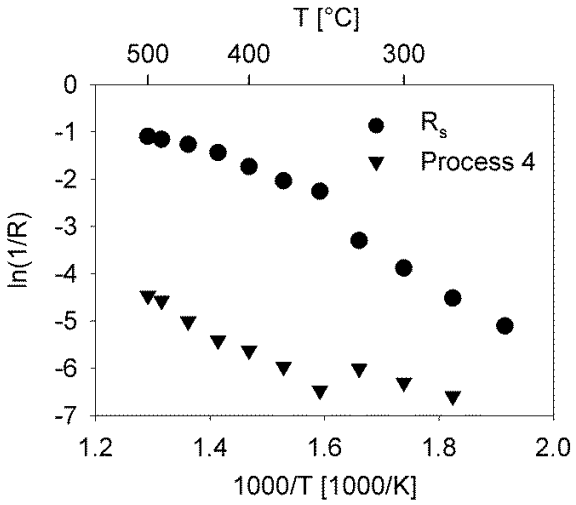

Figure 64. Arrhenius plot showing the serial resistance and resistance of low frequency Arc/Arc4 of K_2O impregnated LSM15-CGO10 cell stack (K2).

In the temperature range 350 °C-500 °C the impedance spectra were in general fitted with a serial resistance and 4 RQ elements. Each of the RQ elements is assumed to describe a physical process in the stack. No effect of flow variations from 2 L/h to 2.5 L/h and 3 L/h was observed on any of the electrode processes. In contrast, changing the NO concentration and the oxygen concentration had a significant effect on the resistance and the C_ω of several of the electrode processes. The characteristics of each of the four identified processes are collected in Table 30 and in the discussion section these processes will be discussed in further detail. A representative impedance spectrum recorded in 1000 ppm NO + 10% O_2 at 400 °C is shown in Figure 65.

Table 30. Characteristics of processes on K_2O impregnated LSM15-CGO10 cell stacks (K_2) in the temperature range 400-500 °C.

Proces	Freq. range	Charactistic
1	2000-130000	- C_ω temperature independent - R dependent on pO_2 and pNO (increase with decreasing pO_2/pNO)
2	200-400	- C_ω increases with temperature from 350 °C
3	0.2-3	- C_ω increases with temperature from 350 °C - R dependent on pO_2 and pNO (increase with decreasing pO_2/pNO) - C_ω dependent on pO_2 (decrease with decreasing pO_2) - C_ω dependent pNO (increase with decreasing pNO)
4	0.01-0.03	- C_ω increases with temperature from 350 °C - R dependent on pO_2 and pNO (decrease with decreasing pO_2/pNO) - C_ω dependent on pO_2 (increase with decreasing pO_2) - C_ω dependent pNO (increase with decreasing pNO)

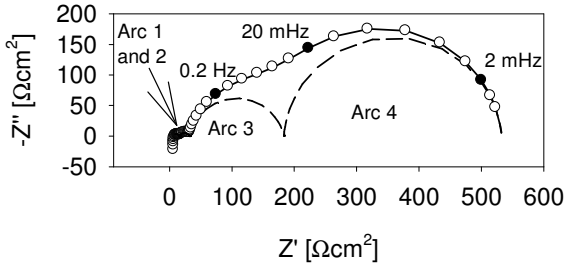

Figure 65. Example of impedance spectrum recorded at 400 °C in 1000 ppm NO + 10% O_2 on a K_2O impregnated cell stack.

9.2.3 SEM

SEM images were recorded with the in-lens detector on cell stacks just broken and placed directly in the microscope, in order to study the microstructure of the impregnated K_2O. In Figure 66a the microstructure of the K_2O-impregnated electrodes before test is shown, and appears to be dominated by many irregular K_2O crystals which lies higgledy-piggledy in the electrode. After testing the electrode appear much different, as the electrode grains now appear covered in a thin, snowlike layer, as observed in Figure 66b.

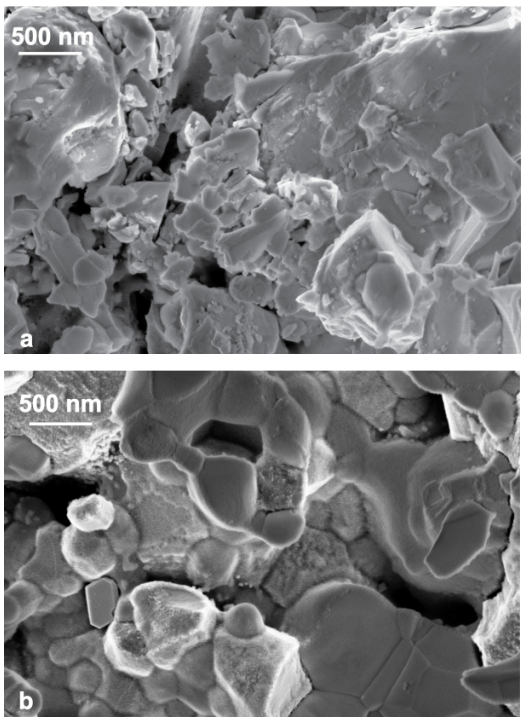

Figure 66. Microstructure of the electrode in a K_2O impregnated LSM15-CGO10 cell stack a) before test and b) after test

To survey the connection between the electrode grains and distribution of LSM15 and CGO10 in the electrodes images were taken with the backscattered detector on epoxy mounted samples, the images are shown in Figure 67. Figure 67a and Figure 67b shows images recorded on a non-impregnated electrode before and after test. In Figure 67c and Figure 67d the images of a K_2O impregnated electrode before test and after test are shown respectively. Finally Figure 67e shows the microstructure of an K_2O impregnated electrode only subjected to EIS testing, which means the electrode has experienced the same temperature profile as the electrode shown in Figure 67d,

but has only been subjected to low polarisation, namely 36 mV rms across the entire cell stack during recording of the EIS. On the non-impregnated electrode and the K_2O impregnated electrode before test the electrode appear to be dominated by the LSM15 phase (dark grey) with the CGO10 phase (light grey) in between. When the electrode microstructure on the K_2O impregnated sample before test is compared to after test a significant change in the connection between the electrode grains appear. Before testing all the electrode grains appeared very well connected while after testing the electrode grains appear separated from each other (Figure 67d). The separation of electrode grains appear for both the LSM phase and the CGO phase, the reason for this change in microstructure will be further discussed in the discussion section.

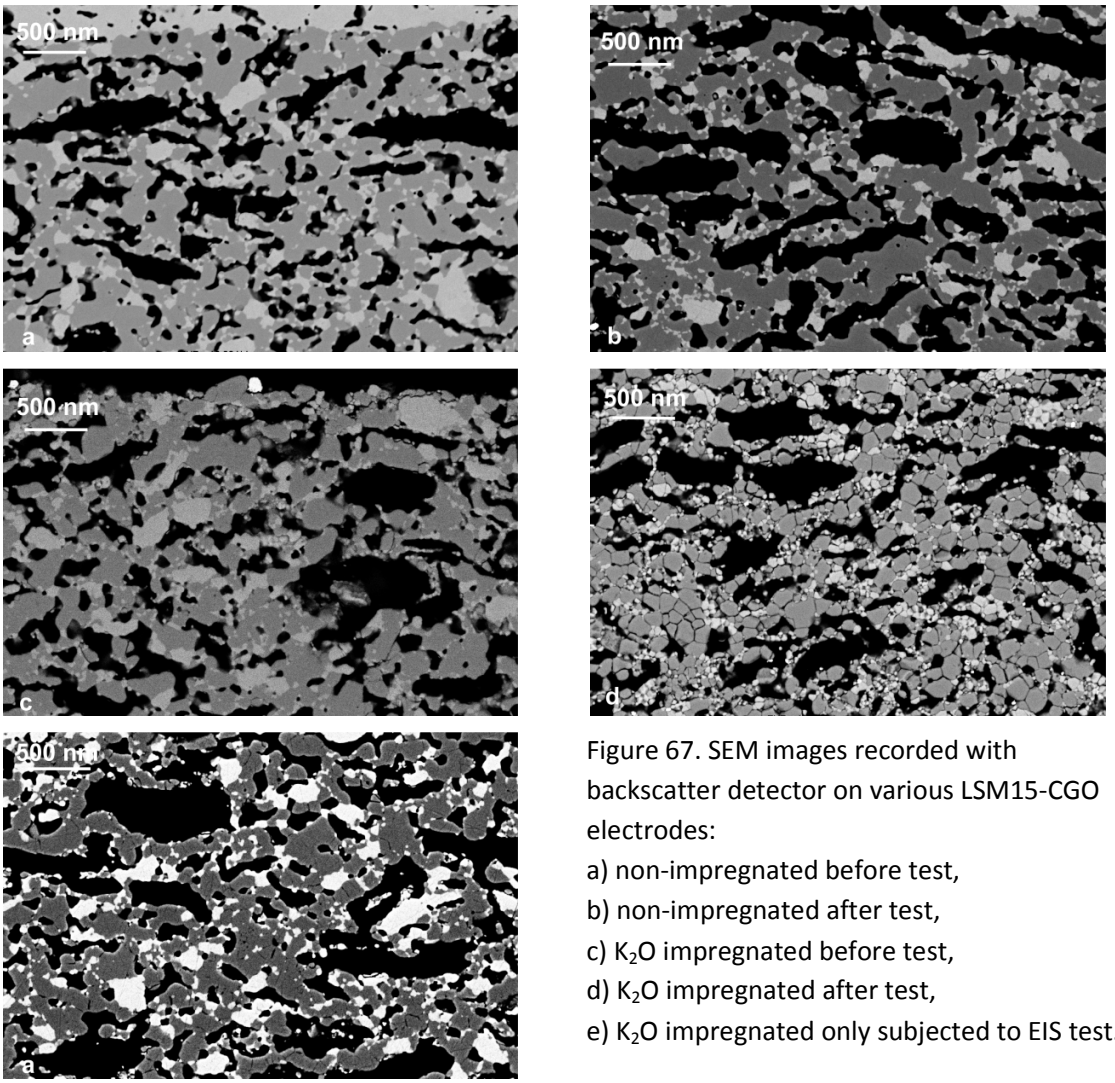

Figure 67. SEM images recorded with backscatter detector on various LSM15-CGO electrodes:
a) non-impregnated before test,
b) non-impregnated after test,
c) K_2O impregnated before test,
d) K_2O impregnated after test,
e) K_2O impregnated only subjected to EIS test.

9.3 Discussion

9.3.1 Identification of electrode processes

On the non-impregnated LSM15-CGO10 cell stacks the polarisation resistance was in the preceding chapter 8 determined to be dominated by three different processes in 1000 ppm NO + 10% O_2. At the highest frequencies of the impedance spectra a processes related to oxygen ion transfer between the LSM and the CGO and possibly through the CGO was identified. Around the middle frequencies a process related to oxygen adsorption/dissociation was identified, and finally at the lower frequencies a process related to adsorbtion, surface diffusion and/or charge transfer related processes involving a NO_x species was identified.

On the K_2O impregnated cell stack four different processes were identified and characterised at 400 and 500 °C. The characteristics of these four processes were listed in Table 30, in general the impedance spectra were entirely dominated by the two processes located at the lower frequencies, while the two processes locate in the high frequency end only constituted a smaller part of the entire polarisation resistance, which is also illustrated in the impedance spectra in Figure 65.

The process located at the highest frequencies (Process 1) had a temperature independent C_ω around $1 \cdot 10^{-7}$ F/cm^2. This value would at first hand fit well with the process related to oxygen ion transfer in the electrode materials[36, 54, 166], which was also identified in the high frequency end of the impedance spectra for the non-impregnated cell stack. However, as stated in Table 30 the resistance of the high frequency process apparently also depends on both the NO concentration and the O_2 concentration, which is not expected for the oxygen ion transport process[36, 54]. A contradistinction for the interpretation of the high frequency process thus exists between the low value of the C_ω indicating an intrinsic oxygen ion transport process, and the dependency on the gas composition indicating a triple phase boundary related process. A possibly explanation could be, that the separation between process 1 and process 2 located at the high frequencies is poor, and characteristics like dependency on gas composition falsely is assigned to process 1 rather than process 2 due to overlap of the two high-frequency processes. To clarify this, further investigations are needed on more K_2O impregnated LSM15-CGO10 electrodes.

With respect to process 2 this process has a C_ω in the range $1\cdot10^{-5}$- $1\cdot10^{-4}$ F/cm^2, which increases with temperature. The range of C_ω is in the low end, but otherwise corresponds well with the capacitances found for oxygen adsorption and dissociation processes on composite electrodes[152]. However, for an oxygen adsorption and dissociation process dependency on the pO_2 is expected[152], which was not observed for arc 2 in this work. The identification of process 2 is due to the limited and contradictory characteristics difficult and further experiments are needed to make identification of this process possible.

The identification of process 3 and process 4 will be discussed together, as the processes share some characteristics. The shared characteristics are C_ω increasing with temperature and increasing with decreasing pNO. The C_w dependency on temperature indicates a broadening of the reactions zone, for instance the TPB, with increasing temperature. The increase in C_ω with decreasing pNO indicates a dependency of both the processes on a NO_x-specie. For process 3 the resistance increases when either the pO_2 or the pNO is decreased, which indicate both O_2 and NO, or similar species, acts as reactants for process 3. With respect to process 4 the resistance also show a dependency on the pNO and the pO_2, but in contrast to process 3 process 4 shows a decrease in resistance when either pNO or pO_2 is decreased. A first thought would be that NO or O_2 species act as inhibitors for process 4, but since NO/O_2 are the only possible reactants in the gas, it seems unlikely they both should act as inhibitors for a process, in which at least one of them is expected to participate. In conclusion, both process 3 and process 4 show a strong dependency on the gas composition, both with respect to the resistance and the C_ω, which indicate the processes are related to adsorption, surface diffusion and/or charge transfer processes in the TPB region.

To summarize, the polarization resistance of the non-impregnated cell stacks was due to 3 processes: oxygen ion transport, O_2 adsorption/dissociation and a TPB process involving a NO_x-specie. On the K_2O impregnated cell stack 4 processes contributed to the polarisation resistance: two small processes located at high frequencies, of which one could be an oxygen ion transport process while the other remained un-identified, and two dominating processes located at lower frequencies, which both were ascribed to TPB related process.

9.3.2 Effect of K_2O impregnation on performance and degradation

As shown in the results section, the non-impregnated cell stacks activated during the test, as R_s decreased by ≈30%, and R_p by ≈45%. The decrease in R_s is explained by improved electric contact, either due to improved attachment of the Au current collector during testing, or due to an improvement in the sintering between the electrode and the electrolyte layers during the test. And improved electric contact through the cell stack will give the same relative decrease in R_p as in R_s[165]. However, as a relatively larger decrease in the R_p is observed, another activation phenomenon only affecting the R_p must have taken place. A suggestion for this activation phenomenon is polarisation induced changes in the electrode microstructure, as this has previously been observed on LSM electrodes, where the mobility of oxygen vacancies and Mn ions were suggested to be main responsible for the activation[58, 59].

When the resistances of the K_2O impregnated cell stack not subjected to polarisation experiments is compared to the resistances of the non-impregnated cell stack, the K_2O impregnated cell stack appear to have both lower R_s and significantly lower R_p. The lower R_s could above 350 °C be explained by the current through the cell stack to some extent passing through the molten KNO_3, as molten KNO_3 has a significantly higher conductivity ($\rho(KNO_3)$=0.699 S/cm at 350 °C [164]) compared to CGO(ρ(CGO)=0.001 S/cm at 350 °C [68]. The K_2O impregnated cell stack subjected to polarisation experiments showed a clear degradation with respect to both R_s and R_p. The SEM images of this cell stack showed after testing a profound breakdown of the electrode microstructure of the outer electrodes in this cell stack. As this breakdown was not observed neither on the non-impregnated cell stacks, nor on the K_2O impregnated stacks not subjected to polarisation, the breakdown must be due to the combination of K_2O presence in the electrode and polarisation. However exactly how this combination K_2O and polarisation leads to detachment between the LSM and the CGO grains remain an un-answered question.

9.4 Conclusion

The conversion of NO_x on a K_2O impregnated LSM15-CGO10 cell stack was measured, and K_2O impregnation was found to increase the NO_x conversion to N_2 in 1000 ppm NO compared to non-impregnated stacks, while in the presence of 10% O_2 no formation of N_2 could be detected during 3V polarisation on the K_2O impregnated cell stack. In the presence of 10% O_2 the K_2O impregnation did however change the conversion between NO and NO_2. Furthermore, impedance spectroscopy was applied on the tested stack and another similar stack to investigate how the K_2O impregnation altered the electrode processes compared to the processes on the non-impregnated stacks. The K_2O impregnation led to a significant reduction in the polarisation resistance, and electrode processes occurring in the TPB zone appeared to have been significantly altered by the impregnation. The K_2O impregnation did also cause severe degradation problems in the cell stacks when they were polarised, which led to a remarkable breakdown of the electrode microstructure of the K_2O impregnated cell stack.

10 Measurements on LSM15-CGO10 electrodes in a 3-electrode set-up.

10.1 Introduction

As described in the experimental chapter (chapter 3), the most detailed electrode studies can be made in a 3-electrode set-up, due to the presence of one single working-electrode in the set-up in combination with a reference electrode with a well-defined potential. For this reason CGO 3-electrode pellets were prepared with non-impregnated and BaO-impregnated LSM15-CGO10 working electrodes and tested in the 3EP set-up described in the experimental chapter. The aim of doing this was to complement the work on symmetric cells and porous cell stacks described in the previous chapters. In this chapter the initial results from testing of a non-impregnated and BaO-impregnated LSM15-CGO10 electrode will be described, the results include conversion measurements, cyclic voltammetry and impedance analysis.

10.2 Experimental

10.2.1 Preparation of CGO-3EP pellets

For preparation of CGO-3EPs low surface area (LSA) CGO10 (Rhodia) was mixed with liquid glycerin (Fluka), stearic acid in solid form (Merck) and polyvinyl butyral (PVB) (Wacker). The weight percentages in the mixture was 93 wt% CGO10, 1 wt% liquid glycerin, 1 wt% stearic acid and 5 wt% PVB. Afterwards ethanol was added to the mixture and the mixture was ball milled for ≈24 h. Following the ball milling the mixture was dried on a hotplate and subsequent crushed to powder with particle size d_{50}=0.5 µm and d_{90}=2 µm in a planetary mill. The powder was pressed into cylinders with diameter 16 mm and height 19 mm first by mechanical pressing at 1 t for 30 s and then by isostatic pressing at 50 tons for 20 s. The CGO cylinders were sintered with the maximum temperature 1500 °C held for 3 hours. After sintering the density of the cylinders was 99% of the theoretical density. Finally the sintered cylinders were shaped into the 3EP form by grinding with diamond tools.

10.2.2 Screen-printing of LSM15-CGO10 electrodes

The LSM15-CGO10 working electrodes were screen-printed on the 3EP exactly like the electrodes were screen-printed on the symmetric cells described in chapter 5 using the same screen printing paste. For this reason the reader is referred to chapter 5 section 5.3.1 for information regarding the fabrication of the screen printed electrodes.

10.2.3 Impregnation with BaO

For impregnation with BaO an aqueous 0.3 M solution of $Ba(NO_3)_2$ (Merck) was prepared. The screen-printed electrode on top of the CGO-3EPs was immersed into the $Ba(NO_3)_2$ solution, while the remainder of the 3EP was kept of the solution. The electrodes/3EPs were subjected to vacuum for 10 s and wiped dry. Finally the impregnated $Ba(NO_3)_2$ was decomposed to BaO by heating to 700 °C for 1 h. This procedure was repeated 3 times.

10.2.4 Electrochemical characterization and conversion measurements

The 3EP was mounted in the 3EP test set-up as described in chapter 3. The set-up was heated to 700 ° for one hour to tighten the Ag sealings whereafter the temperature was decreased and the experiments performed in the temperature range 450 °C-650 °C. This temperature range, which is higher than the temperature range 300-500 °C used in the symmetric cell and porous stack tests, had to be chosen, since below 450 °C the resistance of the CGO 3EP was too high to perform any experiments. The experiments performed were polarisation/conversion experiments, cyclic voltammetry and impedance measurements; all performed by use of a Gamry Ref 600 potentiostat. The polarisations were performed at -0.6 V polarisation for 2 h in 1000 ppm NO and 1000 ppm NO + 10% O_2, while the NO, NO_2 and NO_x concentration was monitored with a chemiluminscence detector (ThermoScientific). The cylic voltammetry was performed in the range ± 0.8 V, at various sweep rates within the range 1-100 mV/s. Impedance spectra were recorded in the frequency range 1 MHz-0.001 Hz with 36 mV rms amplitude and 6 points pr. decade.

10.3 Results

10.3.1 Conversion

Conversion measurements were made by monitoring changes in the gas composition during 2 h polarisation at -0.6 V. In Figure 68 and Figure 69 the conversion is stated for the non-impregnated and BaO-impregnated electrodes respectively, the conversion is stated relative to the NO_x-

concentration measured before the polarisation. For both the non-impregnated and the BaO-impregnated electrode a total NO_x-conversion in the range 60-80% is observed without a clear dependency on temperature. The NO_2 conversion stays within 10-20% in the entire temperature range. On both electrodes the NO conversion apparently increases with temperature, with a jump in the NO conversion between 550 and 600 °C on the non-impregnated sample as the one exception. Impedance spectra recorded before and after each polarisation yielded no information on why a jump was observed in the conversion from 550 °C to 600 °C on the non-impregnated electrode.

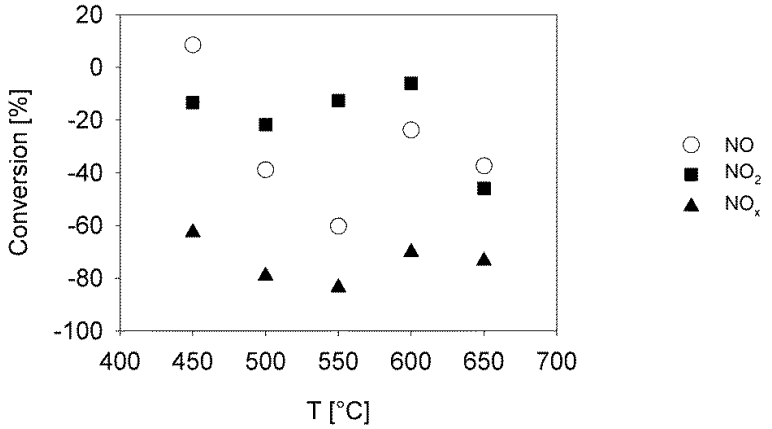

Figure 68. Conversion on non-impregnated LSM15-CGO10 electrode during 2 h polarisation at -0.6 V in 1000 ppm NO.

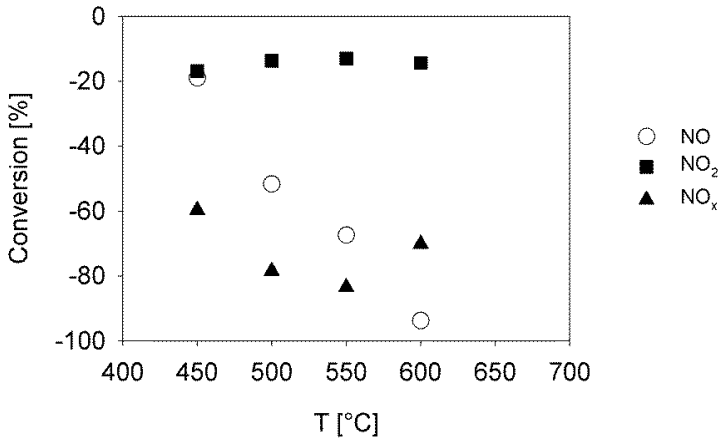

Figure 69. Conversion on Ba-impregnated LSM15-CGO10 electrode during 2 h polarisation at -0.6 V in 1000 ppm NO.

In the presence of 10% O_2 NO_x conversion in the range 1-4% was observed on both the non-impregnated and the BaO-impregnated electrode. Such low conversions are considered below the uncertainty of the experiments, and thus in reality no NO_x conversion was observed in the presence of 10% O_2 at -0.6V polarisation.

In addition to the just described conversion measurements during 2 h of constant polarisation, short "conversion" experiments under variable polarisation were also conducted, as the gas composition was analysed during recording of CVs at various sweep rates (1 mV/s, 5 mV/s, 10 mV/s, 15 mV/s, 50 mV/s and 100 mV/s). For high sweep rates (50 mV/s and 100 mV/s) the concentration changes were too fast for the CLD to detect, but at the lower sweep rates concentration changes during cathodic and anodic sweeps could clearly be distinguished. Exactly the same tendencies with respect to conversion of NO and NO_2 was observed on the non-impregnated and the BaO-impregnated electrode, even though at 450 °C the non-impregnated electrode performed slightly better, i.e. caused the largest concentration changes, compared to the BaO-impregnated electrode, while at 650°C the BaO-impregnated cell stack showed the best performance. In Figure 70 to Figure 73 the changes in NO, NO_2 and total NO_x concentrations are illustrated for the BaO-impregnated electrode, as explained the same tendencies were observed on the non-impregnated sample. In 1000 ppm NO at 450 °C (Figure 70) it is observed how the cathodic polarisation to -0.8V is not enough to reduce the NO_x to N_2, while the anodic polarisation to +0.8V is sufficient polarisation for oxidation of NO to NO_2. At 650 °C in 1000 ppm NO (Figure 71) oxidation of NO to NO_2 is again observed during the anodic sweep, and during the cathodic sweep the polarisation to -0.8V has now become enough to reduce the NO_x into N_2. In the presence of 10% O_2 at 450 °C (Figure 72), NO_2 is reduced to NO during the cathodic sweep, and during anodic sweep the reverse process is going on: NO is oxidized to NO_2. This is also observed in the presence of 10% O_2 at 650 °C (Figure 73), only is the amount converted at this temperature very small, indicating the majority of the current is used for O_2 reduction/O^{2-} oxidation.

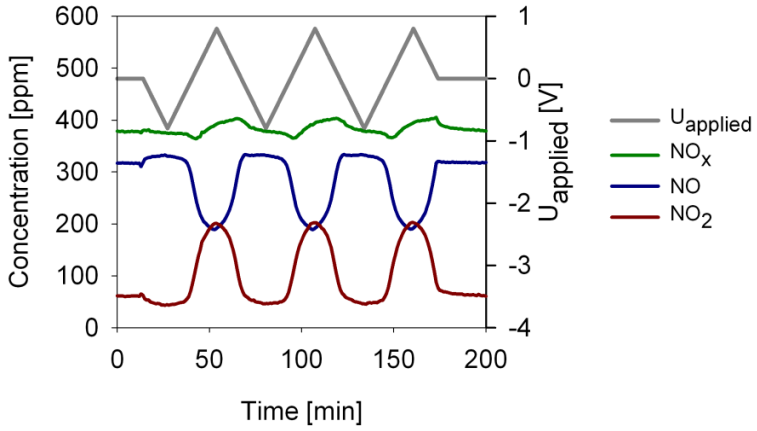

Figure 70. Concentration changes in NO, NO_2 and NO_x during cyclic voltammetry at ±0.8V, sweep rate 1 mV/s in 1000 ppm NO at 450 °C on BaO-impregnated electrode.

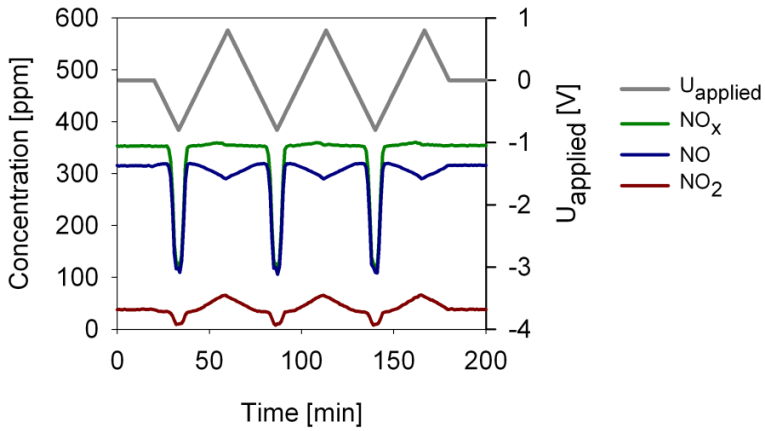

Figure 71. Concentration changes in NO, NO_2 and NO_x during cyclic voltammetry at ±0.8V, sweep rate 1 mV/s in 1000 ppm NO at 650 °C on BaO-impregnated electrode.

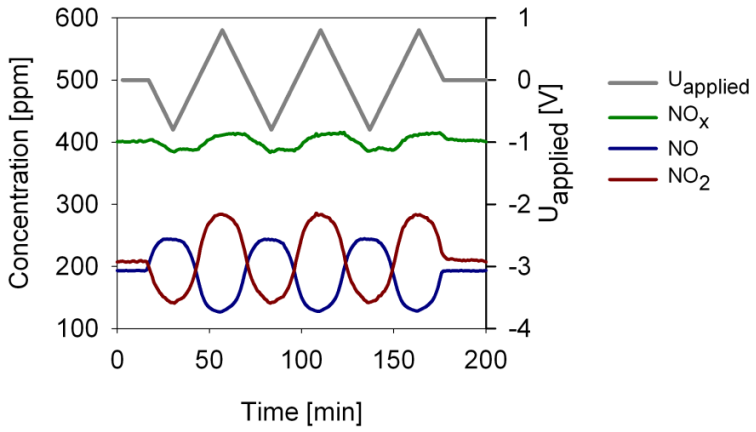

Figure 72. Concentration changes in NO, NO_2 and NO_x during cyclic voltammetry at ±0.8V, sweep rate 1 mV/s in 1000 ppm NO + 10% O_2 at 450 °C on BaO-impregnated electrode.

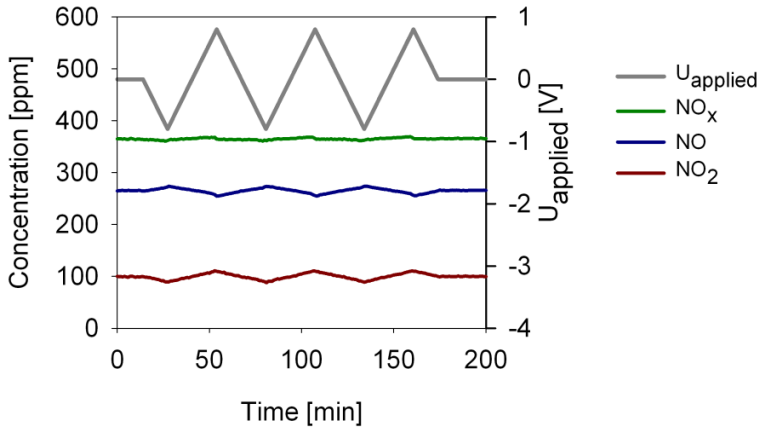

Figure 73. Concentration changes in NO, NO_2 and NO_x during cyclic voltammetry at ±0.8V, sweep rate 1 mV/s in 1000 ppm NO + 10% O_2 at 650 °C on BaO-impregnated electrode.

10.3.2 Cyclic voltammetry

Cyclic voltammograms were recorded between the voltage limits ±0.8V. Even though the potential applied ($U_{applied}$) was ±0.8V the electrode potential ($U_{electrode}$) would differ from $U_{applied}$ due to the potential drop through the thick CGO10 3EP. Theoretically $U_{electrode}$ may be calculated according to equation 10.1:

$$U_{electrode} = U_{applied} - R_s I \qquad 10.1$$

- In which R_s is the serial resistance of the CGO10 3EP. It was attempted to calculate $U_{electrode}$ according to equation 10.1 by using the R_s determined from impedance spectra recorded before and after the cyclic voltammograms. However this led to erroneous results as shown in Figure 74, where it is illustrated how this approach leads to "over-correcting" during the anodic sweep, which after the correction has moved partly to negative polarisations. The over-correction indicates the R_s determined at OCV before the cyclic voltammetry was higher than the actual R_s during the cyclic voltammetry. The R_s decrease during polarisation could be due to resistive heating of the CGO 3EP or an activation phenomenon occurring during polarisation, both possibilities will be discussed further in the discussion section.

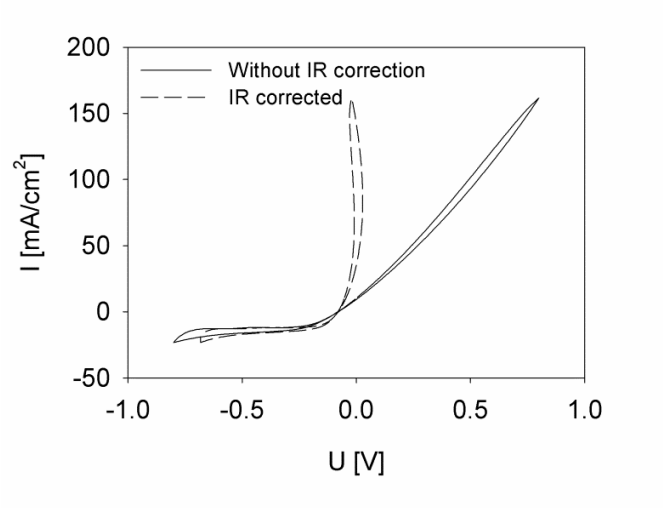

Figure 74. Cyclic voltammogram recorded on BaO-impregnated electrode at 650 °C in 1000 ppm NO at sweep rate 10 mV/s. The cyclic voltammogram without IR correction and with (erroneous) IR correction is shown.

10.3.3 Impedance results

Impedance spectra were recorded on both the non-impregnated and the BaO-impregnated electrode at various conditions. In order to investigate the temperature dependence impedance spectra were recorded in the temperature range 450-650 °C for each 50 °C in both 10% O_2 and 1000 ppm NO + 10% O_2. For a further investigation of the processes contributing to the polarisation resistances impedance spectra were recorded at 450 °C and 650 °C at various concentrations and flow rate: First the NO concentration was varied between 1000 ppm NO, 1500 ppm NO and 2000 ppm NO while the O_2 concentration was fixed at 10%, secondly the O_2 concentration was varied between 10, 5 and 15% while the NO concentration was fixed at 1000 ppm NO, and finally the gas flow rate in both 1000 ppm NO and in 1000 ppm NO + 10% O_2 was varied between 5, 7.5 and 6 ml/min. Furthermore experiments were made during which $U_{applied}$ was increased from OCV to 0.1, 0.2, 0.3, 0.6 and 0.8 V. The impedance spectra recorded were deconvoluted using the Zview2 software[107] and an equivalent circuit consisting of one serial resistance and 3-5 R-CPE elements in series.

10.3.4 General observations

On the non-impregnated electrode the impedance spectra recorded in 10% O_2 at 450 °C are dominated by one single arc, which is slightly distorted in the high frequency part, see Figure 75 for comparison of impedance spectra recorded in 10% O_2 and 1000 ppm NO + 10% O_2. As the temperature is increased from 450 °C to 650 °C, the high frequency part becomes increasingly affected by a capacitive contribution. This capacitive contribution is caused by a large impedance at the reference electrode, and is thus related to the measurement set-up and not working electrode under study[172]. In 1000 ppm NO + 10% O_2 the polarisation resistance at 550 °C and below appear to be significantly smaller compared to in 10% O_2, and furthermore the impedance spectra recorded at 550 °C and below appear to contain contributions from at least two dominating arcs. As the temperature is increased, the impedance spectra recorded in 1000 ppm NO + 10% O_2 become more and more similar to those recorded in 10% O_2, as the polarisation resistances become similar, the spectra appear to be dominated by one arc, and a capacitive contribution in the high frequency becomes visible

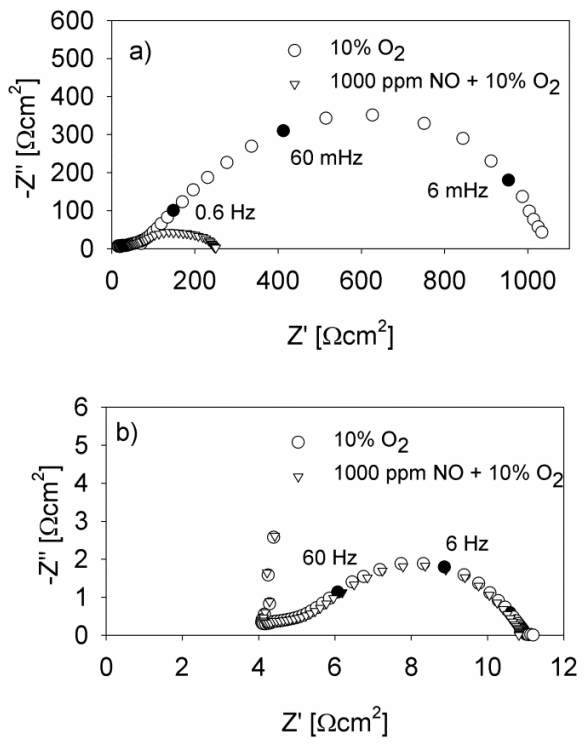

Figure 75. Impedance spectra recorded on non-impregnated LSM15-CGO10 electrode in 10% O_2 or 1000 ppm NO + 10% O_2 at a) 450 °C and b) 650 °C.

For the BaO impregnated electrode the polarisation resistance is first of all significantly lower compared to the non-impregnated electrode, see Figure 76 for a comparison between spectra recorded on the non-impregnated and the BaO-impregnated electrodes at various temperatures. Apart from the difference in total polarisation resistance, many of the tendencies observed on the BaO-impregnated electrodes are similar to the tendencies observed on the non-impregnated electrodes, namely increasing alikeness between the spectra recorded in 10% O_2 and 1000 ppm NO + 10% O_2 with increasing temperature, and the appearance of an capacitive contribution in the high frequency part caused by the measurement set-up. One significant difference is however observed between the non-impregnated and the BaO-impregnated electrodes at 600 and 650 °C, as the high frequency part at these temperatures become dominated by an inductive tail rather than a capacitive contribution, see Figure 76c.

10 Measurements on LSM15-CGO10 electrodes in a 3-electrode set-up.

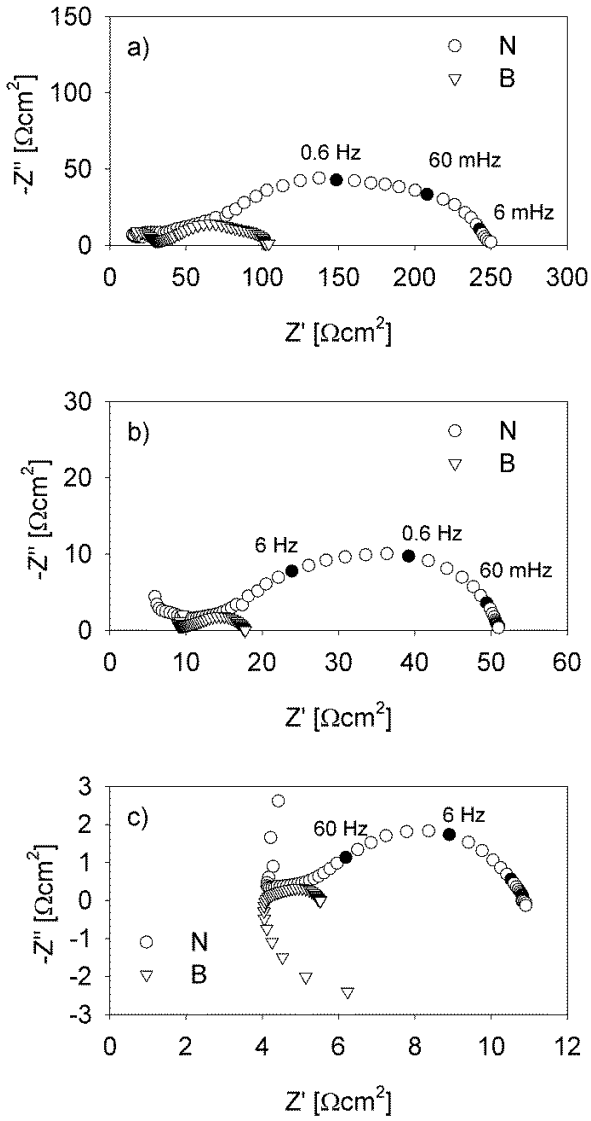

Figure 76. Impedance spectra recorded in 1000 ppm NO + 10% O_2 on non-impregnated (N) and BaO-impregnated (B) electrodes at a) 450 °C, b) 550 °C and c) 650 °C.

10.3.5 Serial resistance and polarisation resistance

The serial resistance obtained from fitting of the impedance spectra recorded in 1000 ppm NO + 10% O_2 and 10% O_2 are shown in Figure 77. Fairly good agreement is obtained for the serial resistances independent of atmosphere and independent of whether the working electrode was impregnated or not. The one exception is the serial resistances obtained in 10% O_2 on the non-impregnated cell stacks, as these values for unknown reasons appear to be slightly lower than the others. Overall, the good agreement between the serial resistances determined indicate, that any differences observed in the polarisation resistances between the non-impregnated and the BaO-impregnated electrodes are due to a difference in electrodes rather than a difference in electric contacting through in the set-up.

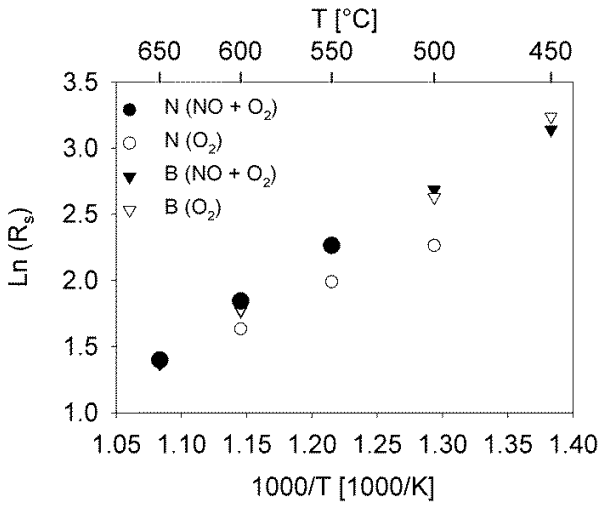

Figure 77. Serial resistance on 3EPs with a non-impregnated (N) and BaO-impregnated (B) working electrode. The values are determined from impedance spectra recorded in 1000 ppm NO + 10% O_2 or 10% O_2 only.

The polarisation resistances for the non-impregnated and the BaO-impregnated electrodes are shown in Figure 78. Clearly the BaO impregnation has caused a general decrease in the polarisation resistance both in 1000 ppm NO + 10 % O_2 and in 10% O_2. Another clear tendency observed in Figure 78 is the polarisation resistance at temperatures ≤550 °C is lower in 1000 ppm NO + 10% O_2 compared to in 10% O_2, whereas above 550 °C the polarisation resistance in the two

different atmospheres become alike. This tendency is observed both on the non-impregnated and the BaO-impregnated electrodes.

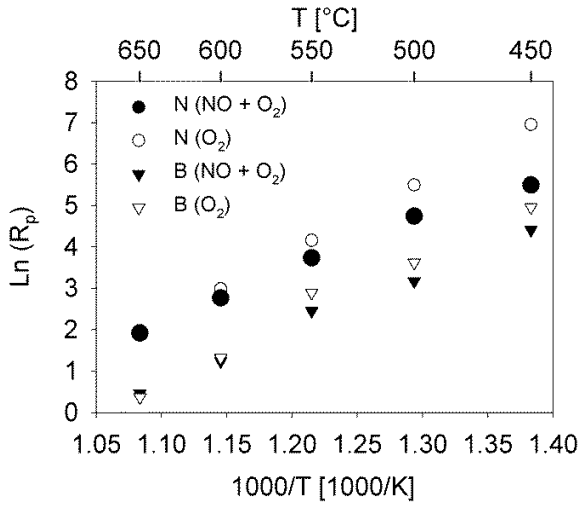

Figure 78. Polarisation resistance on non-impregnated (N) and BaO-impregnated (B) electrodes in 1000 ppm NO +10% O_2 and 10% O_2.

10.3.6 Identification of electrode processes

On the non-impregnated electrodes 4 R-CPE elements were used for fitting of the impedance spectra recorded in 1000 ppm NO + 10% O_2 at 450 °C, indicating that four processes contributed to the polarisation resistance. The fitting of the process located at the highest frequencies was questionable due to distortion of the spectra in this region. The three processes located at the lower frequencies were all similar in size and dominated the impedance spectra, see Figure 79a for an illustration of the deconvolution of an impedance spectra recorded at 450 °C. At 650 °C 4 processes contributed to the polarisation resistance, and of these processes the process located at the lowest frequencies was entirely dominating. A representative example of fitting of the impedance spectra recorded at 650 °C is shown in Figure 79b.

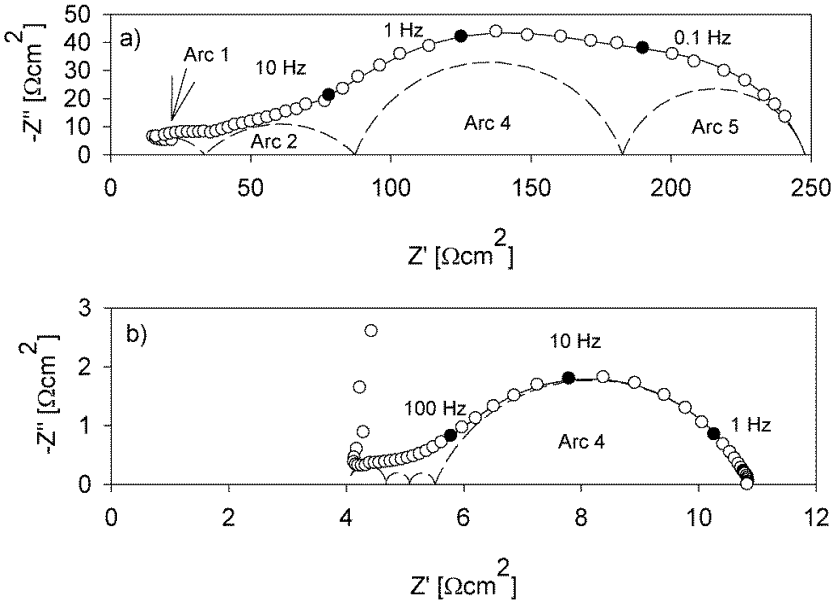

Figure 79. Deconvolution of impedance spectra recorded on non-impregnated electrode in 1000 ppm NO + 10% O_2.at a) 450 °C and b) 650 °C.

As previously explained variations in flow, concentration and polarisation were performed in order to characterize the processes contributing to the polarisation resistance of the electrodes. No effect at all was observed when varying the flow in 1000 ppm NO or 1000 ppm NO + 10% O_2. Furthermore no clear effect on the C_ω's was observed neither when temperature was varied nor while the concentrations were changed. For this reason the characteristics identified and listed in Table 31 are limited to the resistances dependency on concentrations and polarisation. The resistance of the two processes located at the lowest frequencies did at both 450 °C and 650 °C decrease with increasing NO concentration, while only at 650 °C, a decrease in the arc 4 resistance was observed with increasing O_2 concentration. The activation energy of process 4 was calculated to be 0.81 eV in 1000 ppm NO + 10% O_2. The resistance of both arc 2, 3 and 4 changed during polarisation at 450 °C. The effect of the polarisation at 450 °C is illustrated in Figure 80. Fitting of the impedance spectra recorded before and during polarisation showed, that during polarisation at small voltages (0.1V, 0.2V and 0.3V) the resistance of process 3 decreased while the resistance of process 2 and 4 increased, while at higher polarisation (0.6V) the resistances of process 2, 3 and 4 all decreased and the impedance spectra changed shape dramatically, as also evident in Figure 80.

Table 31. Characteristics of processes on the non-impregnated electrodes.

Proces	Freq. range	Characteristic
1	60-300 kHz	
2+3	80-3000 Hz	- R dependent on pNO at 650 °C (decrease with increasing pNO)
		- R dependent on polarisation
4	1-11 Hz	- R dependent on pNO at 450 °C(decrease with increasing pNO)
		- R dependent on pO_2 at 650 °C (decrease with increasing pO_2)
		- R dependent on polarisation
5~	0.07-0.5 Hz	- R dependent on pNO (decrease with increasing pNO)

~only observed at 450 °C

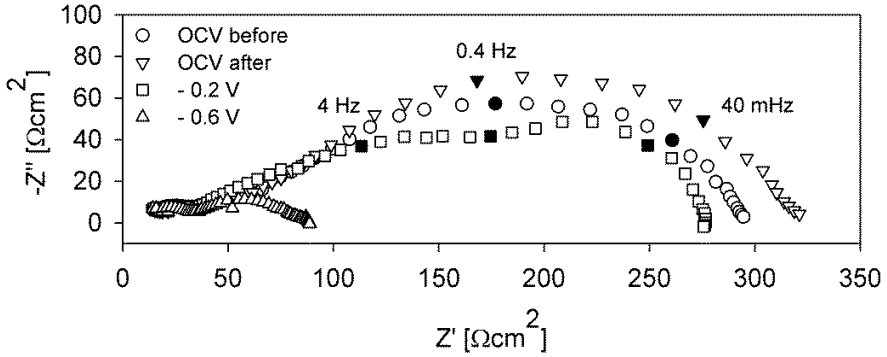

Figure 80. Effect of polarisation on non-impregnated electrode.

For the BaO-impregnated electrodes the impedance spectra recorded at 450 °C were fitted with 5 R-CPE elements, indicating 5 processes contributed to the polarisation resistance. As for the non-impregnated electrode the fitting of the high frequency process was questionable due to a distortion of the spectra in that frequency range. The main contributors to the polarisation resistance was the three processes located at the lowest frequencies, and finally in between the high frequency process and the three low frequency processes a tiny process was located, see Figure 81a for a representative deconvolution of an impedance spectre recorded at 450 °C in 1000 ppm NO + 10% O_2. It should be noted, that even though the arc corresponding to process 2 appears insignificant in size compared to the other arcs, omitting process 2 from the fitting was not an possibility, as this led to a total and unfavourable change in the fit. At 650 °C 4 processes contributed to the polarisation resistance of the BaO-impregnated electrode, 3 of these arcs dominated the impedance spectra; while the last process located at the lowest frequencies only gave a small contribution to the polarisation resistance, see Figure 81b for an example of the deconvolution of an impedance spectra recorded at 650 °C.

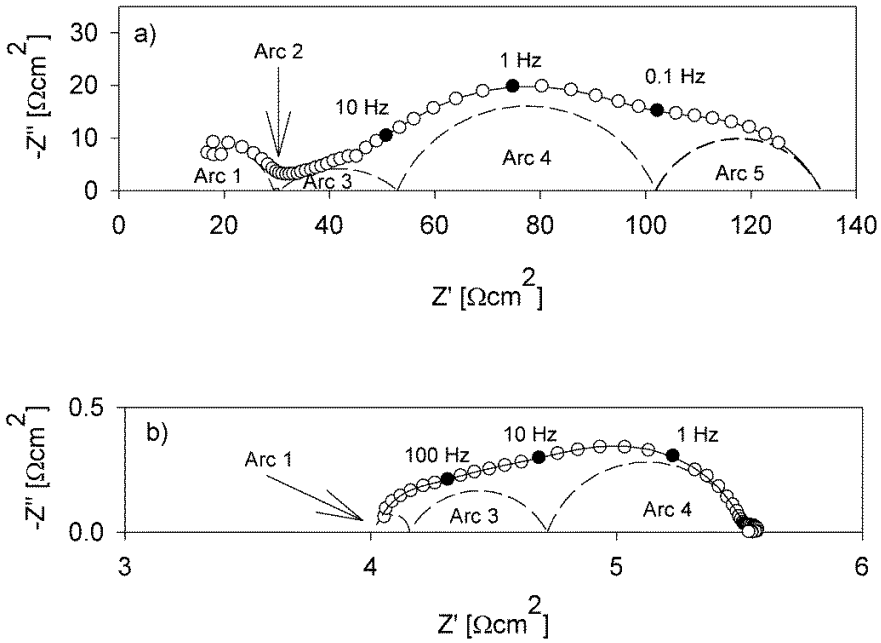

Figure 81. Representative deconvolution of impedance spectra recorded on a BaO-impregnated electrode in 1000 ppm NO + 10% O_2 at a) 450 °C and b) 650 °C.

The characteristics of the electrode processes determined during concentration and polarisation variations are stated in Table 32 and in Figure 82 the effect of polarisation on the impedance spectra is shown. In general, when flow variations were performed no significant changes were observed in the impedance spectra. With respect to the effect of concentration variations, the resistance of process 4 appeared to be the only resistance with a clear dependency on the gas-composition, as the resistance of the process decreased with increasing NO concentration at 450 °C and decreased with increasing O_2 concentration at 650 °C. The activation energy calculated for this process was 1.13 eV. With respect to polarisation some of the processes appeared to be more sensitive towards polarisation than others. At 0.6 V and 0.8 V polarisation the resistance of all the processes decreased, while at lower polarisations (0.1 V, 0.2 V and 0.3 V) only the resistance of process 3 and 5 decreased during polarisation.

10 Measurements on LSM15-CGO10 electrodes in a 3-electrode set-up.

Table 32. Characteristics of processes identified on BaO-impregnated electrodes.

Proces	Freq. range	Characteristic
1	6-25 kHz	- R decreases with polarisation ≥0.6V
2*	4 kHz	
3	0.3-2 kHz	- C_ω dependent on pNO (increase with increasing pNO)
		- R decreases with polarisation
4	2-200 Hz	- R dependent on pNO at 450 °C (decreasing with increasing pNO)
		- R dependent on pO_2 at 650 °C (decreasing with increasing pO_2)
		- R decreases with polarisation ≥0.6V
5’	0.04-60 Hz	- C_ω dependent on pO_2 at 650 °C (increase with increasing pO_2)
		- R decreases with polarisation

* only at 450 °C, ‘ at 450 °C and 650 °C

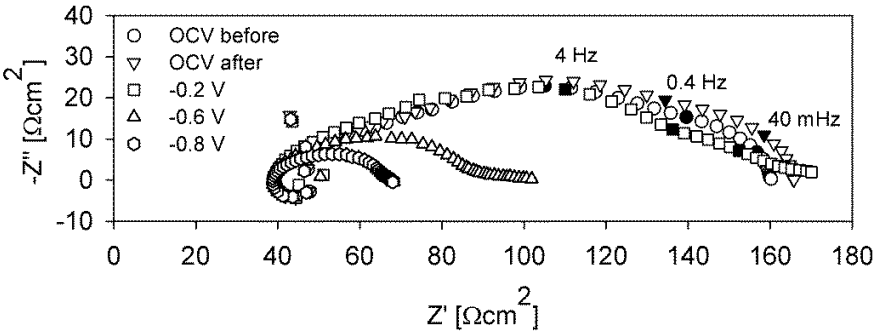

Figure 82. Impedance spectra recorded on BaO-impregnated electrode at OCV and during different polarisations.

10.4 Discussion

10.4.1 Comparison of electrode processes on non-impregnated and BaO-impregnated electrodes

In Table 31 and Table 32 the characteristics of the electrode processes on the non-impregnated and BaO-impregnated electrodes were listed. A common feature for both the non-impregnated and the BaO-impregnated electrodes was process 4 located within the frequency range 1-300 Hz which gave a significant contribution to the polarisation resistance. On both the non-impregnated and the BaO-impregnated electrode process 4 was dependent on the NO concentration at 450 °C and the O_2 concentration at 650 °C and decreased with polarisation. Due to the dependency on gas composition and polarisation, the process is assumed to be due to a dissociative adsorption, surface diffusion or charge transfer at the TPB region, and considering the findings in chapter 8 a first suggestion is the process is due to NO_x adsorption/nitrate formation at the electrode. The fact that process 4 does not depend on the same gas component at 450 °C and 650 °C could at first hand led to the conclusion, that an arc in the impedance spectra falsely had been ascribed to the same process even though the arc in reality was caused by one NO dependent process at 450 °C and a different more O_2 dependent process at 650 °C. To clarify this an Arrhenius plot of the process 4 resistance was made, both with resistances found in 1000 ppm NO + 10% O_2 atmosphere and in only 10% O_2, see Figure 83. On the Arrhenius plot very good linearity is obtained (R^2>0.99) for both kind of electrodes, with the one exception that R^2 in 1000 ppm NO + 10% O_2 on the non-impregnated electrode is only 0.98. This slightly lower R^2 value could indicate a change in the process occurring on the non-impregnated electrode with temperature, but could also just be accidental, considering R=0.98 still is fairly high value. A shift in electrode process with temperature is supported by the finding by Reinhardt et al. that in NO and O_2 containing atmospheres LSM/YSZ electrodes reacts preferably with NO/NO_2 below 650 °C and preferably with O_2 at T≥650 °C[25], which is overlapping with the temperature range used in these experiments. With respect to the BaO-impregnated electrode, no change in process 4 with temperature is observed, as the Arrhenius plot is very linear, and as previously mentioned the characteristic during flow variation and polarisation was very similar for process 4 on both the non-impregnated and the BaO-impregnated electrode. Another clear feature in Figure 83 is the resistance is consequently lower on the BaO-impregnated electrode, both in 1000 ppm NO + 10% O_2 and in

10% O_2 only, the same tendency was observed on the Arrhenius plot of the total polarisation resistance shown in Figure 78, which is consistent with finding in chapter 8 of a general activation of the electrode caused by the BaO impregnation. Finally Figure 83 also show a significant difference in the activation energies for arc 4 on the non-impregnated electrodes (0.81 eV (1000 ppm NO + 10% O_2) and 1.81 eV (10% O_2) whereas on the BaO-impregnated electrodes the activation energies in 1000 ppm NO + 10% O_2 and 10% O_2 are very alike (1.13 eV (1000 ppm NO + 10% O_2) and 1.19 eV (10% O_2)). Further experiments are needed to clarify the reason for this.

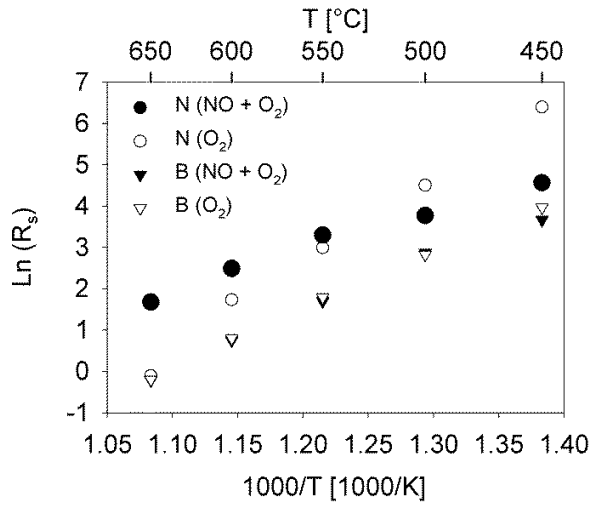

Figure 83. Arrhenius plot of the resistances of process 4 on the non-impregnated and the BaO-impregnated electrode.

With respect to the other processes occurring on the electrodes the characteristics are too few to justify any attempt to identify the processes.

10.4.2 Comparison to conversion on porous cell stacks

The NO_x conversion on the BaO-impregnated LSM15-CGO10 electrodes in the 3EP set-up was 60-80% when the electrode was supplied with 1000 ppm NO in the temperature range 450-650 °C, which is in fairly good agreement with the conversion obtained on the Ba-impregnated LSM15-CGO10 porous cell stacks at similar conditions (see Figure 51 in chapter 8). Surprisingly, the non-impregnated LSM15-CGO10 electrode in the 3EP set-up showed a similar high conversion, while no NO_x conversion was observed on non-impregnated LSM15-CGO10 cell stacks. The difference could be due to the difference in temperature range and flow rate/flow distribution between the

porous cell stack set-up and the 3EP set-up. Furthermore NO_x conversion was observed on the BaO-impregnated porous cell stack in the presence of 10% O_2, which was not observed in the 3EP set-up. Probably this was because the electrode in the 3EP set-up was not polarised enough, but as explained in the following section determining the actual polarisation across the electrode by correcting for the IR drop was problematic in these 3EP experiments.

10.4.3 IR correction

As shown in the Results section IR correction of the cylic voltammograms by means of R_s determined from impedance spectra led to erroneous results. The correction problem occurred on cyclic voltammograms recorded at 650 °C, but not on those recorded at 450 °C. A first possible explanation could be R_s at 650 °C was determined falsely at a too large value, possibly due to the large inductive distortion in the high frequency region of the spectra. However, the inductance of the set-up was determined to 2.2×10^{-6} H, and as this inductance was included in the fitting of the impedance spectra, the R_s of impedance spectra recorded before and after the cyclic voltammegrams was correctly determined. This indicates R_s actually decreased during the cyclic voltammetry/polarisation.

A possible explanation of the decrease in R_s is resistive heating of the CGO 3EP during the polarisation, as resistive heating previously had been observed significantly to affect measurements on YSZ 3EP during polarisation[173]. Unfortunately the temperature of the 3EP could only be measured at OCV, as the probe for temperature measurements was the same probe as used for polarisation of the electrode. The logging frequency of the temperature measurement was once every minute. When the temperature of the 3EP immediately before and immediately after the cyclic voltammetry was compared a temperature difference of maximum 1 °C was observed, which was also the maximum temperature measured before and after the 2 h at constant -0.6V polarisation. If resistive heating is occurring in the 3EP during polarisation it cannot be a dramatic heating, since the 3EP apparently cooled down to the furnace temperature within 1 minute after the polarisation was removed, which questions resistive heating as an explanation of the R_s decrease. An argument against resistive heating is also the problem with overcorrection of CV's appeared at 650 °C but not at 450 °C, whereas resistive heating would be expected to increase with decreasing temperature. This argument is however not as simple, since the resistive heating is not only dependent on the resistance, but also on the current passing, which increase

with the electrode activity, which increases with temperature. In principle it should be also be possible to determine the resistive heating from impedance spectra recorded under current load. However the impedance spectra recorded under current load (as in Figure 80 and Figure 82) where all recorded in a way where the current load was applied exactly when the recording of the impedance spectrum was started. The R_s in the impedance spectrum is determined during less than a minute in the beginning of the measurement, which likely is before the resistive heating start to play a role, which means the impedance spectra recorded under current load in these experiments cannot be used for determination of the resistive heating. For the next experiments it would be advantageous to check for resistive heating by mounting an extra thermocouple for temperature determination at the vicinity of the 3EP.

The decrease in R_s during polarisation could possibly be explained by other reason than resistive heating. During consideration of other explanations it must be kept in mind the R_s decrease occurred only during polarisation, as R_s determined on impedance spectra recorded at OCV immediately before and after polarisation was constant. Activation of LSM-electrodes during polarisation is a well-known phenomenon which has been studied by several groups, but usually only a decrease in the polarisation resistance is observed while the serial resistance remains unaffected or increases[156, 174, 175]. A phenomenon, which may have an impact on the serial resistance was studied by Backhaus-Ricoult[59]. By means of scanning photoelectron microscopy of the LSM-YSZ interface during polarisation, it was observed Mn^{2+} ion spread over the YSZ surface during polarisation, and this strong enrichment of the YSZ surface caused a high electronic conductivity in the electrolyte[59]. The spreading of the Mn^{2}+ ions was a reversible process, as the ions withdraw when the polarisation was removed[59]. Kharton et al. has previously identified that during doping of CGO with manganese, the electronic conductivity increased if the 10% solubility limit of manganese in CGO was exceeded[176]. It is therefore suggested the temporary decrease in R_s during polarisation observed in this work is due to spreading of manganese ions on the CGO electrolyte surface caused by the polarisation, followed by an increase in the electronic conductivity in the CGO surface due to the manganese enrichment.

10.5 Conclusion

Electrochemical measurements (EIS and CV) were made on a non-impregnated and a BaO-impregnated electrode in a 3EP set-up. The experiments were aimed at giving a more detailed insight into the electrochemical deNO_x processes compared to the measurements performed on symmetric cell and porous cell stacks. The more detailed insight was expected as the 3EP set-up contained one well-defined working electrode in a three-electrode set-up with a fixed reference potential, and furthermore the outlet gas from the set-up was monitored by a CLD. Whereas the impedance spectra revealed a decrease in the polarisation resistance due to the BaO impregnation, a better performance of the BaO-impregnated electrodes was not measured during the conversion measurements as measured on the porous cell stacks. The reason for the lack of better performance may be the chosen temperature and polarisation range. Furthermore problems were encountered in determining the IR drop and thereby the electrode polarisation during the polarisation experiments, by comparison to literature this was suggested to be due manganese enrichment of the CGO surface during polarisation. As only two electrodes were investigated in the 3EP set-up (one non-impregnated and one BaO-impregnated) it is recommended to do more experiments in the 3EP set-up to allow for a better comparison to the experiments performed in the other set-ups.

11 Construction of an *in situ* XANES test house

11.1 Introduction

In chapter 4 on DRIFT spectroscopy the focus was on NO_x species adsorbed on the electrode materials, and how the adsorbed species changed depending on the experimental conditions: temperature, atmosphere etc. In order to understand the processes occurring during electrochemical deNO_x it is however important, not only to consider the species adsorbed on the electrode, but also to consider changes occurring in the electrode material during operation. Knowledge on this may increase the understanding of the electrocatalytic properties of different electrode materials and ultimately guide the search for new, better performing electrodes.

During polarization of a solid oxide electrode one of the changes expected to happen is a change in the oxidation state of one or more of the elements in the electrode (for instance Mn in LSM electrodes or Co in LSCF electrodes). A change in oxidation state may be detected by application of X-ray Absorbtion Near Edge Spectroscopy (XANES) and in agreement with the theory a change in oxidation state caused by polarisation has been detected by means of XANES on thin-film electrodes of LSCF[177] and LSM[178]. Unfortunately none of the aforementioned *in situ* XANES studies report clearly how the measurements were made, i. e. how the test house was constructed in order to perform the *in situ* studies. True *in situ* XANES studies require: 1) a controlled atmosphere 2) heating of the sample 3) electric contact to the sample and 4) a "window" through which the X-ray beam can access the electrode surface and a window through which the fluorescence light from the electrode can reach the detector. Due to requirement 4) an *in situ* XANES test house must be designed quite differently from the test houses normally used for electrochemical characterization of solid oxide electrodes.

This chapter describes how an *in situ* XANES test house was designed and constructed, and also the results from the first initial measurements on LSM15-CGO10 composite electrodes are described. The construction of the *in situ* XANES test house and the subsequent measurements was a joint project made together with Anke Hagen, Ragnar Kiebach and Bjørn Sejr Johansen, who all at the time were employed in the Fuel Cell and Solid State Chemistry Division. The projected also resulted in an article published in *Journal of Synchroton Radiation*, see appendix A.

11.2 Theory

11.2.1 XAS[78, 179]

X-ray Absorption Spectroscopy (XAS), is, as the name implies, based on the absorption of X-rays. When an incident X-ray photon hits an element and the X-ray energy matches the binding energy of an electron of the atom, the photon may get absorbed causing a drop in the X-ray intensity. The result is an absorption edge in the X-ray absorption spectrum, which is element specific due to the different binding energies of the electrons in the atoms and furthermore dependent on the oxidation state of the element.

An X-ray absorption spectrum can be recorded either by measuring the transmission or the fluorescence signal, in this project the fluorescence signal was used. Using the fluorescence signal for XAS is based on the following principle: After an absorption event, the atom is in an excited state, with one of the core electron levels left empty (core hole). One important mechanism for the decay of the excited atomic state following an X-ray absorption event is X-ray fluorescence, in which a higher energy electron core-level electron fills the deeper core hole, ejecting an X-ray of well-defined energy. Detection of the fluorescence energies emitted in this way may then be used for creation of an X-ray absorption spectrum.

In an X-ray absorption spectrum the electronic transitions give rise to distinct features like absorption edges, pre-edge features and post-edge features. These features may be used for analyses in X-ray Absorption Near Edge Structures (XANES), which focuses on the region around the absorption edge, or in Extendend X-ray Absorption Fine Structure (EXAFS) spectroscopy, which focuses on the post edge features. In Figure 84 a sketch of an X-ray absorption spectrum is shown and the regions of the spectrum investigated in XANES and EXAFS are marked. EXAFS can be used for determination of the coordination environment around specific atoms, while in XANES the position of the absorption edge may be used for determination of the oxidation state of an element. For transition metals of the 4^{th} period the K absorption edge, which corresponds to transition of a 1*s* core electron into a *p*-like unoccupied state, is typically used in XANES for determination of the oxidation state. Correspondingly, in this work the Mn K absorption edge was investigated during XANES measurement, in order to monitor a possible change in Mn oxidation state due to polarisation.

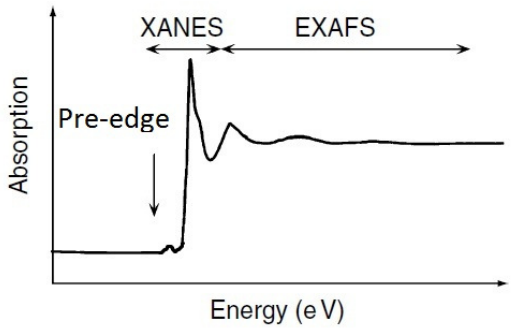

Figure 84. Sketch of X-ray absorption spectrum around an absorption edge.

11.2.2 Polarisation of solid oxide electrodes

As stated in the introduction, a change in oxidation state is expected and has been experimentally measured in solid oxide electrodes during polarization. The change in oxidation state follows from the change in oxygen stochiometry caused by the polarization. Due to the polarization the O^{2-} ions move through the crystal lattice of the solid oxide electrode, which increases the number of oxygen vacancies, and in order to retain charge neutrality the oxidation state of the cations is changing, which may be detected by XANES. However, the change in oxidation state will not occur evenly through the entire electrode[155]. The reason for this is easiest explained with reference to the equivalent circuit for a mixed-conducting electrode shown in Figure 85. As shown in the equivalent circuit, the current may pass through the electrode to the electrolyte either via electronic conduction or ionic conduction, but before the O^{2-} conducting electrolyte is reached the oxygen charge transfer must have taken place. The extension of O^{2-} conduction through the electrode depends on the temperature. At low temperatures the oxygen charge transfer resistance will be much higher than the ohmic resistance of the electrode ($R_{CT}>>R_{\Omega}$), for this reason an extensive ionic conduction will take place through the electrode. In contrast, at higher temperatures, the charge transfer resistance will be much lower compared to the ohmich resistance ($R_{CT}<<R_{\Omega}$) for this reason the oxygen ion conductivity will only take place in the vicinity of the electrolyte, which correspondingly also will be the only part of the electrode in which the cations will change oxidation state. The implication of this is that in order to detect changes in electrode oxidation states by XANES it is necessary to use either very thin electrodes (for instance thin film electrodes) or to go to relatively low temperatures.

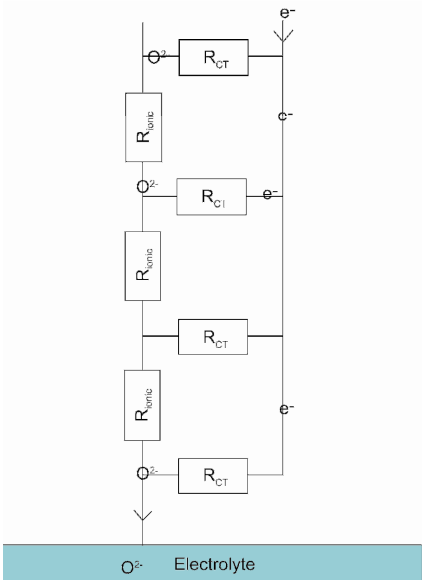

Figure 85. Infinite transmission-line describing a mixed ionic-electronic conductor

In the work described in this chapter conventional 10 µm thick porous LSM15-CGO10 electrodes were employed, and the measurements were performed at 300-350 °C. However, as discussed in the results section the combination of electrode thickness and temperature may have been insufficient for detection of changes in electrode oxidation states by means of XANES.

11.2.3 Previous work on *in situ* XANES on electrochemical devices

To the best of the author's knowledge, *in situ* studies on solid oxide electrodes/electrolytes including polarisation have so far only been reported by Japanese scientists, who studied the effect of polarisation on LSM electrodes[178], LSCF electrodes[177] and Mn doped YSZ electrolyte[180]. However the studies were only reported in short meeting abstracts, which yielded little information on the actual set-up/test-house used for the *in situ* measurements. Inspiration for construction of an *in situ* test house can be gained from another field, namely the lithium-ion battery field, where for instance Braun et al.[181] and Balasubramanian et al.[182] have given detailed descriptions of tests houses used for *in situ* XAS of lithium-ion battery electrodes. Even though these test houses are useful as inspiration, their construction is not directly applicable in the solid oxide electrode field, as the lithium-ion batteries operate at room temperature. For this reason the litium-ion battery *in situ* test house does not need a system for heating the sample, which is a necessity for *in situ* studies of solid oxide electrodes.

11.3 Experimental

11.3.1 Design of *in situ* XANES test house

Two photos of the test house designed for the *in situ* XANES measurements are shown in Figure 86, one front view and one side view. The test house is basically a small aluminium chamber (8 cm x 8 cm x 4 cm) in which the sample is placed in the middle fixed to a thin alumina tube. Heating of the sample is achieved by means of a halogen lamp (Osram, model XENOPHOT® 64635 HLX, max. voltage 15 V, max. effect 15 W) located at the back of the chamber. On the sides of the chamber an inlet and outlet for the gas flow is located, together with windows covered by Kapton® foil for the X-ray beam to pass through. The sample is as mentioned fixed to an alumina tube, which is mounted in the top of the chamber. Finally the front of the chamber is covered by a Kapton® foil window which is 5 cm in diameter. It is through this window the fluorescence signal from the sample is detected.

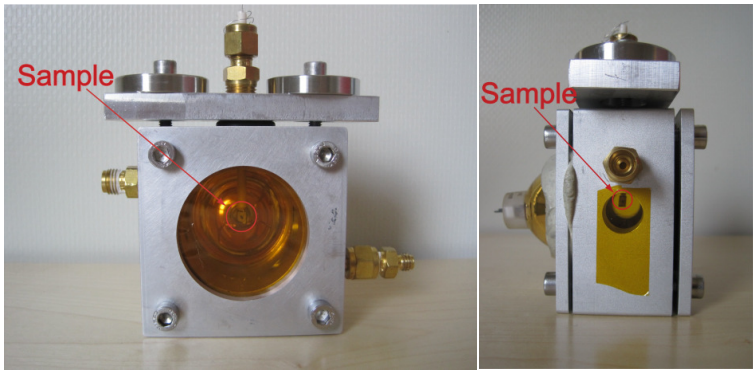

Figure 86. *In situ* XANES cell front view and side view

11.3.2 Sample preparation and mounting

The samples used in this work were symmetric cells with a dense 200 µm thick CGO10 electrolyte (Kerafol) and porous, 10 µm thick LSM15-CGO10 composite electrodes. The LSM15 used for the electrodes was synthesized in-house by the glycine-nitrate combustion synthesis[150] using nitrates from Alfa Aesar. The stochiometry of the synthesized LSM15 was $(La_{0.85}Sr_{0.15})_{0.99}MnO_3$, i.e. the LSM15 was slightly deficient on the A-site. The LSM15 was mixed with CGO10 (Rhodia) in a terpineol based paste with 50 wt% LSM15 and 50 wt% CGO10. Subsequent the paste was screen-printed on the CGO electrolyte and the cells were sintered with the maximum temperature 1050 °C held for 2 h, whereafter they were cut into 6 mm x 6 mm squares.

For mounting of the cells a sample holder with Pt wires was prepared. Two platinum wires were pulled through the channels of an 80 mm long and 4 mm thick alumina tube. The channels were closed and the Pt wires fixed by applying glass paste on each end of the alumina tube and heat to 1000 °C. Pt paste (Ferro) was applied on the electrodes for current collection and as "glue" for fixing the cell to the Pt wires. The one electrode was fully covered by the current collector, on the other a small 1 mm x 1 mm square was left free in the middle for collection of the XRD fluorescence signal from the electrode surface. A close-up of the cell mounted on the alumina tube is shown in Figure 87.

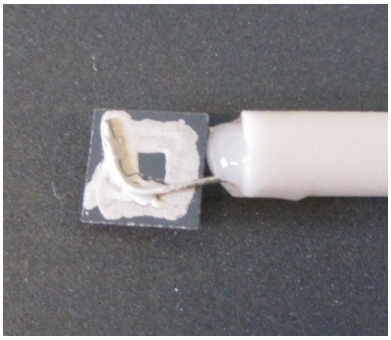

Figure 87. Symmetric cell mounted for *in situ* XANES measurement.

11.3.3 Heating and temperature determination

Heating of the sample was achieved by use of a halogen lamp, as using a lamp made it possible to heat the sample directly without the need for a furnace. In the focal point of the halogen lamp a black body will be heated to 1300 °C when the maximum voltage 15 V is applied on the lamp. Initial experiments showed that placing the sample directly in the focal point caused too vigorously heating of the sample, for this reason the sample was displaced ≈ 6 mm away from the focal point.

The exact temperature of the sample was determined by combining impedance spectra recorded during the *in situ* XANES test with knowledge on the temperature dependence of the cells serial resistance. Prior to the *in situ* XANES tests impedance spectra were recorded on symmetric cells in a conventional furnace set-up in the temperature range 300-500 °C. From these spectra the serial resistance was determined and an Arrhenius plot made, see Figure 88.

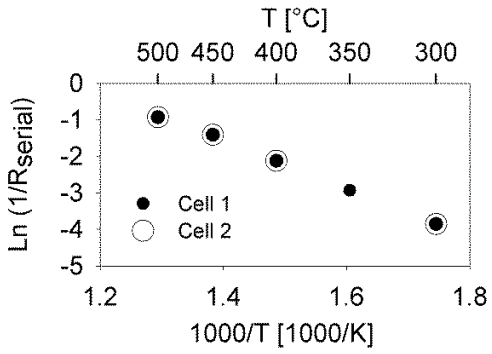

Figure 88. Arrhenius plot of serial resistance

As observed in Figure 88 good linearity was obtained on the Arrhenius plots ($R^2 \geq 0.998$). For this reason sample temperature during the *in situ* XANES measurements could be determined from the Arrhenius expression stated in eq. 11.1, which is calculated from the results shown in Figure 88.

$$\ln\left(\frac{1}{R_0}\right) = 7.6 - 0.79\frac{1000}{T} \qquad 11.1$$

The activation energy determined for the serial resistance was 0.57±0.002 eV, which is below the activation energy 0.7 eV for the ionic conduction in CGO10[154]. As the ionic conduction in CGO10 is expected to be the main contributor to the serial resistance, similar activation energies were expected, the reason for the discrepancy is unknown.

11.3.4 EIS and polarisation experiments

Before and after polarisation of the cells impedance spectra were recorded. This was done in order determine the temperature of the sample, as explained in the previous section, and to monitor if the cells were stable or changed during the experiment due to heating, polarisation etc. Moreover impedance spectra recorded in the *in situ* XANES set-up made it possible to compare to impedance spectra recorded in the conventional furnace set-up, to estimate the reproducibility between the two set-ups. A Gamry reference 600 potentisat was used for the impedance measurements which were made in the frequency range 1 MHz-0.1 Hz with 36 mV rms amplitude and 6 points recorded pr. decade. The Gamry potentiostat was also used for the polarisation experiments, during which the cells were polarised corresponding to 100 mV, 300 mV and 500 mV polarisation across each of the electrodes for ≈ 1 h.

11.3.5 XANES measurements

The *in situ* XANES measurements were carried out at Hamburger Synchrotonstrahlungslabor (Hasylab), DESY (Deutsches Elektronen-Synchroton) in Hamburg. The measurements were made at beamline A1 and two Si 111 crystal pairs were used as monochromaters for the X-ray beam. The K absorption edge of Mn metal is located at 6539 eV while for Mn^{3+} the K absorption edge is located at 6551 eV[183]. In order to cover the energy range around the absorption edge the XANES spectra were for this reason recorded in the energy interval 6490-6590 eV. The step size during the measurements was 0.5 eV at 6490-6534 eV and 6560-6590 eV, while in the energy range closest to the absorption edge, 6534-6560 eV, a stepsize of 0.1 eV was used.

The fluorescence signal from the electrode was detected by a Passivated Implanted Planar Silicon (PIPS) detector, which in principle is a photodiode with a large area. The current signal from the PIPS detector was measured by a Keithley 428 current amplifier. As the PIPS detector is sensitive both to heat and visible light, the detector was during the measurements shielded by two Mylar foils. A top-view schematic of the measurement set-up is shown in Figure 89.

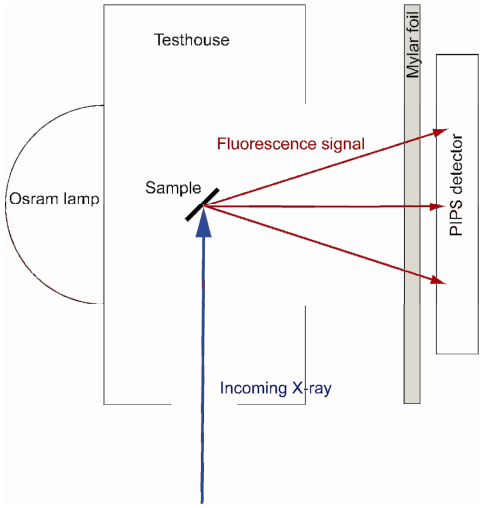

Figure 89. Top-view schematic of the *in situ* XANES test house including incoming X-rays and emitted fluorescence signal.

During the measurement the flow through the test house was 20 ml/min 21% O_2 in He and the oxygen content in the outlet flow was constantly monitored by an oxygen sensor. The temperature of the sample during the measurements was 300-350 °C.

11.4 Results

11.4.1 Impedance measurements

Impedance spectra recorded on a symmetric LSM15-CGO10 cell mounted in the *in situ* XANES test house is shown in Figure 90, and for comparison Figure 91 shows an impedance spectrum recorded on a similar cell mounted in a conventional furnace set-up. Clearly there is a significant difference between the impedance spectra recorded in the two set-ups, as the difference in polarisation resistance is more than an order of magnitude. An order of magnitude is unlikely to be due to the difference in gascomposition (10% O_2 in Ar vs. 21% O_2 in He) and the reason for the dissimilarity is then likely the difference in sample mounting and eventually heating. With respect to the conventional furnace set-up the 4 cells mounted in this set-up in general showed good reproducibility, as the variation in R_p was 12% at 350 °C in 10% O_2. As only one test was made in the *in situ* test house it is hard to estimate a cause for the different impedance response, and further experiments are needed to clarify why the impedance spectra are so different. However the results show, that it is possible to characterize a cell mounted in the *in situ* test house by impedance spectroscopy.

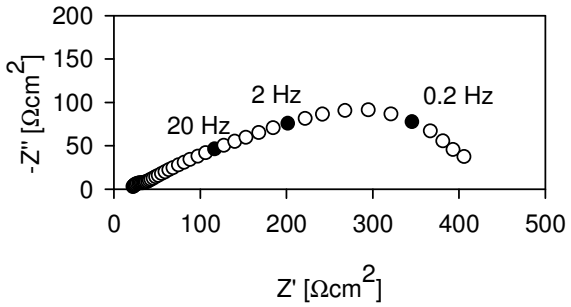

Figure 90. Impedance spectra recorded on a symmetric LSM15-CGO10 cell mounted in the *in situ* XANES test house. The gascomposition was 21% O_2 in He and the sample temperature 356 °C.

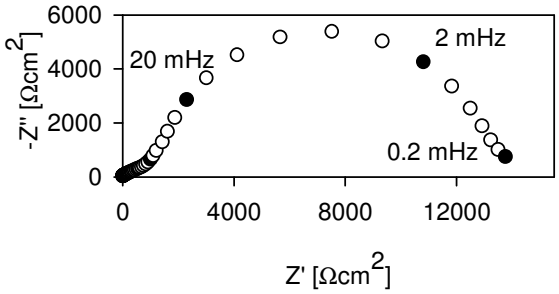

Figure 91. Impedance spectra recorded on symmetric LSM15-CGO10 cell mounted in a conventional furnace set-up. The gas composition was 10% O_2 in Ar and the temperature 350 °C.

The impedance spectra recorded in the *in situ* XANES set-up showed a continuously increase in the polarisation resistance during time as shown in Figure 92. The increase in polarisation resistance was unaffected by the polarisation as the (a) spectra in Figure 92 were recorded before -500 mV polarisation pr. electrode, while the (b) spectra were recorded after the polarisation. The instability in the polarisation resistance only occurred in the low frequency region, whereas the high frequency region and R_s remained entirely stable during the test. Furthermore the impedance spectra in Figure 92 show, that polarisation of the cell in the *in situ* XANES test house did not have a detrimental effect on the cell or the mounting/attachment of the cell, as both R_s and R_p remained unaffected by the polarisation.

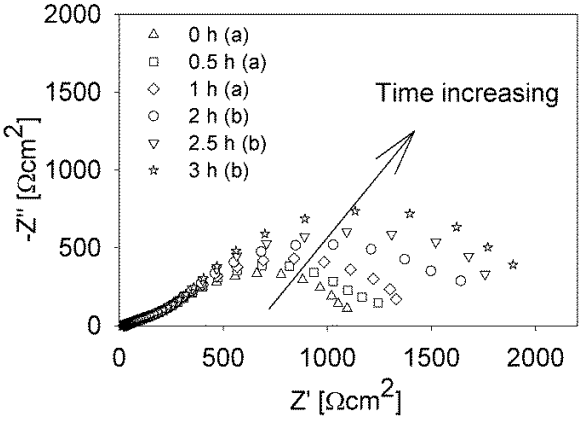

Figure 92. Impedance spectra recorded before (marked by (a)) and after (marked by (b)) 500 mV polarisation of the sample mounted in the *in situ* XANES test house.

11.4.2 XANES

XANES spectra were recorded while the electrode was polarised at 100, 300 and 500 mV; and before and after each of the polarisation experiments. At each experimental condition 3-4 spectra were recorded, and from these spectra the position of the absorption edge was determined, see Table 33 for the absorption edge position and Figure 93 for two representative XANES spectra. As observed in Table 33 and Figure 93 polarisation did not affect the position of the absorption edge, which means no change in Mn oxidation state could be detected during the polarisation. As explained in the theory section a change in Mn oxidation state was expected, why this change was not observed will be discussed in section 11.5.1.

Table 33. Edge energies of the Mn K absorption edge on the electrode wile unpolarised and during polarisation.

Temperature	Electrode polarisation	Mn XANES edge [eV]
356 °C	Unpolarised	6553.6(1)
	100 mV	6553.7(3)
	300 mV	6553.7(1)
	500 mV	6553.6(3)
300 °C	Unpolarised	6553.6(1)
	500 mV	6553.4(2)

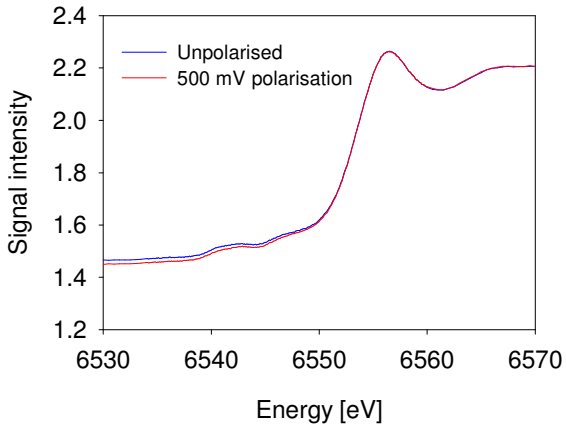

Figure 93. XANES spectra of the Mn absorption edge in the unpolarised electrode and during 500 mV polarisation of the electrode at 300 °C.

11.5 Discussion

11.5.1 Polarisation effect and reproducibility

As described in the results section, the *in situ* XANES test house made it possible to do X-ray absorption spectroscopy on solid oxide electrodes under true *in situ* conditions, i.e. in controlled atmosphere, at elevated temperature and under polarisation. Furthermore impedance spectroscopy could be used during the measurement to monitor the state of the solid oxide cell and to determine the sample temperature. The construction of the *in situ* XANES test house was for this reason to a large extent successful; however the first test on porous LSM15-CGO10 electrodes raised two major questions regarding the results: 1) Why was a change in the manganese oxidation state not observed during the polarisation? 2) Why was the impedance spectra recorded on a cell in the *in situ* XANES test house much different from spectra recorded in a conventional furnace set-up?

Regarding question 1) the explanation is likely, that with the 10 µm thick porous electrode at 300-350 °C the change in the Mn oxidation state is happening in the depth of the electrode near the electrolyte, as explained in the theory section, and not in the bulk Mn in the electrode. This means that only a small proportion of Mn in the electrode will have changed oxidation state during polarisation, and this proportion has apparently been too small to give any detectable changes on the XANES spectra. Repeating the experiment with thinner electrodes would therefore increase the change of detecting a change in the Mn oxidation state, as in thinner electrodes a larger proportion of Mn will change oxidation state during polarisation. Preferably LSM thin film electrodes should be employed, as these electrodes can be fabricated in 200-300 nm thickness.

Regarding question 2) about the cause of the difference in impedance spectra between the *in situ* XANES set-up and the conventional set-up, the answer to this may be found when more tests have been performed in the *in situ* XANES set-up. Preferably tests should be performed where application of the current collector is varied (electrodes fully covered by the current collector vs. with a current collector free hole in the middle), where gas composition and flow rate is varied to allow for identification of the processes contributing to the polarisation resistance and eventually where the position of the cell relative to the halogen lamp is varied. The latter is of interest since

the tilting of sample relative to the halogen lamp (see Figure 89) may cause an uneven heat distribution in the cell. This is discussed further in the next section.

11.5.2 Improvements of the *in situ* XANES tests and test house

The *in situ* XANES test house was a first model, and even though it proved very functional, further improvements can still be made. A major concern during the measurement was the heat distribution in the cell. As shown in Figure 89 the sample had to be tilted relative to the front of the halogen lamp, for the sake of the incoming X-ray beam and the detection of the fluorescence signal. However as the heating from the halogen lamp is dependent on the distance to the lamp, the tilting of the sample meant the cell edge furthest away from the halogen lamp would experience a heat effect only 25% of the effect closest to the halogen lamp. The implication of this is the cell in the *in situ* set-up experiences a constant thermal gradient from the one cell edge to the other, which could explain why one of the mounted cells suddenly cracked through the middle. In order to circumvent this problem a second model of the *in situ* XANES test house should be made with the halogen lamp mounted with the lamp edge parallel to the cell, or alternatives to heating the cell with an halogen lamp should be found.

With respect to the heating of the cell another concern was, if the temperature of the electrode pointing away from the halogen lamp was exactly the same as the temperature determined from the serial resistance, as this electrode may be cooler since it only was heated by heat transfer trough the cell and not directly by the halogen lamp. A way to check this would be to mount a thermocouple through the alumina tube sample holder and let this thermocouple measure the temperature of the electrode.

Regarding the next *in situ* XANES measurements the gas tightness of the test house should be checked, and if tight enough XANES measurements should be made with variation in pO_2 from 1 atm to 0.001 atm. The variation in Mn oxidation state caused by the change in oxygen partial pressure and the corresponding change in oxygen vacancies could then be correlated with the change in Mn oxidation state caused by the polarisation and the corresponding change in oxygen vacancies.

Finally, the constructed *in situ* XANES test house is not limited to XANES measurements only, but could also be used for *in situ* EXAFS measurement, thereby yielding an even deeper understanding of changes occurring in the electrodes during polarisation.

11.6 Conclusion

An *in situ* XANES test house was designed and it was proven the test house could be used for XANES measurements on solid oxide electrodes in controlled atmosphere, at elevated temperatures and under polarisation, i.e. under true *in situ* conditions. The initial experiments on porous LSM15-CGO10 electrodes did not show the expected change in Mn oxidation state during polarisation, likely due to the thickness of the sample. Furthermore the impedance spectra recorded on cells in the *in situ* test house were quite different from impedance spectra recorded at similar conditions in a conventional set-up; further experiments are needed in order to clarify the reason for this difference.

12 Overall Discussion, Conclusion and Outlook

In the preceding chapters several different experiments have been described, which have aimed at clarifying whether impregnation with NO_x storage compounds increases the NO_x-conversion during electrochemical deNO_x on solid oxide electrodes. In this chapter the findings from the different experiments will be discussed in relation to each other before the overall conclusions from the project are drawn and put into perspective.

12.1 Discussion

12.1.1 The optimal electrode composition and NO_x storage compound

The main focus in this project was on LSM15-CGO10 and LSF15-CGO10 electrodes in combination with the NO_x-storage compounds K_2O and BaO. The chapters 6 to 9 describe a series of experiments made in a porous cell stack test set-up with the four different possible combinations of LSM15-CGO10 and LSF15-CGO10 electrodes with K_2O or BaO impregnations. From the point of view of developing the electrochemical deNO_x technology into a commercial state, the most promising finding in the aforementioned chapters was the observation of a significant NO_x conversion in the presence of 10% O_2 on LSM15-CGO10 electrodes with BaO impregnation. This raises the question whether LSM15-CGO10 with BaO impregnation is the best combination of materials of the four aforementioned for electrochemical deNO_x? Definitely K_2O impregnation can be ruled out as method for improving the NO_x conversion on solid oxide electrodes, as K_2O impregnation on both LSM15-CGO10 and LSF15-CGO10 electrodes lead to severe degradation problems, visible as an entire deterioration of the electrode microstructure. The reason for this deterioration is likely the corrosiveness of molten KNO_3, as it is stated by Bloom that molten nitrates may dissolute oxides[184], however in addition to this the degradation does also seem to depend on polarisation as explained in chapter 9. The combination of LSF15-CGO10 with BaO did increase the NO_x conversion without presence of O_2, but no conversion of NO_x was observed in the presence of 10% O_2. A reason for this could be the LSF15-CGO10 cell stacks with BaO impregnation never was polarized at more than 3V, while on the BaO impregnated LSM15-CGO10 cell stack, the NO_x conversion in presence of O_2 was only observed at polarisation larger than 3V. For this reason experiments with LSF15-CGO10 porous cell stacks and BaO impregnation should be repeated at higher polarisation.

12.1.2 Phase formation during testing

Neither the LSM15-CGO10 nor the LSF15-CGO10 electrodes with BaO showed severe sign of degradation during testing, when the serial resistance and the polarisation resistance at the beginning and the end of each test was compared. Consistently all the tests on the BaO impregnated stacks ended with both the serial and the polarisation resistance being lower when compared to the corresponding non-impregnated tests. A common characteristics for the BaO impregnated tests was profound changes in the electrode microstructure at the end of the tests, as the SEM images after test revealed electrode surfaces covered with either an "explosion" of nanoparticles, "fluffy" structures or flake like particles. The dramatic change in microstructure could be a sign of formation of new phases, even though previous studies as described in chapter 8 did not indicate new phase formation would occur. The tested electrodes with BaO impregnation should for this reason be investigated for the formation of new phases. The most suitable technique for this is likely Transmission Electron Microscopy (TEM), as TEM would allow for both elemental analysis and crystal structure determination in the nanometer range at the surface of the electrode grains.

12.1.3 Effect of impregnation

All the impregnations (MnO_x, K_2O, BaO) caused an activation/decrease in polarisation resistance of the electrodes, at least until the undesirable degradation for the MnO_x and K_2O impregnated sample started to influence the experiments. An important observation with respect to the activation caused by the impregnation was it was not only observed in NO_x-containing atmospheres, but also in atmospheres with only 10% O_2. This shows that the impregnations did not only affect the NO_x adsorption on the electrode, but the impregnations also caused a general activation. The question is why this activation occurred? A common explanation is impregnations due to the high surface area of the impregnated nanoparticles increases the TPB in the electrode and thereby causes an activation[147, 185]. This explanation makes most sense, when the impregnated compound is either electronic or ionic conductive, as the TPB is defined as the active reaction zone around the border between gas phase, the ion-conducting phase and the electronic conductive phase. However the findings from literature on conductivities of the NO_x storage compounds, stated in chapter 2, does indicate the conductivity of the compounds is at the best very limited, and thus questions whether an extension of the TPB is the right explanation of the activation

caused by the MnO_x, K_2O, or BaO impregnation. Another possible explanation could be the impregnated compounds act as impurity scavengers, which previously has been suggested as an explanation of why impregnation with non-conductive CeO_2 increased the performance of solid oxide electrodes[186].

In addition to the effect of impregnation on the general electrode activity, the effect on the NO_x adsorption and conversion should also be considered. For the K_2O impregnations the conversion measurements in 1000 ppm NO + 10% O_2 on a porous cell stacks showed a change in the conversion between NO and NO_2 on both the LSF15-CGO10 and the LSM15-CGO10 electrodes. The change in NO_x conversion indicate the NO_x-conversion reaction on the electrode is affected by the presence of K_2O, which also supported by the impedance results, the cyclic voltammetry on the symmetric cells and the results from the DRIFT spectroscopy. With respect to the BaO impregnation the impedance analysis on the non-impregnated and BaO-impregnated LSM15-CGO10 cell stacks show the BaO impregnation affects the NO_x-adsorption, which was also indicated by the results from the DRIFT spectroscopy.

12.1.4 NO_x adsorption studied by DRIFT spectroscopy

DRIFT spectroscopy was performed on the NO_x adsorption on non-impregnated and K_2O or BaO impregnated CGO10. The DRIFT spectroscopy revealed a significant change in the adsorbed NO_x species in the investigated temperature range 300 °C-500 °C, from a variety of adsorbed NO_x-species at 300 °C to predominantly adsorbed NO_3^- species at 500 °C. Furthermore the DRIFT spectroscopy revealed a very significant difference in the adsorbed NO_x species depending on whether only NO was present in the atmosphere or NO_2/NO+O_2 was present in the atmosphere. This last finding implies the reaction mechanism in atmospheres only with NO likely is different from the reaction mechanism in NO_2/NO+O_2, due to the difference in adsorbed species. For this reason results obtained in only NO containing atmospheres are likely only to a very limited extent valid in NO and O_2 containing atmosphere, which is a more realistic atmosphere for electrochemical deNO_x, considering diesel exhaust contain up to 15% O_2 [7]. With respect to the finding that NO_3^- was predominant adsorbed NO_x specie, this finding was used in the interpretation of the results from the impedance measurement, and thus illustrates the strength of combining impedance measurements with other techniques. An even larger advantage would be gained, if electrochemical characterization was combined with surface spectroscopic

techniques like FTIR at in-situ conditions as done by MacLeod et al.[42]. The work on developing an *in situ* test house for XANES spectroscopy showed that doing *in situ* measurements on solid oxide electrodes is not a trivial task, but possibly the experiences gained from developing the *in situ* XANES testhouse may also be used in the development of a set-up for *in situ* FTIR measurements on solid oxide electrodes.

12.1.5 Comparison between test set-ups

In this project three different test set-ups were used for the electrochemical testing: the symmetric cell test-set-up, the porous stack test set-up and the 3EP test set-up. When the results from the different test set-ups were compared, some differences were observed between the set-ups, for instance an NO_2 conversion arc was only observed in impedance spectra recorded on the symmetric cell test set-up, and a significant difference was observed in the conversion obtained on the porous cell stack set-up and the 3EP set-up. This illustrates, that the processes responsible for the polarisation losses are strongly dependent on the flow conditions around the electrodes. Therefore the design of the electrochemical deNO_x filter to be used in real life diesel exhaust is very important for the development of the electrochemical deNO_x technology, and the filter should be designed in a way which minimizes undesirable polarisation losses due to poor gas flow distribution.

12.1.6 Commercialization

As previously stated the future goal is to develop the electrochemical deNO_x technology into a stage where it is useful for cleaning of real diesel engine exhaust. In that perspective it is of interest to consider, how far the results achieved on the porous cell stacks are from the requirements for an operable deNO_x technology. Transferring the results from the porous cell stacks to real engine exhaust must however be taken with a grain of salt, among other reasons as NO_x conversion is much dependent on the flow rate and flow distribution across the electrodes, as illustrated when comparing the results from the porous cell stacks with the measurements on the 3EPs. However with this in mind the results achieved on the porous LSM15-CGO10 cell stack with BaO impregnation will be compared to realistic deNO_x requirements. First of all it will be assumed the electrochemical deNO_x filter is operating at 400 °C with a 10% current efficiency in an exhaust gas containing 1000 ppm NO and 10% O_2, i.e. at conditions corresponding to the experiments described in chapter 8. According to Bosch the requirements for deNO_x technology should be a

mean power consumption measured during the New European Driving Cycle <100 W and the peak power consumption no more than 500 W, while the NO_x conversion should be > 65%[187]. For a 1.4L diesel engine driving 130 km/h at the highway the exhaust gas flow will be ≈400 m^3/h assuming an exhaust temperature of 400 °C[iii]. In the experiments performed on the BaO impregnated LSM15-CGO10, the NO_x conversion was ≈60%, and assuming 60% conversion of the NO_x is enough, a total porous cell stack area of 30 m^2 would be necessary to clean the exhaust from the 1.4 L engine, leading to a total power supply of 70000 W. Obviously 30 m^2 cells stacks and 70000 W power consumption is much too large compared to the Bosch requirements for a $DeNO_x$ technology. This illustrates the need for a continued improvement of the electrochemical $deNO_x$ electrodes, but also for the development of an electrochemical filter for testing in real exhaust, to give a more realistic evaluation of the performance of electrochemical $deNO_x$, compared to just up-scaling results from porous cell stacks.

[iii] The specification of this 1.4. diesel engine corresponds the specifications of the engine in a Citroen C2, a small personal car. Such a diesel engine is used for realistic diesel engine tests at DTU MEK.

12.2 Conclusion

To the best of the author's knowledge, the present project for the first time shows electrochemical reduction of NO_x in the presence of 10% O_2 on all ceramic electrodes. The NO_x conversion in presence of 10% O_2 was measured on a LSM15-CGO10 porous cell stack impregnated with BaO as NO_x storage compound. At 400 °C 60% NO_x conversion was achieved with current efficiency 10%, the conversion was observed to increase with increasing temperature and polarisation. Through impedance analysis and DRIFT spectroscopy it was shown, that BaO impregnation affected the reactions on the LSM15-CGO10 electrodes by causing a general electrode activation, and also by acting as an adsorbent for NO_x adsorption and storage on the LSM15-CGO10 electrodes. However it was not possible to identify, which of the two aforementioned effects was mainly responsible for the increased NO_x conversion observed on the BaO impregnated cell stacks. As no NO_x conversion at all was observed on non-impregnated LSM15-CGO10 cell stacks, neither in the presence of 10% O_2 nor when only NO was present, the results seem to confirm addition of NO_x storage compounds can increase the conversion during electrochemical deNO_x. However, the results also showed significant differences depending on which NO_x storage compounds and solid oxide electrode materials were combined. Even though addition of K_2O as NO_x storage compound increased the NO conversion in the absence of oxygen on both LSM15-CGO10 and LSF15-CGO10 electrodes, the K_2O impregnation caused major degradation issues in the electrodes, and must for this reason be considered unsuitable as a NO_x storage compound in solid oxide electrodes. Similarly significant degradation problems were observed, when MnO_x was impregnated on LSM5-CGO10 electrodes as a NO_x storage compound. The degradation problems on the K_2O and MnO_x impregnated electrodes thus illustrates the compatibility between the solid oxides electrodes and NO_x storage compounds must be carefully considered and studied, when the conversion during electrochemical deNO_x is attempted improved by the addition of a NO_x storage compound. So far the results achieved with increasing the NO_x conversion on LSM15-CGO10 electrodes by BaO impregnation appear very promising, and definitely justify further studies on the LSM15-CGO10/BaO system just as well as investigations of other combinations of solid oxide electrode and NO_x storage compounds.

12.3 Outlook

As stated in the conclusion, the results achieved in this project encourage further studies on solid oxide electrodes in combination with NO_x storage compounds. A general challenge in electrochemical deNO_x, including this project, is to achieve a sufficiently high NO_x conversion in the 200-300 °C temperature range of diesel exhaust, for this reason it is suggested to focus more on mixed electronic-ionic conducting electrodes as LSF in this work, and other materials currently under investigation for use in intermediate temperature solid oxide fuel cell, like for instance LSCF and LSC[62]. Furthermore other NO_x-storage materials than K_2O and BaO should be included in the investigation, for instance other alkaline (Na, Cs) and alkaline earth (Mg, Ca, Sr) oxides.

With respect to further studies on the LSM15-CGO10/BaO system an important point is to clarify, whether any new phases were formed in the electrodes during testing. As stated in the overall discussion, the most suitable technique for that investigation would be TEM. A deeper theoretical understanding of why the NO_x conversion in the presence of 10% O_2 only is observed on the BaO impregnated cell stack at temperatures ≥350 °C and polarisations >3V is also desirable.

Furthermore more focus should be on recording and interpretation of impedance spectra during current load. The majority of the impedance spectra in this work were recorded at OCV, and in general the OCV results appear to correlate well with conversions measurements, as low polarisation resistance at OCV usually is correlated with high NO_x-conversion. However, only using the OCV spectra for evaluation of the electrode processes increases the risk of overemphasizing the importance of one or more processes, since the impedance spectra recorded under current load in general differ from spectra recorded at OCV.

With the identification of BaO impregnated LSM15-CGO10 electrodes as being capable of converting NO_x in the presence of 10% O_2 the development of electrodes for electrochemical deNO_x has been put one step forward, but much more work is needed before commercialization of the technology becomes possible. This work should firstly focus on stability and durability tests of impregnated electrodes, aimed at clarifying at which temperatures and voltages the electrodes can be considered stable. Furthermore it should be investigated how other components in diesel engine exhaust, like unburned hydrocarbons, H_2O, CO_2, CO, SO_2; affects the electrode

performance and stability, and the influence of combining NO_x reduction and hydrocarbon oxidation in the same electrochemical cell should be investigated.

At the end the final goal is the development of a one component electrocatalytic filter, which during polarisation is capable of both reducing the NO_x and oxidizing the unburned hydrocarbons from diesel engine exhaust. The findings in this project contributes to the development of this technology, however much more research with respect to electrode testing and improvement is needed, not to mention research on the actual design and real life testing of the filter, before the technology becomes commercially competitive to other NO_x removal technologies on the market.

References

1 G. Rayner-Canham, *Descriptive Inorganic Chemistry, Second Edition,* W. H. Freeman and Company, New York, 2000.

2 European Environment Agency, *www.eea.europa.eu,* (accessed 22/12, 2011).

3 V. Vestreng, L. Ntziachristos, A. Semb, S. Reis, I. S. A. Isaksen and L. Tarrason, *Atmos. Chem. Phys.,* 2009, **9,** 1503-1520.

4 K. K. Hansen, *Appl. Catal. B,* 2010, **100,** 427-432.

5 H. Bosch and F. Janssen, *Catal. Today,* 1988, **2,** 369-379.

6 J. B. Zeldovich, *C. R. Acad. Sci. URSS,* 1946, **51,** 217-220.

7 J. Kaspar, P. Fornasiero and N. Hickey, *Catal. Today,* 2003, **77,** 419-449.

8 F. Garin, *Appl. Catal. A,* 2001, **222,** 183-219.

9 R. G. Derwent and H. N. M. Stewart, *Atmos. Environ.,* 1973, **7,** 385-401.

10 S. Grice, J. Stedman, A. Kent, M. Hobson, J. Norris, J. Abbott and S. Cooke, *Atmos. Environ.,* 2009, **43,** 2154-2167.

11 K. Wark, C. F. Warner and W. T. Davis, *Air Pollution its Origin and Control, Third Edition,* Addison Wesley Longman, Inc., USA, 1998.

12 Ecopoint Inc., *www. dieselnet. com/standards/eu/hd.php,* (accessed 21/6 2011).

References

13 M. V. Twigg, *Appl. Catal. B,* 2007, **70,** 2-15.

14 P. Granger and V. I. Parvulescu, *Chem. Rev.,* 2011, **111,** 3155-3207.

15 Amminex A/S, *www. amminex.net,* (accessed 30/4 2012).

16 Y. Zhao, J. Hu, L. Hua, S. Shuai and J. Wang, *Ind. Eng. Chem. Res.,* 2011, **50,** 11863-11871.

17 Y. Traa, B. Burger and J. Weitkamp, *Microporous Mesoporous Mater.,* 1999, **30,** 3-41.

18 R. Burch, J. P. Breen and F. C. Meunier, *Appl. Catal. , B,* 2002, **39,** 283-303.

19 N. Takahashi, H. Shinjoh, T. Iijima, T. Suzuki, K. Yamazaki, K. Yokota, H. Suzuki, N. Miyoshi, S. Matsumoto, T. Tanizawa, T. Tanaka, S. Tateishi and K. Kasahara, *Catal. Today,* 1996, **27,** 63-69.

20 S. Matsumoto, *CATTECH,* 2000, **4,** 102-109.

21 W. S. Epling, L. E. Campbell, A. Yezerets, N. W. Currier and J. E. Parks, *Catal. Rev. Sci. Eng.,* 2004, **46,** 163-245.

22 S. Pancharatnam, R. A. Huggins and D. M. Mason, *J. Electrochem. Soc.,* 1975, **122,** 869-875.

23 T. Gür and R. Huggins, *J. Electrochem. Soc.,* 1979, **126,** 1067-1075.

24 D. C. Cicero and L. A. Jarr, *Sep. Sci. Technol.,* 1990, **25,** 1455-1472.

25 G. Reinhardt, H. -. Wiemhoefer and W. Goepel, *Ionics,* 1995, **1,** 32-39.

References

26 T. Hibino, *Chem. Lett.,* 1994, **5,** 927-930.

27 T. Hibino, K. Ushiki, Y. Kuwahara, M. Mizuno, A. Mazegi and H. Iwahara, *J. Chem. Soc. Faraday Trans.,* 1995, **91,** .

28 T. Hibino, T. Inoue and M. Sano, *Solid State Ionics,* 2000, **130,** 19-29.

29 K. J. Walsh and P. S. Fedkiw, *Solid State Ionics,* 1997, **104,** 97-108.

30 K. J. Walsh and P. S. Fedkiw, *Solid State Ionics,* 1996, **93,** 17-31.

31 S. Bredikhin, K. Maeda and M. Awano, *J. Electrochem. Soc.,* 2001, **148,** D133-D138.

32 S. Bredikhin, K. Maeda and M. Awano, *Solid State Ionics,* 2002, **152,** 727-733.

33 K. K. Hansen and E. M. Skou, *Proc. Nordic Workshop on Mat. for Energy Conv.,* 2000, 73.

34 K. K. Hansen, H. Christensen and E. M. Skou, *Ionics,* 2000, **6,** 340.

35 K. K. Hansen, E. M. Skou and H. Christensen, *J. Electrochem. Soc.,* 2000, **147,** 2007-2012.

36 R. M. L. Werchmeister, K. K. Hansen and M. Mogensen, *J. Electrochem. Soc.,* 2010, **157,** P35-P42.

37 R. M. L. Werchmeister, K. Kammer Hansen and M. B. Mogensen, *J. Solid State Electrochem.,* 2011, .

38 R. M. L. Werchmeister, K. K. Hansen and M. Mogensen, *J. Electrochem. Soc.,* 2010, **157,** P107-P112.

39 R. M. L. Werchmeister, K. K. Hansen and M. Mogensen, *Mater. Res. Bull.,* 2010, **45,** 1554-1561.

40 T. Kobayashi, K. Abe, Y. Ukyo and H. Iwahara, *Solid State Ionics,* 2002, **154–155,** 699-705.

41 X. Li and P. Vernoux, *Appl. Catal. B,* 2005, **61,** 267-273.

42 N. MacLeod, F. J. Williams, M. S. Tikhov and R. M. Lambert, *Angewandte Chemie-International Edition,* 2005, **44,** 3730-3732.

43 V. L. E. Simonsen, M. M. Johnsen and K. K. Hansen, *Top. Catal.,* 2007, **45,** 131-135.

44 K. Hamamoto, Y. Fujishiro and M. Awano, *J. Electrochem. Soc.,* 2008, **155,** E109-E111.

45 K. Hamamoto, T. Suzuki, Y. Fujishiro and M. Awano, *J. Electrochem. Soc.,* 2011, **158,** B1050-B1053.

46 A. de Lucas-Consuegra, A. Caravaca, P. Sanchez, F. Dorado and J. L. Valverde, *J. Catal.,* 2008, **259,** 54-65.

47 A. de Lucas-Consuegra, A. Caravaca, F. Dorado and J. L. Valverde, *Catal. Today,* 2009, **146,** 330-335.

48 A. de Lucas-Consuegra, F. Dorado, C. Jimenez-Borja, A. Caravaca, P. Vernoux and J. L. Valverde, *Catal. Today,* 2009, **146,** 293-298.

49 Y. Yoshinobu , Y. Tsuda , H. Ueda , Y. Nakanishi and J. Gong , *SAE Int. J. Fuels Lubr.,* 2010, **3,** 50-60.

50 S. P. Jiang, *J. Mater. Sci.,* 2008, **43,** 6799-6833.

51 H. Kamata, Y. Yonemura, J. Mizusaki, H. Tagawa, K. Naraya and T. Sasamoto, *J. Phys. Chem. Solids,* 1995, **56,** 943-950.

52 M. Kertesz, I. Riess, D. S. Tannhauser, R. Langpape and F. J. Rohr, *J. Solid State Chem.,* 1982, **42,** 125-129.

53 J. H. Kuo, H. U. Anderson and D. M. Sparlin, *J. Solid State Chem.,* 1990, **87,** 55-63.

54 M. J. Jørgensen and M. Mogensen, *J. Electrochem. Soc.,* 2001, **148,** A433-A442.

55 A. Hammouche, E. Siebert, A. Hammou, M. Kleitz and A. Caneiro, *J. Electrochem. Soc.,* 1991, **138,** 1212-1216.

56 J. H. Kuo, H. U. Anderson and D. M. Sparlin, *J. Solid State Chem.,* 1989, **83,** 52-60.

57 Poulsen, F. W., *Solid State Ionics,* 2000, **129,** 145-162.

58 S. P. Jiang and J. G. Love, *Solid State Ionics,* 2003, **158,** 45-53.

59 M. Backhaus-Ricoult, K. Adib, T. St.Clair, B. Luerssen, L. Gregoratti and A. Barinov, *Solid State Ionics,* 2008, **179,** 891-895.

60 W. Wang and S. P. Jiang, *J. Solid State Electrochem.,* 2004, **8,** 914-922.

61 C. Clausen, C. Bagger, J. B. Bilde-Sørensen and A. Horsewell, *Solid State Ionics,* 1994, **70-71,** 59-64.

References

62 C. W. Sun, R. Hui and J. Roller, *J. Solid State Electrochem.,* 2010, **14,** 1125-1144.

63 O. A. Marina, L. R. Pederson, M. C. Williams, G. W. Coffey, K. D. Meinhardt, C. D. Nguyen and E. C. Thomsen, *J. Electrochem. Soc.,* 2007, **154,** B452-B459.

64 J. M. Ralph, C. Rossignol and R. Kumar, *J. Electrochem. Soc.,* 2003, **150,** A1518-A1522.

65 S. P. Simner, J. R. Bonnett, N. L. Canfield, K. D. Meinhardt, J. P. Shelton, V. L. Sprenkle and J. W. Stevenson, *J. Power Sources,* 2003, **113,** 1-10.

66 M. V. Patrakeev, J. A. Bahteeva, E. B. Mitberg, I. A. Leonidov, V. L. Kozhevnikov and K. R. Poeppelmeier, *J. Solids State Chem.,* 2003, **172,** 219-231.

67 K. Kammer Hansen, *Mater. Res. Bull.,* 2010, **45,** 1334-1337.

68 B. Dalslet, P. Blennow, P. V. Hendriksen, N. Bonanos, D. Lybye and M. Mogensen, *J. of Solid State Electrochem.,* 2006, **10,** 547-561.

69 F. Prinetto, G. Ghiotti, I. Nova, L. Lietti, E. Tronconi and P. Forzatti, *J. Phys. Chem. B,* 2001, **105,** 12732-12745.

70 B. Westerberg and E. Fridell, *J. Mol. Catal A: Chem.,* 2001, **165,** 249-263.

71 Y. Ji, T. J. Toops, J. A. Pihl and M. Crocker, *Appl. Catal. , B,* 2009, **91,** 329-338.

72 T. Lesage, J. Saussey, S. Malo, M. Hervieu, C. Hedouin, G. Blanchard and M. Daturi, *Appl. Catal. B,* 2007, **72,** 166-177.

73 T. J. Toops, D. B. Smith, W. S. Epling, J. E. Parks and W. P. Partridge, *Appl. Catal. , B,* 2005, **58,** 255-264.

74 I. Chorkendorff and J. M. Niemantsverdriet , *Concepts of Modern Catalysis and Kinetics,* Wiley-VCH GmbH & Co. KGaA, Weinheim, 2003.

75 Y. Teraoka, K. Kanada and S. Kagawa, *Appl. Catal. B,* 2001, **34,** 73-78.

76 W. F. Shangguan, Y. Teraoka and S. Kagawa, *Appl. Catal. B,* 1998, **16,** 149-154.

77 R. Fricke, E. Schreier, R. Eckelt, M. Richter and A. Trunschke, *Top. Catal.,* 2004, **30-1,** 193-198.

78 J. M. Thomas and W. J. Thomas, *Principles and Practice of Heterogenous Catalysis,* VCH Verlagsgesellschaft mbH, Weinheim, 1997.

79 A. J. McEvoy, *Solid State Ionics,* 2000, **135,** 331-336.

80 M. Baldi, V. Escribano, J. Amores, F. Milella and G. Busca, *Appl. Catal. , B,* 1998, **17,** L175-L182.

81 M. Baldi, E. Finocchio, F. Milella and G. Busca, *Appl. Catal. , B,* 1998, **16,** 43-51.

82 C. Lahousse, A. Bernier, P. Grange, B. Delmon, P. Papaefthimiou, T. Ioannides and X. Verykios, *J. Catal.,* 1998, **178,** 214-225.

83 F. Pinna, *Catal. Today,* 1998, **41,** 129-137.

84 A. Lindholm, N. W. Currier, J. Dawody, A. Hidayat, J. Li, A. Yezerets and L. Olsson, *Appl. Catal. , B,* 2009, **88,** 240-248.

References

85 M. A. Peralta, B. S. Sánchez, M. A. Ulla and C. A. Querini, *Appl. Catal. , A,* 2011, **393,** 184-188.

86 M. Watanabe, H. Uchida, M. Shibata, N. Mochizuki and K. Amikura, *J. Electrochem. Soc.,* 1994, **141,** 342-346.

87 A. V. Virkar, K. Z. Fung and C. W. Tanner, *U. S. Patent 5543239,* 1996, .

88 S. P. Jiang, *Mater. Sci. Eng. A,* 2006, **418,** 199-210.

89 J. M. Vohs and R. J. Gorte, *Adv. Mater.,* 2009, **21,** 943-956.

90 N. Ai, S. P. Jiang, Z. Lue, K. Chen and W. Su, *J. Electrochem. Soc.,* 2010, **157,** B1033-B1039.

91 C. Jin, J. Liu and J. Sui, *J. Electroceram.,* 2011, **26,** 74-77.

92 M. Yang, M. Zhang, A. Yan, M. Yue, Z. Hou, Y. Dong and M. Cheng, *J. Power Sources,* 2008, **185,** 784-789.

93 H. Zhao, D. Teng, X. Zhang, C. Zhang and X. Li, *J. Power Sources,* 2009, **186,** 305-310.

94 J. H. Kim, M. Cassidy, J. T. S. Irvine and J. Bae, *J. Electrochem. Soc.,* 2009, **156,** B682-B689.

95 A. Rolle, N. Preux, G. Ehora, O. Mentre and S. Daviero-Minaud, *Solid State Ionics,* 2011, **184,** 31-34.

96 S. C. Kim and W. G. Shim, *Appl. Catal. , B,* 2010, **98,** 180-185.

97 W. M. Haynes and D. R. Lide, *CRC Handbook of Chemistry and Physics, 91st Edition,* Tayler and Francis Group, LCL, 2010-2011.

References

98 G. W. Coffey, J. Hardy, L. R. Pedersen, P. C. Rieke, E. C. Thomsen and M. Walpole, *Solid State Ionics,* 2003, **158,** 1-9.

99 S. R. Wang, T. Kobayashi, M. Dokiya and T. Hashimoto, *J. Electrochem. Soc.,* 2000, **147,** 3606-3609.

100 G. J. Janz, U. Krebs, H. H. Siegenthaler and R. P. T. Tomkins, *J. Phys. Chem. Ref. Data.,* 1972, **1,** .

101 O. Bjorseth, J. H. Fermor and A. Kjekshus, *Acta Chem. Scand.,* 1971, **25,** 3791-&.

102 O. Ghodbane, J. Pascal and F. Favier, *ACS Appl. Mater. Interfaces,* 2009, **1,** 1130-1139.

103 M. Maneva and N. Petroff, *J. Therm. Anal.,* 1990, **36,** 2511-2520.

104 J. Winkler, P. V. Hendriksen, N. Bonanos and M. Mogensen, *J. Electrochem. Soc.,* 1998, **145,** 1184-1192.

105 T. Z. Sholklapper, C. Lu, C. P. Jacobson, S. J. Visco and L. C. De Jonghe, *Electrochem. Solid-State Lett.,* 2006, **9,** A376-A378.

106 M. Lundberg, B. Skarman, F. Cesar and L. R. Wallenberg, *Microporous Mesoporous Mater.,* 2002, **54,** 97-103.

107 D. Johnson, Scribner Associates 1990-2007, **ZView2, 3.1 c,** .

108 K. Skalska, J. S. Miller and S. Ledakowicz, *Sci. Total Environ.,* 2010, **408,** 3976-3989.

109 M. Stoukides, *Catal. Rev. - Sci. Eng.,* 2000, **42,** 1-70.

References

110 S. Bredikhin, K. Hamamoto, Y. Fujishiro and M. Awano, *Ionics,* 2009, **15,** 285-299.

111 K. K. Hansen, *Appl. Catal. B,* 2005, **58,** 33-39.

112 F. Braestrup and K. K. Hansen, *J. Solid State Electrochem.,* 2009, **13,** 1241-1250.

113 M. L. Traulsen and K. K. Hansen, *Accepted for Publication in J. of Solid State Electrochem. DOI 10. 1007/s10008-012-1684-9,* 2011, .

114 A. Martinezarias, J. Soria, J. C. Conesa, X. L. Seoane, A. Arcoya and R. Cataluna, *J. Chem. Soc. , Faraday Trans.,* 1995, **91,** 1679-1687.

115 M. Niwa, Y. Furukawa and Y. Murakami, *J. Colloid Interface Sci.,* 1982, **86,** 260-265.

116 S. Philipp, A. Drochner, J. Kunert, H. Vogel, J. Theis and E. Lox, *Top. Catal.,* 2004, **30-31,** 235-238.

117 M. O. Symalla, A. Drochner, H. Vogel, S. Philipp, U. Gobel and W. Muller, *Top. Catal.,* 2007, **42-43,** 199-202.

118 S. Hodjati, C. Petit, V. Pitchon and A. Kiennemann, *Appl. Catal. , B,* 2000, **27,** 117-126.

119 Y. Chi and S. Chuang, *J. Phys. Chem. B,* 2000, **104,** 4673-4683.

120 V. G. Milt, C. A. Querini, E. E. Miró and M. A. Ulla, *J. Catal.,* 2003, **220,** 424-432.

121 V. G. Milt, M. A. Ulla and E. E. Miró, *Appl. Catal. , B,* 2005, **57,** 13-21.

122 Y. Zhu, D. Wang, F. Yuan, G. Zhang and H. Fu, *Appl. Catal. , B,* 2008, **82,** 255-263.

References

123 A. Laachir, V. Perrichon, A. Badri, J. Lamotte, E. Catherine, J. Lavalley, J. Elfallah, L. Hilaire, F. Lenormand, E. Quemere, G. Sauvion and O. Touret, *J. Chem. Soc. Faraday Trans.,* 1991, **87,** 1601-1609.

124 R. Roque-Malherbe, O. N. C. Uwakweh, C. Lozano, R. Polanco, A. Hernandez-Maldonado, P. Fierro, F. Lugo and J. N. Primera-Pedrozo, *J. Phys. Chem. C,* 2011, **115,** 15555-15569.

125 C. Li, Y. Sakata, T. Arai, K. Domen, K. Maruya and T. Onishi, *J. Chem. Soc. , Faraday Trans.,* 1989, **85,** 929-943.

126 G. Busca and V. Lorenzelli, *J. Catal.,* 1981, **72,** 303-313.

127 M. Adamowska, A. Krzton, M. Najbar, P. Da Costa and G. Djega-Mariadassou, *Catal. Today,* 2008, **137,** 288-291.

128 L. Cerruti, E. Modone, E. Guglielminotti and E. Borello, *J. Chem. Soc. , Faraday Trans. 1,* 1974, **70,** 729-739.

129 E. Kugler, A. Kadet and J. Gryder, *J. Catal.,* 1976, **41,** 72-81.

130 C. Morterra, F. Boccuzzi, S. Coluccia and G. Ghiotti, *J. Catal.,* 1980, **65,** 231-234.

131 D. A. Outka, R. J. Madix, G. B. Fisher and C. Dimaggio, *Surf. Sci.,* 1987, **179,** 1-24.

132 B. J. Adelman, T. Beutel, G. -. Lei and W. M. H. Sachtler, *J. Catal.,* 1996, **158,** 327-335.

133 G. Delahay, B. Coq, E. Ensuque, F. Figueras, J. Saussey and F. Poignant, *Langmuir,* 1997, **13,** 5588-5592.

References

134 M. Niwa, T. Minami, H. Kodama, T. Hattori and Y. Murakami, *J. Catal.,* 1978, **53,** 198-207.

135 M. Haneda, T. Morita, Y. Nagao, Y. Kintaichi and H. Hamada, *Phys. Chem. Chem. Phys.,* 2001, **3,** 4696-4700.

136 J. Bates and G. Boyd, *Appl. Spectrosc.,* 1973, **27,** 204-208.

137 A. Zecchina, C. Arean, G. Palomino, F. Geobaldo, C. Lamberti, G. Spoto and S. Bordiga, *Phys. Chem. Chem. Phys.,* 1999, **1,** 1649-1657.

138 F. Vratny, *Appl. Spectrosc.,* 1959, **13,** 59-70.

139 K. Williams, P. Li and J. Devlin, *J. Chem. Phys.,* 1968, **48,** 3891-&.

140 W. Fateley, H. Bent and B. Crawford, *J. Chem. Phys.,* 1959, **31,** 204-217.

141 M. Nagao, T. Yoshii, T. Hibino, M. Sano and A. Tomita, *Electrochem. Solid-State Lett.,* 2006, **9,** J1-J4.

142 J. Liu, Z. Zhao, C. Xu, A. Duan and G. Jiang, *J. Phys. Chem. C,* 2008, **112,** 5930-5941.

143 B. Klingenberg and M. A. Vannice, *Appl. Catal. B,* 1999, **21,** 19-33.

144 S. Bredikhin, K. Matsuda, K. Maeda and M. Awano, *Solid State Ionics,* 2002, **149,** 327-333.

145 N. Takahashi, K. Yamazaki, H. Sobukawa and H. Shinjoh, *Appl. Catal. B,* 2007, **70,** 198-204.

146 V. G. Milt, M. L. Pissarello, E. E. Miró and C. A. Querini, *Appl. Catal. B,* 2003, **41,** 397-414.

147 C. Lu, T. Z. Sholklapper, C. P. Jacobson, S. J. Visco and L. C. De Jonghe, *J. Electrochem. Soc.,* 2006, **153,** A1115-A1119.

148 S. P. Jiang, Y. Y. Duan and J. G. Love, *J. Electrochem. Soc.,* 2002, **149,** A1175-A1183.

149 K. K. Hansen, M. Wandel, Y. Liu and M. Mogensen, *Electrochim. Acta,* 2010, **55,** 4606-4609.

150 L. A. Chick, L. R. Pederson, G. D. Maupin, J. L. Bates, L. E. Thomas and G. J. Exarhos, *Mater Lett,* 1990, **10,** 6-12.

151 B. A. A. L. van Setten, M. Makkee and J. A. Moulijn, *Catal. Rev. - Sci. Eng.,* 2001, **43,** 489.

152 E. Barsoukov and J. R. Macdonald, *Impedance Spectroscopy Theory, Experiment and Applications, Second Edition,* John Wiley and Sons, Inc., Hoboken, New Jersey, 2005.

153 T. Jacobsen, B. Zachau-Christiansen, L. Bay and S. Skaarup, *High Temperature Electrochemistry: Ceramics and Metals,* 1996, 29-40.

154 S. Omar, E. D. Wachsman, J. L. Jones and J. C. Nino, *J. Am. Ceram. Soc.,* 2009, **92,** 2674-2681.

155 S. B. Adler, J. A. Lane and B. C. H. Steele, *J. Electrochem. Soc.,* 1996, **143,** 3554-3564.

156 H. Y. Lee, W. S. Cho, S. M. Oh, H. D. Wiemhofer and W. Gopel, *J. Electrochem. Soc.,* 1995, **142,** 2659-2664.

157 Y. Teraoka, H. M. Zhang, K. Okamoto and N. Yamazoe, *Mater. Res. Bull.,* 1988, **23,** 51-58.

158 Z. Zhang, Y. Zhang, Q. Su, Z. Wang, Q. Li and X. Gao, *Environ. Sci. Technol.,* 2010, **44,** 8254-8258.

159 Z. He, K. Bohm, A. L. Keel, F. B. Nygaard, M. Menon and K. K. Hansen, *Ionics,* 2009, **15,** 427-431.

160 T. J. Toops, D. B. Smith and W. P. Partridge, *Catal. Today,* 2006, **114,** 112-124.

161 W. S. Epling, A. Yezerets and N. W. Currier, *Appl. Catal. B,* 2007, **74,** 117-129.

162 J. Bruno, A. Cavalheiro, M. Zaghete and J. Varela, *Ceram. Int.,* 2006, **32,** 189-194.

163 A. Nzihou, B. Adhikari and R. Pfeffer, *Ind. Eng. Chem. Res.,* 2005, **44,** 1787-1794.

164 G. J. Janz, *Molten Salts Handbook,* Academic Press Inc., New York, 1967.

165 J. I. Gazzarri and O. Kesler, *J. Power Sources,* 2007, **167,** 430-441.

166 E. Murray, T. Tsai and S. Barnett, *Solid State Ionics,* 1998, **110,** 235-243.

167 S. Bredikhin, K. Maeda and M. Awano, *Solid State Ionics,* 2001, **144,** 1-9.

168 S. Gordon and C. Campbell, *Anal. Chem.,* 1955, **27,** 1102-1109.

169 F. Lazarini and B. S. Brcic, *Monatshefte Für Chemie Und Verwandte Teile Anderer Wissenschaften,* 1966, **97,** 1318-&.

170 A. L. Kustov and M. Makkee, *Appl. Catal. B,* 2009, **88,** 263-271.

References

171 K. Adams, J. Cavataio and R. Hammerle, *Appl. Catal. B,* 1996, **10,** 157-181.

172 J. Bentzen and J. V. T. Høgh, *Report on the Influence of Current Density and Temperature on the Cr evaporation/poisoning and the Cr Poisoning Sensitivity of Two Cathode Types,* 2007, Deliverable No. 2.2.1 in the SOFC600 project.

173 J. Bentzen, *Personal Communication with J. Bentzen, Senior Development Engineer in Department of Energy Conversion and Storage, Technical University of Denmark,* April 2012.

174 S. P. Jiang and J. G. Love, *Solid State Ionics,* 2001, **138,** 183-190.

175 S. Koch, M. Mogensen, P. V. Hendriksen, N. Dekker and B. Rietveld, *Fuel Cells,* 2006, **6,** 117-122.

176 V. Kharton, A. Kovalevsky, A. Viskup, F. Figueiredo, A. Yaremchenko, E. Naumovich and F. Marques, *J. Electrochem. Soc.,* 2000, **147,** 2814-2821.

177 Y. Orikasa, T. Ina, T. Fukutsuka, Y. Uchimoto, K. Amezawa and T. Kawada, *Meet. Abstr. - Electrochem. Soc.,* 2008, **802,** 1304.

178 Y. Orikasa, T. Ina, T. Nakao, T. Fukutsuka, A. Mineshige, K. Amezawa, T. Kawada and Y. Uchimoto, *Meet. Abstr. - Electrochem. Soc.,* 2010, **1001,** 531-531.

179 A. R. West, *Basic Solid State Chemistry,* John Wiley and Sons, LTD, Chichester, England, 1999.

180 K. Amezawa, T. Ina, Y. Orikasa, A. Unemoto, H. Watanabe, F. Iguchi, Y. Terada, T. Fukutsuka, T. Kawada, H. Yugami and Y. Uchimoto, *ECS Trans.,* 2009, **25,** 345-348.

References

181 A. Braun, S. Shrout, A. C. Fowlks, B. A. Osaisai, E. J. Cairns, S. Shrout, B. A. Osaisai, A. C. Fowlks, S. Seifert, E. Granlund and E. J. Cairns, *J. Synchrotron Radiat.,* 2003, **10,** 320-325.

182 M. Balasubramanian, X. Sun, X. Q. Yang and J. McBreen, *J. Power Sources,* 2001, **92,** 1-8.

183 M. Sikora, C. Kapusta, K. Knizek, Z. Jirak, C. Autret, M. Borowiec, C. Oates, V. Prochazka, D. Rybicki and D. Zajac, *Phys. Rev. B,* 2006, **73,** 094426.

184 H. Bloom, *The Chemistry of Molten Salts,* W. A. Benjamin, Inc., New York, 1967.

185 S. P. Jiang and W. Wang, *J. Electrochem. Soc.,* 2005, **152,** A1398-A1408.

186 M. B. Mogensen, M. Søgaard, P. Blennow Tullmar and K. Kammer Hansen, *In: Proceedings (on CD-ROM) 8. European Solid Oxide Forum, Lucerne,* 2008.

187 C. Engel and S. Käfer, *Personal Communication, Advanced Functional and Sintered Materials - Ceramics Department, Bosch,* 2010.

Appendix A

The article “Spectroelectrochemical Cell for *in situ* studies of solid oxide fuel cells” published in Journal of Synchroton Radiation.

Journal of
Synchrotron Radiation

ISSN 0909-0495

Received 13 December 2011
Accepted 15 February 2012

Spectroelectrochemical cell for *in situ* studies of solid oxide fuel cells

Anke Hagen,* Marie Lund Traulsen, Wolff-Ragnar Kiebach and Bjoern Sejr Johansen

Department of Energy Conversion and Storage, DTU, Risoe Campus, Frederiksborgvej 399, Roskilde 4000, Denmark. E-mail: anke@dtu.dk

Solid oxide fuel cells (SOFCs) are able to produce electricity and heat from hydrogen- or carbon-containing fuels with high efficiencies and are considered important cornerstones for future sustainable energy systems. Performance, activation and degradation processes are crucial parameters to control before the technology can achieve breakthrough. They have been widely studied, predominately by electrochemical testing with subsequent micro-structural analysis. In order to be able to develop better SOFCs, it is important to understand how the measured electrochemical performance depends on materials and structural properties, preferably at the atomic level. A characterization of these properties under operation is desired. As SOFCs operate at temperatures around 1073 K, this is a challenge. A spectro-electrochemical cell was designed that is able to study SOFCs at operating temperatures and in the presence of relevant gases. Simultaneous spectroscopic and electrochemical evaluation by using X-ray absorption spectroscopy and electrochemical impedance spectroscopy is possible.

Keywords: XANES; *in situ*; SOFC; LSCF; impedance spectroscopy.

1. Introduction

Solid oxide fuel cells (SOFCs) produce electricity and heat from hydrogen- or carbon-containing fuels with high efficiencies and low pollution degrees; no NO_x or particles are emitted. CO_2, formed when using carbon-containing fuels, emerges concentrated and is thus cheaper to collect and to process further. SOFCs consist of two electrodes on the opposite sides of a solid electrolyte layer. The catalytic processes in a SOFC involve reduction of oxygen at the cathode, transport of oxygen ions through the cathode and electrolyte into the anode, where oxidation of the fuel (hydrogen, methane, carbon monoxide) occurs. Materials for state-of-the-art SOFCs comprise Ni/YSZ (yttria stabilized zirconia) anodes, YSZ electrolytes and LSM/YSZ (lanthanum strontium manganite) or LSCF (lanthanum strontium cobaltite ferrite) cathodes. Typical operating temperatures are in the range between 923 K and 1123 K (see, for example, Huang & Goodenough, 2009). One of the main challenges to be solved for SOFC technology is maintaining high performance over a long lifetime.

Large efforts have been focused on studying degradation processes, identifying origins of degradation and developing improved, more durable SOFCs [see recent status in the review by Knibbe *et al.* (2011)]. Usually, SOFCs are tested for electrochemical performance and afterwards (*post mortem*) structural and spectroscopic analysis is carried out. One of the problems with this approach is the lack of information under operating conditions, and the obtained results from *post mortem* evaluation are not always related to the actual performance/changes of performance. For detailed mechanistic studies on the microscopic/atomic level, materials, single crystals or specifically designed model systems are used instead of the full electrochemical cell, mostly owing to restrictions of the applied characterization method. *In situ* techniques have been developed to overcome this barrier.

The *in situ* studies investigated, for example, spectroscopic and structural properties separately from the electrochemical characteristics, often using model systems, *i.e.* material powders, instead of real electrochemical cells. The effect of oxygen partial pressure on barium strontium cobaltite ferrite perovskite-type SOFC cathode materials was, for example, investigated by Mueller *et al.* (2009) using XANES (X-ray absorption near-edge spectroscopy) and EXAFS (extended X-ray absorption fine structure) at relevant operating temperatures of 773–923 K, revealing the detailed reduction processes of the transition metals.

The recent progress of *in situ* investigations of SOFCs achieved by optical methods has been summarized by Pomfret *et al.* (2010).

Also, for other electrochemical devices, *in situ* methods have been further developed. The redox behaviour of cuprate- and nickelate-based electrodes for the direct electrochemical NO_x reduction was studied using *in situ* XANES at high

temperature and in the presence of relevant gases (NO or air) (Mueller *et al.*, 2009; Simonsen *et al.*, 2009). The results were related to separately determined electro-catalytic properties and the necessity of a combination of the two method approaches was concluded in order to be able to identify the relevant mechanisms.

The combination of an electrochemical cell with X-ray characterization was, for example, reported by Rodriguez *et al.* (2000), who successfully investigated Li-ion batteries. These *in situ* studies were carried out at room temperature. Also, for the study of Li-ion battery electrodes, an electrochemical *in situ* reaction cell was designed and successfully realised by Braun *et al.* (2003), allowing for the combination of XRD, ASAXS, XANES and EXAFS characterization.

Ultimately, it is desired to carry out studies under high-temperature conditions, where electrochemical cells like the SOFCs are operating, in order to understand phenomena which only occur under real operating conditions, *i.e.* under polarization (current/voltage). It is, for example, well known that some processes such as the activation of LSM-based cathodes in SOFCs are only occurring under polarization, which is therefore needed to elucidate the underlying mechanisms. Yildiz *et al.* (2006) investigated this effect on LSM and LSCM (lanthanum strontium calcium manganite) based electrodes deposited on single-crystal YSZ electrolytes and related the activation under polarization at higher temperatures to the change of the chemical state of lanthanum. Backhaus-Ricoult *et al.* (2008), on the other hand, studied the same subject on patterned LSM cathodes on YSZ electrolytes with an *in situ* photoelectron microscopy cell and suggested an extension of the active area for oxygen incorporation over the electrolyte surface by partially reduced manganese oxide species to be responsible for the activation. The mechanism of electrochemical oxygen reduction on samarium strontium cobaltite cathodes was studied in detail using *in situ* potential-dependent FTIR emission spectroscopy (Lu *et al.*, 2002).

These examples demonstrate that different spectroscopic methods can be applied during electrochemical operation of SOFCs. It is important though to consider the used SOFC configurations and sets of operating conditions before general conclusions can be drawn. For example, can the different studies reveal phenomena related to the surface, the bulk or interface and thus possibly give different feedback for the same system.

In this paper, an *in situ* cell is presented that enables the study of real electrochemical cells such as SOFCs at relevant temperatures and in the presence of relevant gases with respect to electrochemical and spectroscopic properties, using electrochemical impedance spectroscopy (EIS) and XANES, respectively.

A combination of these two methods was chosen as EIS is a powerful method for evaluating the resistances of the SOFC in detail; in particular, it is possible to deconvolute the total resistance of the SOFC into contributions from the single layers and processes in the cell (*e.g.* Højgaard Jensen *et al.*, 2009). The chemical and, to a lesser extent, electronic properties of the constituents of the SOFC can be characterized by using XANES, and the method can be carried out under conditions relevant for the electrochemical cells. In this paper the spectroelectrochemical cell was used for SOFCs. They were characterized by EIS and XANES under conditions typical for operation of a SOFC.

2. Experimental section

2.1. Samples

In order to verify the potential of the spectro-electrochemical cell, the following solid oxide cell configuration was chosen: on one side of the fuel cell a thin-film LSCF electrode ($La_{0.58}Sr_{0.4}Co_{0.2}Fe_{0.8}O_{3-\delta}$) was deposited by pulsed laser deposition onto a 500 µm-thick YSZ single crystal at 973 K and an oxygen partial pressure (pO_2) of 300 mtorr. The thickness of the electrode was ~270 nm; on the other side of the electrolyte, the electrode was a ~20 µm-thick conventional LSCF–CGO10 (cerium gadolinium oxide) composite electrode deposited by screen-printing on the YSZ single crystal. The cell was subsequently sintered at 1073 K for 72 h.

The cells were cut into 5 mm × 5 mm pieces. Pt-paste current collection layers were painted on the electrodes while leaving a small 1 mm × 1 mm area in the middle of the electrode free on the thin-film electrode that was used as the working electrode (see Fig. 1*a*). This area was used for detection of the fluorescence signal when recording the XANES spectrum. The cell was placed on the sample holder (see Fig. 1*b*) and heated to a temperature of 973 K in order to firmly attach the Pt onto the electrodes.

(*a*)

(*b*)

Figure 1
(*a*) Illustration of the fuel cell configuration: one thin film and one porous electrode on either side of a single-crystal electrolyte, Pt-paste current collection layer on top of the thin-film electrode. (*b*) Image of a 5 mm × 5 mm SOFC piece (grey) in the ceramic sample holder. Au wires are attached using the Pt current-collector layer (white); the spot in the centre marks the synchrotron beam inlet and fluorescence detection signal outlet.

To verify the results from the spectroelectrochemical cell, LSCF powders with compositions $La_{0.3}Sr_{0.7}Co_{0.5}Fe_{0.5}O_{3-\delta}$ (powder 1) and $(La_{0.6}Sr_{0.4})_{0.99}Fe_{0.8}Co_{0.2}O_3$ (powder 2) were investigated in another XANES cell set-up. About 3 mg of the powdered samples were mixed with ~20 mg alumina in a mortar, subsequently pressed to pellets of diameter 13 mm, and placed vertically in a glass *in situ* XANES cell heated by a tube furnace (for details, see Hagen, 2011). Here, spectra of the sample and the respective metal foil as reference were measured simultaneously in transmission.

2.2. Spectroelectrochemical cell

The cell (see Fig. 2) was made of aluminium with Kapton windows (~15 mm diameter) for the beam inlets and outlets straight through the cell and one larger 50 mm window perpendicular to the beamline for fluorescence detection. It is equipped with gas inlet and outlet fittings and an insert for the sample holder, including wires. Radiative heating was realised by an Osram lamp, and the sample was mounted 6 mm from the focal point of the Osram lamp, to avoid a too violent heating of the sample. The surroundings of the sample and the cell itself remained cold. Using this approach, active cooling to avoid high temperatures in the close vicinity of the spectroelectrochemical cell and at beamline components was not needed. If a voltage of 15 V is applied on the lamp, a black body in the focal point of the Osram lamp will be at 1573 K.

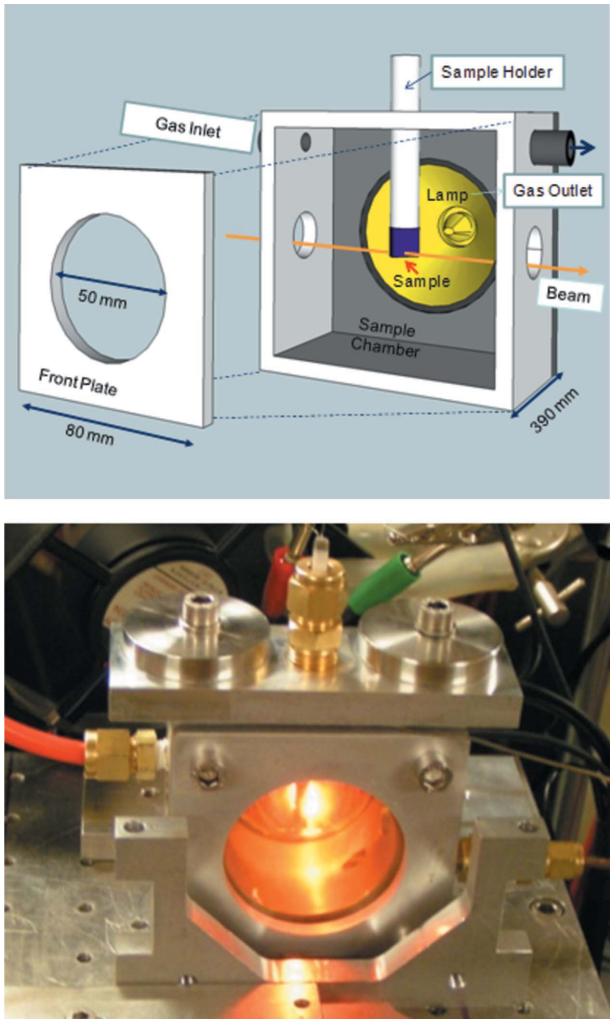

Figure 2
Drawing of the spectroelectrochemical cell and a photograph of it in operation. The sample holder is inserted vertically from the top. The heating lamp is on the back and a Kapton window, to measure the fluorescence, is in front of the cell.

The temperature was determined directly on the sample spot by combining EIS with knowledge of the conductivity of the YSZ electrolyte. Specifically, EIS was recorded and the serial resistance was determined from the high-frequency interception of the impedance spectrum with the real part of the complex impedance. The serial resistance is related to the conductivity of the YSZ according to equation (1), in which σ_{YSZ} is the conductivity of the YSZ electrolyte, A is the area of the cell and l is the thickness of the electrolyte. The temperature dependency of σ_{YSZ} is given in equation (2), and by combining (1) and (2) it was possible to precisely determine the temperature of the sample from the recorded EIS,

$$R_{\rm Serial} = \frac{1}{\sigma_{\rm YSZ}} \frac{l}{A}, \tag{1}$$

$$\sigma_{\rm YSZ}\, S\,[{\rm cm}] = 3.34 \times 10^4 \exp(-10300/T). \tag{2}$$

The heating rate for the sample was ~10 K min^{-1}. The sample was tilted approximately 45° compared with the light beam from the lamp. The gases (21% O_2 in He and pure He) were supplied through mass flow controllers, usually with a flow rate of 20–50 ml min^{-1}. Different oxygen partial pressures were obtained by mixing the gas flows appropriately.

2.3. EIS and XANES measurements

The tests were carried out at beamline A1, HASYLAB (Hamburger Synchrotronstrahlungslabor) at DESY (Deutsches Elektronen-Synchrotron) in Hamburg. A 1/2 demagnified focused beam provided a working range of 2.4–8.3 keV. Two Si 111 crystal pairs are installed as monochromators. In order to focus the beam and effectively suppress higher harmonics, two mirrors can be used, one Ni coated and one partly Ni coated and uncoated SiO_2.

The cell was positioned between the first ionization chamber (after the incoming synchrotron beam) and the second one (before the chamber for reference foils).

A passivated implanted planar silicon (PIPS) detector was used for the detection of fluorescence X-rays from the sample. The current through the PIPS detector was measured using a Keithley 428 current meter. Two Mylar foils were used to shield the light from the spectroelectrochemical cell.

The used XANES energy ranges and step sizes for the relevant metals are summarized in Table 1. XANES spectra were recorded periodically during heating and at constant temperature without and under polarization. The raw data were treated using the program *WinXAS*. Typically, the spectra were smoothed using the Fourier function. The first inflection point (zero of the second derivative) was assigned

Table 1
Energy intervals and step sizes for XANES measurements.

Fe edge: 7112 eV				
Energy (eV)	7063	7107	7140	7210
Step size (eV)	0.5	0.1	0.5	Stop
Co edge: 7709 eV				
Energy (eV)	7660	7704	7737	7807
Step size (eV)	0.5	0.1	0.5	Stop

the edge. The background was corrected using two linear functions and the edge jump was normalized to unity.

The energy calibration was established before and after the *in situ* experiments with absorption measurements on a 5 µm-thick Cr metal foil, which was placed between the second and third ionization chamber.

For impedance spectra and polarization of the cells, a Gamry Reference 600 Potentiostat was used. The impedance spectra were recorded in the frequency range 1 MHz–0.1 Hz with the voltage amplitude 36 mV r.m.s. and six points recorded per decade. The thin-film electrode/working electrode assembly of the fuel cell was polarized cathodically at −100 mV, −300 mV and −500 mV for 1–2 h.

3. Results and discussion

3.1. Selection of samples

The probing depth for the *K*-edges of the investigated transition metals using a fluorescence detector is several micrometres, depending on the intensity of the incoming beam. The recorded spectra therefore truly represent the bulk material, since the measurements in the used mode are not surface sensitive (like, for example, in total-electron-yield measurements). Thin-film electrodes were chosen for this study because a change in oxidation state owing to the polarization should be easier to detect on thin-film electrodes compared with conventional porous electrodes for the following reason: when a conventional screen-printed electrode of 20–30 µm thickness is polarized, the current flow owing to the migration of O^{2-} ions, and thereby the change in oxidation states in the electrode material, will be largest in the electrode part closest to the electrolyte (Nielsen *et al.*, 2011). As the XANES spectrum is probing the bulk, a XANES spectrum recorded on conventional electrodes under polarization will probably not be able to detect the changes in the oxidation states occurring only in the deeper electrode layers closer to the electrolyte. By choosing a thin-film sample of ∼300 nm thickness, the O^{2-} migration and change in oxidation state is expanded through the entire thin film, and will therefore be better detectable in the XANES spectrum.

3.2. XANES verification

The fuel cells contained LSCF layers that are used for SOFC cathodes on a YSZ electrolyte. In order to assign the comparability of XANES spectra of LSCF for different sample compositions, preparations, measuring conditions and XANES configurations, room-temperature XANES spectra were recorded. In Fig. 3 (for values see Table 2), room-temperature Fe XANES spectra for two fuel cells from different batches are shown together with a LSCF powder pressed to a pellet with alumina and measured previously at room temperature in the XANES cell described by Hagen (2011). The spectra show pre-edge features originating from 1*s* to 3*d* transitions, while the white line (maximum at the edge) is due to dipole-allowed 1*s* to 4*p* transitions [for a detailed discussion see also Haas *et al.* (2009)]. The edge energies for the main Fe edge were around 7.128 keV in all cases (7.1282 and 7.1283 keV for the two fuel cells). Consequently, comparing the two different types of LSCF samples, a good agreement can be concluded. The LSCF electrodes in the two fuel cells from different batches yield almost identical XANES spectra; small differences are only visible after the pre-edge feature, which indicate a robust and reproducible way of sample preparation and measurement.

Table 2
Edge energy values for LSCF in fuel cells ($La_{0.58}Sr_{0.4}Co_{0.2}Fe_{0.8}O_{3-\delta}$), measured in the spectroelectrochemical cell, LSCF powder 1 ($La_{0.3}Sr_{0.7}Co_{0.5}Fe_{0.5}O_{3-\delta}$) and LSCF powder 2 [$(La_{0.6}Sr_{0.4})_{0.99}Fe_{0.8}Co_{0.2}O_3$], both measured in the XANES cell presented by Hagen (2011), obtained from XANES spectra at room temperature and 773 K or 873 K.

	Room temperature	773 K	873 K	ΔE
Fe XANES edge				
Fuel cell (eV)	7128.2		7127.8	0.4
Powder 1 (eV)	7128.1	7128.0		0.1
Powder 2 (eV)	7127.3			
Co XANES edge				
Fuel cell (eV)	7726.0		7724.9	1.1
Powder 1 (eV)	7724.6	7723.7		0.9
Powder 2 (eV)	7724.1			

The Co valence (and thus edge) is very sensitive to the stoichiometry/oxygen vacancies of the perovskite sample. Therefore, the edge energies are to some extent different for

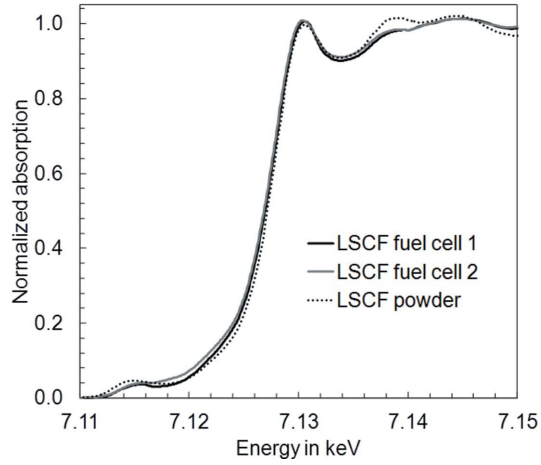

Figure 3
Room-temperature Fe XANES spectra of two fuel cells with LSCF layers deposited on YSZ from two batches (measured in 21% O_2 in He using fluorescence detector in the spectroelectrochemical cell) and one LSCF powder, pressed into a pellet using alumina [measured in air in transmission, in the *in situ* cell presented by Hagen (2011)].

the different LSCF samples (see Table 2), where the formal valence of Co at room temperature is in the order $La_{0.58}Sr_{0.4}Co_{0.2}Fe_{0.8}O_{3-\delta}$ (fuel cell) > $(La_{0.6}Sr_{0.4})_{0.99}Fe_{0.8}Co_{0.2}O_3$ (powder 2) $\simeq$ $La_{0.3}Sr_{0.7}Co_{0.5}Fe_{0.5}O_{3-\delta}$) (powder 1). Thus, the differences can be related to the chemical composition of the LSCF samples and not to the configuration of the XANES set-up.

The fuel cells were heated to 873 K in 21% O_2 in He. In Fig. 4 the Fe and Co XANES spectra are shown for room temperature and 873 K. For the case of iron, only small changes were observed comparing room temperature and 873 K spectra. Quantitative analysis revealed a change of the edge energy by 0.4 eV towards lower energies (see Table 2). Such a small change is close to the error of the measurement of 0.1–0.2 eV. Evaluating the cobalt in the LSCF, on the other hand, a significant shift of the XANES spectrum towards lower energies was observed. The energy value for the main absorption edge decreased by 1.1 eV, indicating a reduction of cobalt ions in the perovskite structure from four to lower valance. The same effect was observed when a LSCF powder was studied, although the highest temperature in this case was only 773 K and the gas atmosphere was synthetic air (see Table 2).

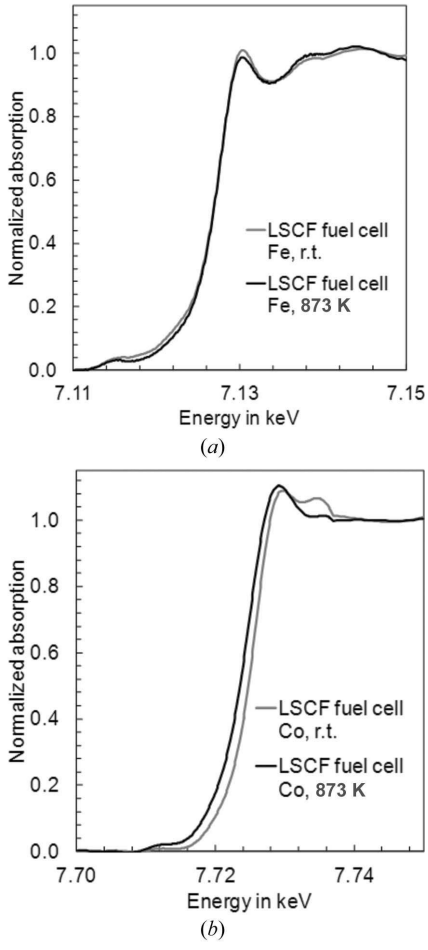

Figure 4
Fe-XANES (*a*) and Co-XANES (*b*) spectra of the fuel cell with LSCF electrodes recorded at room temperature and at 873 K in 21% O_2 in He.

The positions of the energy features (threshold, pre-edge peak, main edge and 1*s* to 4*p* transition) in XANES spectra of metal oxides are strongly dependent on the oxidation state of the absorbing transition metal. It was found that they shifted linearly to higher-energy values (so-called chemical shift) with increasing oxidation state of the metal (Wong *et al.*, 1984). In addition to the valence, the chemical shift is due to electronegativity of ligands, coordination number and other structural features. Typically, the edge energy shifts by 2–4 eV when the oxidation state shifts by one unit [see, for example, Wong *et al.* (1984) and Rasmussen *et al.* (2003) for vanadium, Figueroa *et al.* (2005) for manganese, and Le Toquin *et al.* (2006) for copper in different oxidic structures]. In the present studies the energy shift of 1.1 eV would correspond to a mean oxidation state of cobalt in the reduced state of ~3.7 or a reduction of up to ~1/3 Co(IV) to Co(III) ions [see also discussion in Hagen & Mikkelsen (2005)].

The partial reduction of Co ions in the LSCF perovskite structure can be related to the change of the oxygen stoichiometry in samples of the general formula $La_{1-x}Sr_xCo_{1-y}Fe_yO_{3-\delta}$, where δ expresses the degree of oxygen non-stoichiometry. It was found by, for example, temperature-programmed reduction and solid electrolyte coulometry that δ increased with increasing temperature, decreasing oxygen partial pressure and increasing Sr or Co content (Mantzavinos *et al.*, 2000; Scott *et al.*, 2002).

Using the edge energy shift obtained by XANES between room and elevated temperature in this work and the related estimated portion of reduced Co in the perovskite, a δ of ~0.05 can be estimated. This value fits well into the general trend found by Scott *et al.* (2002) or by Plonczak *et al.* (2012). The strength of the XANES method as applied here is that the reduction as a consequence of a change of the oxygen stoichiometry can be mainly related to the Co ions in the perovskite. With these first measurements at room and elevated temperature, the spectroelectrochemical cell was verified with regard to choice of sample (powder *versus* fuel cell), temperature (different heating methods and temperature probes) and reproducible XANES spectra (transmission *versus* fluorescence in different set-ups).

3.3. EIS verification

The electrochemical properties were studied by EIS at temperatures around 873 K. In order to verify the spectroelectrochemical cell regarding EIS, the results are compared with impedance spectra recorded in a typical set-up for EIS on symmetric cells with thin-film LSCF electrodes on both sides of a YSZ electrolyte crystal ('thin-film cells'). In Fig. 5 the impedance spectra are presented by Nyquist and Bode plots.

The primary resistance values obtained from the Nyquist plot of impedance spectra of an electrochemical cell are the serial and the polarization resistance (see Fig. 5*a*). The serial resistance (R_s) in the impedance plot is the value of the high-frequency interception of the curve with the real part of the complex impedance and originates mainly from the ohmic

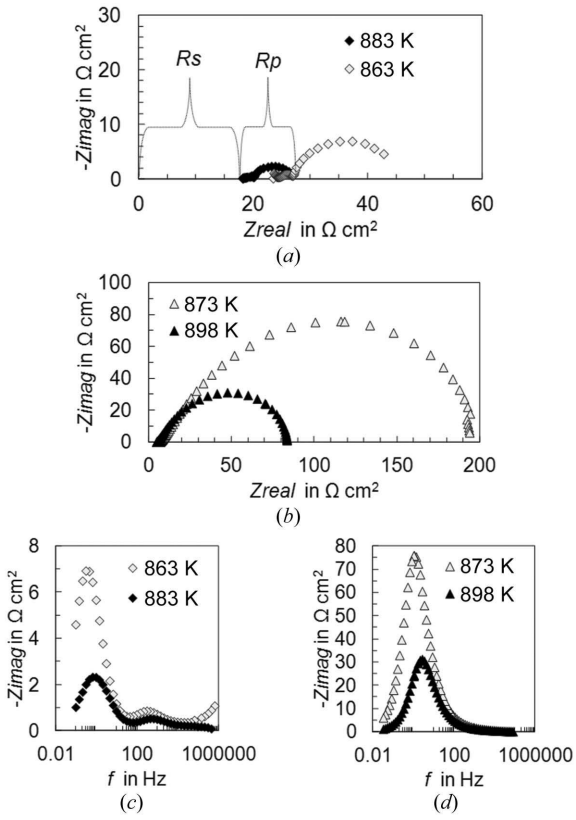

Figure 5
Impedance spectra, Nyquist plots (*a*, *b*) and Bode plots (*c*, *d*) measured on the fuel cell in the spectroelectrochemical cell at 863 K and 873 K in 21% O_2 in He (*a*, *c*), and on the thin-film cell, measured in the EIS set-up at 873 K and 898 K in 100% O_2 (*b*, *d*). R_s and R_p are illustrated on the impedance spectrum at 883 K (*a*).

resistance of the electrolyte. This value is for a given electrolyte (and known thickness) correlated with the temperature [see equations (1) and (2)]. The polarization resistance (R_p) is the difference between the low- and high-frequency interceptions (see Fig. 5*a*) and is a measure of the losses (activity) of the electrode. The smaller the resistance, the more active is the electrode. Further, time-resolved elementary processes on the electrode appear as single arcs that partly overlap in the polarization part of the plot. They become more visible in a first approximation by the Bode plot of the impedance spectrum [see Figs. 5(*c*) and 5(*d*)]. The impedance spectra are sensitive to the structural and compositional characteristics of a specific electrode, and the operating conditions.

The impedance spectrum of the fuel cell (Fig. 5*a*) yields the combined resistances from both electrodes, one being a thin-film LSCF electrode and the other a porous LSCF/CGO composite. By far the largest impedance contribution [factor ~100, compare with typical values for porous LSCF-based cathodes in Nielsen *et al.* (2011)] arises from the thin-film electrode, owing to the small surface area and thus very low activity. When evaluating the impedance spectra, the focus can therefore be placed on the thin-film electrode.

The two impedance spectra in Fig. 5(*a*) were obtained at 863 and 883 K. The increase of the temperature by only 20 K leads to a decrease of the polarization (electrode) resistance by a factor of ~3, which corresponds to an increase of the electrochemical activity. In Fig. 5(*b*) the impedance spectra of the thin-film cells measured in the EIS set-up are shown for two temperatures. A significantly larger polarization resistance was obtained at 873 K (the same temperatures as in the spectroelectrochemical cell). This could be due to a thicker electrode and/or lower surface area. By increasing the temperature to 898 K, the polarization resistance decreased significantly and thus the trend measured in the spectroelectrochemical cell was confirmed.

The Bode plots for both cells [Fig. 5(*c*) and 5(*d*)] indicate a pronounced process around frequencies of 1 Hz, which is assigned to oxygen stoichiometry changes in the LSCF thin-film electrodes.

Despite the different absolute values for the polarization resistances, the spectra obtained in the spectroelectrochemical cell and the EIS set-up show, in general, similar characteristics and trends with temperature and the results from the first can be used to evaluate electrochemical properties simultaneously with XANES.

3.4. Polarization of the fuel cell

As outlined in the *Introduction*, the ultimate objective is to characterize electrochemical cells under operating conditions that include the effect of polarization. The fuel cell was heated to 873 K and subjected to different potentials. Impedance spectra were recorded and XANES spectra as well. Polarization changes the local pO_2 and is thus expected to affect the oxidation state of cobalt in particular (Orikasa *et al.*, 2011).

During the heating, the periods of polarization and the periods at open circuit voltage, Co and Fe XANES spectra were recorded. In Fig. 6 the edge energy values for Co and Fe, the polarization and temperatures are shown over the whole

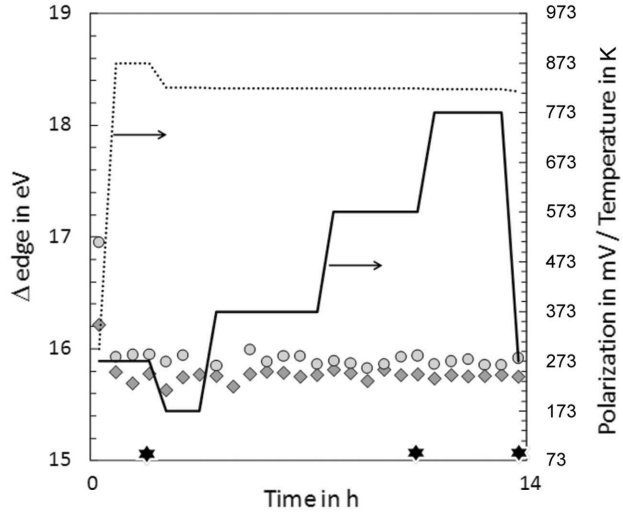

Figure 6
Co (circles) and Fe (diamonds) edge energies deduced from XANES spectra, expressed as ΔE ($E_{edge} - E_{edge\text{-}Me}$), are shown for the whole test sequence together with the polarization (full line) and temperature (dotted line); the stars on the time axis mark the times of recording impedance spectra (shown in Fig. 7).

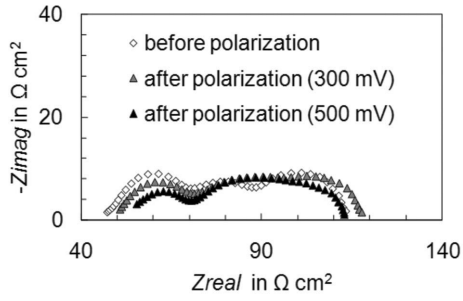

Figure 7
Impedance spectra of the fuel cell with LSCF electrodes recorded in 21% O_2 in He in the spectroelectrochemical cell before polarization (open symbols, 873 K), after polarization at initially −100 mV, later 100 mV, followed by 300 mV (grey symbols, 823 K), and after additional ∼3 h polarization at 500 mV (black symbols, 823 K).

test sequence. When heating from room temperature to 873 K without polarization, the edge energies for Co and Fe decreased, more significantly for cobalt (see Table 2), indicating a reduction of mainly cobalt ions in the perovskite structure, as presented and discussed in §3.2. In the period following the start of polarization at different degrees, both edge energies remained almost constant. The XANES spectra demonstrated that temperature has a larger effect on the oxidation states of cobalt (and iron) than polarization.

In Fig. 7 impedance spectra recorded before and after polarization at 300 and 500 mV are shown. Only small changes have occurred. The slight change of the serial resistance is most likely due to small temperature changes and not a result of the polarization. The spectrum recorded after exposure to the highest polarization of 500 mV indicates a slight decrease of the polarization resistance, *i.e.* the electrode seems to have activated. In general, the EIS results from before and after polarization are thus in line with the obtained XANES spectra, where no significant changes were observed as an effect of the polarization (see Fig. 6). It can be argued whether there should have occurred more significant changes of the oxidations states of cobalt and iron owing to polarization. The following issues have to be considered. The magnitude of polarization could be an important factor, *i.e.* that it was too low in this study to induce changes. Electrode thickness could be another parameter, even though the measurements were made on thin-film electrodes in this study. Further, the oxygen non-stoichiometry of the thin-film electrode used in this study could be a reason why no significant effects were observed owing to polarization. It has been shown to be lower when compared with bulk samples, maybe owing to 'imperfect' thin films (Plonczak *et al.*, 2012). The lower oxygen-nonstoichiometry means a lower number of positive ions with a change in polarization state during polarization and thus a smaller effect observable by XANES.

Future work should comprise thin layers of porous LSCF electrodes with a larger oxygen non-stoichiometry and cathodes with varying Co/Fe ratios to explore the mechanism of oxygen reduction under polarization in the SOFC in more detail.

4. Conclusion

The spectroelectrochemical cell used in this study for the first time proved to be able to provide reliable data for electrical impedance and for XANES under relevant conditions of a fuel cell, *i.e.* at elevated temperature, in the presence of relevant gases and under polarization. It has the potential to measure on a real solid oxide fuel cell and thus provide simultaneously information about the electrochemical performance and state of the transition metal components in the electrodes under operation.

Fuel cells with thin-film LSCF electrodes were studied at ∼873 K in synthetic air. When heating from room temperature, cobalt ions in the perovskite structure were reduced. The application of a polarization on the electrodes did not affect the oxidation states of iron or cobalt. Neither were the electrochemical properties, *i.e.* electrode processes, affected to a large extent as revealed by electrical impedance spectroscopy.

Further investigations are needed to reveal the effects of polarization, electrode composition and structure, pO_2, *etc.* on the electrode activity and the related characteristic oxidation states of the electrode components. Furthermore, a refined study might be able to distinguish processes occurring at the electrode/electrolyte interface from bulk processes in the electrode.

HASYLAB is gratefully acknowledged for providing beamline facilities and technical support. The authors thank Pawel Plonczak for providing EIS of thin film samples for comparison and for manufacturing the thin-film electrodes studied in this work, and Martin Soegaard for fruitful scientific discussions. This work was supported by The Programme Commission on Sustainable Energy and Environment, The Danish Council for Strategic Research, *via* the Strategic Electrochemistry Research Center (SERC) (http://www.serc.dk/), contract No. 2104-06-0011.

References

Backhaus-Ricoult, M., Adib, K., St Clair, T., Luerssen, B., Gregoratti, L. & Barinov, A. (2008). *Solid State Ion.* **179**, 891–895.
Braun, A., Shrout, S., Fowlks, A. C., Osaisai, B. A., Seifert, S., Granlund, E. & Cairns, E. J. (2003). *J. Synchrotron Rad.* **10**, 320–325.
Figueroa, S. J. A., Requejo, F. G., Lede, E. J., Lamaita, L., Andres Peluso, M. & Sambeth, J. E. (2005). *Catal. Today*, **107–108**, 849–855.
Haas, O., Vogt, U. F., Soltmann, C., Braun, A., Yoon, W.-S., Yang, X. Q. & Graule, T. (2009). *Mater. Res. Bull.* **44**, 1397–1404.
Hagen, A. (2011). *Chem. Phys. Lett.* **502**, 235–240.
Hagen, A. & Mikkelsen, L. (2005). *Proceedings of the 26th Risø International Symposium on Materials Science: Solid State Electrochemistry*, edited by S. Linderoth, A. Smith, N. Bonanos, A. Hagen, L. Mikkelsen, K. Kammer, D. Lybye, P. V. Hendriksen, F. W. Poulsen, M. Mogensen and W. G. Wang, pp. 197–202, Risø National Laboratory, Roskilde, Denmark.
Højgaard Jensen, S., Hjelm, J., Hagen, A. & Mogensen, M. B. (2009). *Handbook of Fuel Cells*, p. 1090. New York: Wiley.
Huang, K. & Goodenough, J. B. (2009). Editors. *Solid Oxide Fuel Cell Technology: Principles, Performance and Operations.* Oxford: Woodhead.

Knibbe, R., Hauch, A., Hjelm, J., Ebbesen, S. D. & Mogensen, M. (2011). *Green*, **1**, 141–169.
Le Toquin, R., Paulus, W., Cousson, A., Prestipino, C. & Lamberti, C. (2006). *J. Am. Chem. Soc.* **128**, 13161–13174.
Lu, X., Faguy, P. W. & Liu, M. (2002). *J. Electrochem. Soc.* **149**, A1293–A1298.
Mantzavinos, D., Hartley, A., Metcalfe, I. S. & Sahibzada, M. (2000). *Solid State Ion.* **134**, 103–109.
Mueller, N., De Souza, R. A., Brendt, J., Samuelis, D. & Martin, M. (2009). *J. Mater. Chem.* **19**, 1960–1963.
Nielsen, J., Jacobsen, T. & Wandel, M. (2011). *Electrochem. Acta*, **56**, 7963–7974.
Orikasa, Y., Ina, T., Nakao, T., Mineshige, A., Amezawa, K., Oishi, M., Arai, H., Ogumi, Z. & Uchimoto, Y. (2011). *Phys. Chem. Chem. Phys.* **13**, 16637–16643.
Plonczak, P., Bierberle-Hütter, A., Søgård, M., Hendriksen, P. V. & Gauckler, L. J. (2012). *J. Electrochem. Soc.* **159**, B1–B12.
Pomfret, M. B., Owrutsky, J. C. & Walker, R. (2010). *Annu. Rev. Anal. Chem.* **3**, 151–174.
Rasmussen, S. B., Hagen, S., Masters, S., Hagen, A., Ståhl, K., Eriksen, K. M., Simonsen, P., Jensen, J. N., Berg, M., Chorkendorff, I. & Fehrmann, R. (2003). *PowerPlant Chem.* **5**, 360–369.
Rodriguez, M. A., Ingersoll, D. & Doughty, D. H. (2000). *Adv. X-ray Anal.* **42**, 267–275.
Scott, S. P., Mantzavinos, D., Hartley, A., Sahibzada, M. & Metcalfe, I. S. (2002). *Solid State Ion.* **152–153**, 777–781.
Simonsen, V. L. E., Nørskov, L., Hagen, A. & Kammer Hansen, K. (2009). *J. Solid State Electrochem.* **13**, 1529–1534.
Wong, J., Lytle, F. W., Messmer, R. P. & Maylotte, D. H. (1984). *Phys. Rev. B*, **30**, 5596–5610.
Yildiz, B., Chang, K.-C., Myers, D., Carter, J. D. & You, H. (2006). *Proceedings of the 7th European Solid Oxide Fuel Cell Forum*, 3–7 July 2006.